

POLITECNICO DI TORINO

Collegio di Ingegneria Civile

**Corso di Laurea Magistrale
in Ingegneria Civile**

Tesi di Laurea Magistrale

Seismic vulnerability of historical and monumental buildings

Modena Cathedral



Relatori

Prof. Donato Sabia

Prof. Takayoshi Aoki

Candidato

Manuel Rovesti

Marzo 2020

*Quelli che s'innamorano di pratica
senza scienza sono come il nocchiero
che entra in naviglio senza timone
o bussola e mai ha la certezza di
dove si vada. Sempre la pratica deve
essere edificata sopra buona teoria.*

Leonardo da Vinci

Alla mia famiglia



Ringraziamenti/Acknowledgements

In primis vorrei ringraziare i miei Professori Donato Sabia e Takayoshi Aoki per avermi aiutato a svolgere il lavoro di Tesi e per avermi trasmesso la loro passione per la materia. Vorrei ringraziarli per la loro disponibilità e per avermi dato l'opportunità di svolgere la mia Tesi in Giappone. Un'esperienza indimenticabile che mi ha fatto crescere sia dal punto di vista professionale che come persona.

Un grande ringraziamento va alla mia famiglia che mi ha sempre sostenuto dandomi la forza di non mollare mai. Li ringrazio per l'aiuto e le possibilità che mi hanno dato, consentendomi il conseguimento di questo importante traguardo.

Un ultimo ringraziamento va a tutti i miei amici e colleghi incontrati in questi due anni di Laurea Magistrale e durante la mia esperienza in Giappone, li ringrazio per i momenti condivisi insieme all'interno e all'esterno del Politecnico e per le avventure indimenticabili trascorse insieme.

Grazie a tutti

Manuel



Contents

Ringraziamenti/Acknowledgements.....	i
List of Figures.....	7
List of Tables.....	23
Chapter 1 Introduction.....	25
1.1 Collapse mechanisms of churches	26
Chapter 2 The Historical Masonry	35
2.1 Introduction.....	35
2.2 Constituent materials.....	36
2.2.1 Stone bricks	36
2.2.2 Clay bricks.....	38
2.2.3 Mortar	38
2.3 Types of historical masonry	41
2.3.1 Opus quadratum	44
2.3.2 Filling-core masonry	54
2.3.3 Ordinary masonry.....	59
2.4 Art rules	61
2.4.1 Monolithic behaviour	61
2.4.2 Horizontal planes.....	63
2.4.3 Mortar function	64
Chapter 3 Mechanical behaviour.....	65
3.1.1 Mortar and joints.....	65
3.1.2 Brick.....	73
3.1.3 Composite material.....	74



Chapter 4 Masonry Modelling	85
4.1 Introduction	85
4.2 Micro and macro-modelling.....	85
4.2.1 Micro-modelling	87
4.2.2 Macro-modelling	97
Chapter 5 Case Study: Modena Cathedral	107
5.1 Introduction	107
5.2 Location and seismic classification.....	108
5.3 History	112
5.4 Construction phases	115
5.4.1 State of the art.....	116
5.4.2 New hypotheses on anomalies	122
5.5 Information needed for modelling	131
5.5.1 Material identification.....	131
5.5.2 Foundation.....	133
5.5.3 Current structural reinforcement: tie-rods.....	134
5.5.4 Monitoring system.....	135
Chapter 6 Construction of the Structural Model	143
6.1 Introduction	143
6.2 From the point cloud data to the geometry	143
6.2.1 The point cloud model.....	144
6.2.2 Construction of the geometry	149
6.3 Geometric simplifications adopted	155
6.4 The structural model	159
6.4.1 Finite elements used.....	159



6.4.2	Boundary condition	162
6.4.3	Mesh	165
Chapter 7 Calibration: Model Updating.....		167
7.1	Introduction.....	167
7.2	Model updating theory	168
7.2.1	Modal assurance criterion (MAC)	168
7.2.2	Modal updating technique	169
7.3	Experimental dynamic identification	172
7.3.1	Experimental vibration mode.....	173
7.4	Model updating results.....	176
7.4.1	Initial model	176
7.4.2	Modal analysis of the initial model	179
7.4.3	Comparison between the experimental and the initial model data.....	185
7.4.4	Updated model.....	186
Chapter 8 Seismic analysis.....		193
8.1	Introduction.....	193
8.2	Linear transient response analysis	193
8.2.1	Amatrice (Lazio) earthquake of 24-08-2016.....	194
8.2.2	Finale Emilia (Emilia-Romagna) earthquake of 29-05-2012 .	202
8.3	Non-linear dynamic analysis - Dome	220
8.3.1	Input data	220
8.3.2	Assumptions adopted in modelling.....	225
8.3.3	Material properties.....	226
8.3.4	Results.....	228



Chapter 9 Conclusions	242
Appendix A – Drawings	247
Appendix B – Model Material	261
Bibliography.....	267

List of Figures

Figure 1.1 - Macro-elements of church buildings [1].	27
Figure 1.2 - Macro-elements of church buildings [1].	28
Figure 1.3 - Macro-elements of church buildings [1].	29
Figure 1.4 – Left: Overturning of the façade - detachment of the facade from the walls or evident out of plumb; Right: Mechanisms on the top of the facade - overturning of the tympanum [2].	30
Figure 1.5 – Left: Mechanisms on the top of the facade - overturning of the tympanum with V-shaped damage; Right: Vaults of the lateral naves - damage in the vaults, disconnections of the arches and of the side walls [2].	30
Figure 1.6 – Vaults of the central nave - damage in the vaults of the central hall, disconnections of the vaults with arches [2].	31
Figure 1.7 – Triumphal arches - lesions in the arch and sliding of the segments [2].	31
Figure 1.8 - Dome - tambour/lantern - damages in the dome with possible continuation in the tambour [2].	32
Figure 1.9 - Shear mechanisms in the walls of the transept - complete collapse [2].	32
Figure 1.10 - Overturning of the apse - vertical or curved lesions in the walls of the apse [2].	33
Figure 1.11 - Bell tower - damage near the detachment from the body of the church [2].	33
Figure 2.1 – An example of opus quadratum [5].	44
Figure 2.2 – Vertical load diffusion [6].	45
Figure 2.3 - Inclined load diffusion [6].	45
Figure 2.4 – The pseudo tensile strength of the masonry wall [5].	46

Figure 2.5 – The two collapse mechanisms [5].	47
Figure 2.6 - Monolithic wall with horizontal and a vertical force and graphic solution [5].	49
Figure 2.7 - Analysis of the opus quadratum with concentrated force [5].	50
Figure 2.8 - Difference between a wall with and without bond stones [5].	52
Figure 2.9 - Ultimate load according to the arrangement of the bond stones and distribution of the voltages on the blocks.	53
Figure 2.10 – a) Vertical section of the Greek masonry with èmplekton;	55
Figure 2.11 – External wall: a) Opus quadratum b) Opus incertum c) and d) Opus reticulatum e) Opus testaceum f) Opus vittatum. [7]	55
Figure 2.12 - Filling-core wall schematization [3].	56
Figure 2.13 - Instability problems due to lateral actions for filling expansion [3].	58
Figure 2.14 - Lateral actions due to expansion of the without cohesion filling [3].	58
Figure 2.15 - Vertical section of the ordinary masonry [7].	59
Figure 2.16 - Ordinary masonry: a) with different external walls; b) with external walls in semi-square blocks [7].	60
Figure 2.17 - a) Inclined action inside the masonry; b) Instability problems [8].	62
Figure 2.18 – Horizontal planes and respective cinematic mechanism [6].	63
Figure 2.19 – a) Correct thickness of the joints; b) Excessive thickness of the joints [6].	64
Figure 3.1 - Measured properties for different confining stresses: a) Type M strong mortar; b) Type O weak mortar [9].	66
Figure 3.2 – Variation of Young’s modulus with normal and confining stresses: a) Type “M” strong mortar; b) Type “O” weak mortar [9].	66
Figure 3.3 – Variation of Poisson’s coefficient with normal and confining stresses: a) Type “M” strong mortar; b) Type “O” weak mortar [9].	67



Figure 3.4 - Global cyclic loading response curves for four-cycle shear test on masonry specimen consisting of old Bricks and 1:2:9 mortar mixture with 13-mm joint thickness at constant normal load equal to 13.7 kN [10]. 68

Figure 3.5 – Enlargement of the pre-peak loading response [10]...... 68

Figure 3.6 - Normal displacement-shear displacement response [10]...... 68

Figure 3.7 - Peak and residual shear strength envelopes for old bricks and 1:2.9 Mortar specimens and bed joint thicknesses of 13 mm [10]. 69

Figure 3.8 - Peak and residual shear strength envelopes for old bricks and 1:2.9 mortar specimens and bed joint thicknesses of 7 mm [10]...... 69

Figure 3.9 - Variation of shear stiffness k_s in function of the shear displacement u for different normal stresses σ_n ranging between 0.5 and 5.0MPa: old brick and 1:2:9 mortar specimens with 7-mm thick bed joints [10]...... 70

Figure 3.10 - Variation of shear stiffness k_s in function of the shear displacement u at normal stress of 3MPa for three types of laboratory specimens [10]. 70

Figure 3.11 - Tensile behaviour of the masonry joint and test equipment [11]. 71

Figure 3.12 – a) Shear behaviour of the masonry joint for different confinement levels b) Shear-normal stress envelope for different types of laboratory specimens [12]. 72

Figure 3.13 - Measured biaxial interaction diagram for brick specimens [9]. 73

Figure 3.14 - Typical splitting failure of test prism [9]...... 74

Figure 3.15 - Measured stress-strain curves for test prisms constructed with brick type 1 and different mortar types [9]. 75

Figure 3.16 – Comparison between masonry and its components behaviour [15]. 75

Figure 3.17 – Compression stress-strain curves [17]. 76

Figure 3.18 - Variation of prism compressive strength with mortar joint thickness [18]...... 77

Figure 3.19 - Shear stress-strain curves [17]. 77

Figure 3.20 - a) Combined failure of the secondary joints and blocks; b) Failure of the secondary joints due to the sliding of the main ones [19]. 78

Figure 3.21 – Stress-strain curve for the a) collapse [19].	78
Figure 3.22 - Stress-strain curve for the b) collapse [19].	79
Figure 3.23 - Failure modes for biaxial compression tests on brickwork: a) Uniaxial compression; b) Biaxial compression [20].	79
Figure 3.24 - Failure surface for half-scale brickwork under biaxial compressive stress [20].	80
Figure 3.25 - Failure surface for brickwork under biaxial compression projected onto σ_1 - σ_2 plane [20].	80
Figure 3.26 - Stress and strain transformations [21].	81
Figure 3.27 - Measured stress-strain curves for panel under biaxial compression-compression (1MPa = 145psi) [21].	81
Figure 3.28 – Failure modes for biaxial tension-compression tests on brickwork [20].	82
Figure 3.29 - Failure surface for half-scale brickwork under biaxial tension-compressive stress [20].	83
Figure 3.30 - Failure surface for brickwork under biaxial tension-compression projected onto σ_1 - σ_2 plane [20].	83
Figure 3.31 - Measured stress-strain curves for panel under biaxial tension-compression (1MPa = 145psi)	84
Figure 4.1 - Modelling strategies for masonry structures: (a) masonry sample; (b) detailed micro-modelling; (c) simplified micro-modelling; (d) macro-modelling [22].	86
Figure 4.2 - Hyperbolic yield criterion [23].	88
Figure 4.3 – Non-associated flow rule [23].	88
Figure 4.4 - Constitutive model for masonry units: (a) yield criterion for masonry units; (b) uniaxial behaviour of masonry units [23].	89
Figure 4.5 – Walls with header blocks subject to vertical and to the ultimate horizontal body forces: analysis results in comparison with the experimental one [24].	90
Figure 4.6 – Failure mechanisms of masonry.	91

Figure 4.7 - Suggested modelling strategy. Units (u) are modelled with continuum elements. Mortar joints (m) and potential cracks in the units are modelled with zero-thickness interface elements [25]. 92

Figure 4.8 - Proposed model for interfaces. An “interface cap model” [25]. 92

Figure 4.9 – Yield conditions represented in the stress space [26]. 94

Figure 4.10 – Hyperbolic asperity model [26]. 95

Figure 4.11 – Masonry specimen extracted from an infinitely long wall under tensile loading parallel to the bed joint [26]. 95

Figure 4.12 – Load-displacement curves for different values of the initial asperity angles [26]..... 96

Figure 4.13 - (a) Geometry of a structural masonry panel; (b) Medium 1; (c) Medium 1 intercepted by bed joints [27]. 97

Figure 4.14 – Fundamental mechanisms of uncontained flow: I) Pure opening; II) Pure sliding; III) Opening at staggered joints and sliding along the aligned ones; IV) Opening at aligned joints and sliding along the staggered ones [28]. 99

Figure 4.15 - Piecewise linear limiting surface of local possible equilibrium for $a/h = 0.5$ and $p = 0.5$: (a) in the space of the stress state components $\sigma_x, \sigma_y, \tau_{xy}$; (b) on a plane $\sigma_y = \text{constant}$; (c) on the plane $\tau_{xy} = 0$ [28]. 100

Figure 4.16 - Mechanism I: Slipping on mortar joints [29]. 101

Figure 4.17 – a) b) Mechanism II: Slipping on bed joints; c) Mechanism III: Splitting of bricks and slipping on mortar joints [29]. 101

Figure 4.18 - Mechanism IV: Splitting of bricks and head joints [29]. 101

Figure 4.19 – a) Mechanism V: Slipping of bed joints and splitting of head joints for tension parallel to bed joints; Mechanism VI: Splitting of bed joints for: (b) Compression parallel to bed joints; (c) Tension normal to parallel to bed joints; d) e) Mechanism VII: Slipping and splitting of mortar joints [29]. 102

Figure 4.20 – Mechanism VIII: Middle plane spalling [29]. 102

Figure 4.21 – Repetitive unit cell for the regular masonry material [30]. 102

Figure 4.22 - Possible damaged states of old masonry material [30]. 103

Figure 4.23 – a) Limit surface for the state S1 obtained by using the energy criterion;
b) Limit surface for the state S1 obtained by using the cohesive local criterion [30].
..... 104

Figure 4.24 - Proposed composite yield criterion with iso-shear stress lines [31].
..... 105

Figure 4.25 – a) Stress-strain response in uniaxial tension along the two material
axes; b) Stress-strain response in uniaxial compression along the two material
axes [31]...... 105

Figure 5.1 – 3D view of the Modena Cathedral (Google Maps images 2019)..... 107

Figure 5.2 - Location of Modena Cathedral - Northern Italy view..... 108

Figure 5.3 – Location of Modena Cathedral – City view (Google Maps images) 108

Figure 5.4 - Seismic hazard map of the national territory, of Modena and
surrounding areas (National Institute of Geophysics and Volcanology)..... 109

Figure 5.5 - Seismic classification of the Emilia-Romagna region (DGR 1164 del
23/07/2018 " Update of the first application seismic classification of the
municipalities of Emilia-Romagna") 110

Figure 5.6 - Relatio sive descriptio de innovatione ecclesie santi Geminiani [33]
..... 113

Figure 5.7 – Modena cathedral façade (Photography Manuel Rovesti survey 29-08-
2019) 114

Figure 5.8 - State of the art on the construction phases [34]: diagram of the division
into phases proposed by [43] in continuity with the idea of Porter (1927). 117

Figure 5.9 - State of the art on the construction phases [34]: graphic revision of the
division in phases as published by [43] and [44] based on drawings by G.Palazzi.
A part of the north side and the Porta Pescheria, due to the various restorations
undergone, are not attributed by Peroni to a precise phase. However, in the
contribution of [44] they are attributed to phase B..... 118

Figure 5.10 - Wall thickening on the north side (Photography Manuel Rovesti
survey 29-08-2019)..... 119

Figure 5.11 - Anomaly minor arch on the south side (Photography Manuel Rovesti
survey 29-08-2019)..... 120

Figure 5.12 – Anomalies in the facade (Photography Manuel Rovesti survey 29-08-2019).	121
Figure 5.13 - Visible settlements in east and north directions (Photography Manuel Rovesti survey 29-08-2019).	122
Figure 5.14 - Correspondence between construction phases and crack pattern. .	124
Figure 5.15 - View of the Modena Cathedral from Piazza Grande (Photography Manuel Rovesti survey 29-08-2019).....	125
Figure 5.16 - Re-reading of phase C: interruptions left in phase A due to settlements and connected later [34].	126
Figure 5.17 - Wall thickening damage - Note the cracks reopened and some stuccowork carried out following the subsidence of the 1970s, before the intervention restoration project in the 1980s [34]. Survey of the cracks (Silvestri Technical Study) on drawings by G.Palazzi - Photographs by C.Leonardi extracted from [49].	127
Figure 5.18 – Front loggias (Photography Manuel Rovesti survey 29-08-2019)..	128
Figure 5.19 - Example diagram of the origin of the 28 cm gap [34].	129
Figure 5.20 - Re-reading of the construction sequence of phases A, B, C (excluding Campionesi interventions). Scheme by E. Silvestri [34]. The sequence A, A', and A'' is represented as theorized by Peroni and Lomartire, however doubts are expressed about the anteriority of phase A' with respect to A''.	130
Figure 5.21 – Plan of the Modena Cathedral with the test areas [50].	132
Figure 5.22 - Experimental reconstructive scheme of the foundation [51].	133
Figure 5.23 – Tie-rods position (in blue dotted the chains added thanks to the inspection of the 29/08/2019) [52].....	134
Figure 5.24 - Capacitive uniaxial accelerometer [35].....	136
Figure 5.25 - Plan, fronts and section of the Cathedral with indication of the position of the monitoring points [35].	137
Figure 5.26 - Measurement point 1 - Recording channels and accelerometers 1, 2 and 3 [35].	138

Figure 5.27 - Measurement point 2 - Recording channels and accelerometers 4 [35].	138
Figure 5.28 - Measurement point 3 - Recording channels and accelerometers 5 [35].	138
Figure 5.29 - Measurement point 4 - Recording channels and accelerometers 6 [35].	139
Figure 5.30- Measurement point 5 - Recording channels and accelerometers 7 and 8 [35].	139
Figure 5.31 - Measurement point 6 - Recording channels and accelerometers 9 [27].	139
Figure 5.32 - Measurement point 7 - Recording channels and accelerometers 10 [27].	140
Figure 5.33 - Measurement point 8 - Recording channels and accelerometers 11 [27].	140
Figure 5.34 - Measurement point 9 - Recording channels and accelerometers 12 [27].	140
Figure 5.35 Measurement point 10 - Recording channels and accelerometers 13 [27].	141
Figure 5.36 Measurement point 11 - Recording channels and accelerometers 14 [27].	141
Figure 5.37 Measurement point 12 - Recording channels and accelerometers 15 and 16 [27].	141
Figure 6.1 – a) Location map of the scanning positions b) Terrestrial laser scanner model Scan Station 2 by Leica Geosystems, during survey operations [53].	144
Figure 6.2 – a) Overhang analysis in south-north direction;	145
Figure 6.3 – a) Inclination analysis of the north side in the vertical plane;	146
Figure 6.4 – Inclination analysis of the south side in the vertical plane [51].	146
Figure 6.5 - Geometrical anomaly with respect to verticality of the pillars [54].	146
Figure 6.6 – Point cloud model: overall view of the Cathedral [51].	147



Figure 6.7 – Point cloud model: internal view of the Cathedral [51].	147
Figure 6.8 – Point cloud model in the Infipoints software: view of the apse.	148
Figure 6.9 – Point cloud model in the Infipoints software: view of the façade..	148
Figure 6.10 – 3D geometric model on Rhinoceros - Perspective view 1.....	149
Figure 6.11 – 3D geometric model on Rhinoceros - Perspective view 2.....	150
Figure 6.12 – 3D geometric model on Rhinoceros - Top view	150
Figure 6.13 – 3D geometric model on Rhinoceros - South facade view	151
Figure 6.14 – 3D geometric model on Rhinoceros - North facade view.....	151
Figure 6.15 – 3D geometric model on Rhinoceros - West facade view.....	152
Figure 6.16 – 3D geometric model on Rhinoceros - East facade view	152
Figure 6.17 – 3D geometric model on Rhinoceros - Top view without roof.....	153
Figure 6.18 – 3D geometric model on Rhinoceros - Internal view of the sectioned model	153
Figure 6.19 – 3D geometric model on Rhinoceros - Internal view of the sectioned model	154
Figure 6.20 - 3D geometric model on Rhinoceros - Apse detail	154
Figure 6.21 - Pillars supporting the arches on the facade: a) 3D geometric model on Rhinoceros; b) Real detail (Photography Manuel Rovesti survey 29-08-2019). ..	155
Figure 6.22 - Arches on the facade: a) 3D geometric model on Rhinoceros; b) Real detail (Google Maps Street View).....	156
Figure 6.23 – Internal main columns: a) 3D geometric model on Rhinoceros; b) Real detail (UNESCO Modena Website).....	156
Figure 6.24 – Apse basement modelled with an equivalent plate: 3D geometric model on Rhinoceros.....	157
Figure 6.25 – Apse basement modelled with domes: 3D geometric model on Rhinoceros.....	158
Figure 6.26 – a) ABAQUS/CAE C3D4 linear isoparametric tetrahedron element b) ABAQUS/CAE C3D10 quadratic isoparametric tetrahedron element [55].....	160
Figure 6.27 – Foundation layout adopted.....	162

Figure 6.28 – Trusses disposition for modelling Cathedral-Ghirlandina Tower interaction.....	163
Figure 6.29 – Tie-rods reinforcement system at the base.....	164
Figure 6.30 – Tie-rods reinforcement system at the top.....	164
Figure 6.31 – Meshed model – View 1.....	165
Figure 6.32 – Meshed model – View 2.....	166
Figure 7.1 – 3D view of the first experimental mode	173
Figure 7.2 – 3D view of the second experimental mode	174
Figure 7.3 – 3D view of the third experimental mode	175
Figure 7.4 – Material ID explanation (Drawing of Giancarlo Palazzi).	176
Figure 7.5 – Material ID explanation (Drawing of Giancarlo Palazzi).	177
Figure 7.6 - FEA model with the different materials assigned – View1	178
Figure 7.7 - FEA model with the different materials assigned – View 2.....	178
Figure 7.8 – First mode of the initial model – 4 nodes elements (2.22Hz).....	181
Figure 7.9 – First mode of the initial model – 4 nodes elements (2.22Hz).....	181
Figure 7.10 – Second mode of the initial model– 4 nodes elements (3.56Hz).....	182
Figure 7.11 – Second mode of the initial model – 4 nodes elements (3.56Hz).....	182
Figure 7.12 – Third mode of the initial model – 4 nodes elements (4.01Hz).....	183
Figure 7.13 – Third mode of the initial model – 4 nodes elements (4.01Hz).....	183
Figure 7.14 – Fourth mode of the initial model – 4 nodes elements (4.69Hz).....	184
Figure 7.15 – Fourth mode of the initial model– 4 nodes elements (4.69Hz).....	184
Figure 7.16 – First mode of the updated model – 4 nodes elements (1.99Hz).	188
Figure 7.17 – First mode of the updated model – 4 nodes elements (1.99Hz).	188
Figure 7.18 – Second mode of the updated model – 4 nodes elements (3.06Hz).189	
Figure 7.19 – Second mode of the updated model – 4 nodes elements (3.06Hz).189	
Figure 7.20 – Third mode of the updated model – 4 nodes elements (3.20Hz)...190	
Figure 7.21 – Third mode of the updated model – 4 nodes elements (3.20Hz)...190	



Figure 7.22 – Fourth mode of the updated model – 4 nodes elements (3.41Hz). 191

Figure 7.23 – Fourth mode of the updated model – 4 nodes elements (3.41Hz). 191

Figure 8.1 – Acceleration time history recorded during earthquake of 24-08-2016 X direction..... 194

Figure 8.2 – Acceleration time history recorded during earthquake of 24-08-2016 Y direction..... 195

Figure 8.3 – Acceleration time history recorded during earthquake of 24-08-2016 Z direction..... 195

Figure 8.4 – Pseudo acceleration spectrum of the input signal – CH1-X (Base). 196

Figure 8.5 – Pseudo acceleration spectrum of the input signal – CH1-Y (Base). 196

Figure 8.6 – Pseudo acceleration spectrum of the input signal – CH1-Z (Base). 196

Figure 8.7 – Comparison pseudo acceleration spectrum: Experimental, Initial model and Updated model – CH2-Y..... 197

Figure 8.8 – Comparison pseudo acceleration spectrum: Experimental, Initial model and Updated model – CH3-Y..... 198

Figure 8.9 – Comparison pseudo acceleration spectrum: Experimental, Initial model and Updated model – CH4-Y..... 198

Figure 8.10 – Comparison pseudo acceleration spectrum: Experimental, Initial model and Updated model – CH5-X..... 199

Figure 8.11 – Comparison pseudo acceleration spectrum: Experimental, Initial model and Updated model – CH5-Y..... 199

Figure 8.12 – Comparison pseudo acceleration spectrum: Experimental, Initial model and Updated model – CH6-X..... 200

Figure 8.13 – Comparison pseudo acceleration spectrum: Experimental, Initial model and Updated model – CH7-X..... 200

Figure 8.14 – Comparison pseudo acceleration spectrum: Experimental, Initial model and Updated model – CH8-X..... 201

Figure 8.15 – Acceleration time history recorded during earthquake of 29-05-2012 X direction..... 202



Figure 8.16 – Acceleration time history recorded during earthquake of 29-05-2012 Y direction.	203
Figure 8.17 – Acceleration time history recorded during earthquake of 29-05-2012 Z direction.	203
Figure 8.18 – Pseudo acceleration spectrum of the input signal – CH1-X (Base).	204
Figure 8.19 – Pseudo acceleration spectrum of the input signal – CH1-Y (Base).	204
Figure 8.20 – Pseudo acceleration spectrum of the input signal – CH1-Z (Base).	205
Figure 8.21 – Pseudo acceleration spectrum – Numerical model – CH2-Y.....	206
Figure 8.22 – Pseudo acceleration spectrum – Numerical model – CH3-Y.....	207
Figure 8.23 – Pseudo acceleration spectrum – Numerical model – CH4-Y.....	207
Figure 8.24 – Pseudo acceleration spectrum – Numerical model – CH5-X.....	208
Figure 8.25 – Pseudo acceleration spectrum – Numerical model – CH5-Y.....	208
Figure 8.26 – Pseudo acceleration spectrum – Numerical model – CH6-X.....	209
Figure 8.27 – Pseudo acceleration spectrum – Numerical model – CH7-X.....	209
Figure 8.28 – Pseudo acceleration spectrum – Numerical model – CH8-X.....	210
Figure 8.29 - Points of application of the time histories at the base of the dome.	211
Figure 8.30 – Comparison pseudo acceleration spectrum: Input X and numerical PointA-X output.	211
Figure 8.31 – Comparison pseudo acceleration spectrum: Input Y and numerical Point A-Y output.	212
Figure 8.32 – Comparison pseudo acceleration spectrum: Input Z and numerical Point A-Z output.	212
Figure 8.33 – Comparison pseudo acceleration spectrum: Input X and numerical Point B-X output.	213
Figure 8.34 – Comparison pseudo acceleration spectrum: Input Y and numerical Point B-Y output.	213



Figure 8.35 – Comparison pseudo acceleration spectrum: Input Z and numerical Point B-Z output..... 214

Figure 8.36 – Comparison pseudo acceleration spectrum: Input X and numerical Point C-X output. 214

Figure 8.37 – Comparison pseudo acceleration spectrum: Input Y and numerical Point C-Y output. 215

Figure 8.38 – Comparison pseudo acceleration spectrum: Input Z and numerical Point C-Z output. 215

Figure 8.39 – Comparison pseudo acceleration spectrum: Input X and numerical Point D-X output. 216

Figure 8.40 – Comparison pseudo acceleration spectrum: Input Y and numerical Point D-Y output. 216

Figure 8.41 – Comparison pseudo acceleration spectrum: Input Z and numerical Point D-Z output. 217

Figure 8.42 – Amplifications on the structure at the accelerometers..... 218

Figure 8.43 – Amplifications at the base of the dome.. 218

Figure 8.44 - Points of application of the time histories at the base of the dome.220

Figure 8.45 – Acceleration time history: 2012 earthquake - point A - X direction. 221

Figure 8.46 – Acceleration time history: 2012 earthquake - point A - Y direction. 221

Figure 8.47 – Acceleration time history: 2012 earthquake - point A - Z direction. 221

Figure 8.48 – Acceleration time history: 2012 earthquake - point B - X direction. 222

Figure 8.49 – Acceleration time history: 2012 earthquake - point B - Y direction. 222

Figure 8.50 – Acceleration time history: 2012 earthquake - point B - Z direction. 222



Figure 8.51 – Acceleration time history: 2012 earthquake - point C - X direction.	223
Figure 8.52 – Acceleration time history: 2012 earthquake - point C - Y direction.	223
Figure 8.53 – Acceleration time history: 2012 earthquake - point C - Z direction.	223
Figure 8.54 – Acceleration time history: 2012 earthquake - point D - X direction.	224
Figure 8.55 – Acceleration time history: 2012 earthquake - point D - Y direction.	224
Figure 8.56 – Acceleration time history: 2012 earthquake - point D - Z direction.	224
Figure 8.57 - Mesh and subdivision of the dome material.	225
Figure 8.58 – Stress-strain compressive masonry behaviour.	227
Figure 8.59 – Stress-strain tensile masonry behaviour.	227
Figure 8.60 - Damage scenario corresponding to 80% of the 2012 earthquake - Step: 18 seconds - Bottom view.	229
Figure 8.61 - Damage scenario corresponding to 80% of the 2012 earthquake - Step: 24 seconds - Bottom view.	229
Figure 8.62 - Damage scenario corresponding to 80% of the 2012 earthquake - Step: 18 seconds - Top view.	230
Figure 8.63 - Damage scenario corresponding to 80% of the 2012 earthquake - Step: 24 seconds - Top view.	230
Figure 8.64 - Damage scenario corresponding to 100% of the 2012 earthquake - Step: 18 seconds - Bottom view.	231
Figure 8.65 - Damage scenario corresponding to 100% of the 2012 earthquake - Step: 24 seconds - Bottom view.	231
Figure 8.66 - Damage scenario corresponding to 100% of the 2012 earthquake - Step: 18 seconds - Top view.	232



Figure 8.67 - Damage scenario corresponding to 100% of the 2012 earthquake -
Step: 24 seconds - Top view..... 232

Figure 8.68 - Damage scenario corresponding to 120% of the 2012 earthquake -
Step: 18 seconds - Bottom view..... 233

Figure 8.69 - Damage scenario corresponding to 120% of the 2012 earthquake -
Step: 24 seconds - Bottom view..... 233

Figure 8.70 - Damage scenario corresponding to 120% of the 2012 earthquake -
Step: 18 seconds - Top view..... 234

Figure 8.71 - Damage scenario corresponding to 120% of the 2012 earthquake -
Step: 24 seconds - Top view..... 234

Figure 8.72 - Damage scenario corresponding to 160% of the 2012 earthquake -
Step: 18 seconds - Bottom view..... 235

Figure 8.73 - Damage scenario corresponding to 160% of the 2012 earthquake -
Step: 22 seconds (Collapse) - Bottom view..... 235

Figure 8.74 - Damage scenario corresponding to 160% of the 2012 earthquake -
Step: 18 seconds - Top view..... 236

Figure 8.75 - Damage scenario corresponding to 160% of the 2012 earthquake -
Step: 22 seconds (Collapse) - Top view..... 236

Figure 8.76 – Acceleration time history point A – X direction - 16 seconds. 237

Figure 8.77 – Acceleration time history point B – X direction - 16 seconds. 237

Figure 8.78 – Acceleration time history point A – X direction - 21 seconds. 238

Figure 8.79 – Acceleration time history point B – X direction - 21 seconds. 238

Figure 8.80 – Acceleration time history point A – Y direction - 15 seconds. 238

Figure 8.81 – Acceleration time history point B – Y direction - 15 seconds. 239

Figure 8.82 – Acceleration time history point A – Y direction - 23 seconds. 239

Figure 8.83 – Acceleration time history point B – Y direction - 23 seconds. 239

Figure 8.84 - Damage obtained by recent earthquakes..... 240

Figure 8.85 - Damage obtained by recent earthquakes..... 241



Figure 9.1 - Damage scenario corresponding to 100% of the 2012 earthquake - Step:
24 seconds..... 243

Figure 9.2 - Damage scenario corresponding to 160% of the 2012 earthquake - Step:
22 seconds (Collapse)..... 244



List of Tables

Table 3-1 – Possible damage paths [30].....	104
Table 4-1 - Static elastic modulus and waves speed for each area $\nu=0.2$ $\rho=1.8\text{kN/m}^3$ [50].....	132
Table 4-2 - Technical characteristics of the measuring instruments	136
Table 6-1 - Experimental vibration mode data	172
Table 6-2 – Modal analysis results - Initial model: Frequency and Participation factor	179
Table 6-3 – Modal analysis results - Initial model: Frequency and Modal mass	180
Table 6-4 - Experimental and Numerical data – Initial model	185
Table 6-5 - Experimental and Numerical data – Initial model	186
Table 6-6 - Experimental and Numerical data – Updated model – 4 nodes elements	186
Table 6-7 – Modal analysis results - Updated model: Frequency and Participation factor	187
Table 6-8 – Modal analysis results - Updated model: Frequency and Modal mass	187
Table 7-1 - Earthquake of 24-08-2016 - Main data.	194
Table 7-2 - Main station data.	202
Table 7-3 - Earthquake of 29-05-2012 - Main data.	202
Table 7-4 – Amplification of the input acceleration.	219
Table 7-5 – Material elastic parameter	226
Table 7-6 – Material plasticity parameters.....	226
Table 7-7 – Material compressive inelastic behaviour	226
Table 7-8 – Material tensile cracking behaviour	226



Table 7-9 – PGA input at the base of the structure	228
Table-1 – Initial and Updated material - Masonry	261
Table 2 – Initial and Updated material – Truss Ghirlandina Tower	266
Table 3 – Tie-rods properties (for the position refer to chapter 5.5.3).....	266

Chapter 1

Introduction

In the last few years, Italy has been affected by a high number of earthquakes causing victims and high damage to structures. Among these we can remember the earthquake of 6 April 2009 with epicentre in L'Aquila (Abruzzo) and magnitude 5.9 on the Richter scale, the earthquake of 29 May 2012 with epicentre in Finale Emilia (Emilia-Romagna) and magnitude 5.9, the earthquake of 24 August 2016 with epicentre in Amatrice (Lazio) and magnitude 6.0 and finally the earthquake of 30 August 2016 with epicentre in Norcia (Umbria) and magnitude 6.1. The main problems that have been encountered after these events concern the malfunction of the structures under the action of the earthquake. This is mainly because of the Italian civil and cultural heritage is represented by historical structures made of ancient masonry, often with a high state of deterioration or not adequately reinforced to resist horizontal actions such as those of an earthquake.

Furthermore, after these events, there was a high loss of cultural heritage, such as churches, monuments, towers etc. Being our country rich in monuments, it is necessary to adapt them correctly as regards structural behaviour in order to have a conservation and limit the damage of them even in the aftermath of major earthquakes. For this reason, in this thesis work I wanted to study the behaviour of historic masonry and how it is modelled in the FEM software, but above all to study the seismic vulnerability of the Cathedral of Modena belonging to the *UNESCO* Heritage of Cultural Heritage.

The difficulties encountered in the construction of structural models, such as the one in question, are as many as for example the geometry of the structure in most cases very complex. In addition, it is not possible to carry out destructive mechanical tests, being a structure belonging to the UNESCO Heritage as reported in "*Guidelines for the evaluation and reduction of the seismic risk of cultural heritage with reference to technical standards for construction*" in Chapter 4.1.7, therefore for the definition of materials you have to proceed in other ways, for example as in our case using monitoring. Finally, the presence of complicated geometries and many finite elements make the analyses heavy and with a high computational burden. To solve all these problems, the structure was modelled by creating a solid 3D model, starting from the point cloud acquired with Laser Scanner. Subsequently, the model was calibrated by defining the materials so that it had a behaviour close to the real one. This was possible thanks to the monitoring data and the model updating methodology. Finally, linear analyses were carried out for a comparison with the experimental data and non-linear analyses to derive the vulnerability under seismic action.

1.1 Collapse mechanisms of churches

For a general view of the collapse mechanisms of buildings without rigid connecting floors as churches, the main macroelements found in existing churches after a seismic event, are reported in this chapter. These mechanisms are defined in the "*Guidelines for the evaluation and reduction of the seismic risk of cultural heritage with reference to technical standards for construction*" [1] and the complete list is given in the following figures.

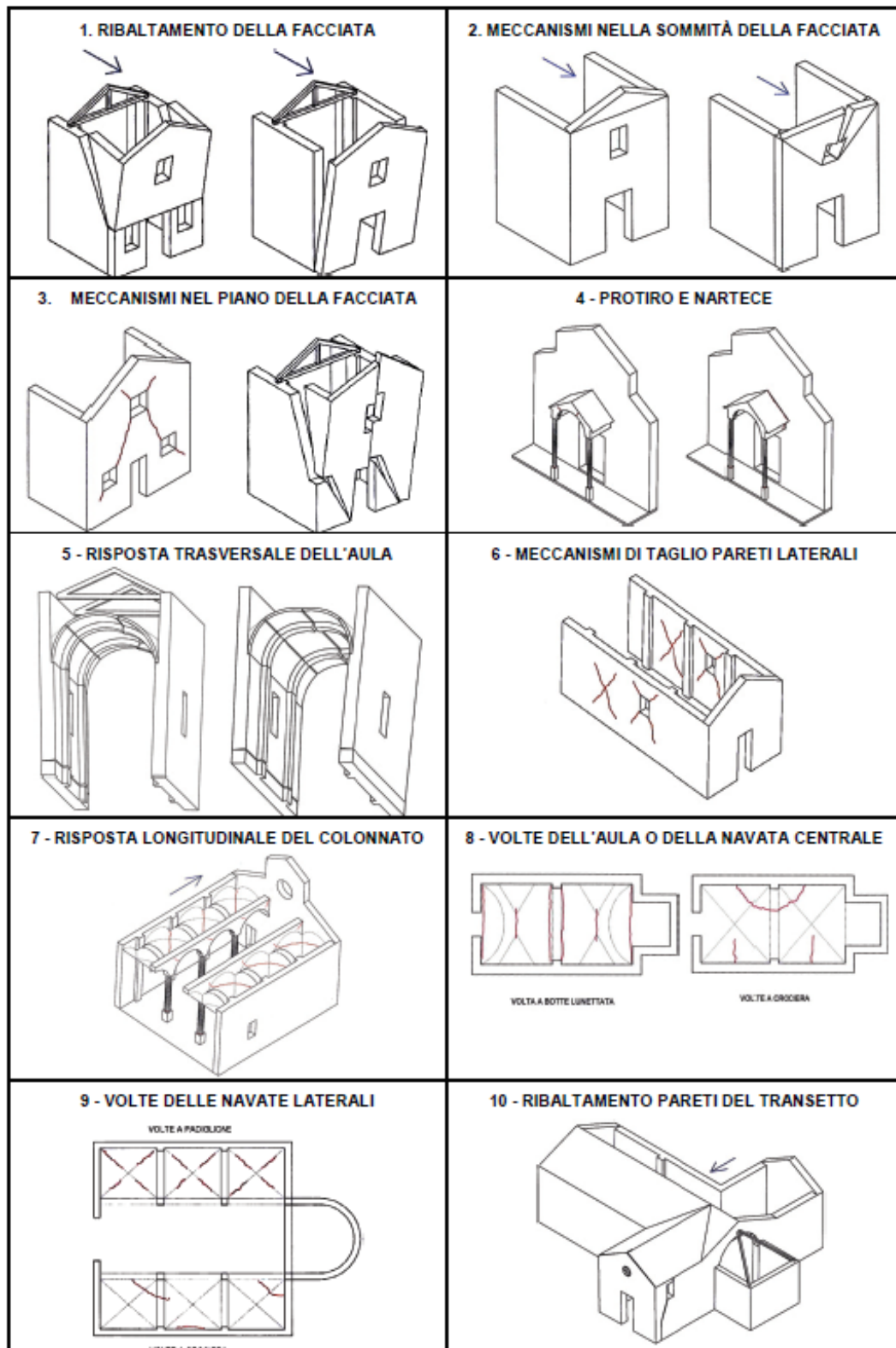


Figure 1.1 - Macro-elements of church buildings [1].

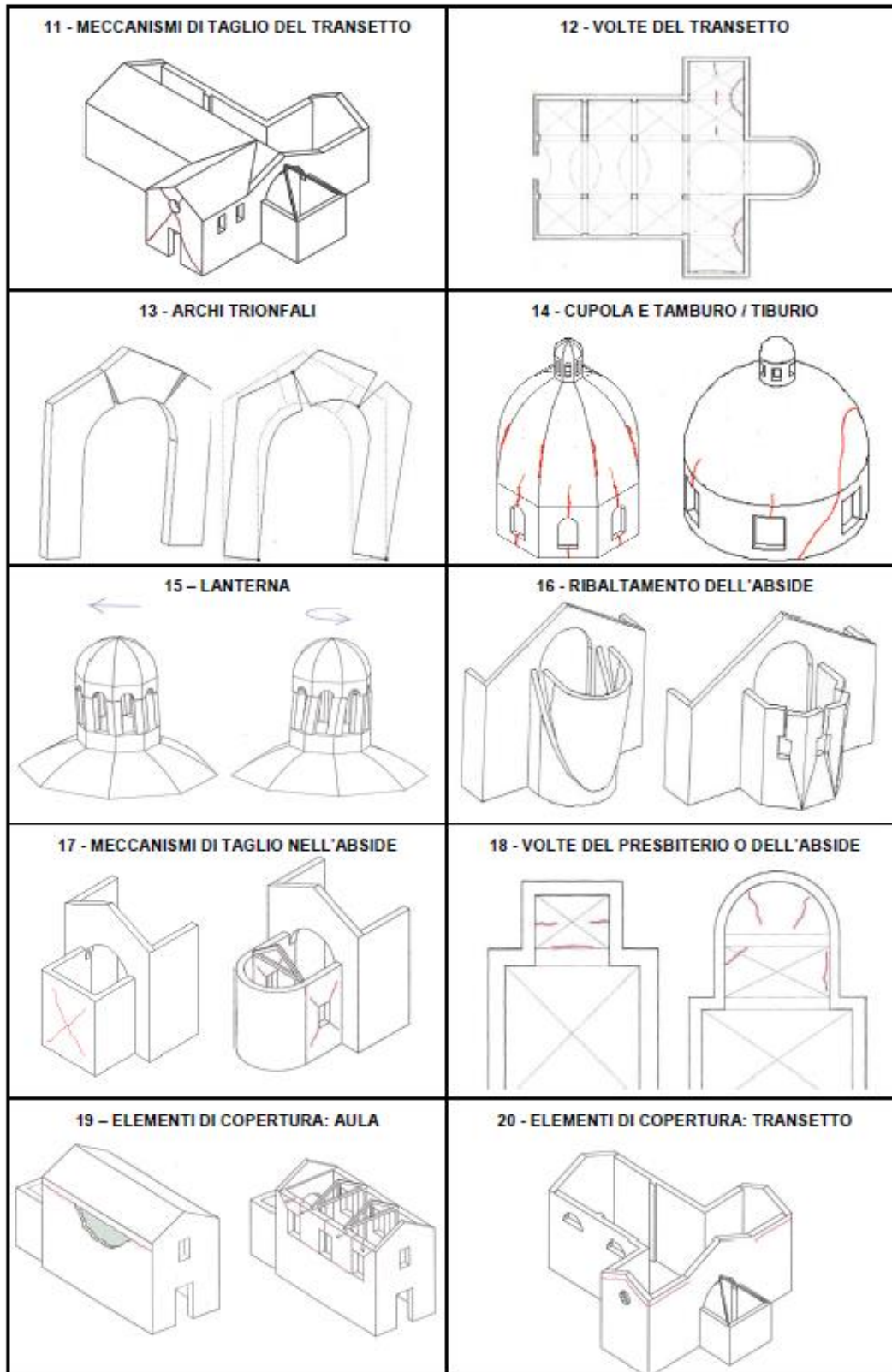


Figure 1.2 - Macro-elements of church buildings [1].

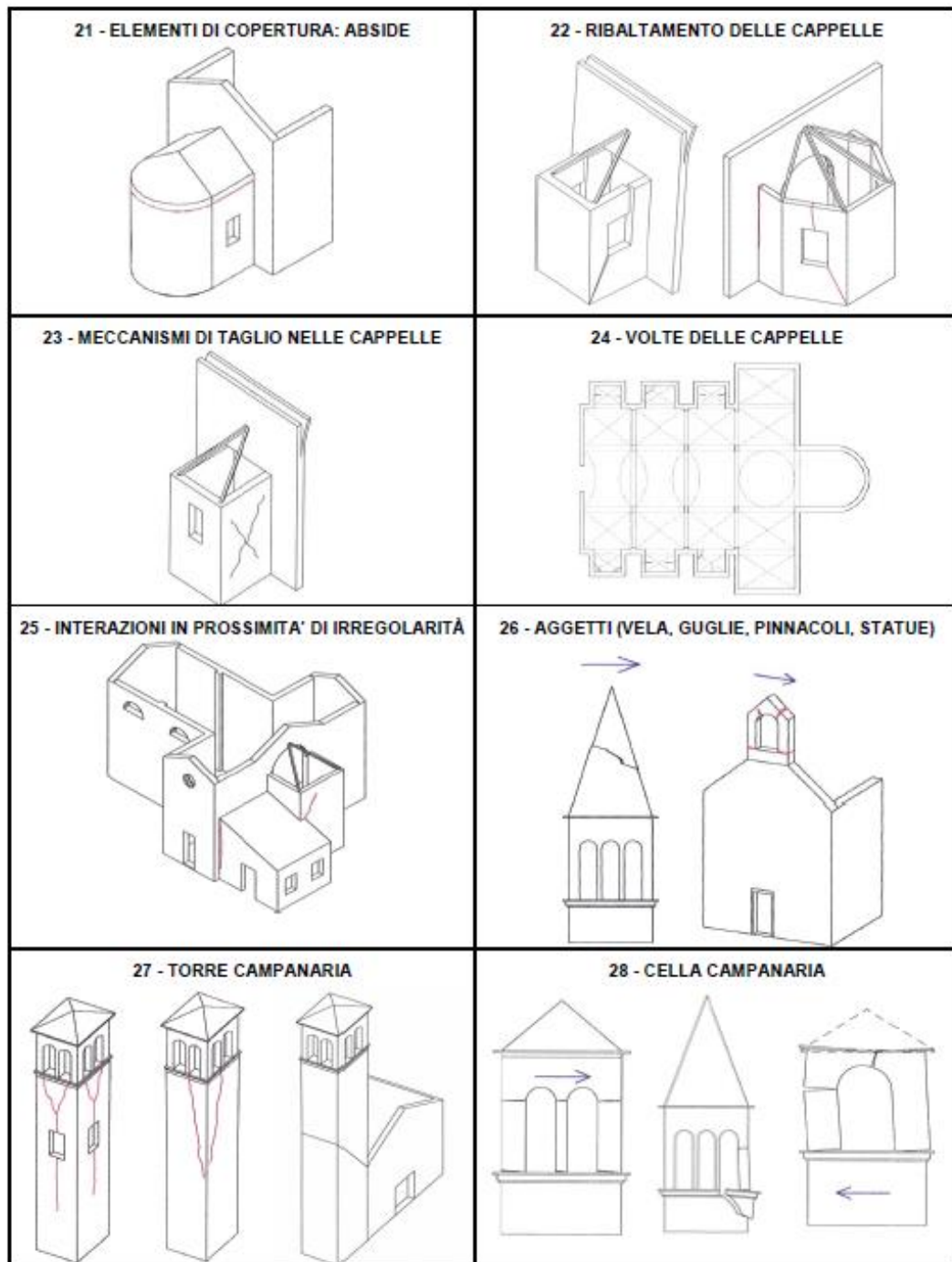


Figure 1.3 - Macro-elements of church buildings [1].

Below are some images of the damage detected during the most significant earthquakes that occurred in Italy. This is to make it clear how vulnerable these types of structure are, under the action of the earthquake and how important it is to study their structural behaviour and proceed with interventions to protect our cultural heritage.



Figure 1.4 – Left: *Overturning of the façade - detachment of the facade from the walls or evident out of plumb*; Right: *Mechanisms on the top of the facade - overturning of the tympanum* [2].



Figure 1.5 – Left: *Mechanisms on the top of the facade - overturning of the tympanum with V-shaped damage*; Right: *Vaults of the lateral naves - damage in the vaults, disconnections of the arches and of the side walls* [2].



Santa Maria dei Raccomandati - San Demetrio ne Vestini (AQ)

Figure 1.6 – Vaults of the central nave - damage in the vaults of the central hall, disconnections of the vaults with arches [2].



Chiesa dei SS. Marciano e Nicandro, L'Aquila

Figure 1.7 – Triumphal arches - lesions in the arch and sliding of the segments [2].



Figure 1.8 - Dome - tambour/lantern - damages in the dome with possible continuation in the tambour [2].



Figure 1.9 - Shear mechanisms in the walls of the transept - complete collapse [2].



Figure 1.10 - Overturning of the apse - vertical or curved lesions in the walls of the apse [2].



Figure 1.11 - Bell tower - damage near the detachment from the body of the church [2].





Chapter 2

The Historical Masonry

2.1 Introduction

The chapter deals with morphological aspect of historical masonry, describing the various art rules for a correct wall behaviour. Only by knowing the building art and culture, it is possible to correctly describe the structural behaviour and carry out maintenance interventions without modifying or ruining the cultural heritage. The difficulty of knowing historical masonry is due to the presence of walls with brick and mortar composed by different materials, with irregular shape and often not correctly realized. Furthermore, the masonry typologies are dependent on the area in which the building was carried out and, on the materials, available. The mechanical behaviour of the masonry as a whole and its various constituent elements will also be described, under the action of different loads.

Finally, the characteristic damage mechanisms of special structures will be illustrated, such as churches and cathedrals, without box-like behaviour due to the absence of the rigid floor in its own plan.

2.2 Constituent materials

As reported in [3] in these chapters the materials constituting the ancient masonry will be introduced, pointing out the problems concerning its characterization.

The masonry can be defined like an aggregate of overlapping stone elements, which can be natural or artificial, with or without mortar interposition. Since Romans times, clay bricks were the most widely used material for the building construction, especially in areas where the stone material was limited. The clay brick had the advantage of being economical and allowed rapidity in the execution phase.

2.2.1 Stone bricks

The stone bricks were made with rock fragments of varying shape and size depending on the building work carried out and the characteristics of the rock itself. It is among the first masonry typology made by man, thanks to its easy availability in nature.

The natural stone used in construction can be classified as follows:

- *Cutting stones*: thanks to their characteristics of compactness and workability, they allowed to realize processes such as to reduce them in regular geometric shapes and appropriate dimensions. They were used to make structural elements such as walls, arches and columns, using them in the parallelepiped, cylindrical or truncated cone shape.

Among the characteristics that these materials must have for the structural behaviour purpose are an adequate mechanical strength mainly to compression and high durability to limit the degradation phenomenon due to atmospheric agents. They were often used in masonry without the use of mortar.



- Building stones: there are different types:
 - All those stones that do not have the necessary properties for a perfect processing and not very durable. If they are characterized by a good mechanical strength can be used for the realization of masonry with mortar. To avoid degradation phenomenon due to atmospheric agents, this typology was made using a protective blaster;
 - Rough stone from quarry fragments with a more or less square shape.
 - Rough stone from rock fragments produced by atmospheric agents or deriving from extraction operations of worked stones.
 - Stones from rock fragments extracted in alluvial deposits. This typology due to the rounded shape faces does not guarantee sufficient stability to the masonry.

2.2.2 Clay bricks

The historical brick was very used by the Mediterranean civilizations to carry out the buildings, realized with raw clay and dried in the sun. From the 4th century BC the Romans acquired the art of cooking clay, these techniques allowed to reach temperatures of up to 700-800°C. The realization of the brick was totally done by hand and the dimensions varied from place to place. Production control was purely empirical and for this reason, the mechanical and qualitative characteristics were very dependent on the production process. This type of masonry was widely used by the Romans for its speed of execution and above all for the qualitative and resistance reliability, which allowed it to create structures even of considerable heights. The "*ludio*" Roman raw brick had the dimensions of about 44x29,6x35,5cm. The ancient Roman works were made with optimum quality masonry compared to those made in a later period, especially for the use of thin joints compared to the bricks thickness. Following the years, the production of the bricks collapsed even if in the Middle Age the northern Italy remained one of the bricks construction centres, where they also became a standardized element.

2.2.3 Mortar

The mortar is defined as a mixture of inorganic binder, mainly fine aggregates, water and possibly organic and inorganic components calibrated in such a way that in the fresh state has good workability characteristics, whereas in the hardened state they must have adequate physical-mechanical characteristic and durability. The historical mortar differs from the modern one in the interaction with the blocks because the latter has both mechanical and chemical interaction, while in the historical one this adhesion is less efficient or in some cases even completely absent. Its elasto-mechanical characteristics are practically impossible to know due to the impossibility to take mortar samples of adequate size for the

realization of a mechanical characterization test. However, it is possible to take samples for a component characterization.

It can happen that the mortar composition can vary in the same place depending on the realization period, due to the availability of the raw materials. Further heterogeneity is given by the fact that the mortar mixing was done by hands and the doses roughly made in parts. The portions that since ancient times ensured a good mortar are binder and aggregate ratio of 1:3 and 1:2 respectively with possible further small variations necessary to give different properties to the mortar, varying the type of grain size distribution used, the type of binder used and the presence of any additives. The quality and the type of water, the type of aggregates and particularly the worker influence must also be taken into consideration. From these observations it is possible to understand how complicated it is to obtain a relationship between composition and final mortar characteristics in the case of historical masonry.

The main components used in the ancient mortars are as follows:

- Gypsum: first binder produced by man was obtained by firing chalky rocks (130-170°C). It was widely used at the time of the Romans, Greeks and over the following centuries due to its simplicity in the mixing and its cost-effectiveness, even if its performances were worse than lime;
- Hydrated lime: it is a non-hydraulic binder that in the past was used in the form of slaked lime and was obtained by firing very hard compact stone available in the site, for economic reasons the stones available in the place were used, selecting among those that could give best results. The mixing occurred with greater than lime because it required higher firing temperatures (around 900°C);
- Aggregates: in the Roman period, much importance was given to aggregates, establishing certain requirements for the mortars mixing. The aggregates were used mainly for two reasons: the

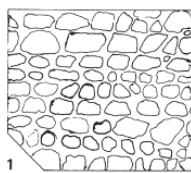
first was for economic reason, since the binder was expensive, therefore it was diluted with sand, ground stone and pebbles. The second was for practical reasons, the mortar in presence of aggregates was less subjected to shrinkage phenomenon;

- Pozzolana and cocchiopesto: these materials are not classified either as a binder or as an aggregate. The pozzolana is produced in the volcanic eruptions and is mainly composed of silicon oxides, aluminium, iron, calcium and magnesium oxides. It was used for its property of turning the lime from slaked into hydraulic and therefore increasing mechanical strength, speeding up hardening and increasing resistance to water washout. The Romans learned this technique from the Greeks and Etruscans, and they used it a lot in construction. To obtain the same effect, cocchiopesto was also used instead of pozzolana, consisting of finely ground bricks.

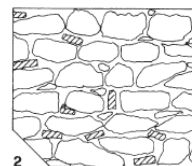
2.3 Types of historical masonry

In the construction of the civil works, rules, improved by the observation of the results tested on the structures already built, were not always followed. Such rules are called art rules, but in the most cases they are respected only in noble buildings, as can be palaces and cathedrals. Most of the buildings that are part of a historical centre are classified as minor buildings and often did not respect these rules, for economic reasons, of available materials and from the skills of the builders [3]. For this reason, the variety of masonries that can be found is very wide, the most common types are shown below and in the next chapters some of these will be examined, describing the various problems and their main characteristics. This chapter contains some images present in [4].

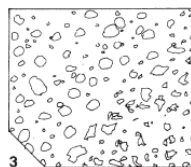
- Types of masonry in stone material



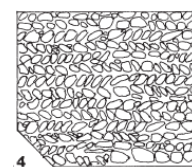
Sub-horizontal courses weaving, with erratic stones



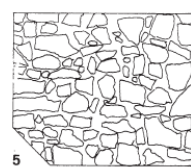
Sub-horizontal courses weaving, rough with brick or stone wedge



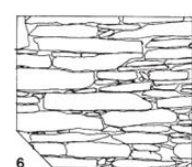
Concrete, with rounded or broken aggregates



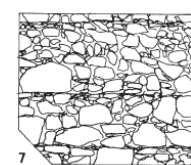
Fishbone weaving, with pebbles, stones or brick fragments



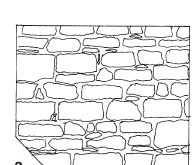
Irregular with no courses, split blocks, with or without wedges



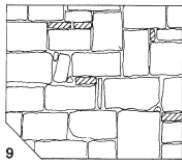
Irregular, with flaked blocks, with or without wedges



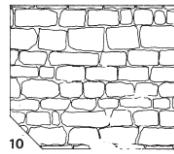
Irregular, split blocks, with horizontal courses every 40-60 cm



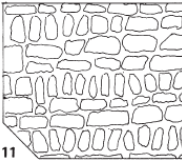
Sub-horizontal and parallel courses, with split blocks, with or without wedges;



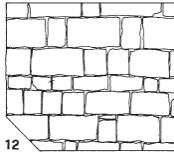
Without courses, with square blocks, often with brick wedges



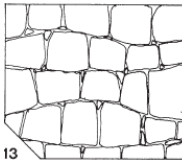
Horizontal and parallel courses, with split blocks of different heights;



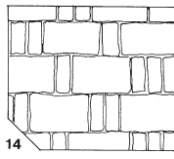
Horizontal, sub-parallel courses with mainly vertical split blocks



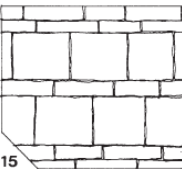
Horizontal and parallel courses with squared and flat ashlar



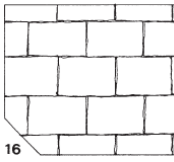
Undulating courses with or without wedges



Horizontal and parallel courses, Arabic

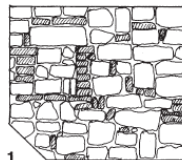


Parallel and horizontal courses with plates, "pseudo-isodoma"

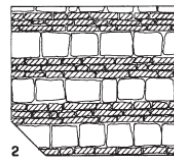


Horizontal and parallel courses, with ashlar, "isodoma"

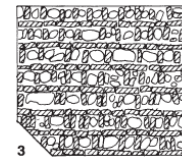
• Types of masonry in mixed material:



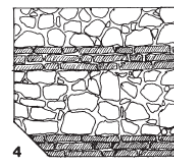
Sub-horizontal courses, blocks and wedges



Flat surface in brick and ashlar

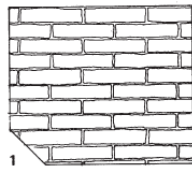


Box shape and rounded ashlar

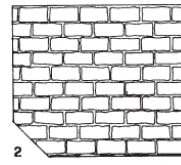


Flat surface in brick and blocks

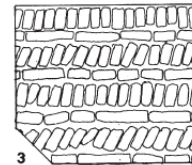
- Types of masonry in clay material:



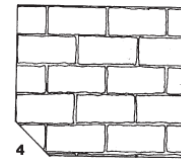
Band masonry



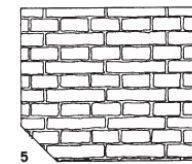
Head masonry



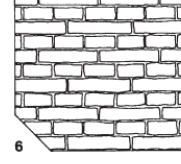
Knife masonry



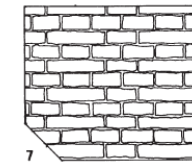
Masonry with bricks positioned on the low side



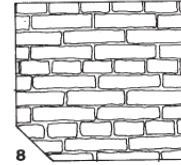
English block masonry



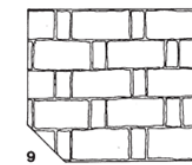
English cross masonry



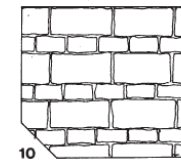
Dutch masonry



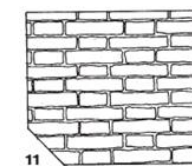
English masonry for garden



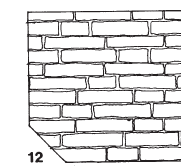
"Rat trap"



"Dearne"



Gothic or Flemish masonry



"Monk" or "senese" masonry

2.3.1 Opus quadratum

Following as reported in [5] the *opus quadratum* or “*isodoma*” is a type of masonry belonging to the cultured traditions. It consists of two orders of stones:

- *Orthostates*: fired clay or stones blocks arranged with the longest side in the wall direction;
- *Bond stones*: fired clay or stones blocks arranged with the longest side in the direction orthogonal to the wall;

Moreover, the vertical joints must be arranged in a staggered manner, avoiding “sisters” that is vertically aligned joints. This type of masonry is the one that most approximates the monolithic mechanical schematization.

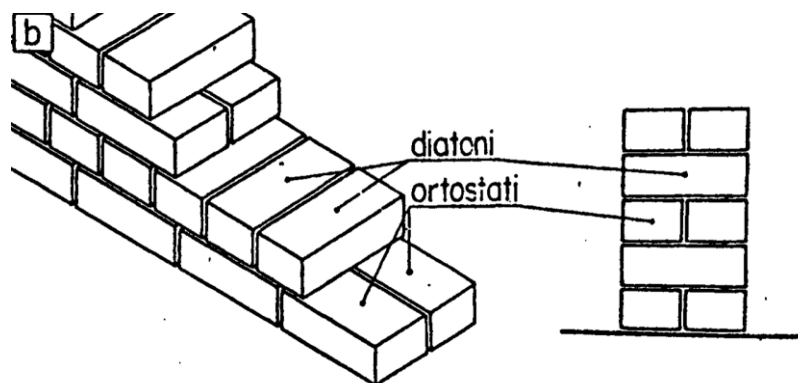


Figure 2.1 – An example of *opus quadratum* [5].

To describe this typology from the mechanical point of view, it can be said that each block is supported on the other with a simple support restraint and can withstand both traction and compression. Instead, the joints between the blocks react to compression and not to traction actions. This means that along the main and secondary joints, the stone coherence does not exist.

Furthermore, the contact surfaces of the main joints have friction and follow the Coulomb model:

$$F = \mu \cdot P \quad (2.1)$$

where:

F : applied force;

μ : friction coefficient;

P : normal force on the sliding surface.

Thanks to the vertical joints offset, of which we spoke previously, a vertical concentrated load is distributed over the underlying layer as shown in *Figure 2.2*. As can be seen, this blocks arrangement allows a load diffusion, thus generating a vertical band.

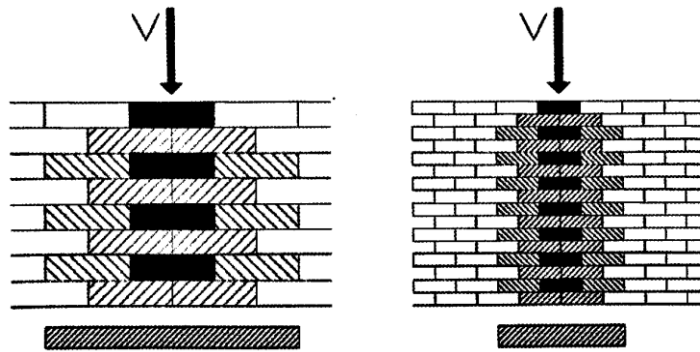


Figure 2.2 – Vertical load diffusion [6].

If, on the other hand, the inclined load is taken into consideration, since a horizontal action is present, the main joints friction intervenes which will give rise to reactions that will depend on the normal surface load. As can be seen, therefore, the wall intervenes only partially to the static load response, this load diffusion is a fundamental mechanical behaviour of this typology.

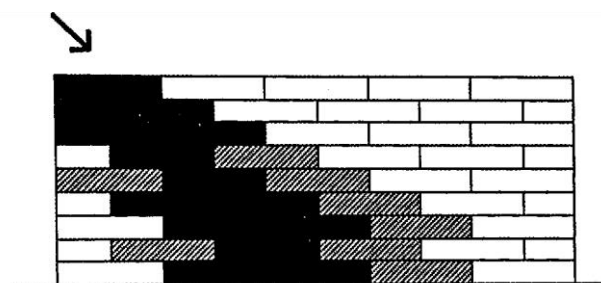


Figure 2.3 - Inclined load diffusion [6].

Another advantage, which has the *opus quadratum* due to its regular vertical joints offset, is the “chain” function. The “chain” function is the resistance that has a masonry wall when it is subjected to a horizontal traction. This pseudo tensile strength is exerted by the joints, the blocks would tend to flow over each other, but the friction and the vertical load prevent it.

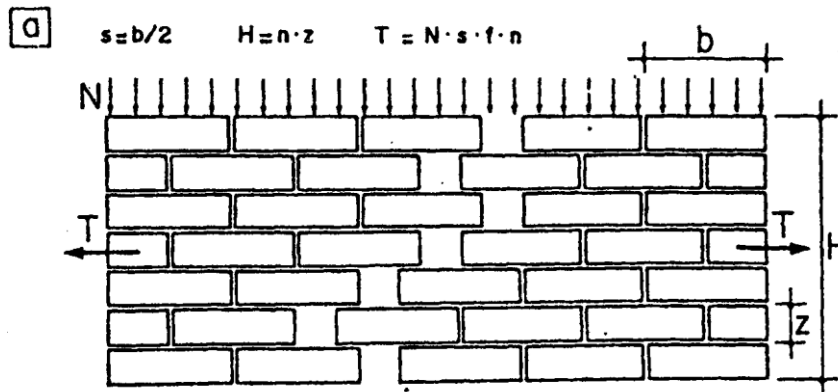


Figure 2.4 – The pseudo tensile strength of the masonry wall [5]

The pseudo tensile strength of a masonry can be calculated as follows:

$$T = N \cdot \frac{b}{2} \cdot \mu \cdot n \quad (2.2)$$

where:

T : total pseudo tensile strength;

N : load per unit of surface normal to the sliding surface;

b : length of the single block;

n : number of sliding surfaces.

$$t = \frac{T}{n \cdot z} = \frac{N \cdot b \cdot \mu}{2 \cdot z} \quad (2.3)$$

where:

t : pseudo tensile strength per unit of height;

z : block thickness.

It is evident that as the length of the blocks increases, the resistance increases, but as their height increases, with the same wall height, this resistance decreases. This mechanism is important in the case of seismic actions because it allows the preservation of the structural integrity, for instance in masonry composed of small stone pebbles and without orthostates, this effect is absent [6].

Now let us analyse the most dangerous action for a masonry, that is the one outside its plane and we will study it considering the monolithic wall. In this way, we will understand which elements are necessary and which rules must be respected so that the masonry has an optimal behaviour under this action.

If we consider a rigid monolith body with its own weight P and subject to a horizontal action F , two collapse mechanisms can occur that will depend only on the geometry of the wall:

- Sliding: when F exceeds the friction resistance at the base, there is therefore a movement of translation along the direction parallel to the supporting surface;
- Overturing: when the own weight is not sufficient to counter the overturning moment given by the force F , there is therefore a rigid rotation with respect to the external vertex.

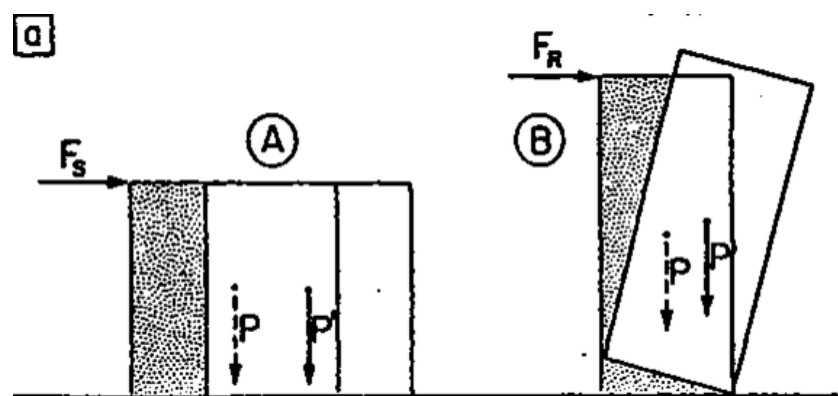


Figure 2.5 – The two collapse mechanisms [5].

The first collapse (*sliding*) mechanism will occur when it is verified that:

$$F = F_s = \mu \cdot \gamma \cdot b \cdot H \quad (2.4)$$

where:

F : applied force;

F_s : limit force for sliding collapse;

μ : friction coefficient;

γ : specific weight of the material;

b : wall thickness;

H : wall height.

It can be seen how the sliding force increases as the thickness and height of the masonry increases.

The second collapse (*overturning*) mechanism will occur when it is verified that:

$$M_R = M_s \quad (2.5)$$

$$F_R \cdot H = (\gamma \cdot b \cdot H) \cdot \frac{b}{2} \rightarrow F_R = \gamma \cdot \frac{b^2}{2} \quad (2.6)$$

where:

M_R : overturning moment;

M_s : stabilizing moment.

It can be seen how the overturning force depends only on the thickness and not on the height of the masonry.

If you want to derive the transition limit between one mechanism and another, it is enough to equal the two forces:

$$F_R = F_s \quad (2.7)$$

$$\gamma \cdot \frac{b^2}{2} = \mu \cdot \gamma \cdot b \cdot H \rightarrow H_L = \frac{b}{2\mu} \quad (2.8)$$

where:

H_L : height limit of the wall that generates the passage from a collapse mechanism and the other.

Thus, if $H < H_L$ the first collapse mechanism occurs, even if $H > H_L$ the second mechanism occurs.

We will now study the case of a monolithic wall subject to both a horizontal force F and a vertical one N (Figure 2.6). In this case, the first collapse (*sliding*) mechanism will occur when it is verified that:

$$F = F_s = \mu \cdot (\gamma \cdot b \cdot H + N) \quad (2.9)$$

where:

N : vertical load.

The second collapse (*overturning*) mechanism will occur when it is verified that:

$$M_R = M_S \quad (2.10)$$

$$F_R \cdot H = N \cdot (b - a) + \gamma \cdot b \cdot H \cdot \frac{b}{2} \rightarrow F_R = \gamma \cdot \frac{b^2}{2} + \frac{N \cdot (b - a)}{H} \quad (2.11)$$

where:

M_R : overturning moment;

M_S : stabilizing moment;

a : vertical load distance from the inner edge.

This analysis points out that the additional N force increases the resistance of both collapses of the wall and for high heights tends asymptotically to the case of $N = 0$ (Figure 2.6).

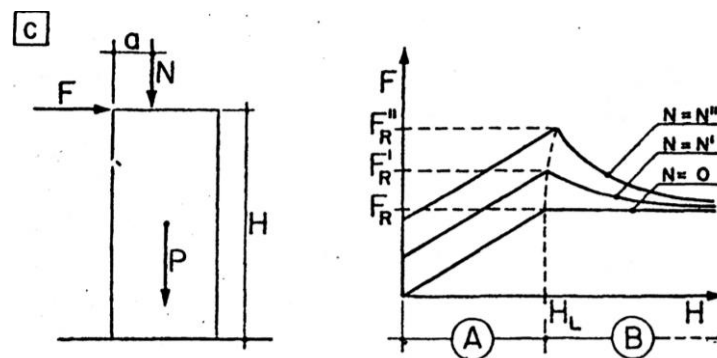


Figure 2.6 - Monolithic wall with horizontal and a vertical force and graphic solution [5].

Since we are studying the *opus quadratum*, now we analyse the case of force F applied at the top of a wall composed of overlapping blocks (Figure 2.7).

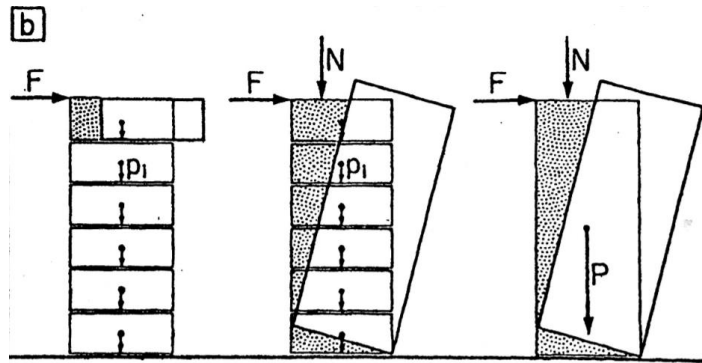


Figure 2.7 - Analysis of the *opus quadratum* with concentrated force [5]

Taking into consideration only the first block at the top, the first collapse mechanism (*sliding of the single block*) occurs when:

$$F = F_s = \mu \cdot \gamma \cdot b \cdot h \quad (2.12)$$

where:

F : applied force;

F_s : limit force for sliding collapse;

μ : friction coefficient;

γ : specific weight of the material;

b : wall thickness;

h : brick height.

As the block height decreases, the force F_s that generates the sliding of the block at the top decrease. If, on the other hand, there was also an applied force N (Figure 2.7), the necessary condition to have no sliding either on the first joint or on all the others is the following:

$$F < F_s = \mu \cdot (\gamma \cdot b \cdot h + N) \quad (2.13)$$

where:

N : vertical load.

The friction generated by the vertical load ensures a monolithic behaviour of the wall, even if made with overlapping blocks and therefore the limits obtained previously are valid.

Considering now a horizontal distributed load applied to each block and proportional by the coefficient β to the weight of each of them, as could be the earthquake action. The necessary condition to have no sliding at the i -th joint is the following:

$$F_i = \sum_{j=1}^m F_j = \beta \cdot \sum_{j=1}^m P_j < F_{Ri} = \mu \cdot \sum_{j=1}^m P_j \quad (2.14)$$

where:

F_i : applied force to the i -th block;

F_{Ri} : limit force for sliding collapse to the i -th block;

P_i : weight of the i -th block;

μ : friction coefficient;

β : proportionality coefficient with respect to weight.

Therefore, the proportionality coefficient must respect the following upper limit $\beta < \mu$ to avoid the sliding.

The necessary condition, instead, to have no overturning at the i -th joint is the following:

$$M_R = M_S \quad (2.15)$$

$$M_R = \beta \cdot P \cdot \frac{H}{2} = M_S = P \cdot \frac{b}{2} \rightarrow \beta = \frac{b}{H} \quad (2.16)$$

where:

M_R : overturning moment;

M_S : stabilizing moment;

P : weight of the wall;

b : wall thickness;

H : wall height.

Finally, to avoid both sliding and overturning of a part composed of overlapping blocks and subjected to a distributed horizontal action, the coefficient β must be less than the friction coefficient μ and less than the ratio between base and height of the wall. From the condition $\beta = b/H$ reveals the effectiveness of the bond stones in the overturning mechanism. If we consider a wall made up only by orthostates (*Figure 2.8*) the overturning mechanism can take place respect to A and A' , for this reason is like consider two facing walls of half the total thickness. Thus, the wall without bond stones, which prevent the slipping between the inner faces, resists a thrust equal to half of that with bond stones.

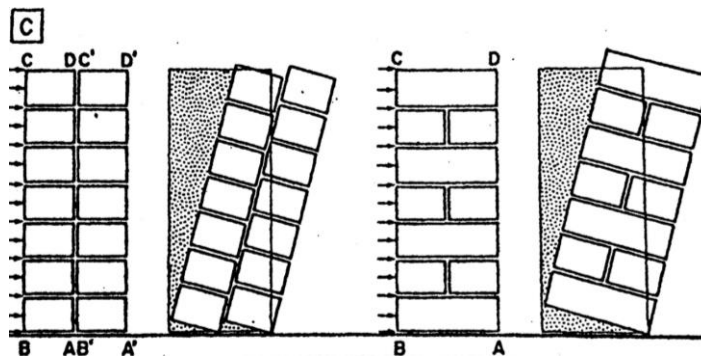


Figure 2.8 - Difference between a wall with and without bond stones [5].

In addition, the bad disposition of the bond stones varies the resistance of the wall, which breaks up before reaching the collapse load in the ideal monolithic masonry case (*Figure 2.9*).

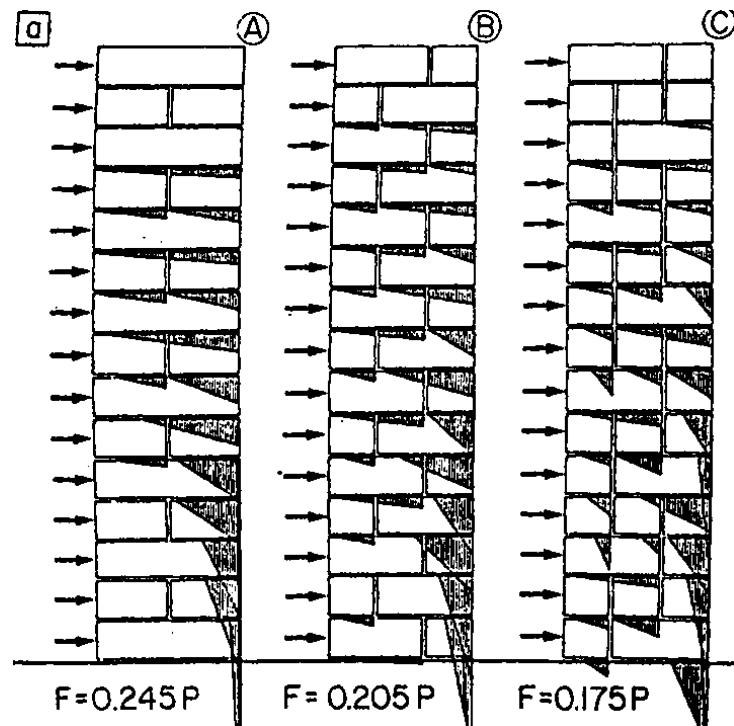


Figure 2.9 - Ultimate load according to the arrangement of the bond stones and distribution of the voltages on the blocks

The purpose of this type of masonry is to behave like a compact wall, which if under the earthquake action oscillates alternately on one edge and on the other at the base of the wall without breaking up.

2.3.2 Filling-core masonry

An excellent dissertation of this topic can be found in [3]. Both Greek and Roman used the filling-core masonry. It consisted in the creation of the external walls in one head brick or in stone material, which were used as formwork for the realization of the internal filling, in this way it was more economical and practical to realize. The two different masonries are shown below:

- *Emplekton*: typical Greek filling-core masonry, made with a filling in irregular stones, ordered with vertical joints offset. This filling was connected to the external walls by means of bond stones. The external walls were made of stone blocks, they were smaller and less regular than those of the *opus quadratum* [7] and the mortar had the function of a support surface, in fact was made from a terrain mixture with small amount of lime.
- *Opus caementicium*: typical Roman filling-core masonry descending from the *emplekton*, made with overlapping layers of *caementa*, that is stone fragments and hydraulic mortar pressed to fill all the interstices. The hydraulic mortar had the advantage of being able to harden even in the absence of air inside the thick wall and be subject to less shrinkage. This typology, unlike the *emplekton*, had a filling with a greater thickness than the external walls and for this reason, the latter did not have a specific load-bearing function, but only that of formwork, protection and decoration one. This is demonstrated by the fact that in several Roman ruins the masonries are now devoid of external covering, which has become detached or eroded, without compromising the wall stability [7]. As already mentioned, the external walls served as decoration, in *Figure 2.11* some types of coatings made by the Romans are reported. To avoid cracks and detachments between filling and external walls, horizontal planes were frequently created, that is a plane

in clay brick (*bipedales*) or tuff brick with the function of binder. In this way, the wall assumed an overall behaviour that allowed the oscillating kinematic mechanism on its base [5].

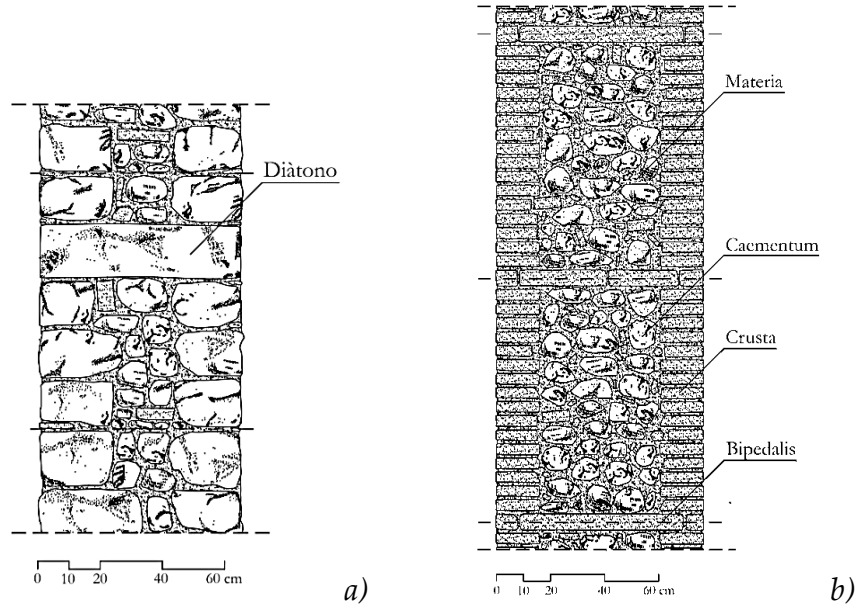


Figure 2.10 – a) Vertical section of the Greek masonry with èmplekton;
b) Vertical section of the masonry in opus caementicium [7].

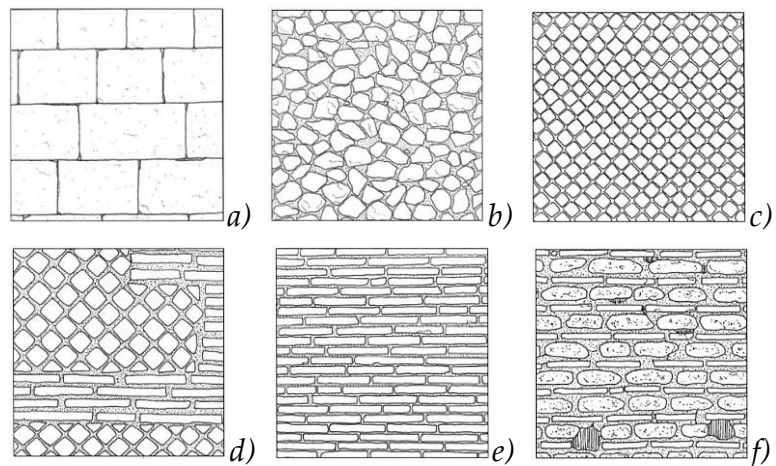


Figure 2.11 – External wall: a) Opus quadratum b) Opus incertum c) and d) Opus reticulatum e) Opus testaceum f) Opus vittatum. [7]

The behaviour of this type of masonry depends on the organization of the filling and on the method of connection with external walls. The two extreme cases are studied below:

- *Filling well organized and equipped with a good binder*: in this case, the filling and the external coverings, having different elastic modulus, do not distribute the vertical load equally. To obtain the load on each of them, some simplification are realized, we hypothesize isotropic, homogeneous and schematized as pendulums as in the *Figure 2.12*:

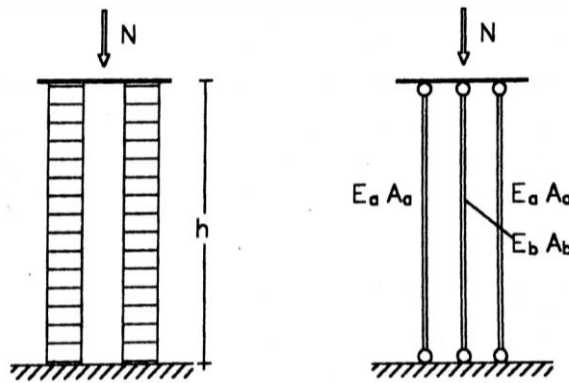


Figure 2.12 - Filling-core wall schematization [3].

Then we can say that:

$$N = 2\sigma_a A_a + \sigma_b A_b \quad (2.17)$$

For congruence:

$$\delta_a = \delta_b \rightarrow \frac{\sigma_a A_a h}{E_a A_a} = \frac{\sigma_b A_b h}{E_b A_b} \rightarrow \frac{\sigma_a}{E_a} = \frac{\sigma_b}{E_b} \quad (2.18)$$

By replacing *Eq. 2.18* in *Eq. 2.17*, we have:

$$N = \sigma_a \left[2A_a + \frac{E_b}{E_a} A_b \right] \quad (2.19)$$

$$\sigma_a = \frac{N}{\left[2A_a + \frac{E_b}{E_a} A_b \right]} \quad (2.20)$$

$$\sigma_b = \frac{N}{\left[2A_a \frac{E_a}{E_b} + A_b \right]} \quad (2.21)$$

Placing:

$$A_a = A_b = 1 \quad (2.22)$$

$$\frac{E_a}{E_b} = 2 \quad (2.23)$$

Finally, we have:

$$\sigma_a = \frac{N}{2,5} \quad (2.24)$$

$$\sigma_b = \frac{N}{5} \quad (2.25)$$

In this model tangential stresses on the contact faces between filling and external covering does not arise, this is true when the load is centred. The presence of flexural actions gives rise to tangential action on contact faces, this interaction between the external wall covering is difficult to study due to the different deformability of the materials.

The external walls constrain the expansion of the filling but the latter subjects to horizontal action to external layers that tend to bend and have problems of instability (*Figure 2.13*). To avoid this problem there are horizontal planes (*bipedaes*) and the bond stones that ensure a link between the three elements.

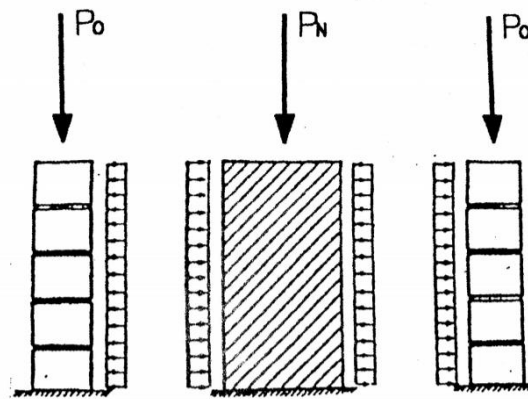


Figure 2.13 - Instability problems due to lateral actions for filling expansion [3].

- *Filling with poor cohesion or made with loose material*: in this type, the external wall covering must carry more load and the filling acts on them through a pressure variable with the height. The trend of the horizontal pressure is like that of a loose earth, in fact it depends on the internal friction angle of the material, on the specific weight and on the height. In this case, even if the load is centred tangential stresses occurs due to the friction between the filling and the external wall covering.

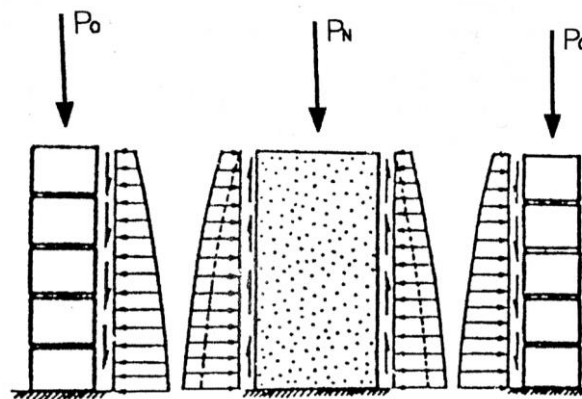


Figure 2.14 - Lateral actions due to expansion of the without cohesion filling [3].

2.3.3 Ordinary masonry

This type of masonry is well explained in [7]. It is reported that it derives from the Greek to *emplekton*. It is composed of two external walls covering made with stone ashlar regularized with the hammer, filled with stone fragments, placed one by one on a mortar surface and pressed to guarantee the mutual contrast.

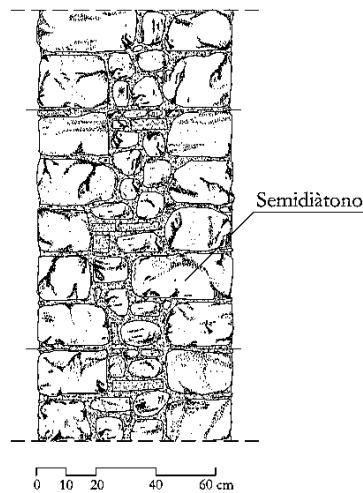


Figure 2.15 - Vertical section of the ordinary masonry [7].

Its quality decreased as the thickness of the internal layer increased compared to that of the external wall covering and above all when the latter were made with small-sized material. The best performances were when the external wall was made with large and squared ashlar, moreover when semi-bond stone were used ($\frac{2}{3}$ the thickness of the wall) guaranteeing a link between the walls. They tried to position the ashlar in such a way that the lower and upper support planes were as regular as possible while the lateral and posterior contours could be irregular. To fill the spaces created between the ashlar small fragments and mortar were used and then suitably pressed.

At the end of the realization of the wall, the facade was regularized by filling the depressions with fragments and mortar and then a layer of plaster was made.

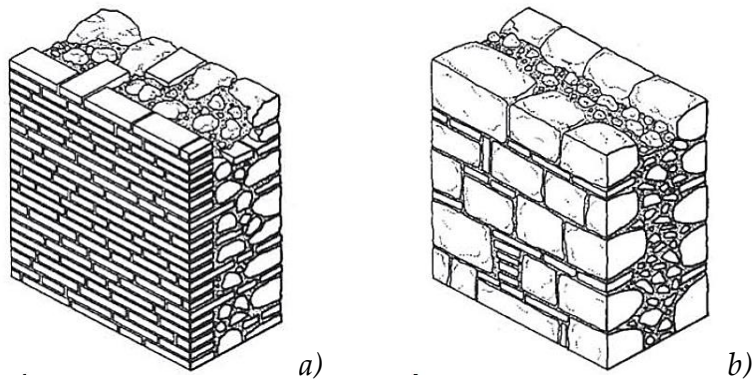


Figure 2.16 - Ordinary masonry: a) with different external walls; b) with external walls in semi-square blocks [7].

2.4 Art rules

The considerations made so far for each types of masonry allow to observe the main rules necessary for a good mechanical overall behaviour of the masonry. Each masonry of any types has the *opus quadratum* as the upper limit, which has an optimal behaviour when subjected to vertical and horizontal loads. Obviously, the masonry typologies deviate from this ideal behaviour and therefore it is up to the observer understand the aspects and the fundamental characteristics for a correct reading of the wall that will determine its mechanical characteristics. The following chapters refer to the considerations present in [6] and [7].

2.4.1 Monolithic behaviour

The best behaviour under vertical and horizontal action is that of a rigid body and therefore of monolithic wall. This type of behaviour is very close to the *opus quadratum*, only if certain rules are respected:

- Use of regular, well squared and of large dimensions ashlars: especially in the highly stressed areas, it allows a greater involvement of the wall and therefore a better behaviour under the action of vertical loads. Regarding the response under the seismic action, the large size of the segments compared to the thickness of the wall and the regularity of the laying plan allow a better stability and behaviour.
- Transversal meshing: this requirement is entrusted to the use of bond stones, regularly distributed over the entire height development of the wall. In this way, there is a correct static behaviour by distributing the load throughout the thickness of the masonry even in case of eccentric loads. Moreover, if a sufficient degree of meshing is not achieved, inclined stresses can arise between the various segments, which could generate expulsion phenomenon and instability problems (*Figure 2.17*).

Regarding the response under seismic action, the bond stones ensure a monolithic behaviour otherwise, disintegrations would occur before arrival to the ultimate calculated load for a wall with rigid body behaviour.

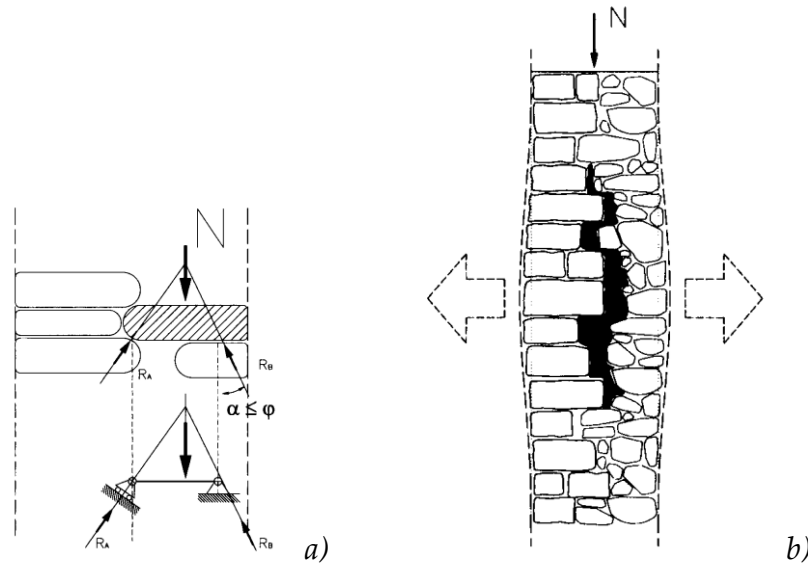


Figure 2.17 - a) Inclined action inside the masonry; b) Instability problems [8].

- Regular joints offset avoiding “sister” joints: this requirement allows an adequate distribution of both horizontal and vertical loads and allows the development of the pseudo tensile strength of which we spoke in the previous chapters. In case of small stone pebbles with no orthostates, this last resistance is not present.

2.4.2 Horizontal planes

In case of stones, the addition of horizontal sections with a certain interval allows to obtain horizontal planes that guarantee an optimal static response thus avoiding slippage of the ashlar or stress concentrations. Furthermore, they allow the development of horizontal cylindrical hinges that generate small oscillations during the seismic event, avoiding dangerous effects of disintegration. This happens, however, only if the wall between the horizontal sections has a monolithic behaviour. Finally, only in the case of the *opus caementicium* these horizontal sections, as already described in the previous chapters, are necessary to absorb the filling shrinkage action and avoid detachment from the external covering walls.

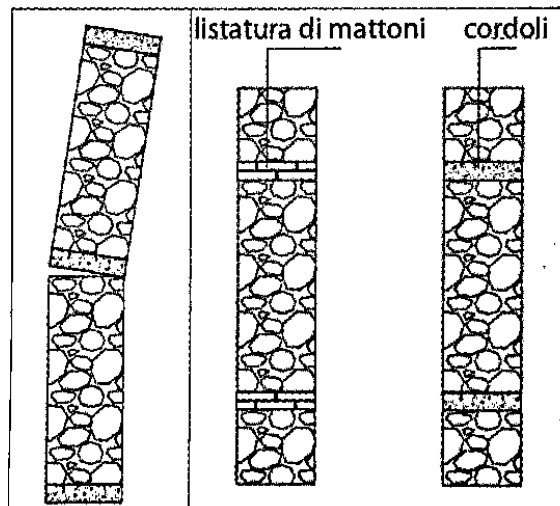


Figure 2.18 – Horizontal planes and respective cinematic mechanism [6].

2.4.3 Mortar function

The mortar has the function of regularizing the contact between the different blocks and contributing to the monolithic behaviour of the wall. Its importance increases as the size of the stones decreases with respect to the thickness of the wall and above all in the presence of masonry composed of non-regular elements. As for the first function, it avoids stress concentrations and equally distributes the loads over the entire thickness of the wall. Referring to the second function, on the other hand, when there is no meshing due to the presence of non-regular stone elements, the mortar has a very important role in the meshing function. In fact, it is fundamental in masonry of the *opus caementicium* type, whereas in masonry of the *opus quadratum* type the mortar is not essential. It also gives the masonry a certain degree of cohesion that determines the mechanical resistance, to ensure this resistance the joints must not be too thick.

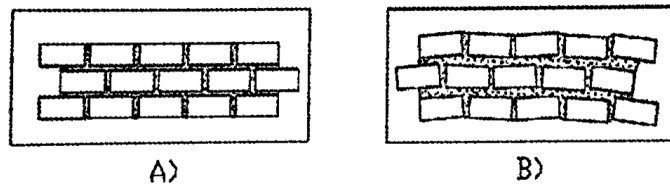


Figure 2.19 – a) Correct thickness of the joints; b) Excessive thickness of the joints [6]

Chapter 3

Mechanical behaviour

The masonry behaviour is very complex because it depends on the properties of the elements that constitute it, which have different behaviour between them. This is very important for the realization of non-linear FEM analysis and for the correct interpretation of the masonry mechanics under the action of static and mostly dynamic loads. In this chapter the experimental tests carried out by researchers in the past will be analysed, to understand what the behaviour of the constituent materials is taken individually and then of the masonry. Therefore, the behaviour of the mortar, the brick and the mortar-brick interface will be showed.

3.1.1 Mortar and joints

- **Load: Triaxial compression**

McNary and Abrams [9] studied the behaviour of the mortar subjected to triaxial compression tests, the main aspects of the research are reported below. The triaxial tests are achieved on four types of mortar, obtaining the stress-strain curves, the Young's modulus and the Poisson's coefficient of the weakest and strongest mortar by varying the confinement stress.

As can be seen in *Figure 3.1*, the mortar behaviour depends on the confinement and on its composition. For all the tests carried out the failure stress and the axial strain failure increases with increasing confinement. Instead, the ultimate strain decreases with increasing of the confinement. In general, both mortars show a fragile behaviour due to low confinement

pressures, but as regards high confinement pressures, it can be seen that both have ductile behaviour but the strong mortar collapse to an axial deformation of three times the weak one.

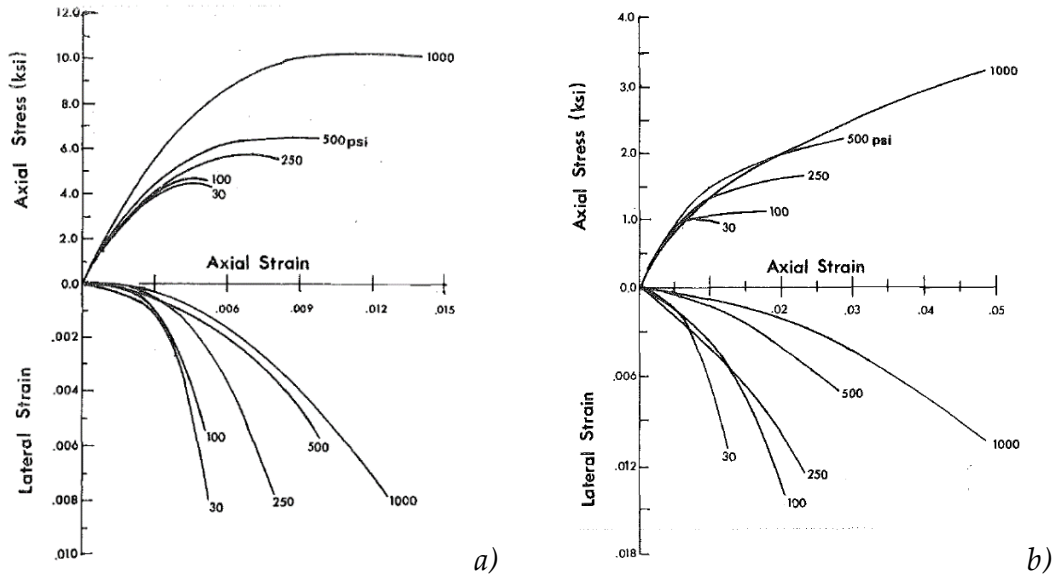


Figure 3.1 - Measured properties for different confining stresses: a) Type M strong mortar; b) Type O weak mortar [9].

The following are the Young's modulus and the Poisson's coefficients of the mortar, when the stress state varies, achieved using a triaxial test.

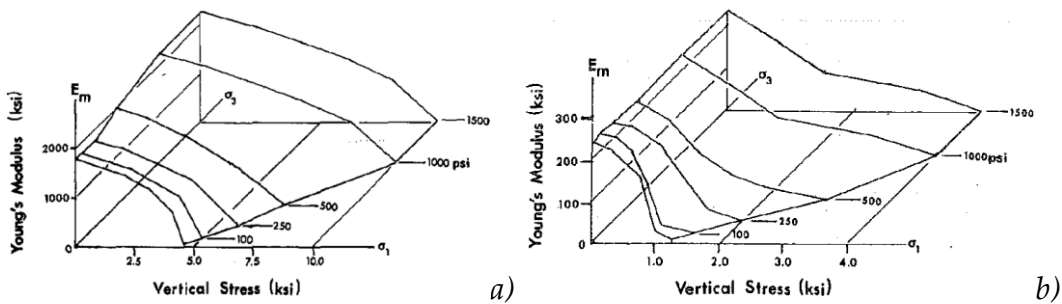


Figure 3.2 – Variation of Young's modulus with normal and confining stresses: a) Type "M" strong mortar; b) Type "O" weak mortar [9].

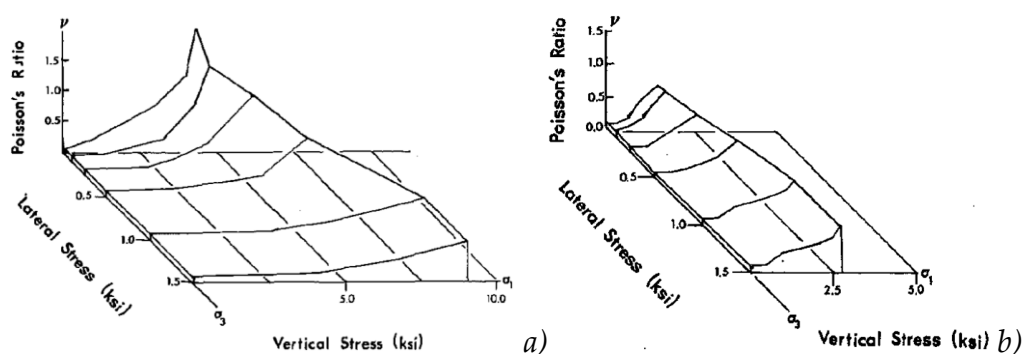


Figure 3.3 – Variation of Poisson's coefficient with normal and confining stresses: a) Type "M" strong mortar; b) Type "O" weak mortar [9].

The results of the experimentation with a triaxial machine for each type of mortar have shown a non-linear stress-strain behaviour.

- **Load: Cyclic direct shear**

As regards the shear behaviour of the joint the research achieved by Atkinson [10], who studied the response of the masonry under the cyclic action of lateral load, will be analysed. The shear collapse is the dominant mode of collapse in case of lateral actions such as the earthquake or the wind, which therefore produce diagonal cracks and damages on the wall or by sliding of a mortar joint. Knowing the behaviour of the masonry subjected to these types of actions is necessary when making models and analysis to study the in-plane behaviour of the wall. By performing direct shear tests, he was able to plot the response curve under shear cyclic loads. As can be seen in the *Figure 3.4* there is a peak at the first cycle that do not appear in the following ones, in which the masonry assumes a residual shear strength. This last strength is not affected by the load cycles. *Figure 3.5* shows an enlargement of the pre-peak phase, the curve in this phase is not constant but decreases with increasing load. This phenomenon is due to a softening behaviour of the mortar joint subjected to shear load. *Figure 3.6*, on the other hand, shows the relationship between the average vertical displacement and the relative horizontal displacement associated with four shear cycles. A dilatant behaviour of the joint is noted in the initial phase, which regresses as the cycles increase.

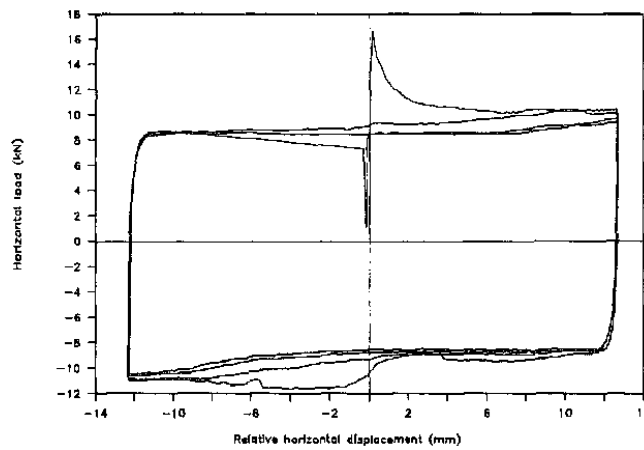


Figure 3.4 - Global cyclic loading response curves for four-cycle shear test on masonry specimen consisting of old Bricks and 1:2:9 mortar mixture with 13-mm joint thickness at constant normal load equal to 13.7 kN [10].

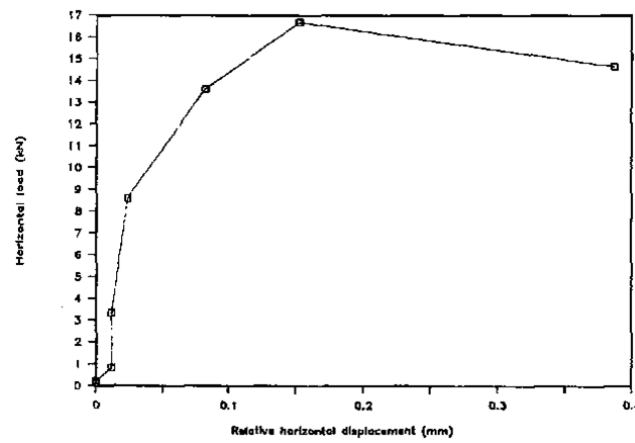


Figure 3.5 – Enlargement of the pre-peak loading response [10].

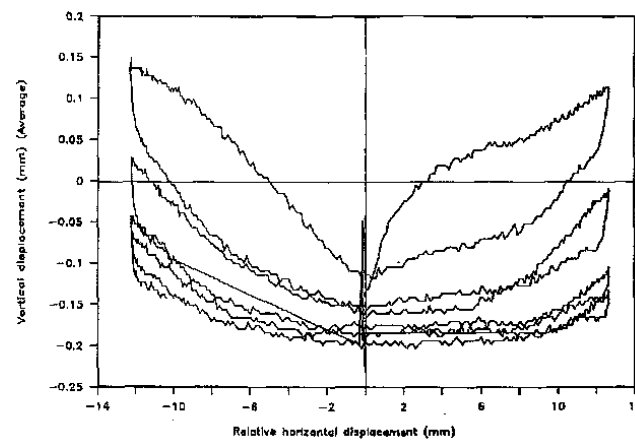


Figure 3.6 - Normal displacement-shear displacement response [10].

Reporting the data of the nominal shear strength of the peak in the first cycle and the residual one as a function of the nominal normal stress level, the data are distributed over a straight line (*Figure 3.7* and *Figure 3.8*). This means that both strengths can be modelled using the Coulomb's criterion:

$$\tau = c + \sigma_n \cdot \tan \varphi \quad (3.1)$$

where:

c : cohesive strength;

$\sigma_n \cdot \tan \varphi$: frictional strength.

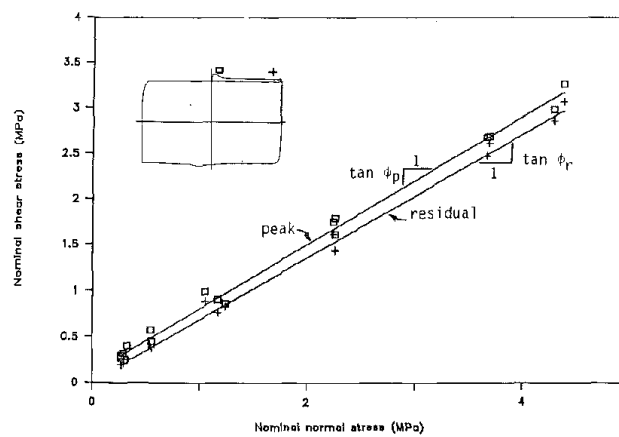


Figure 3.7 - Peak and residual shear strength envelopes for old bricks and 1:2.9 Mortar specimens and bed joint thicknesses of 13 mm [10].

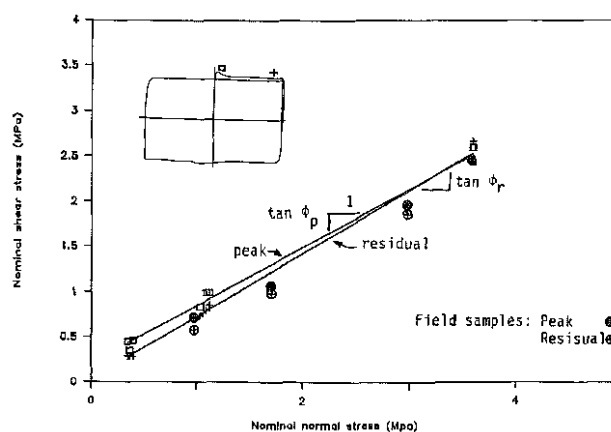


Figure 3.8 - Peak and residual shear strength envelopes for old bricks and 1:2.9 mortar specimens and bed joint thicknesses of 7 mm [10].

Finally, he based on the pre-peak curve (Figure 3.6) and an empirical hyperbolic model, he represented the non-linear pre-peak response of the mortar joints subjected to shear load. Two graphs relating to the variation in shear stiffness as a function of the relative horizontal displacement are reported below. The first one was obtained by varying the normal stresses (Figure 3.9) and the other varying the composition type of the specimens (Figure 3.10), for a more detailed discussion refer to [10]. As can be seen, the initial shear stiffness of the mortar joint increases with the normal stress, decreasing the joints thickness and it is greater for the new brick.

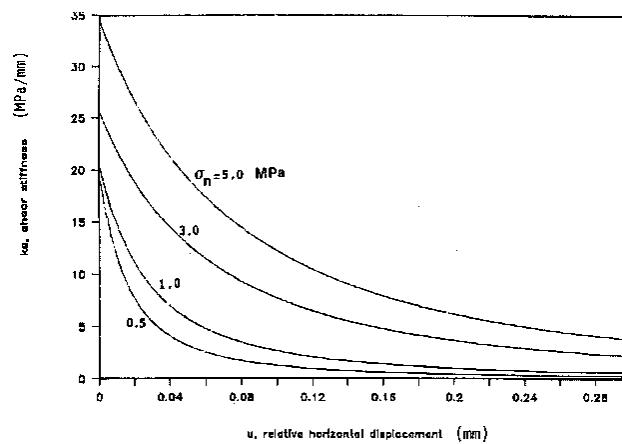


Figure 3.9 - Variation of shear stiffness k_s in function of the shear displacement u for different normal stresses σ_n ranging between 0.5 and 5.0MPa: old brick and 1:2:9 mortar specimens with 7-mm thick bed joints [10].

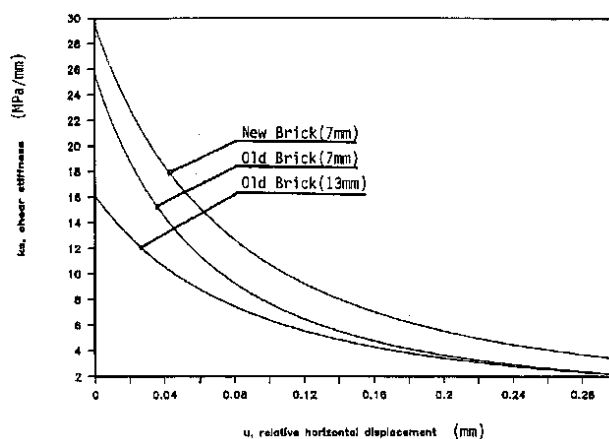


Figure 3.10 - Variation of shear stiffness k_s in function of the shear displacement u at normal stress of 3MPa for three types of laboratory specimens [10].

- **Load: Direct traction**

Van Der Pluijm [11] studied the joint behaviour subjected to direct traction. *Figure 3.11* shows the equipment for the realization of the test and the crack opening-stress curve obtained. As can be seen, the tensile strength of the joint is very low with an extended softening behaviour.

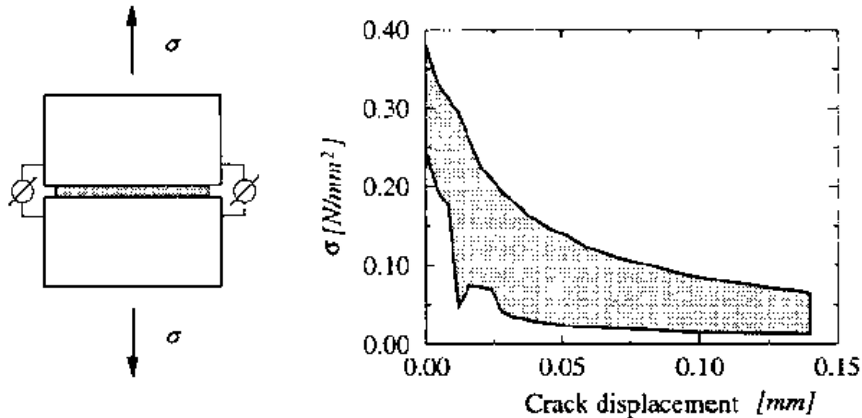
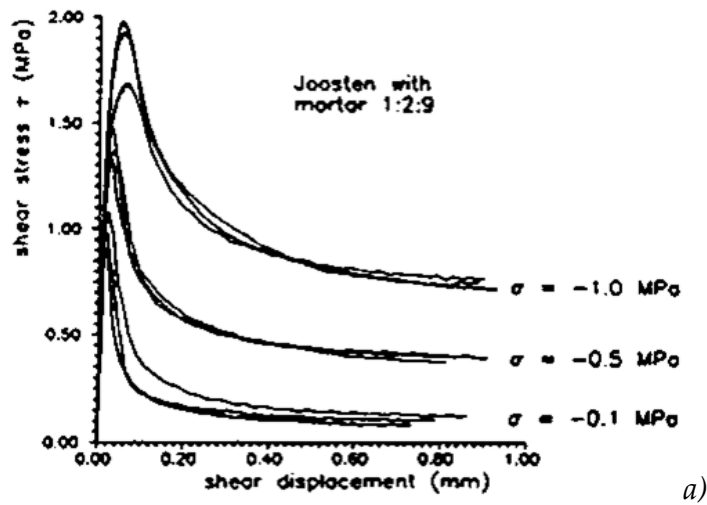


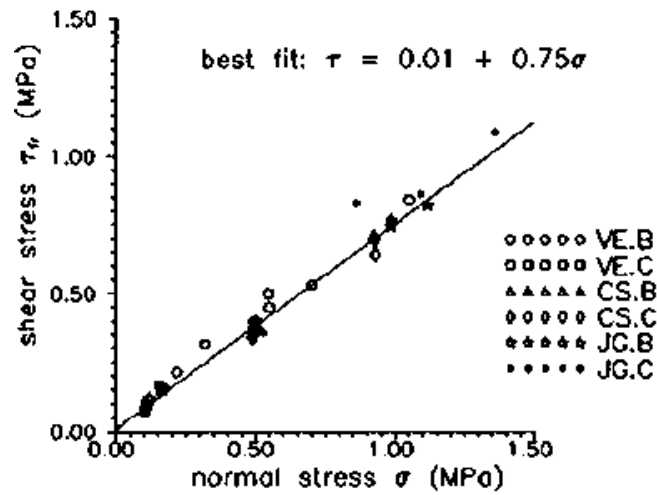
Figure 3.11 - Tensile behaviour of the masonry joint and test equipment [11].

- **Load: Direct shear**

Van Der Pluijm [12] also studied the joint behaviour subjected to direct shear. As can be seen in *Figure 3.12a*, the shear strength increase with the increase of the applied normal compression and in the post-peak phase, after having overcome the cohesion, the tangential stresses tend to a horizontal asymptote which represents the friction of the interface. *Figure 3.12b* shows the shear strength values as a function of the applied normal compression for specimens made with a combination of different materials. It is evident that all these experimental data can be describe by a straight line. This means that the friction force is independent of the materials that make up the interface, as is also emphasized in *Figure 3.12a* all curves, once the applied normal compression is fixed, tend to the same asymptote. The peak that describes the interface cohesion depend on the mortar strength.



a)



b)

Figure 3.12 – a) Shear behaviour of the masonry joint for different confinement levels
 b) Shear-normal stress envelope for different types of laboratory specimens [12].

3.1.2 Brick

- **Load: Biaxial tension-compression**

McNary e Abrams [9] also studied the behaviour of the bricks subjected to biaxial tension-compression tests, the main aspects of the research are reported below. The biaxial tests were carried out on two different types of bricks, in *Figure 3.13* the results of this test and those of a similar test achieved by Khoo [13] are reported. The data were then non-dimensionalized with respect to the uniaxial compression strength, C_o , and the direct tensile strength T_o . As can be seen, the experimental data obtained are distributed in a concave band and the 0.58 coefficient was derived statistically by minimizing the deviation between the experimental data, the equation that describe this curve is reported below:

$$\frac{C}{C_o} = 1 - \left(\frac{T}{T_o} \right)^{0.58} \quad (3.2)$$

where:

C : compressive stress in block;

T : tensile stress in brick.

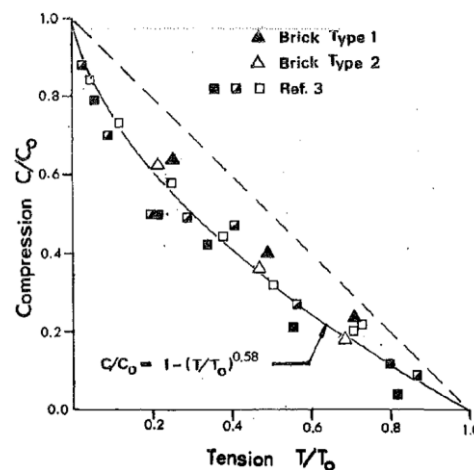


Figure 3.13 - Measured biaxial interaction diagram for brick specimens [9].

This failure domain is lower than that determined using the Coulomb's criterion, this means that the tensile loads on the blocks have a great influence on the compressive strength.

3.1.3 Composite material

- **Load: Uniaxial compression**

Hilsdorf [14] was the first to find out that the failure of the masonry depends on the interaction between blocks and mortar, and therefore by studying the splitting phenomenon he discovered that the greater compression deformability of the mortar, due to the Poisson's effect, generates an expansion in the orthogonal direction to the load. However, the mortar is in a triaxial compression state because it is confined by the surrounding blocks. This generates on the blocks tensile stress orthogonal to the load that causes the splitting phenomenon (*Figure 3.14*).

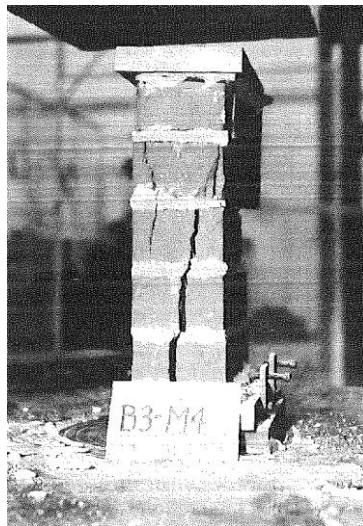


Figure 3.14 - Typical splitting failure of test prism [9].

McNary e Abrams [9] studied the behaviour of the masonry subjected to uniaxial compression tests, the main aspects of the research will be reported below. The masonry walls were made with combinations of two type of bricks and four types of mortar. From the research it was observed that the types of failure and the ultimate strength of the masonry depends on the type of the mortar used, which however does not restrict the failure domain. Furthermore, as the mortar strength decreases, the stress-strain curve becomes increasingly non-linear, as can be seen in *Figure 3.15* below:

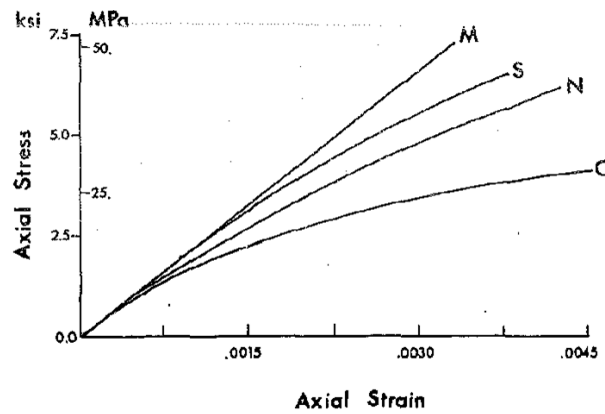


Figure 3.15 - Measured stress-strain curves for test prisms constructed with brick type 1 and different mortar types [9].

This shows how important it is to know the mortar properties to describe the strain behaviour of the wall. Finally, they confirm the idea of Hilsdorf [14], which states that due to the mortar tensile stresses arise in the block generating the splitting phenomenon.

As Binda states in [15], comparing the mechanical behaviours of the masonry and those of the individual components it is difficult to find a correlation between them. In Figure 3.16, the behaviours of the various materials are reported and it can be seen how the blocks have a purely elastic-fragile behaviour, the mortar an elastic-plastic one and instead that of the masonry a middle between these last two.

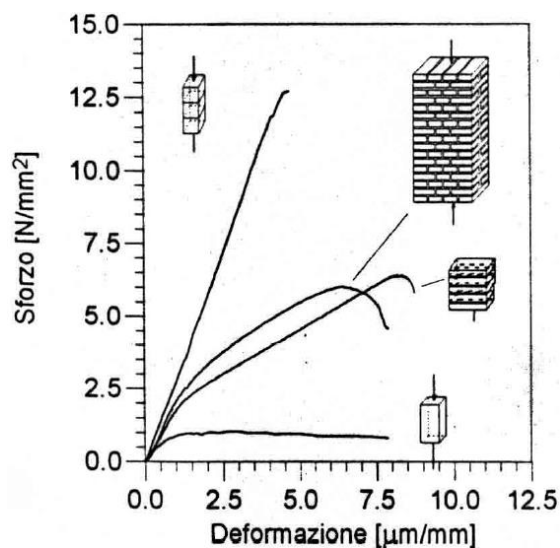


Figure 3.16 – Comparison between masonry and its components behaviour [15].

A complete analysis of the behaviour of the individual components was carried out by Page in [16], using the stress-strain curve and with FEM models, he obtained the behaviour of the masonry. The results of the compression tests are shown below:

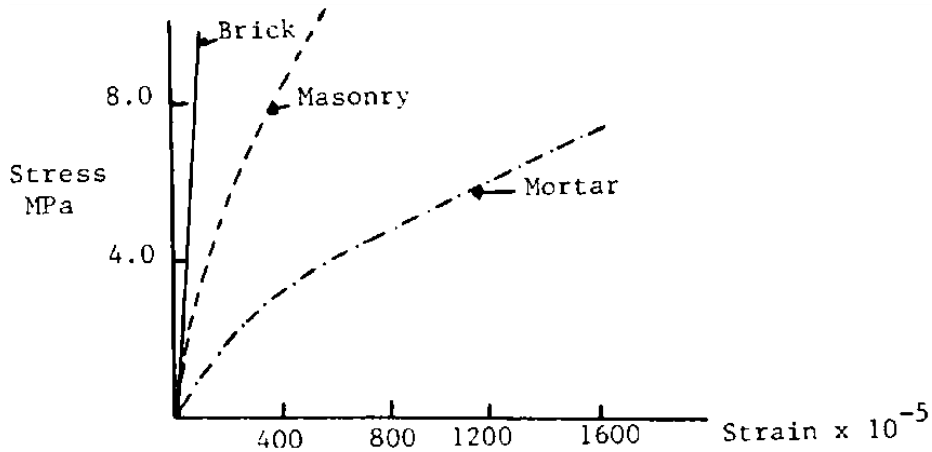


Figure 3.17 – Compression stress-strain curves [17].

From this research, the non-linearity of the masonry is mainly attributable to the mortar as the blocks have a purely linear behaviour.

Francis [18] analysed the factors that modify the compressive strength of the masonry. In *Figure 3.18*, the variation in the compression strength of the masonry is shown, when the thickness of the mortar joint changes and therefore as the thickness decreases there is an increase in resistance. The ancient Egyptians, Greeks and Romans already used this detail, thanks to their intuition and good practice in the realization of the masonry constructions. Moreover, the effect of the vertical joints is reported in that document, which have less lateral tensile strength than blocks and for this reason more frequent they are in the masonry and lower is the compression strength. Finally, it is stated that as the compressive strength of the brick increase, the resistance of the wall increases.

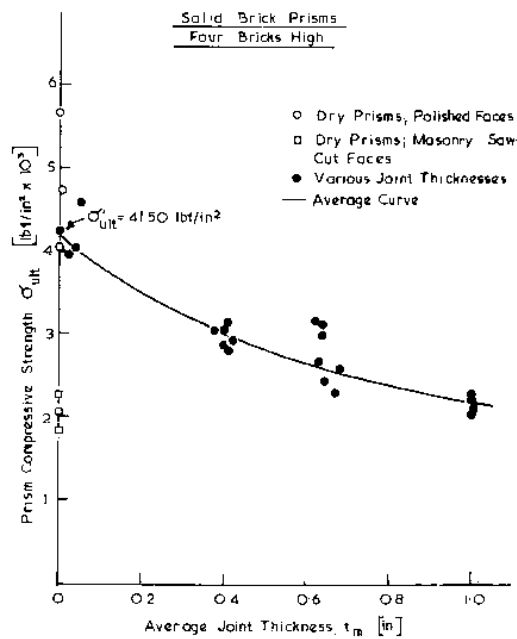


Figure 3.18 - Variation of prism compressive strength with mortar joint thickness [18].

- **Load: Direct shear**

Page, in [16] using FEM models, obtained the masonry behaviour under shear action. The results of the shear tests are shown below:

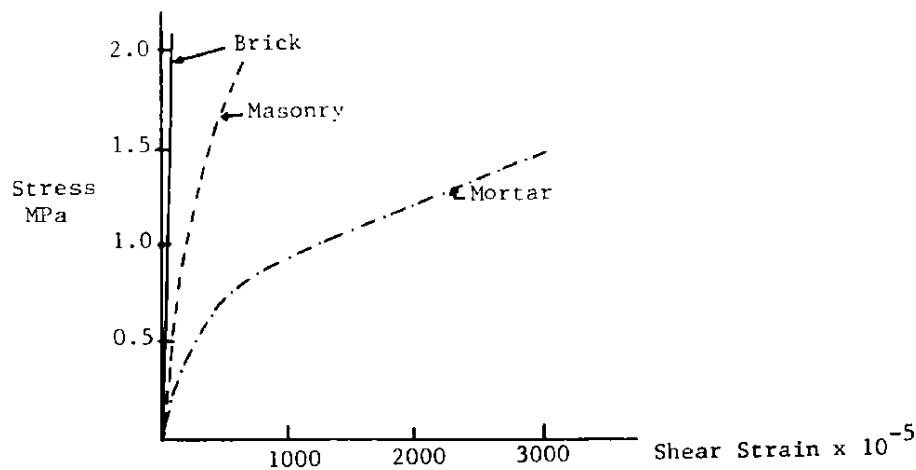


Figure 3.19 - Shear stress-strain curves [17].

Also, in case of shear action, the non-linearity of the masonry is mainly attributable to the mortar since the blocks have a purely linear behaviour.

- **Load: Uniaxial tension**

Backes [19] analysed the masonry behaviour under the action of traction perpendicular to the secondary joints. The collapse mechanisms obtained are of two types:

- a) Combined failure of the secondary joints and blocks (*Figure 3.20a*);
- b) Failure of the secondary joints due to the sliding of the main ones (*Figure 3.20b*).

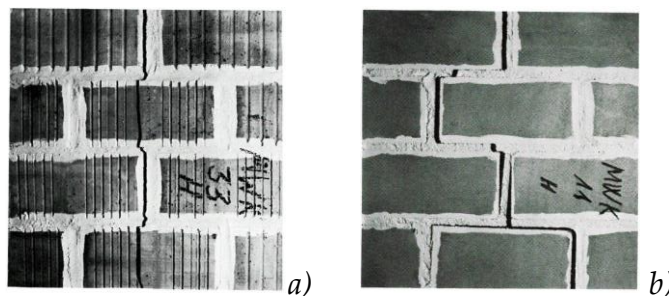


Figure 3.20 - a) Combined failure of the secondary joints and blocks;
b) Failure of the secondary joints due to the sliding of the main ones [19].

The deformation in the parallel direction to the main joints depend on the brick and mortar deformation and on their bonding properties. In general, the longitudinal deformation decreases as the mortar strength increases. The following are the stress-strain curve for the two collapse mechanisms:

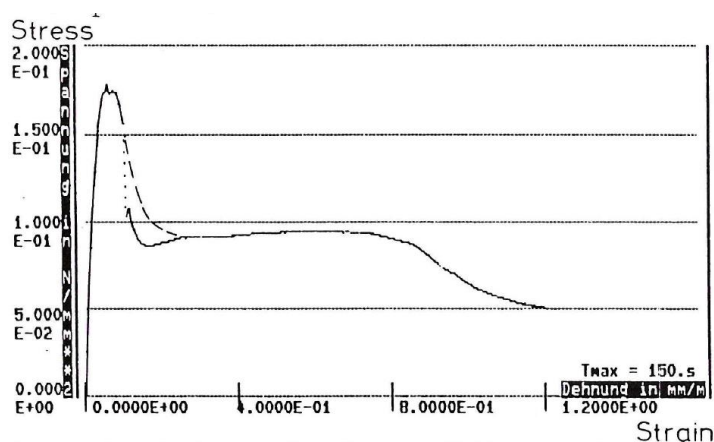


Figure 3.21 – Stress-strain curve for the a) collapse [19].

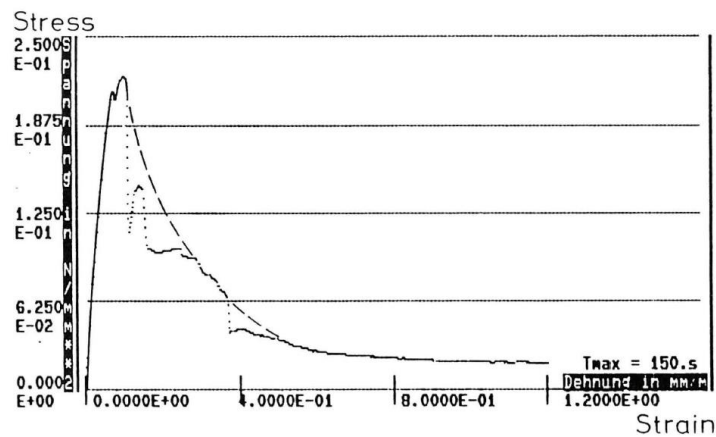


Figure 3.22 - Stress-strain curve for the b) collapse [19].

- **Load: Biaxial compression**

Most masonry walls are subject to in-plane cyclic loads that generate a biaxial stress state. As reported in the research of Page [20], the masonry exhibits different properties as the direction changes due to the mortar joints, which are plans of weakness. The collapse can only occur in joints or in a combined mechanism in blocks and joints. He observed two types of collapse depending of the stress ratio. In case of uniaxial compression load, the collapse occurs in the normal plane to the wall and by cracking and sliding in the joint plane or with a combined collapse generating cracks both in the joint and in the bricks (*Figure 3.23a*). In case of biaxial compression, the previous collapse no longer occurs because the new load prevents it, so there is a collapse due to splitting in a parallel plane to the wall at about half the thickness (*Figure 3.23b*).

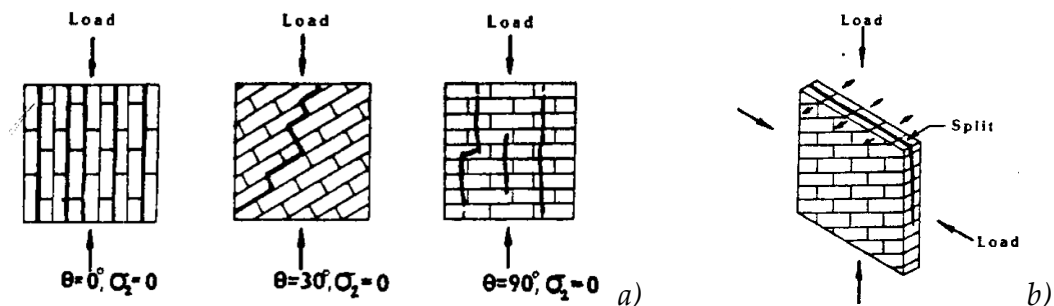


Figure 3.23 - Failure modes for biaxial compression tests on brickwork:
a) Uniaxial compression; b) Biaxial compression [20].

In *Figure 3.24*, the three-dimensional failure surface is represented, which is non-dimensionalized at the minimum compression strength of the specimens.

The collapse mechanism *b*) is not influenced to the joint strength, the mortar type and their orientation. However, when one of the two main stresses are dominant, there is a collapse of type *a*) and therefore the joints orientation and the mortar type influence the masonry strength, generating collapse in its plane.

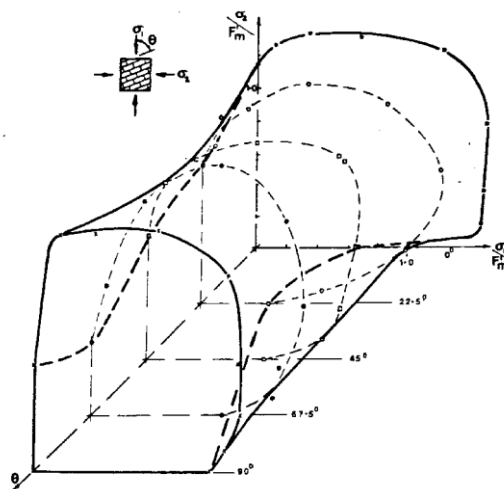


Figure 3.24 - Failure surface for half-scale brickwork under biaxial compressive stress [20].

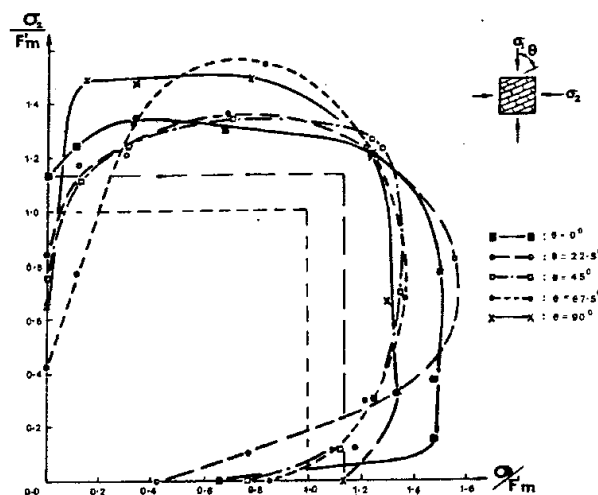


Figure 3.25 - Failure surface for brickwork under biaxial compression projected onto σ_1 - σ_2 plane [20].

A further research using biaxial compression tests are carried out by Dhanasekar [21], in which he traced the stress-strain curve of the various tests realized respect to the local axes indicated in *Figure 3.26*. As can be seen in *Figure 3.27*, the tangent to the curve changes with increasing stresses. Only the first section of the curve can be considered elastic and, as stated in the paper, in this area the behaviour is isotropic, this isotropy is eliminated in the non-linear field due to the weakness of the main joints with respect to the bricks.

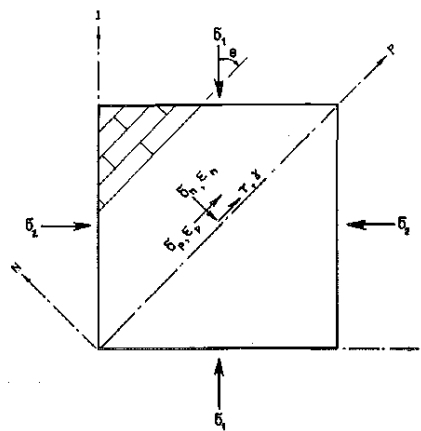


Figure 3.26 - Stress and strain transformations [21].

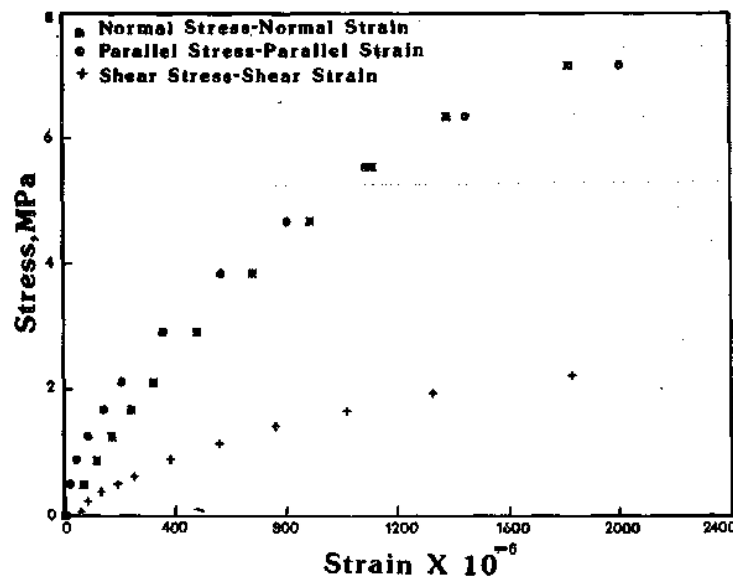


Figure 3.27 - Measured stress-strain curves for panel under biaxial compression-compression (1MPa = 145psi) [21].

• **Load: Biaxial tension-compression**

Page [20] also carried out biaxial tension-compression tests and he observed that in contrast to the previous case, the failure always occurred in a plane normal to the wall. *Figure 3.28* shows the different modes of failure depending on the joints orientation and the relationship between the main stresses. The failure occurs only in the joints or through combined mechanisms that involve both joints and blocks. In *Figure 3.29*, which shows the three-dimensional failure surface, it can be seen that as the joints angle increases, the biaxial strength of the masonry decreases, except in passing from $\theta=67.5^\circ$ to $\theta=90^\circ$ that there is an increase in resistance to biaxial compression. This phenomenon is caused by a change in the failure mechanism, in case of $\theta=67.5^\circ$ there is a failure due to sliding instead of $\theta=90^\circ$ there is a failure due to splitting in the direction parallel to the mortar joints.

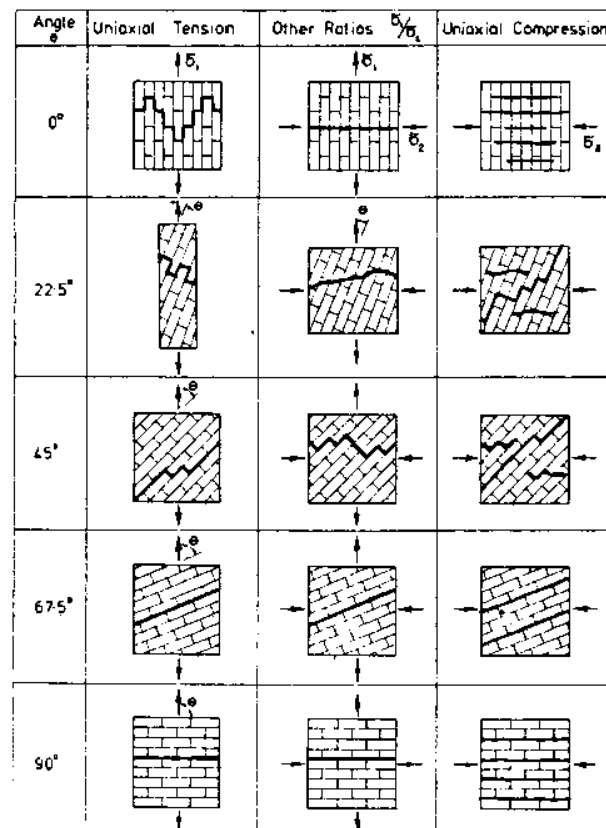


Figure 3.28 – Failure modes for biaxial tension-compression tests on brickwork [20].

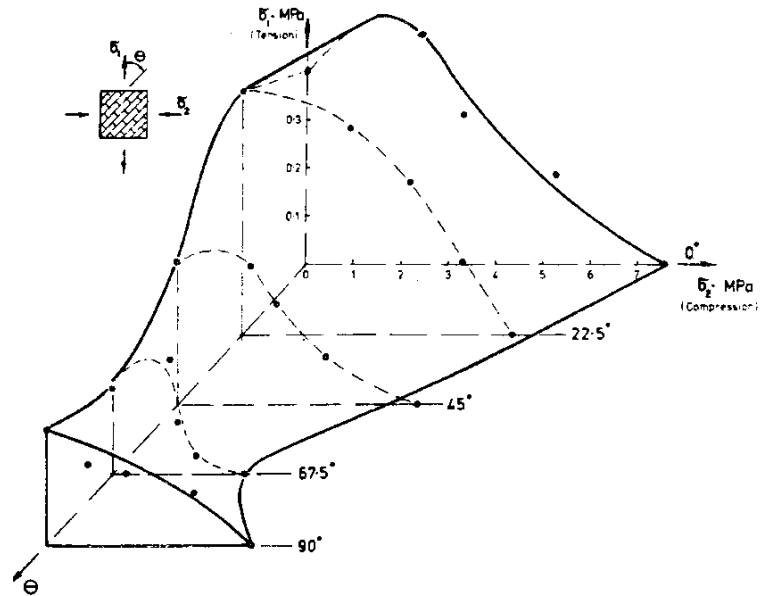


Figure 3.29 - Failure surface for half-scale brickwork under biaxial tension-compressive stress [20].

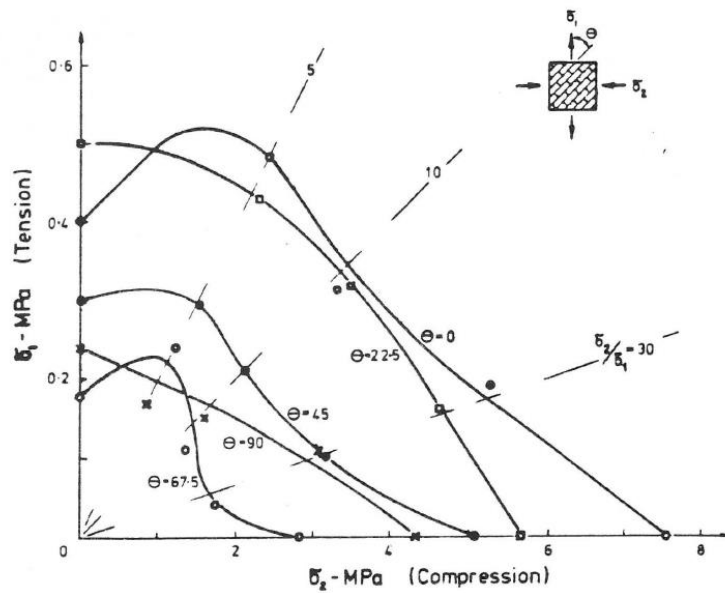


Figure 3.30 - Failure surface for brickwork under biaxial tension-compression projected onto σ_1 - σ_2 plane [20].

A further research using this type of test was carried out by Dhanasekar [21], in which he traced the stress-strain curves of the various tests obtained with respect to the local axes indicated in *Figure 3.26*. As can be seen in *Figure 3.31*, in case of biaxial tension-compression load the failure occurs in the linear field unlike the case of biaxial compression.

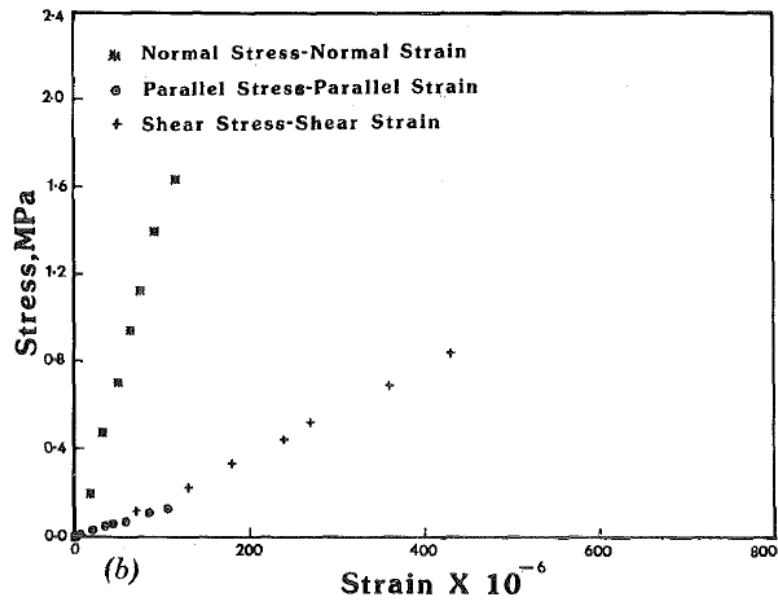


Figure 3.31 - Measured stress-strain curves for panel under biaxial tension-compression
(1MPa = 145psi)



Chapter 4

Masonry Modelling

4.1 Introduction

In this chapter the problem of the masonry modelling will be dealt. It is a difficult topic as the masonry is subjected to a many type of collapses due to joints which are plans of weakness on which the cracks can develop and for this reason it is considered a heterogeneous and anisotropic material. As reported in *Chapter 3* , the masonry behaviour depends on many factors such as the mortar type, the joint thickness, the block disposition, etc. All these variables and in addition its non-linear behaviour makes the modelling very complicated and difficult to treat. In the following chapters, as reported in [22], the most used modelling techniques will be discussed reporting the advantages and the disadvantages.

4.2 Micro and macro-modelling

The masonry modelling can be realized through two types of approach:

a. Discrete approach:

- Detailed micro-modelling: the mortar and the blocks are represented by continuous elements, whereas the block-mortar interface is represented by discontinuous elements. This approach requires a very refined mesh that determine a high computational load and therefore suitable for small structure. Furthermore, in order to correctly describe the behaviour of

each individual element, a detailed knowledge of the characteristics of the individual materials is required, which is often difficult to achieve.

- Simplified micro-modelling: the blocks are expanded and represented by continuous elements, whereas the mortar and the block-mortar interface are combined in a single discontinuous element. In this approach the Poisson's effect of the mortar is ignored and this means less accuracy in assessing the compression on the mortar.

b. Continuous approach:

- Macro-modelling: the blocks, the mortar and the block-mortar interface are not distinct, but they are modelled together in a single continuous anisotropic element applying a homogenization of the materials. In this case the lower computational load allows the modelling of large structure, in fact it will be used for modelling the case study of this thesis.

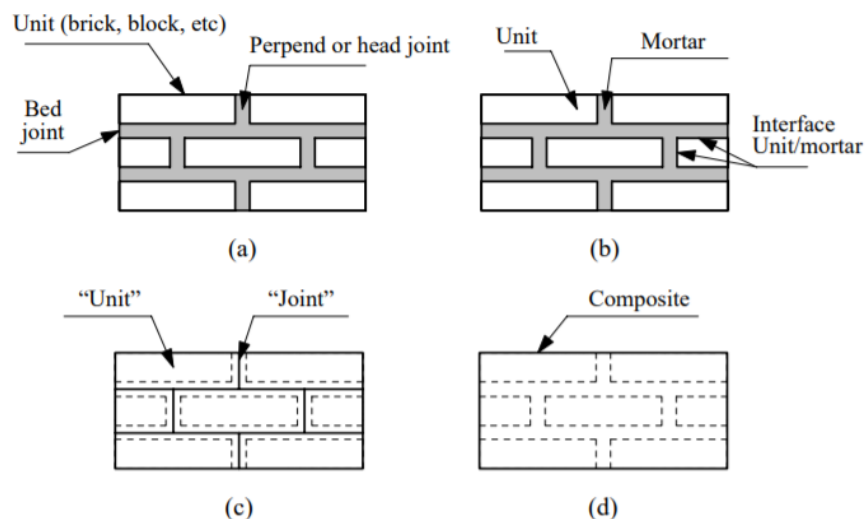


Figure 4.1 - Modelling strategies for masonry structures: (a) masonry sample; (b) detailed micro-modelling; (c) simplified micro-modelling; (d) macro-modelling [22].

4.2.1 Micro-modelling

The micro-modelling is among the best methods to understand the behaviour of the masonry, because it gives the possibility to consider all the different collapse mode.

Lofti and Shing [23] were the first to treat the existing masonry under the action of the earthquake by means of an elasto-plastic dilatant interface model combined with a smeared crack model of the bricks. The model can simulate the beginning and the propagation of the crack under the combined action of normal and shear stresses, in addition it can consider of the joint dilatancy. For the description of the mortar joint behaviour, the Mohr-Coulomb's plasticity criterion was used combined with a tension cut-off criterion to allow tensile cracks. Thus, the resulting domain is hyperbolic with a smooth transition between the Mohr-Coulomb's criterion and the tension cut-off criterion. This domain depends on three parameters which are: traction strength, cohesion and friction angle. The equation of failure domain reported in *Figure 4.2*, is shown below:

$$F(\sigma, q) = \tau^2 - \mu^2 \cdot (\sigma - s)^2 + 2 \cdot r \cdot (\sigma - s) = 0 \quad (4.1)$$

where:

$r = (c^2 - \mu^2 \cdot s^2) / 2s$: radius of the yield surface at the vertex of the hyperbola;

s : tensile resistance;

c : cohesion;

μ : friction coefficient.

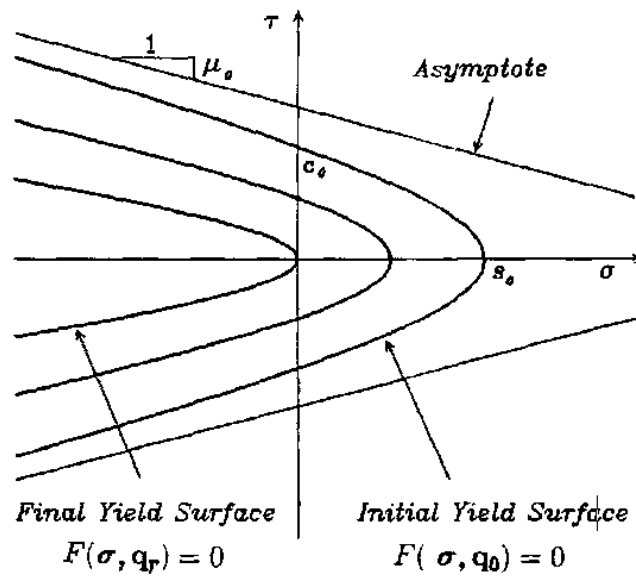


Figure 4.2 - Hyperbolic yield criterion [23].

In Figure 4.3 for a given compression stress, passing from the initial plasticity surface to the final one, the dilatancy angle decrease to zero.

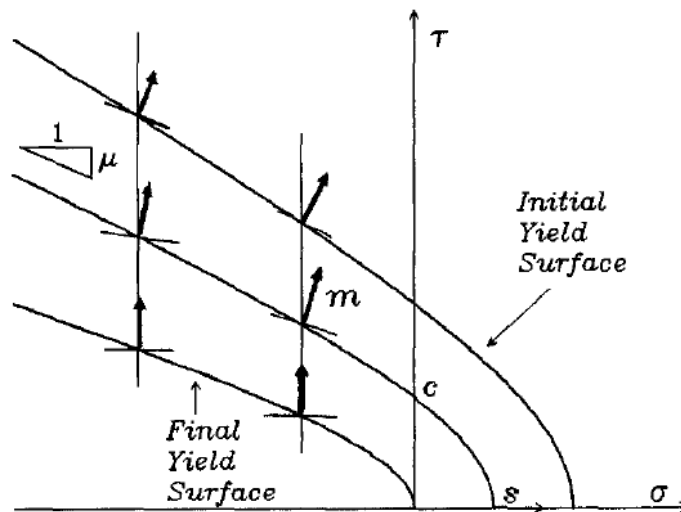


Figure 4.3 – Non-associated flow rule [23].

In this model, if plastic loadings are applied in the tension-shear region the tensile strength s is reduced, while the shear strength remains unchanged. Moreover, if plastic loadings are applied in the compression-shear region there is a reduction both tensile and compression strength.

A smeared crack model was used to simulate tensile and compression failure of the blocks. In *Figure 4.4*, Von Mises' plastic model is combined with the traction cut-off of Rankine's failure surface. Once reached the failure domain a rotating crack mode is used to model the cracked brick behaviour.

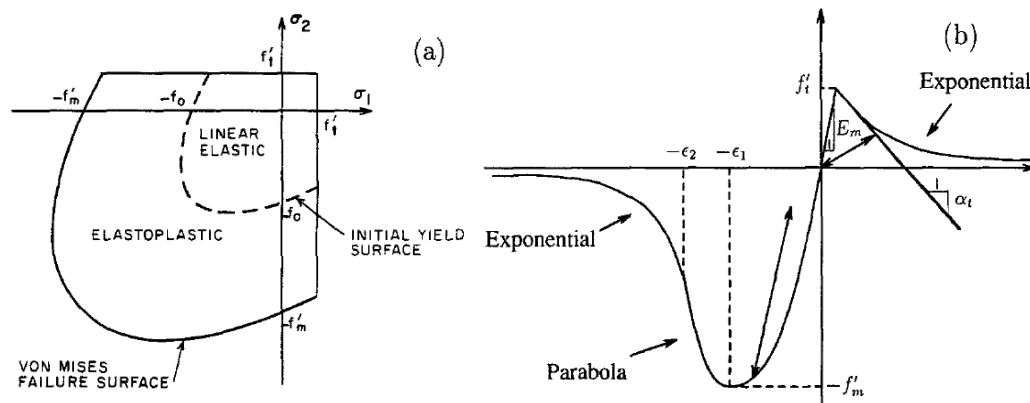


Figure 4.4 - Constitutive model for masonry units: (a) yield criterion for masonry units; (b) uniaxial behaviour of masonry units [23].

This numerical model can obtain the capacity of the structure and crack pattern of a given masonry element subject to seismic action.

Baggio and Trovalusci [24] studied the behaviour of the ancient masonry for the evaluation of its resistance under the action of in-plane horizontal load such as earthquakes. Since, the ancient masonries, are generally made with joints without mortar or poor-quality mortar, they studied dry brick walls. Due to the deterioration of the mortar, the ultimate load of the wall depends mainly on the interlock. The model is made up of rigid blocks and by an interface that does not withstand traction but is resistant to sliding thanks to friction. Once the friction resistance is overcome, there are some slips on the joints. The contact surfaces are modelled as interface elements that respond only to compression in the normal direction of the joint and shear in the other. The applied load is self-weight and an increasing horizontal force proportional to it, which statically simulates the earthquake.

Two ways of collapse were observed:

- Rotation and loss of interlocking between blocks (*Figure 4.5-1*);
- Sliding in the upper plans (*Figure 4.5-3*).

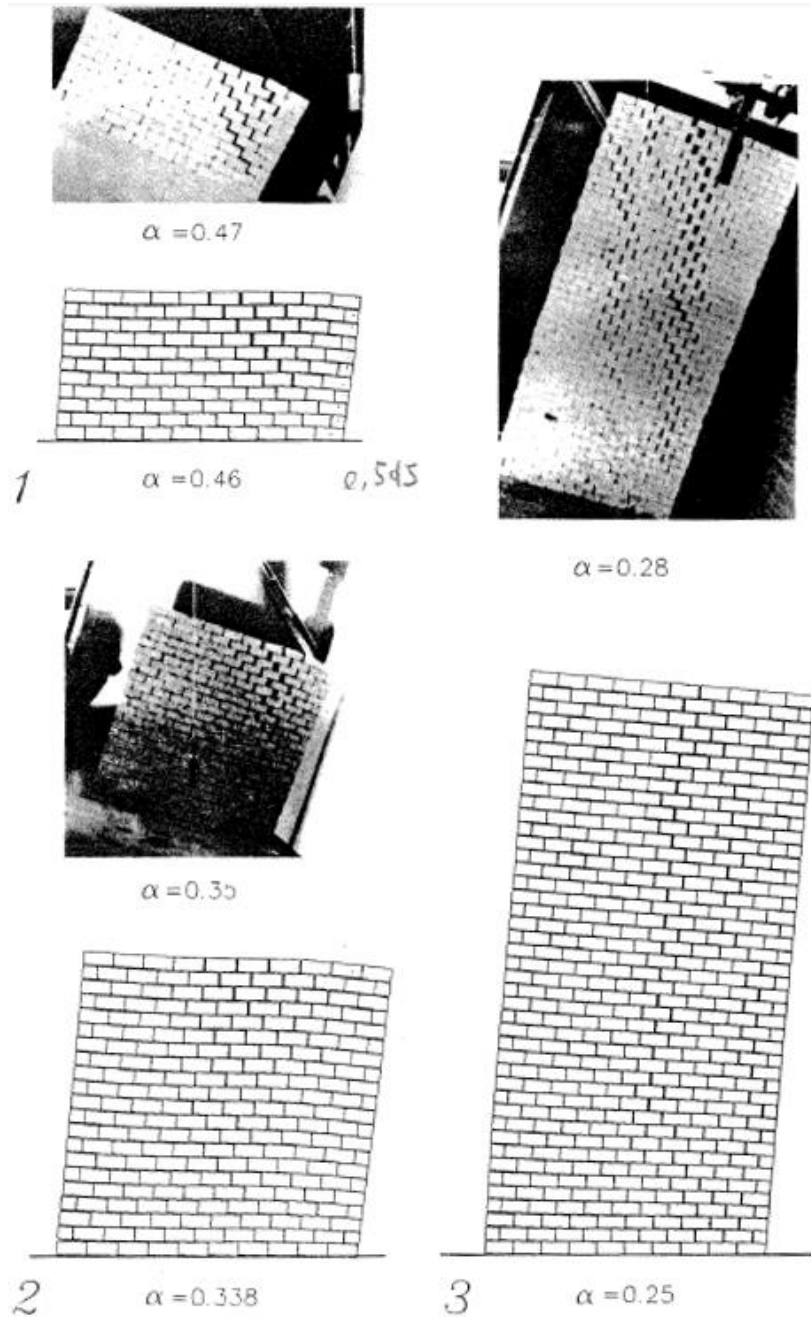


Figure 4.5 – Walls with header blocks subject to vertical and to the ultimate horizontal body forces: analysis results in comparison with the experimental one [24].

Lourenço and Rots [25] created a model that includes a tension cut-off that limits the tensile strength, a Coulomb's friction envelope and a cap model for the compression failure. The innovation of this model is the insertion of a fictitious interface element that considers the tensile collapse of the blocks. The difference with Lofti and Shing's model [23] is the hiring that all inelastic phenomenon take place in the interface elements, this choice allows to have a robust type of modelling and to completely understand the stiffness degradation. Then, it can describe all the collapse mechanisms of a masonry:

- a. Cracking in the joints;
- b. Sliding along a bed or head joint at low values of normal stress;
- c. Cracking of the masonry units in direct tension;
- d. Diagonal tension cracking of the masonry units in direct tension;
- e. Splitting of units in tension as a result of mortar dilatancy at high values of normal stress.

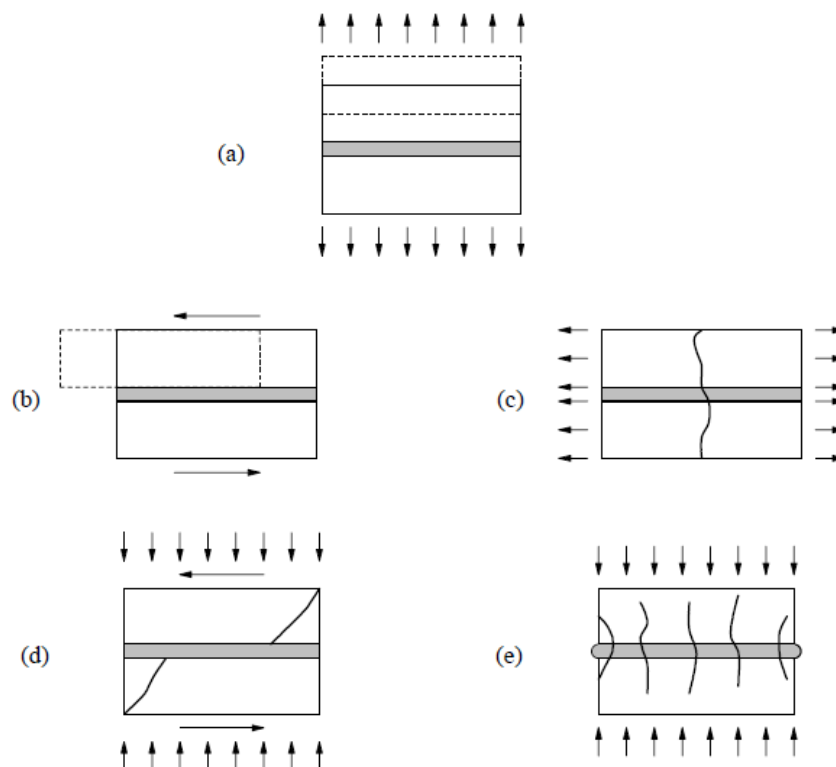


Figure 4.6 – Failure mechanisms of masonry.

The approach used concentrates all the damage in the joints and, if necessary, in the block collapse due to pure traction (Figure 4.7). The resistance domain of the interface joint includes all the above mechanisms except the tensile collapse of the block and limiting the combination of compression and shear considers the compression fracture, the shear failure of the joints and the diagonal collapse of the block. An interface element allows discontinuity in the field of the displacements and its behaviour is described by a relation between traction and relative displacements. The interface model includes a compressive cap, introduced for the first time by Druckler-Prager, where the inelastic behaviours of the masonry are concentrated, instead the elastic domain is composed of surfaces that include failure for traction, shear and compression with softening (Figure 4.8).

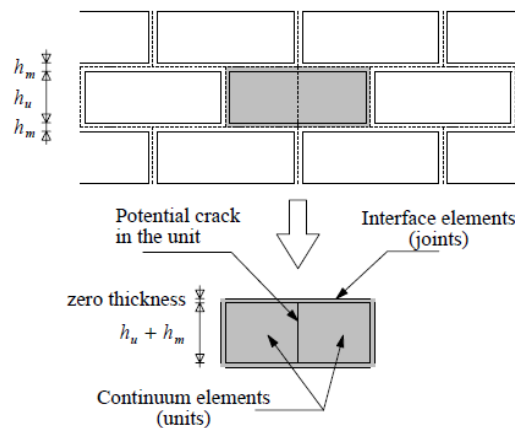


Figure 4.7 - Suggested modelling strategy. Units (u) are modelled with continuum elements. Mortar joints (m) and potential cracks in the units are modelled with zero-thickness interface elements [25].

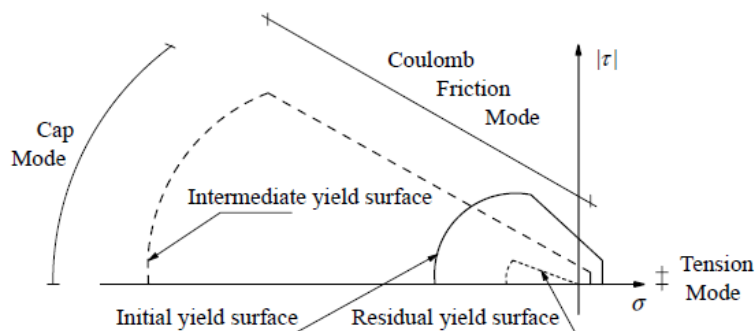


Figure 4.8 - Proposed model for interfaces. An "interface cap model" [25].

For the tension mode, exponential softening on the tensile strength is assumed according to the mode I experiments by Van Der Pluijm [11] (*Figure 3.11*) and for the shear mode, the Coulomb criterion based on micro-shear experiments by Van Der Pluijm [12] is used. The exponential softening is assumed for the cohesion and the softening of the friction angle is taken proportional to the softening of the cohesion.

The dilatancy is considered as a function of the shear relative displacement and of the confinement normal stress, increasing these values the dilatancy angle tends to zero. This phenomenon is realistic due to the micro-granular structure of the mortar and it is confirmed also by Van Der Pluijm's test. The model can produce the total degradation of the masonry without numerical difficulties, instead the modelling strategies adopted is mesh insensitive.

Giambanco et al. [26] created a model similar to the previous researchers but with particular attention to the cohesive-frictional joint transition taking into consideration the geometric dilatancy that arises in the pure friction state. Using a tribological law to describe the evolution of the contact surface and the variation of the shear strength. The model is composed by linear elastic blocks with mortar joints modelled with interface elements, which simulate the non-linear behaviour developed in the joints responsible of the non-linear behaviour of the masonry as a whole. This type of model is useful in case of ancient masonry walls with joints deteriorated by agents present in aggressive environments. The law used for the interface is elasto-plastic for not standard materials, paying attention to the cohesive-frictional joint transition. The process of loss of cohesion and the formation of a rough fracture surface is taken into account, considering a tribological law. All this treatment allows a better modelling due to the additional geometrical dilatancy and to the increase of residual shear strength.

Discontinuous and irreversible displacements appear when the stresses state reach the limit conditions. The elastic domain (*Figure 4.9*) is defined by the intersection of the two following convex surfaces:

$$\Phi_1 = |\tau_n| + \sigma_n \cdot \tan \varphi - c = 0 \quad (4.2)$$

$$\Phi_2 = \sigma_n - s = 0 \quad (4.3)$$

where:

τ_n : normal stress component;

σ_n : normal stress component;

φ : internal friction angle of the contact layer;

c : cohesion;

s : tensile strength.

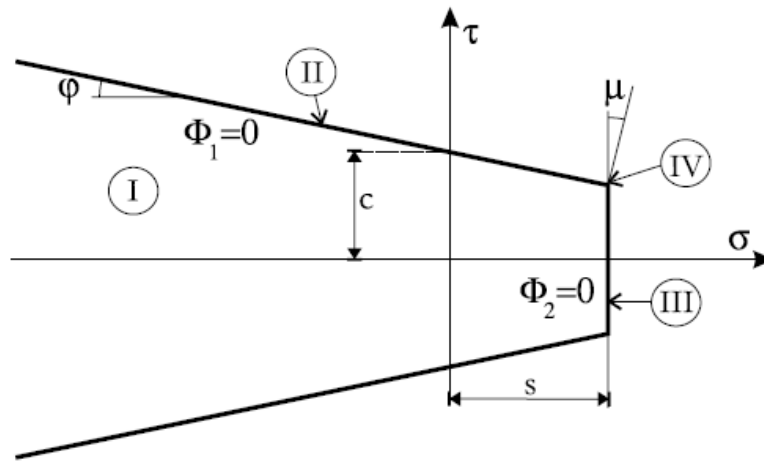


Figure 4.9 – Yield conditions represented in the stress space [26].

The interface law used allow a shear strength peak and a subsequent loss of cohesion, the shear resistance collapses to the residual resistance provided by the Coulomb's criterion. The response of the rough surface is modelled by two sliding surfaces, having asperity wedges (Figure 4.10), in particular these asperities are included by a certain angle α with respect to the nominal plane of the interface. Therefore, we have that the Coulomb's criterion changes as follow:

$$|\tau| = \sigma_n \cdot \tan(\varphi + \alpha) \quad (4.4)$$

where:

α : angle between the plane of the asperity and the nominal interface plane.

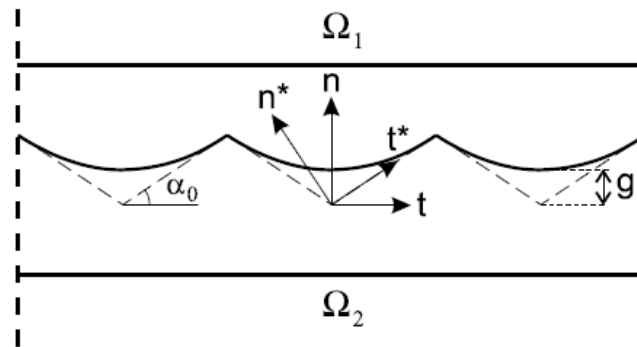


Figure 4.10 – Hyperbolic asperity model [26].

They used their model to simulate the behaviour of a part of masonry under the action of uniform traction parallel to the bed joints. This analysis was carried out to understand, at the joint level, the effect of the roughness surface and the evolution of behaviour, especially in the post-peak phase. Some numerical problems were solved obtaining local snap-back phenomenon related to the decrease in masonry elongation due to crack propagation. The FEM model analysed is shown below:

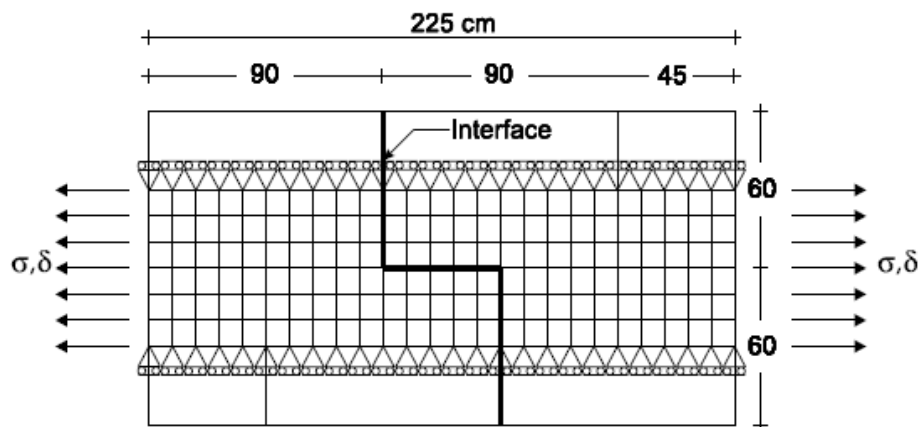


Figure 4.11 – Masonry specimen extracted from an infinitely long wall under tensile loading parallel to the bed joint [26].

The main results of this analysis are shown in *Figure 4.12*, it is evident how the behaviour can be divided in two stages:

- In the first stage there is a peak in A corresponding to cracking of the head joints and therefore a resistance collapse with snap-back phenomenon occurs, in point B the joints are opened and therefore the load is transferred to the bed joints. A second peak occurs in C which correspond to the maximum load that the bed joints can take in direct shear and after that another snap-back phenomenon occurs in correspondence of the beginning of the sliding on bed joints;
- The second stage that starts from the point D shows significant differences depending on the angle of the asperity adopted, therefore the residual strength depends on the latter.

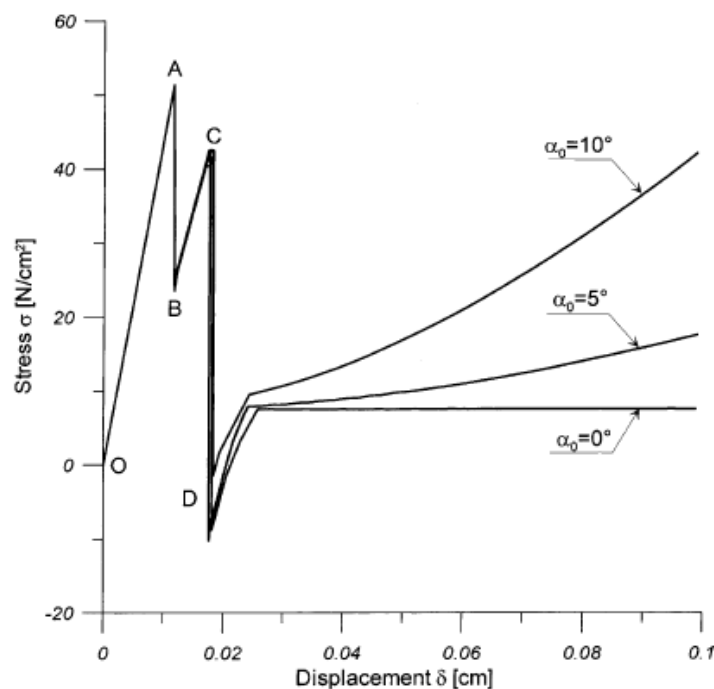


Figure 4.12 – Load-displacement curves for different values of the initial asperity angles [26].

This behaviour is similar to that reported in the Backes's experimental tests [17] in the *Chapter 3.1.3*.

4.2.2 Macro-modelling

The macro-modelling consists in modelling the masonry as a continuum having the mechanical characteristics equal to the average of the properties of the blocks and masonry. This method can be used when the dimensions of the structure are such that the local stress state can be considered almost homogeneous, that is, when its dimensions are greater than the dimensions of the blocks belonging to the masonry.

Pietruszczak and Niu [27] presented a mathematical formulation to describe the average of the mechanical properties of the masonry. They considered the masonry as an element composed of blocks matrix intercepted by head and bed joints. The head joints are considered as weak inclusions uniformly distributed instead the bed ones are considered with weak continuous planes.

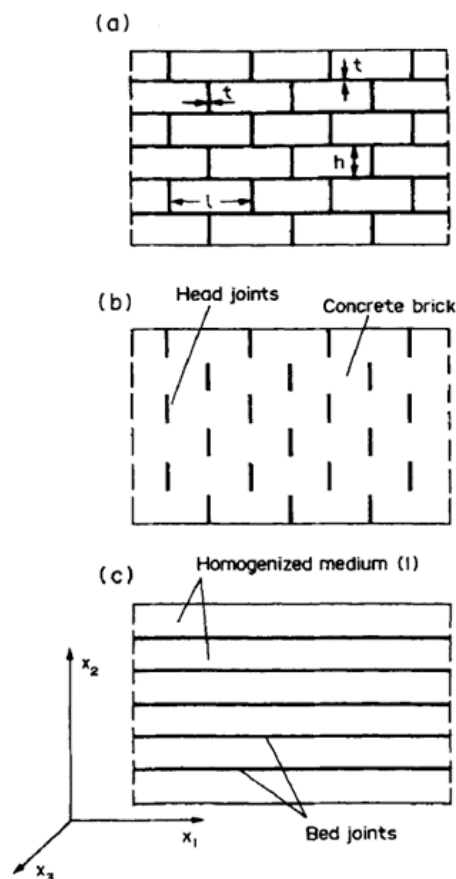


Figure 4.13 - (a) Geometry of a structural masonry panel; (b) Medium 1; (c) Medium 1 intercepted by bed joints [27].

In *Figure 4.13* the homogenization of the material occurs in two phases:

- First homogenization: occurs between vertical joints and blocks (medium 1). Assuming an elastic-brittle behaviour, the solution of this problem is obtained through Eshelby's solution (1957) for the ellipsoidal inclusions associated with the theory of the middle fields of Mori-Tanaka (1973);
- Second homogenization: occurs between the material obtained in the previous homogenization (medium 1) and the bed joints. For the bed joint an elastic-plastic behaviour was assumed and using a perfect cohesion to the interface.

They developed a criterion of damage to the masonry by defining two types of collapse one concerning the brick matrix which determines a fragile collapse and the other concerning ductile/brittle failure of the bed joints. The collapse of the head joints was not considered because they cause a local failure which does not produce the collapse in the macroscale. The medium 1 material is considered with orthotropic elastic behaviour, imposing a transient elastic-brittle behaviour for the blocks and an elastic-plastic behaviour expressed with Coulomb's law for bed joints. For the mathematical formulation of the constitutive relation, it is advisable to refer to [27]. From their study it is understood that the elastic characteristics are strongly influenced by the thickness of the mortar joint and that the collapse mode is a function of the load history applied. Finally, the head joints have a very small contribution in macroscopic collapse and are therefore considered with linear elastic isotropic behaviour.

An important research was carried out by Alpa and Monetto [28] who studied, with microstructural considerations, the behaviour of the dry block masonry wall under the action of in-plane forces. For this type of masonry, they obtained the constitutive equations concerning the linear, non-linear field and the strength domain. The masonry was modelled as an assembly of rectangular blocks with frictional forces acting on the joint surfaces.

The behaviour of the blocks was modelled as an elastic solid with plane stable frictional microcracks, without considering the crush collapse of the blocks. The displacement jumps that can occur in microcracks and joints are considered as inelastic deformation contributions, defined through a homogenization procedure. The constitutive equations proposed by them therefore consists of:

- An elastic part having as a limit the stress state that activates the displacement jumps in the microcracks and joints;
- An inelastic part characterized by controlled plastic deformations caused by the displacement jumps of the microcracks and joints;
- A third part characterized by an uncontrolled plastic flow dependent on the assembly and size of the blocks, the phase in which the collapse occurs.

As regards the third point, various failure mechanisms can be activated as shown in the following figure, the other mechanisms can be obtained by combining the fundamental ones.

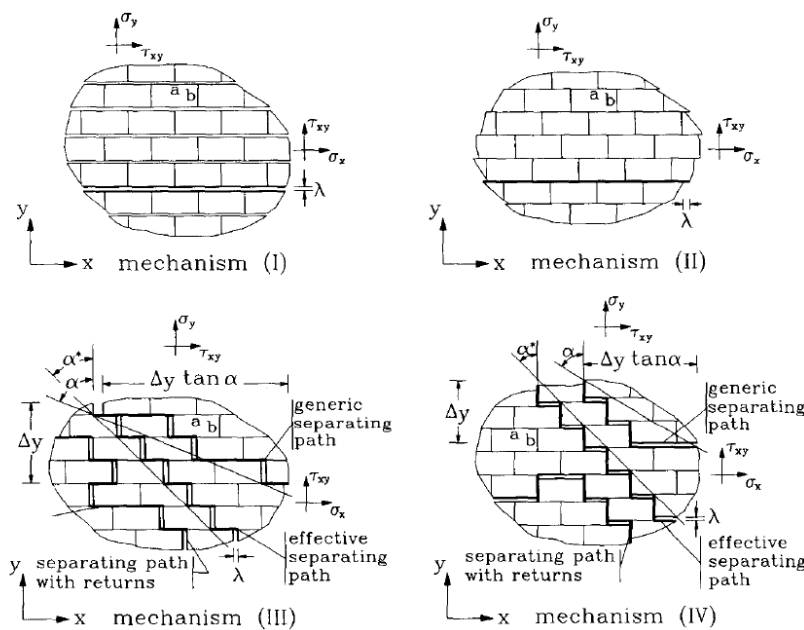


Figure 4.14 – Fundamental mechanisms of uncontained flow: I) Pure opening; II) Pure sliding; III) Opening at staggered joints and sliding along the aligned ones; IV) Opening at aligned joints and sliding along the staggered ones [28].

The most significant aspect of the model is the failure domain reported in *Figure 4.15*. Thanks to its completeness of the damage that it includes and for its direct dependence on the characteristics of the geometric wall texture.

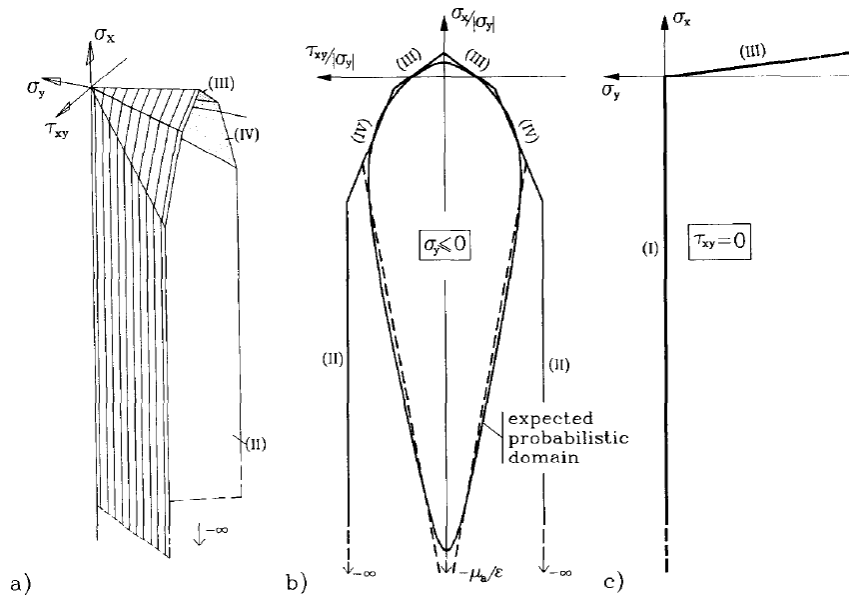


Figure 4.15 - Piecewise linear limiting surface of local possible equilibrium for $a/h = 0.5$ and $p = 0.5$: (a) in the space of the stress state components σ_x , σ_y , τ_{xy} ; (b) on a plane $\sigma_y = \text{constant}$; (c) on the plane $\tau_{xy} = 0$ [28].

Through their study it was understood that:

- The dry block masonry with in-plane loads behaves as an anisotropic material without tensile strength in the normal direction of the bed joints but having tensile strength in the direction parallel to them, depending on friction and the stress state;
- Four collapse mechanisms are generated for the uncontrolled flow of deformations dependent on the block size;
- An uncontrolled sliding flow of deformation can occur both by pure shear and by combination with elongation;
- The limit state flow rules are non-associated;
- With the assumption of small flow, the uncontrolled flow rules derived from a microstructural approach can be implemented in continuum analyses.

Another study on continuous modelling was developed by Adreaus [29] by studying the masonry panels under the action of in-plane loads. He obtained three ways of collapse:

- Slipping of the mortar joint: described by a frictional law which considers for the shear strength the non-linear dependence on normal stresses, using the modified Mohr-Coulomb approach.
- Cracking of clay blocks;
- Splitting of mortar joints: described using maximum tensile strain criterion of Saint Venant and the material was considered orthotropic, elastic and nonsymmetric;
- Spalling of the middle plane: governed by the maximum compressive stress of Navier.

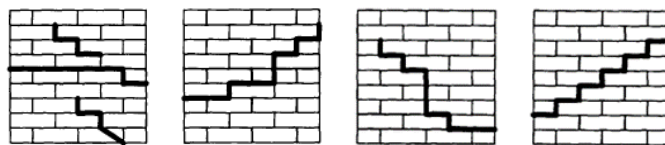


Figure 4.16 - Mechanism I: Slipping on mortar joints [29].

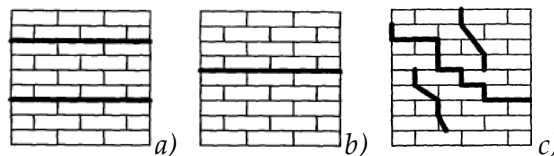


Figure 4.17 – a) b) Mechanism II: Slipping on bed joints; c) Mechanism III: Splitting of bricks and slipping on mortar joints [29].

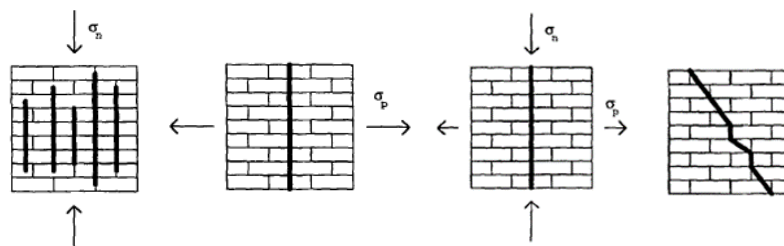


Figure 4.18 - Mechanism IV: Splitting of bricks and head joints [29].

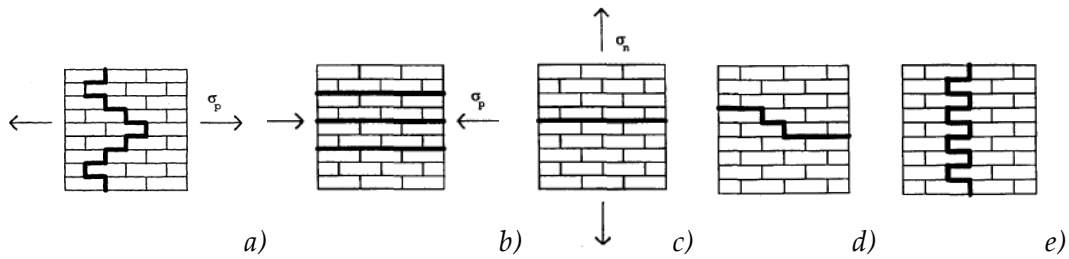


Figure 4.19 – a) Mechanism V: Slipping of bed joints and splitting of head joints for tension parallel to bed joints; Mechanism VI: Splitting of bed joints for: (b) Compression parallel to bed joints; (c) Tension normal to parallel to bed joints; d) e) Mechanism VII: Slipping and splitting of mortar joints [29].

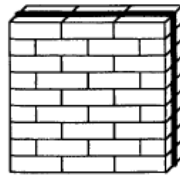


Figure 4.20 – Mechanism VIII: Middle plane spalling [29].

Luciano and Sacco [30] studied a completely micromechanical approach aimed at modelling historic masonry. The procedure for defining the damage model is shown below:

- Definition of the representative volume element (RVE);
- Definition of a damage kinetic law;
- Estimate the overall non-linear behaviour of the RVE using a micromechanical homogenization approach.

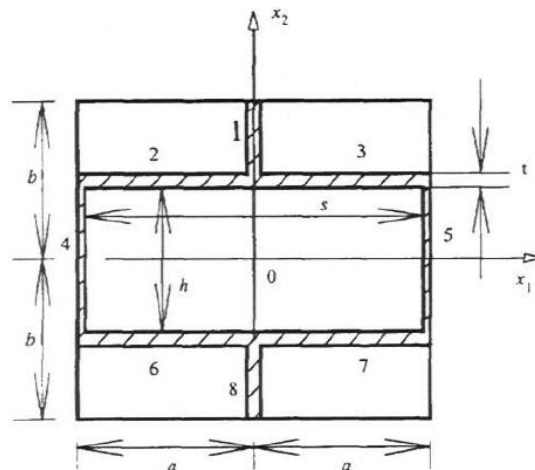


Figure 4.21 – Repetitive unit cell for the regular masonry material [30].

The kinematic damage law is defined by a finite number of failure configurations of the reference volume. Each configuration will be characterized by a certain distribution of cracks and voids (*Table 4-1*). The following assumptions were made to define the kinematic damage law:

- Cracks are formed only in the mortar joints and have elastic-brittle behaviour;
- Blocks have infinitely elastic behaviour;
- The thickness of the mortar joints is small and therefore the cracks can only develop vertically or horizontally;
- When the crack develops, the entire joint breaks and grows until it finds the blocks (*Figure 4.22*).

This type of model is very useful for modelling ancient walls, in which the mortar has much less resistance than blocks and therefore the crack develops mainly in the mortar.

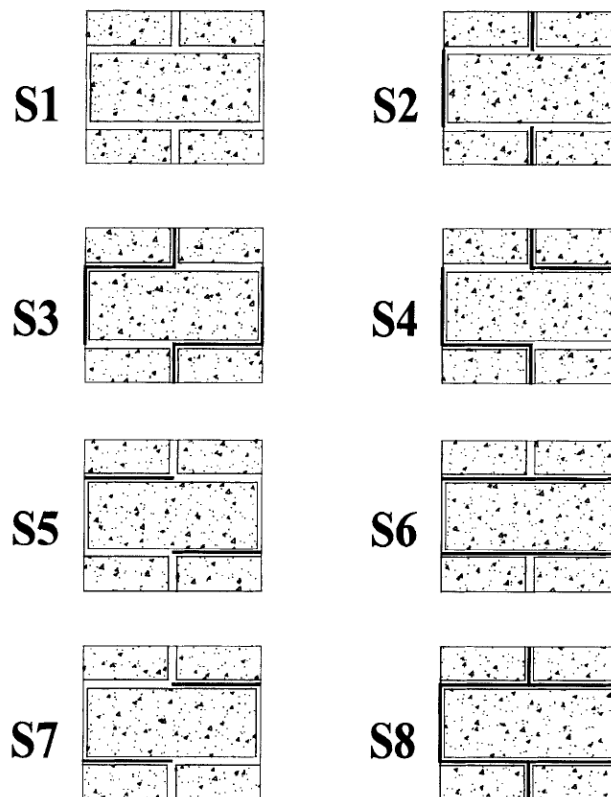


Figure 4.22 - Possible damaged states of old masonry material [30].

Table 4-1 – Possible damage paths [30].

Path 1	Path 2	Path 3	Path 4	Path 5	Path 6
S1	S1	S1	S1	S1	S1
S2	S2	S5	S5	S7	S7
S3	S4	S3	S6	S4	S6
S8	S8	S8	S8	S8	S8

Table 4-1 shows all the damage combinations that can be generated, but the model considers that for each state of damage, cracks can be opened or closed. And therefore, it is possible for each state of damage to associate the respective overall elastic characteristics of the masonry, means that the response of the masonry can completely vary during the damage process. Subsequently, the homogenization theory can be applied to derive the overall characteristics for each state of the masonry to obtain the non-linear constitutive law of the material. Luciano and Sacco proposed two different macroscopic damage laws associated with the strength of the mortar joints. The first is based on the energy approach typical of elastic fracture mechanics, while the second is a cohesive law local to Coulomb.

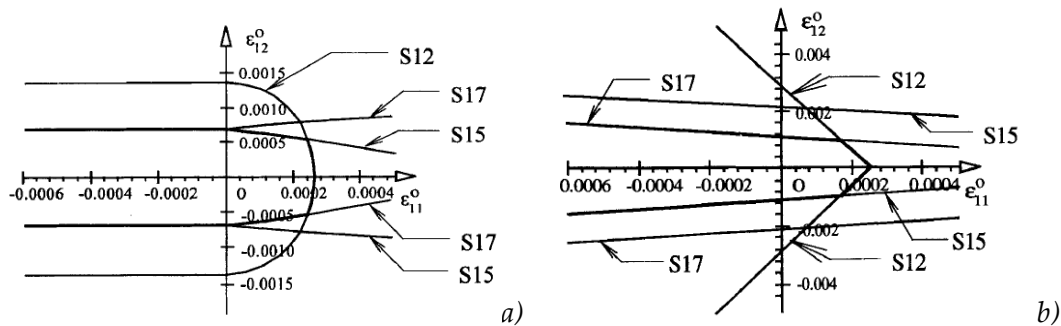


Figure 4.23 – a) Limit surface for the state S1 obtained by using the energy criterion;
 b) Limit surface for the state S1 obtained by using the cohesive local criterion [30].

In Lourenco et al [31] can be find a study aimed at plane stress models having quasi-brittle orthotropic materials. They used a yield criterion combines the advantages of modern plasticity concepts with a powerful representation of anisotropic material behaviour, which includes different hardening/softening behaviour along each material axis. Two different criteria for traction and compression were considered, the first criterion is focused on a localized fracture process (*Cracking of the material*) and the second is focused on a more distributed fracture process (*Crushing of the material*). Hill's criterion for compression and Rankine's modified criterion for traction were used. The behaviour of the material in tension is associated and with nonlinear post-peak softening behaviour, as reported in *Figure 4.25a*. Instead, the behaviour of the material in compression is also associated and with nonlinear hardening-softening behaviour, as reported in *Figure 4.25b*. The internal damage mechanism is described by two internal parameters one for tensile damage and one for compression. By formulating the model in this way, each internal parameter corresponds to two independent fracture energies along each axis of the material.

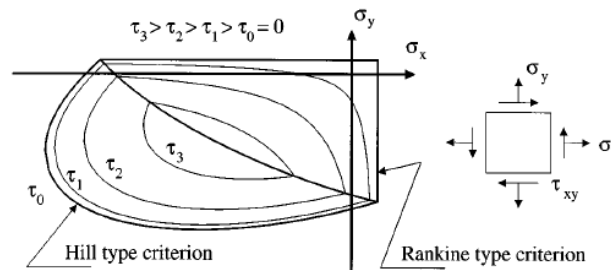


Figure 4.24 - Proposed composite yield criterion with iso-shear stress lines [31].

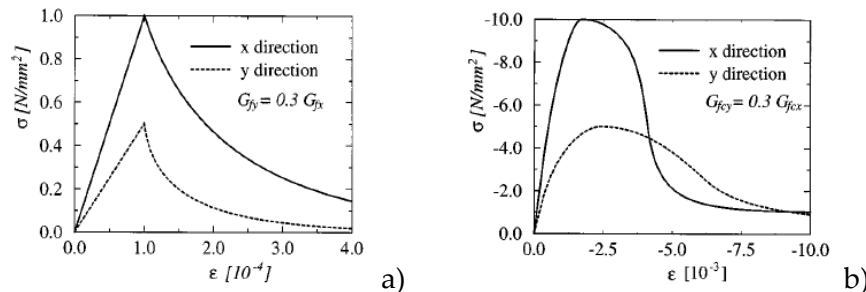


Figure 4.25 – a) Stress-strain response in uniaxial tension along the two material axes;
 b) Stress-strain response in uniaxial compression along the two material axes [31].

Finally, the model created by Lagomarsino and Gambarotta [32] is reported. This model aims at describing the behaviour of a masonry wall subjected to cyclic action in the plan. The constitutive model takes into consideration the mechanical behaviour of each component of the masonry by means of a process of homogenization of a representative stratified medium of the masonry. This approach considers two typical layers:

- Mortar bed joint layer: modelled to take into consideration the decohesion caused by a tensile stress acting orthogonally to the joint plane and surface frictional sliding due to a tangential tension acting on the joint plane;
- Brick and mortar head joints layer: modelled to take into consideration the damage and failure of the blocks due to normal compression on the plane of the main mortar joints and for shear acting on the joints position.

Therefore, the mechanical discontinuity caused by the secondary mortar joints is not considered. It was assumed that the medium deformation tensor, expressed as a function of the medium stress tensor, consists of an elastic contribution provided by the homogenized material and an inelastic contribution associated with the damage. The evolution of the damage, to which the degradation of the stiffness and strength of the material is connected, is regulated through two types of evolution laws:

- First law of evolution: based on the fracture mechanics and on the principles of the *Toughness Function* . It describes the loss of cohesion as the damage increases.
- Second law of evolution: based on the Mohr-Coulomb criterion and represents the frictional response of the joints.

Chapter 5

Case Study: Modena Cathedral

5.1 Introduction

This chapter focuses on the history of the structure and the reinterpretation of the construction phases. Through the latter, a critical historical analysis of the building was carried out. Modena cathedral constitutes one of the most important pieces of Romanesque culture in Europe and since 1997 it has become part of the World Heritage. It is still included in the list of *UNESCO* cultural, historical, artistic and environmental sites. As regards the history of the building reference was made to [33], instead for the construction phases to [34]. Finally, the masonry characterization tests and the installed monitoring system [35] are reported.



Figure 5.1 – 3D view of the Modena Cathedral (Google Maps images 2019)

5.2 Location and seismic classification

The cathedral is located in the heart of Modena city between Piazza Grande and Corso Duomo. The building is isolated from the surrounding structures except at the Ghirlandina Tower where the two structures are connected by two pointed arches.

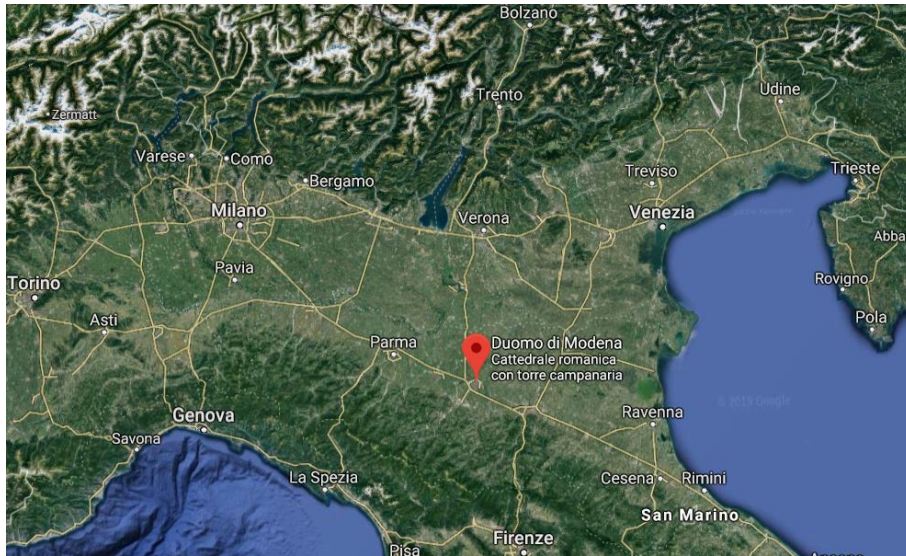


Figure 5.2 - Location of Modena Cathedral - Northern Italy view
(Google Maps images)



Figure 5.3 – Location of Modena Cathedral – City view (Google Maps images)

For the evaluation and classification of earthquakes we can refer to the seismic risk, which depends on three variables:

- *Seismic hazard* is the probability of occurring in a given place or within a given area and within a certain period of time of an earthquake capable of causing damage;

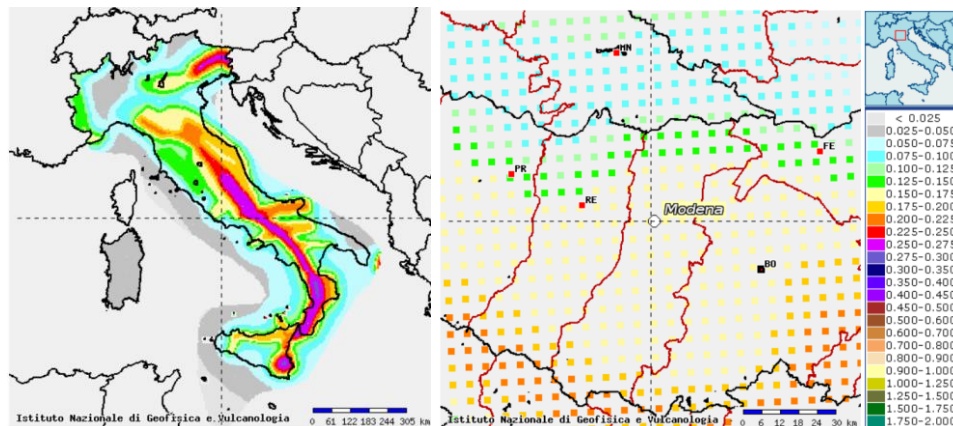


Figure 5.4 - Seismic hazard map of the national territory, of Modena and surrounding areas (National Institute of Geophysics and Volcanology)

- *Vulnerability* consists in the predisposition by people, goods or activities to suffer damages or modifications due to the occurrence of an earthquake. These damages can lead to the temporary reduction of efficiency or even to a total loss of functionality;
- *Exposure* can be defined as the location, consistency, quality and value of the assets and activities in the area that can be directly or indirectly influenced by the seismic event (towns, buildings, economic-productive activities, infrastructure and population density).

In relation to the seismic macro zoning (Figure 5.5), present in the DGR 1164 of 07/23/2018 " Update of the first application seismic classification of the municipalities of Emilia-Romagna ", Modena is classified in zone 3 (area with medium-low seismicity).

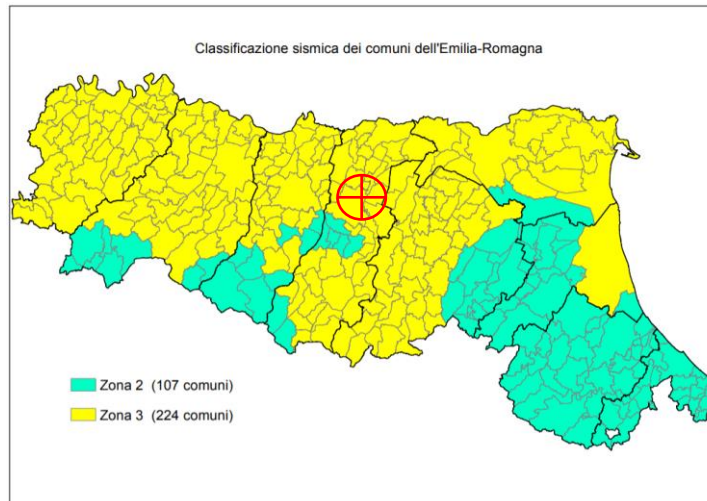


Figure 5.5 - Seismic classification of the Emilia-Romagna region (DGR 1164 del 23/07/2018 " Update of the first application seismic classification of the municipalities of Emilia-Romagna")

The four classification categories are:

- Zone 1: high seismicity $a_g > 0.25g$
- Zone 2: medium-high seismicity $0.15g < a_g \leq 0.25g$
- Zone 3: medium-low seismicity $0.05g < a_g \leq 0.15g$
- Zone 4: low seismicity $a_g \leq 0.05g$

This classification constitutes a technical-administrative reference to manage the project control activities and to establish a priority on the actions and measures for the prevention and mitigation of the seismic risk. Each zone or subzone is assigned a basic hazard value, expressed in terms of maximum acceleration on rigid ground (a_g : horizontal acceleration with probability of exceeding 10% in 50 years), based on the intensity and frequency of past earthquakes. However, this basic hazard value, as previously reported, has no influence on the design. Therefore, it is normal



to find a_g values of earthquakes greater than the values of the seismic macro zoning. In fact, for the design, reference is made to a local seismicity map with 5km meshes in which the ground acceleration value and other parameters are defined at each point of this mesh.

5.3 History

A complete and concise description of the history of the cathedral is given in [33], in addition the construction of the Modena Cathedral is described in the famous text entitled *Relatio sive descriptio de innovatione ecclesie santi Geminiani*, written in the 12th century. The decision to erect a new cathedral was taken at a particular moment in the Modena history, when Eriberto, bishop from 1055 to 1094, was removed from the city and the Emilian regional county seat remained without a bishop. At the end of the 11th century, the church appeared ancient and damaged. Because of the fear of a possible collapse both, the clerical order and the entire population of the diocese began to discuss what to do and therefore they decided to rebuild a new church. At this point also, Matilde of Canossa intervened and began to look for an architect capable to design such a work and to build such an important structure. Thus, Lanfranco was found.

Lanfranco, learned and competent, famous for his ingenuity, is the architect and the person responsible for the construction and the construction site. He was the first and foremost artist of this architectural work, started, as the *Relatio* recall, with the laying of the foundation stone on June 9 of 1099.

Together with Lanfranco, the great stonecutter Wiligelmo works, embellishing the temple with his sculptures. The cathedral of Modena is in fact an exception in the panorama of the medieval churches of the Italian peninsula. It is one of the rare buildings in which the rich set of reliefs, both traditional and photogrammetric, all performed with methodological rigor and philological emphasis, allows us to know its peculiar aspects and makes it possible to interpret the structure.

The *Relatio*, although extraordinarily detailed, does not allow solving all the questions that researchers have advanced over the last two centuries. One of the major unknowns concerns the structure of the previous building, described as unsafe and ancient, and how the new building has been oriented towards it.

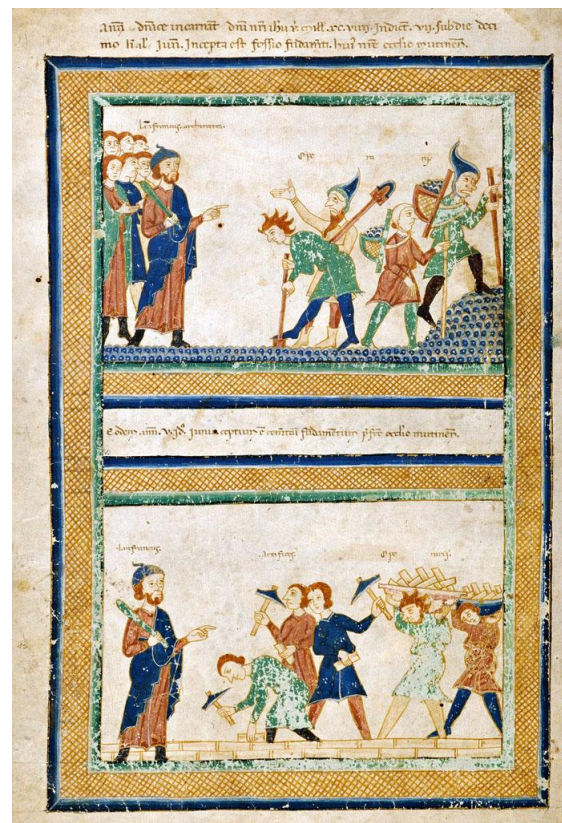


Figure 5.6 - *Relatio sive descriptio de innovatione ecclesie sancti Geminiani* [33]

At the beginning of the twentieth century, some works carried out in the cathedral through a certain number of excavations, produced incomplete and in some cases unclear data, which are subjected to different interpretations [36]. The hypothesis proposed by Bertoni [37] of a cathedral with five naves dating back to the early Middle Ages, related to some elements of the choir enclosure, now preserved in the Cathedral Lapidary Museum, has raised some uncertainties. In fact, it has been rightly observed that the shape of the four-sided pillars could not and cannot be earlier than the eleventh century. Consequently the remains found in the excavations have been referred to the building promoted by the bishop Eriberto, who wanted to destroy and rebuild to show the city's adherence to the papal political faction, ending up contradicting the *Relatio* in the only point where it describes the previous church in ruins and very old [38].

More persuasive, on the other hand, is the reconstruction advanced by Gandolfo [36] based on the careful reading of the *Relatio* and on the notes of

the excavation reports that are still preserved. According to the researcher, the traces of foundation are not of to the previous building, in which a different orientation was hypothesized, but to the remains of an atrium placed before the cathedral and built around 1070. Even if numerous uncertainties remain on the configuration of the previous cathedral, it is certain, that the construction of the new one was set up in such a way as not to demolish the old church. Then proceed to its demolition, once the works of the new church had reached such a point as to allow the liturgical celebrations. This idea was later denied in 2013 by the Elena Silvestri's work, reported in the next chapter.



Figure 5.7 – Modena cathedral façade (Photography Manuel Rovesti survey 29-08-2019)



5.4 Construction phases

Learn the cathedral construction phases evolution is fundamental to know the materials used and to identify the principal structural elements. It is also important to observe the damage, the crack pattern and taking into consideration the past maintenance interventions carried out on the building, to have a complete and in-depth view of the structural behaviour. These analyses are extremely important in Modena cathedral case for its articulated history, starting from its construction in different phases up to the modifications made over time. Furthermore, the following interventions were realized: gradual insertion of chains, inversion of the roof frame, support placed in adherence with internal and external walls and post-earthquake consolidation operations.

Studying the settlements and the constituent anomalies of the fronts, the hypotheses previously supported by the researchers have been re-evaluated by E. Silvestri [34]. She introduced a new point of view, never previously studied, based on the differential settlement on which the structure has been subject since the first years of its construction. In the following chapters, her work is partially reported.

5.4.1 State of the art

It is initially introduced the state of the art of the historical researcher studies present in [34]. In the early twentieth century, several historians studied this topic. Arthur Kingsley Porter [39] claimed the presence of two construction sites, one that started from the apses and one from the facade. Due to the maintenance of the old cathedral part in which the remains of the protector St. Geminiano were kept. Frankl [40] introduces a hypothesis on the position of the prelanfranchiana cathedral and identifies the anomalies on lateral fronts justified as connection of the two construction sites. Also, Peroni [38] supports the hypothesis of two opposing building sites because of the presence of the various asymmetries and irregularities. Gandolfo [36] and Montorsi [41] maintain that the placement of the stone covering took place later than the brick structure. According to Gandolfo, the installation of the covering took place starting from the facade [42]. Peroni and Lomartire, studying the sculptural apparatus and the wall facing, identified three construction phases:

- *Phase A*: identifies the first large construction site that began, in 1099, from the apses and proceeds towards the west;
- *Phase B*: identifies the second large construction site that started, around 1106, from the facade and then proceeds on the east sides raising part of the aisles. In this phase Wiligelmo's activity is placed;
- *Phase C*: dated around 1130, is the phase of completions, connections and anomalies.

Peroni supported Porter's hypothesis, reinforcing the idea of two building sites and maintain that the phase A, the apse, is represented by the figure of Lanfranco, whereas the phase B, the facade, is represented by the figure of Wiligelmo [38]. Thus, historians influenced by a vision of two opposing artistic poles, Architecture and Sculpture, assume this thesis.

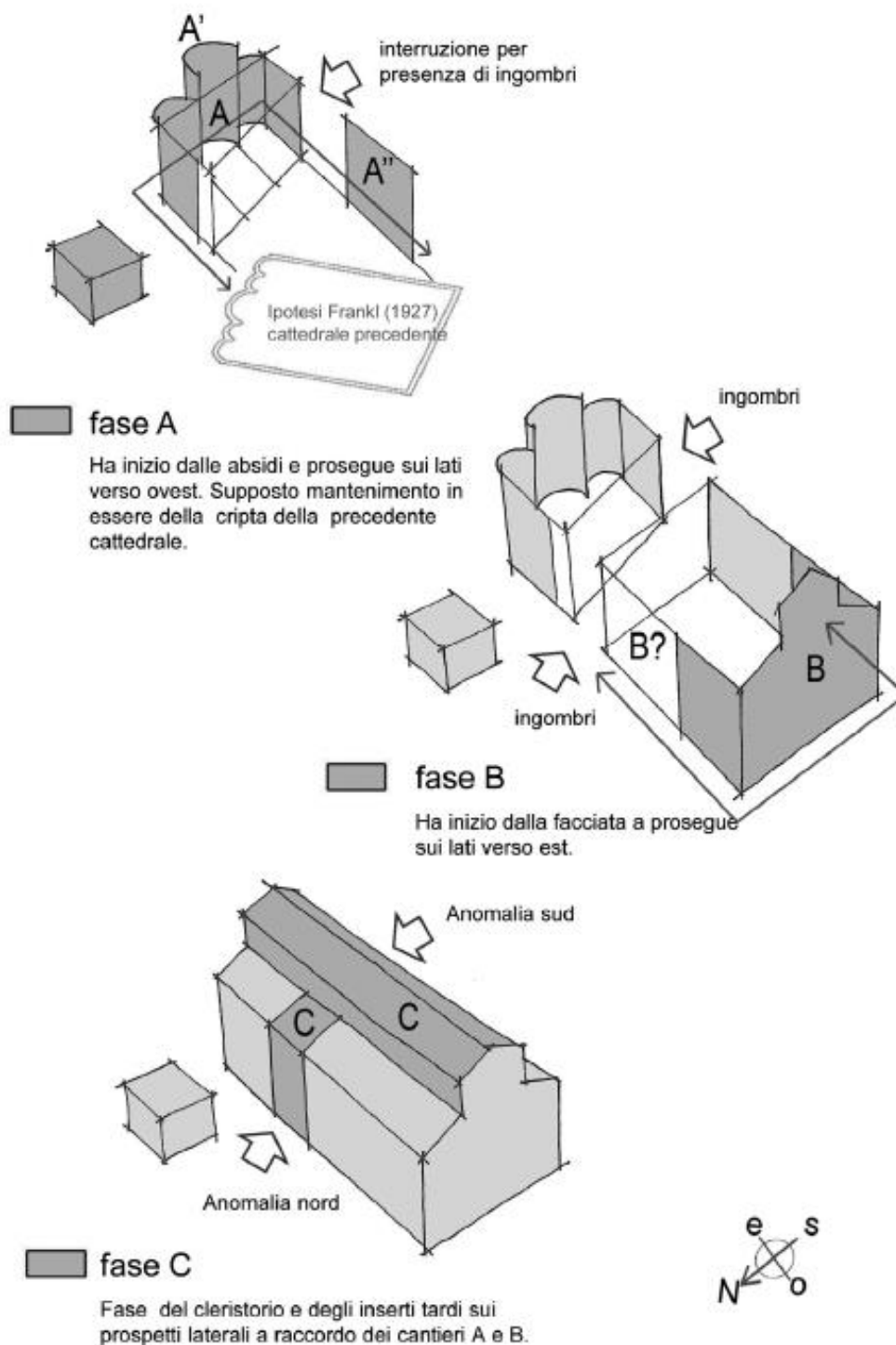


Figure 5.8 - State of the art on the construction phases [34]: diagram of the division into phases proposed by [43] in continuity with the idea of Porter (1927).

The constituent anomalies present at the architectural level on the facades led to the identification of the various construction phases previously reported. Among these anomalies, we have:

- The phase C connections on the side fronts, which the researchers have justified with the presence of obstructions, remains of the previous cathedral, which would have hindered the continuation of the construction site, removed at a later time [45];
- The constituent anomaly of the north side front with wall thickening (*Figure 5.10*), where the composition of the tripartite loggias is broken, just west of the Porta of the Pescheria, by an anomalous thickening of the wall, preceded to the east by a minor bipartite arch. Lomartire [45] states that this thickening had a structural role with the function of temporary support of the facade wall, waiting for the demolition of the obstacles;

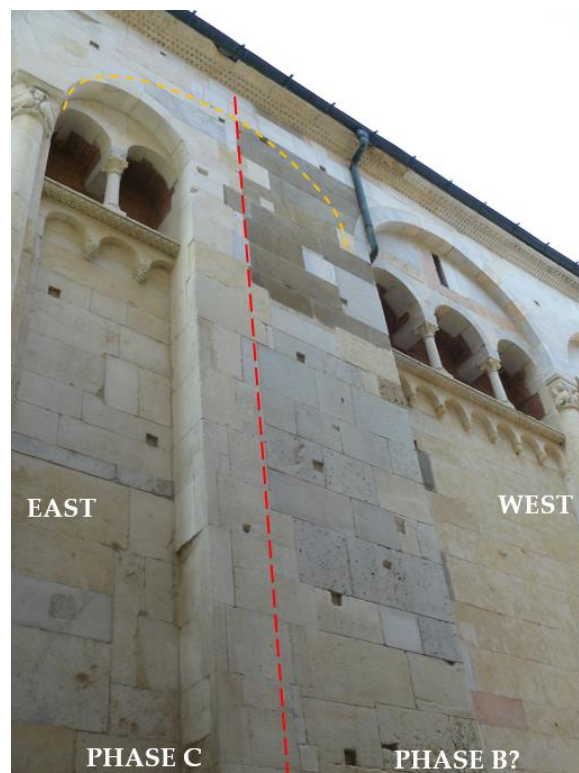


Figure 5.10 - Wall thickening on the north side (Photography Manuel Rovesti survey 29-08-2019).

- The constituent anomaly of the south side front (*Figure 5.11*), where the architectural composition of the arches and the tripartite loggias is broken with a minor arch within which a large double-arched window with pointed arches were inserted. In addition, in this case, Lomartire supported the hypothesis of the presence of obstructions;



Figure 5.11 - Anomaly minor arch on the south side (Photography Manuel Rovesti survey 29-08-2019).

- The constituent anomalies of the façade (*Figure 5.12*), where there are evident contractions and dilation in width of the arches that contain the tripartite loggias. Due to the presence of central buttresses in a forced position, the incongruity of the two modules of the aisles and the absence of corner buttresses. According to Peroni, the presence of so many irregularities weakens the overall architectural composition of the facade, in favour of the sculptural reasons. The compositional inconsistencies attributable to the original facade are motivated by the hypothesis of a Wiligelmo construction site, which grants greater freedom of expression [38].



Figure 5.12 – Anomalies in the facade (Photography Manuel Rovesti survey 29-08-2019).

5.4.2 New hypotheses on anomalies

The technical office Silvestri in [34] has carried out a re-reading of these constructive phases observing them from a different point of view, the structural settlements. The credit of this re-reading also goes to Gian Carlo Palazzi who was the first to investigate the inclinations of the apse and to have carried out very significant surveys with the tools available [46]. From these studies and further observations, inclinations towards the north and west of the apsidal body were found, which are due to the presence to the north of the Ghirlandina tower and to the east of a softer ground, an area where the previous cathedral was not present [47].



Figure 5.13 - Visible settlements in east and north directions (Photography Manuel Rovesti survey 29-08-2019).



The study of damage [48] has pointed out what has been over the centuries and what is now the crack pattern of the cathedral structure. In particular, this study has shown that the privileged break points of the Cathedral have always manifested themselves, over the centuries, near the intermediate band between the presbytery body and the naves body. A different structural behaviour was therefore noted between the part of the presbytery block and that of the naves. The fractures are concentrated at the connection point of the two blocks. This behaviour is related to the ground below and to the presence of the Ghirlandina tower. This vulnerable zone coincides with an autonomous and separated construction phase, phase C. Therefore, this band has a structural function of union between two disconnected blocks. However, being a rigid area and not being able to move, it continued to break, absorbing and releasing the tensions induced by the two blocks that behave in a different manner and manifesting the cracks exactly at the connection point of the different construction sites.

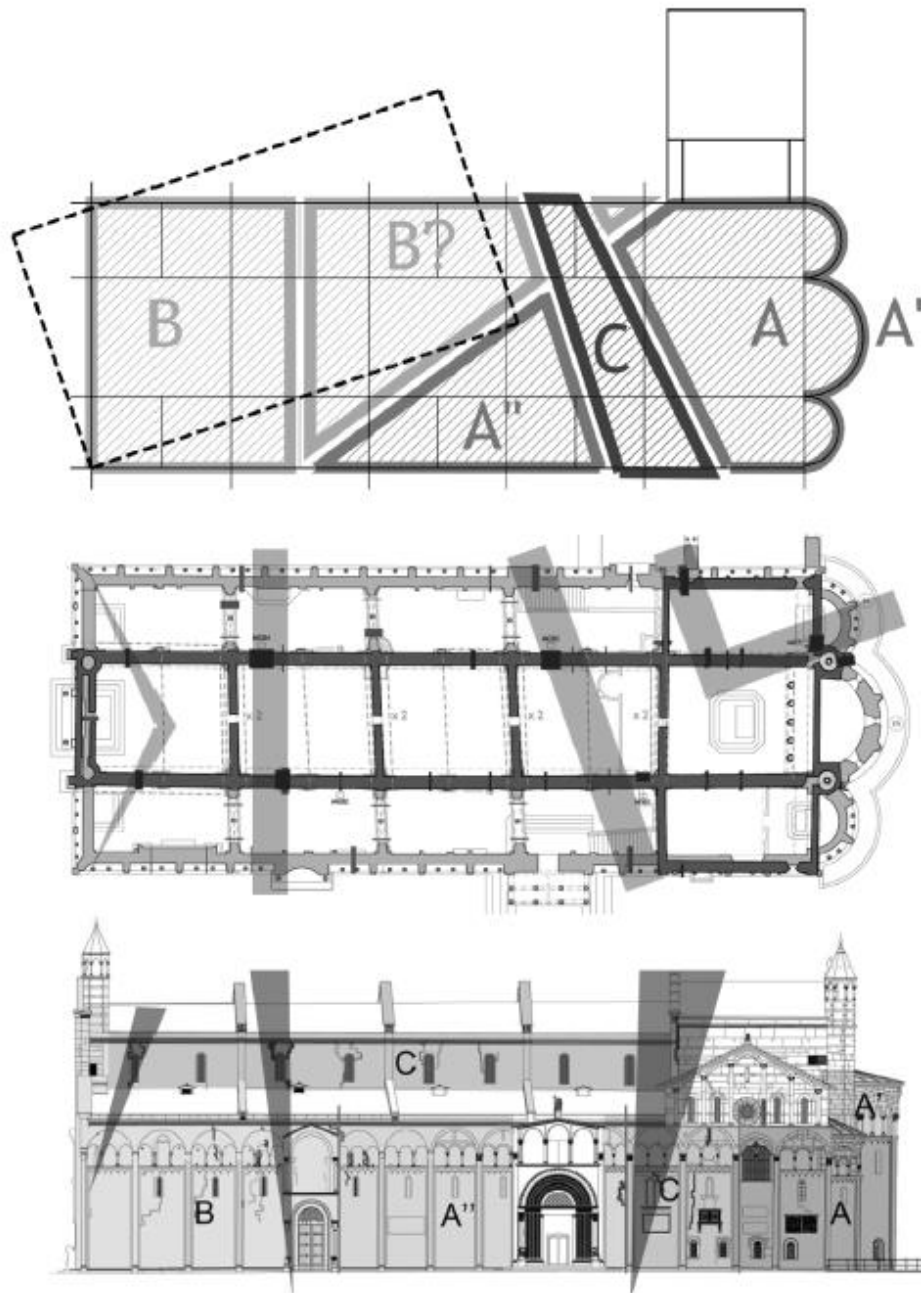


Figure 5.14 - Correspondence between construction phases and crack pattern
(Silvestri Technical Study surveys on drawings by G. Palazzi)
a) Exemplification of the construction phases published by Peroni, 1989;
b) Summary table of the crack pattern with bands identifying major cracks;
c) South front: overlapping of construction phases with fractures detected and with bands more damaged [34].

From this first introduction, the technical office Silvestri claims that the settlements determined the phases. Stating that the most probable hypothesis is that the construction of the Cathedral started from the apse body showed settlements and inclinations, therefore it was decided to suspend the construction to give time to complete settlements and to prevent one block from dragging the other. Meanwhile, the building site moved to the area of less settlement, the one in which the previous cathedral was present. In this way a gap was left between the two construction sites. Successively the connection was made, phase C, an area in which there are several architectural anomalies. These anomalies are due to the presence of two walls, differently rotated in space, had to be connected. Therefore, the workers had to modify the architectural project to solve these technical-constructive problems.



Figure 5.15 - View of the Modena Cathedral from Piazza Grande (Photography Manuel Rovesti survey 29-08-2019)

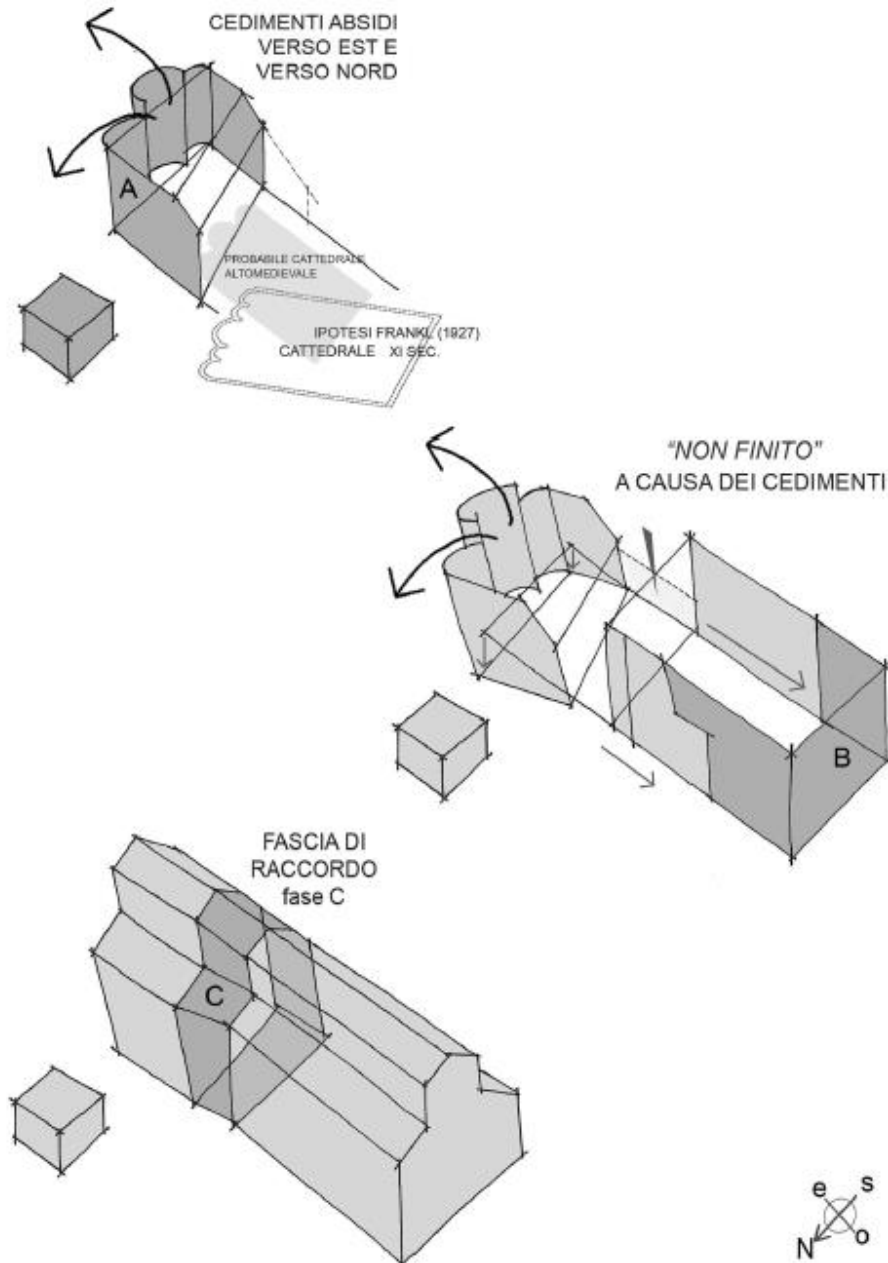


Figure 5.16 - Re-reading of phase C: interruptions left in phase A due to settlements and connected later [34].

The north front in correspondence with the phase C, have origin some point settlements that generate sudden inclinations and high stresses, therefore a reinforcing masonry wall was created. The thickening of the wall is a support for the first phase of construction, then connecting two blocks, which move differently and independently.

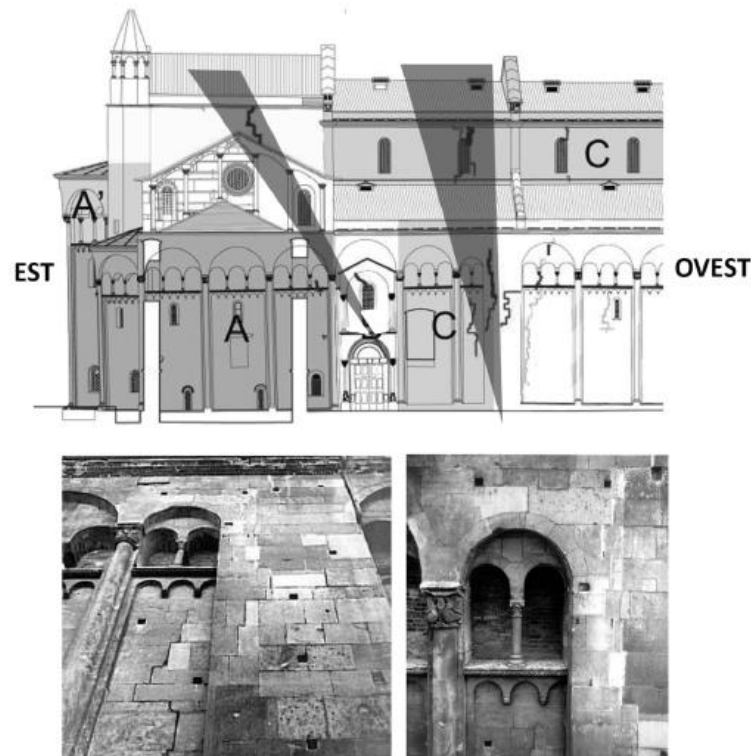


Figure 5.17 - Wall thickening damage - Note the cracks reopened and some stuccowork carried out following the subsidence of the 1970s, before the intervention restoration project in the 1980s [34]. Survey of the cracks (Silvestri Technical Study) on drawings by G.Palazzi - Photographs by C.Leonardi extracted from [49].

On the south side, on the other hand, the effect of the Ghirlandina Tower is smaller and consequently the settlements and the inclinations are more gradual and controlled, consequently a masonry wall with a structural function on this side is not necessary.

As for the facade, according to Elena Silvestri [34], it was not the beginning of a new construction site directed by Wiligelmo, but the

conclusion of the construction site coming from the apses, started by Lanfranco. Therefore, she claims the presence of a single construction site that starts from the apses crosses the interruptions and ends in the facade, where the inconsistencies are resolved. This hypothesis is justified by the presence, in correspondence of the cornice that marks the shutter level of the loggias, with a gap of 28 cm.



Figure 5.18 – Front loggias (Photography Manuel Rovesti survey 29-08-2019).

This means that the facade was not only built last, but also after the settlements. From some measurements obtained by Palazzi, it was discovered that in the external fronts, corresponding to the aisles, the plane of the cornice is from the basement of a different size in the north to the south even if the height of the two fronts is the same. On the north side, just west of the wall thickening, the loggias are closer to the base than about 25 cm from the south side and this gap is maintained advancing towards the west, up to the facade. However, in the arches to the east of the wall thickening, the compositional scheme is attributable to that of the south side. The gap is not compensated and is dragged up to the facade, where the presence of the porch hides the error.

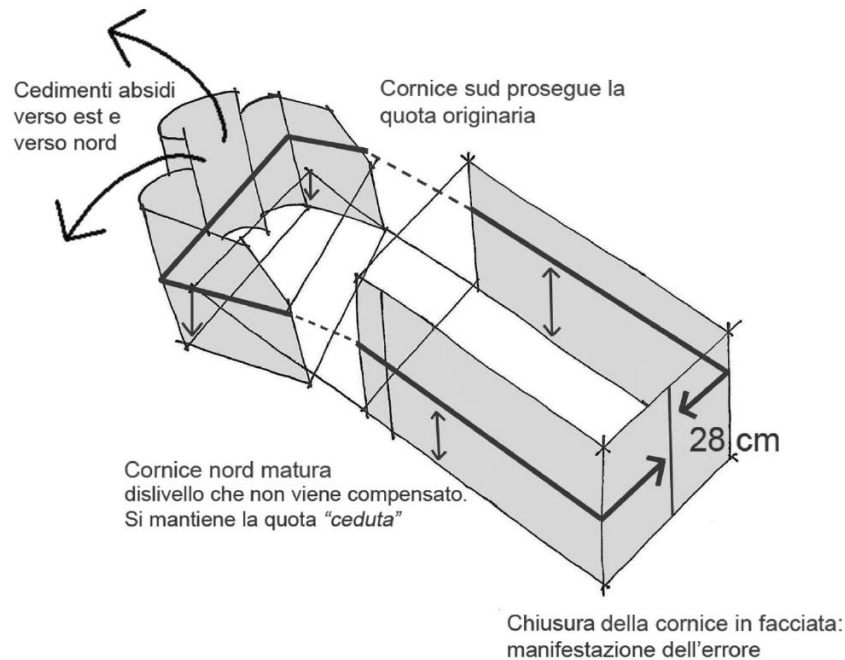


Figure 5.19 - Example diagram of the origin of the 28 cm gap [34].

In conclusion, the work [34] states that the interruption of the building site at the presbytery can be explained from a different point of view than the one studied up to that time. The settlements forced the workers to leave the structure from the inclined and compromised apsidal body, to start a little further on from a new verticality. Phase C waits a few years for the depletion of settlements and intervenes only later to solidify two disconnected and disjointed bodies, assuming the form and function of a connecting strip. Consequently, the constituent anomalies present in the lateral fronts, in relation with the phase C, find a new justification in the complex resolution of a connection between two bodies differently rotated in two different directions.

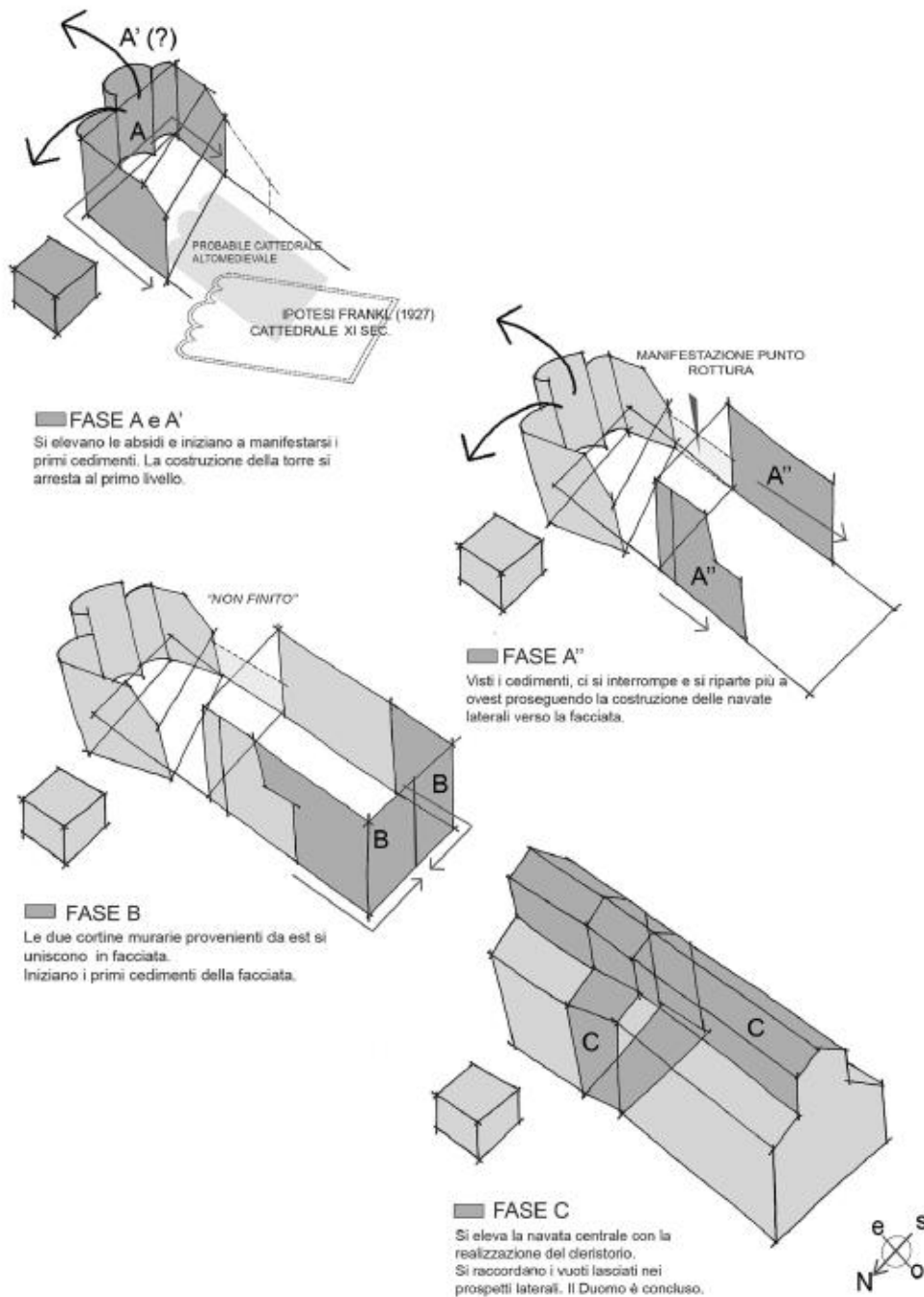


Figure 5.20 - Re-reading of the construction sequence of phases A, B, C (excluding Campionesi interventions). Scheme by E. Silvestri [34]. The sequence A, A', and A'' is represented as theorized by Peroni and Lomartire, however doubts are expressed about the anteriority of phase A' with respect to A''.

5.5 Information needed for modelling

Below, some essential information for the realization of a model is presented, having a structural behaviour as close as possible to reality.

5.5.1 Material identification

Being the monument of the Cultural Heritage of the *UNESCO*, the Modena Cathedral cannot be used for destructive tests or to take specimens for the characterization of materials [1]. For this reason, it is not possible to have a knowledge of the mechanical characteristics of the masonry necessary for the construction of the structural model. Below is a study carried out by Arch. Camilla Colla from the University of Bologna, using a non-destructive technique.

- **Non destructive sonic tests**

Arch. Camilla Colla [50] has carried out a study on a very limited area of the cathedral as can be seen in the figure. This obviously makes the characterization of the masonry in other areas of the building very difficult, above all because some areas will be more damaged than others and therefore the elastic modules of the different areas may vary. The non-destructive experimentation was realized with sonic tests, in this way it was possible to calculate the speed of propagation of the waves in the material. Starting from the speed of the waves V_p , it is possible to obtain the dynamic elastic modulus of the material with the following formulation, by decreasing this modulus by 30%, the static elastic modulus can be obtained:

$$E_d = \rho V_p^2 \sqrt{\frac{(1+\nu) \cdot (1-2\nu)}{(1-\nu)}} \quad (5.1)$$

where:

E_d : dynamic elastic modulus;

ρ : density of the material;

ν : Poisson's coefficient.

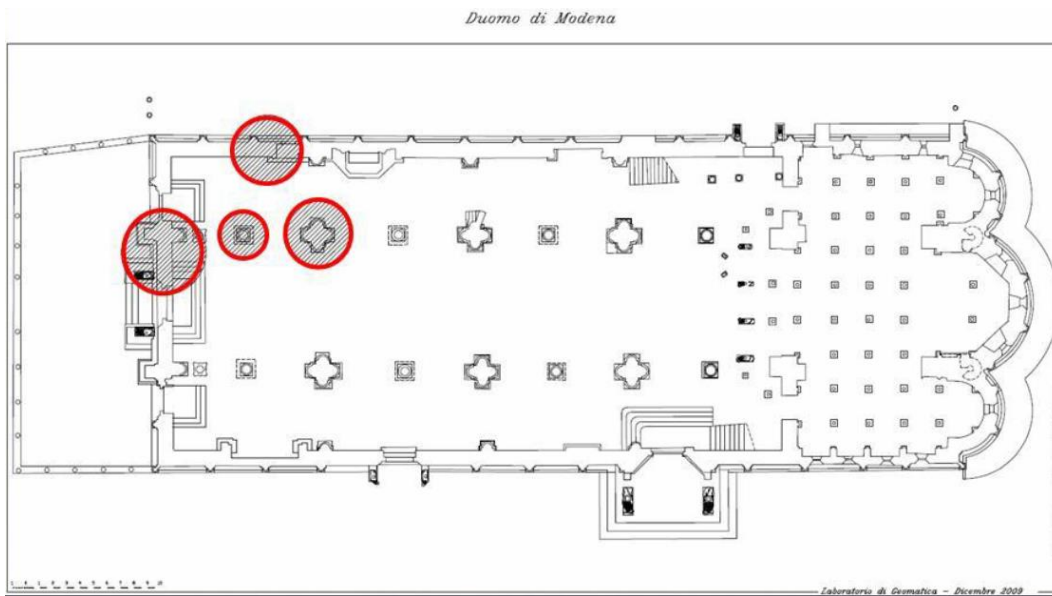


Figure 5.21 – Plan of the Modena Cathedral with the test areas [50].

The data obtained from the experimentation are shown below:

Table 5-1 - Static elastic modulus and waves speed for each area $\nu=0.2$ $\rho=1.8\text{kN/m}^3$ [50].

Area	V_m (m/s) and variation coefficient	E (N/mm ²)
North facade	1862 (0.09)	4144
Main facade	1350 (0.25)	2179
Masonry column	1202 (0.32)	1727
Stone column	4709 (0.12)	26506

5.5.2 Foundation

Information regarding the foundations of the Cathedral was found in the document created by the Department of Civil, Environmental and Materials Engineering, University of Bologna [51]. The foundations of the Cathedral develop with perimeter continuity with a thickness of 1.20m, probably in their thickness the projection of the walls above them is contained, while there are no transverse joints, at the level of the foundations, between the perimeter walls and the colonnades, and respectively between the latter two. The excavations of 1913 suggest that the foundations of the two colonnades after the perimeter were laid in the Cathedral of Modena. A further excavation of 1919 revealed a transversal foundation corresponding to the delimitation of the primitive choir and the crypt, clearly front than that of the partition of the naves.

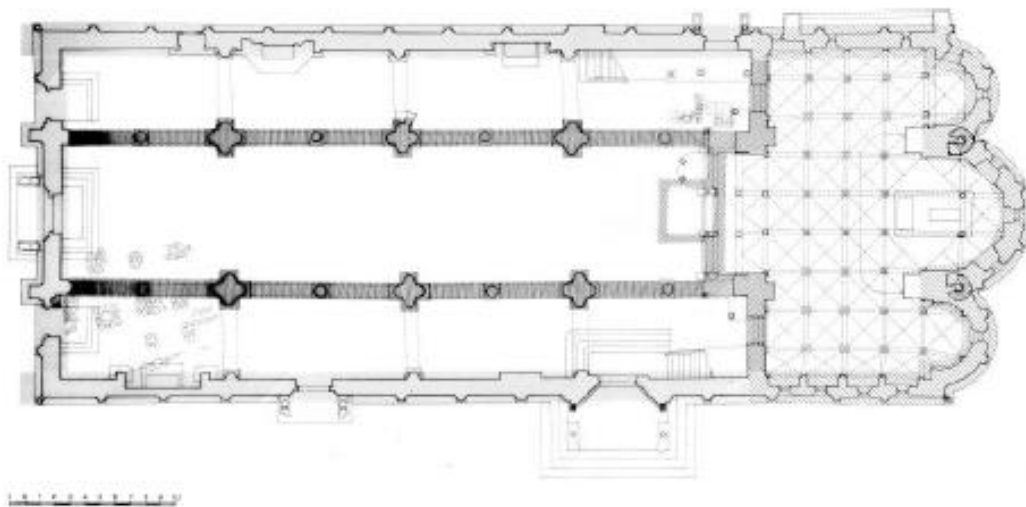


Figure 5.22 - Experimental reconstructive scheme of the foundation [51].

5.5.3 Current structural reinforcement: tie-rods

Due to the damage that has occurred over the years due to the earthquakes that hit the structure, a tie-rods system has been installed that allows to have a behaviour as close as possible to the box one. This avoids the activation of the collapse mechanisms of the macro-elements such as the overturning of the facade or perimeter walls (*Chapter 1.1*). The information relating to the chains was found in the document [52] and also on the basis of an inspection that I made on 29-08-2019, refer to *Appendix B* for the main characteristics. The drawings of the position of the tie-rods used in the model are shown below:

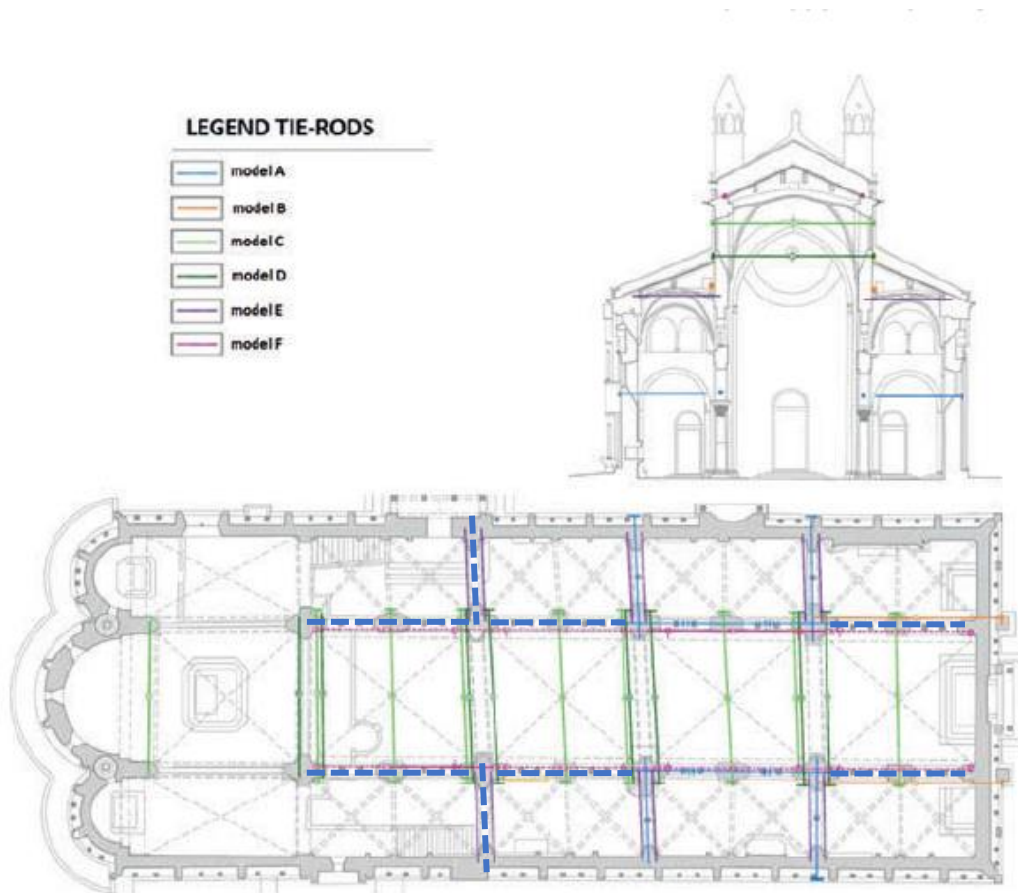


Figure 5.23 – Tie-rods position (in blue dotted the chains added thanks to the inspection of the 29/08/2019) [52].

5.5.4 Monitoring system

The monitoring system is necessary for the calibration of the FEM model, especially when there are uncertainties on the mechanical masonry parameters. Therefore, by means of the model updating it is possible to converge close to the exact solution.

- **System management**

The Polytechnic of Turin and Nagoya City University have stipulated a contract with the Metropolitan Church of Modena for the implementation and management of the monitoring system of the Modena cathedral. The monitoring activity involves Mons. Giacomo Morandi, as legal representative of the Metropolitan Church, Profs. Renato Lancellotta and Donato Sabia scientific managers of the project for the Department of Structural and Geotechnical Engineering (DISEG) of the Politecnico di Torino and Prof. Takayoshi Aoki scientific responsible of the project for the Graduate School of Design and Architecture, Nagoya City University.

In June 2015, the Nagoya City University and the DISEG installed the instrumentation (accelerometers) for detecting the dynamic response of the Modena Cathedral. The data is acquired continuously and is processed by the DISEG.

- **Instrumentation and positioning**

Monitoring involves the continuous measurement, with a sampling frequency of 100 Hz, of accelerations in 12 points identified on the structure. The instrumentation installed in the Modena Cathedral consists of:

- 16 capacitive uniaxial accelerometers (*Figure 5.24* and *Table 5-2* show the technical characteristics of the measuring instruments);
- 4 thermocouples;
- 1 power supply box for accelerometers;

- 1 UPS “Phoenix Contact” power supply with batteries for power continuity;
- 1 National Instruments “CompactRiD” acquisition system, with sampling frequency at 100 Hz;
- 24-Bit Analog Input module (4Ch, 10J);
- 1 Ethernet switch, an IP WatchDog Lite;
- 1 2TB Hard Disk.

Table 5-2 - Technical characteristics of the measuring instruments

<i>Sensitivity</i>	mV/(m/s ²)	203.9 ± 5%
<i>Frequency response</i>	Hz	0 ~ 100 ± 1 dB
<i>Frequency response</i>	Hz	0 ~ 400 ± 3 dB
<i>Resonance frequency</i>	kHz	± 0.4
<i>Acceleration range</i>	± m/s ² pk	29.42
<i>Electrical noise</i>	m/s ² sms	± 0.000049
<i>Shock limit</i>	± m/s ² pk	980
<i>Temperature range</i>	°C	- 25 ~ 70
<i>Amplitude non linearity</i>	%	± 0.1
<i>Transverse sensitivity</i>	%	± 1
<i>Power requirements</i>	VDC	11 ~ 16
	mA	20
<i>Weight</i>	g	50



Figure 5.24 - Capacitive uniaxial accelerometer [35].

The accelerometers have been positioned, individually (uniaxial accelerometers) or suitably coupled to measure acceleration components in the plane (biaxial accelerometers) or in space (triaxial accelerometers).

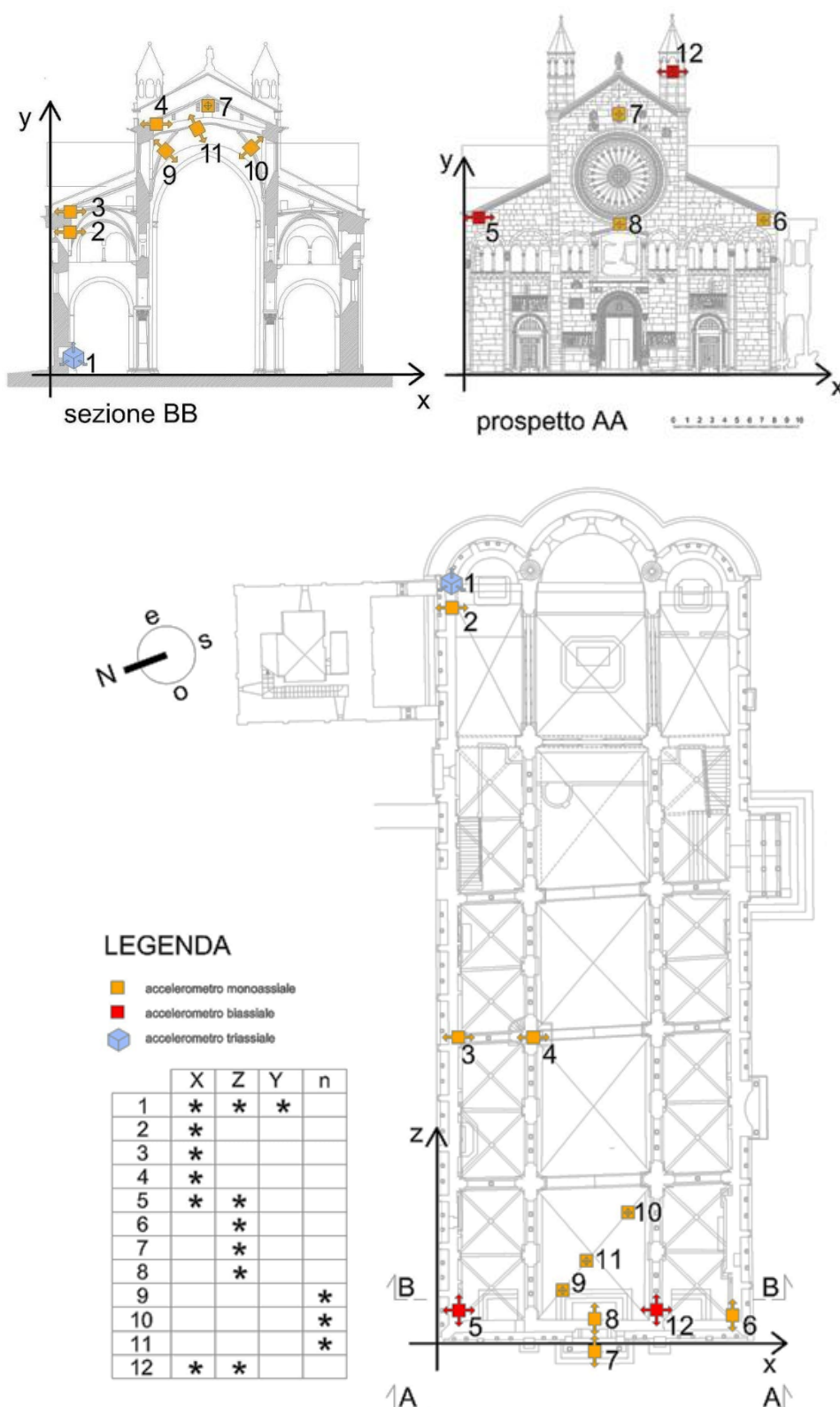


Figure 5.25 - Plan, fronts and section of the Cathedral with indication of the position of the monitoring points [35].



Figure 5.26 - Measurement point 1 - Recording channels and accelerometers 1, 2 and 3 [35].



Figure 5.27 - Measurement point 2 - Recording channels and accelerometers 4 [35].



Figure 5.28 - Measurement point 3 - Recording channels and accelerometers 5 [35].



Figure 5.29 - Measurement point 4 - Recording channels and accelerometers 6 [35].



Figure 5.30- Measurement point 5 - Recording channels and accelerometers 7 and 8 [35].



Figure 5.31 - Measurement point 6 - Recording channels and accelerometers 9 [27].



Figure 5.32 - Measurement point 7 - Recording channels and accelerometers 10 [27].



Figure 5.33 - Measurement point 8 - Recording channels and accelerometers 11 [27].



Figure 5.34 - Measurement point 9 - Recording channels and accelerometers 12 [27].



Figure 5.35 Measurement point 10 - Recording channels and accelerometers 13 [27].



Figure 5.36 Measurement point 11 - Recording channels and accelerometers 14 [27].



Figure 5.37 Measurement point 12 - Recording channels and accelerometers 15 and 16 [27].



Chapter 6

Construction of the Structural Model

6.1 Introduction

The first step needed to describe the behaviour of a structure is realize the geometric model of the principal structural elements. The construction of the model of a cathedral is complicated because of the geometric irregularity, vertical inclination of the wall, the presence of the domes and presence of complicated details that make it difficult to recognize the structural parts. Furthermore, sometimes in structure with complex geometry as the case of study, it is needed to realize some simplifications to decrease the computational burden. This chapter explain how the model was built and the problems met in building it.

6.2 From the point cloud data to the geometry

The construction of a FEM model of a cathedral has always been a problem, mostly for the presence of irregular elements, inclinations and curved elements. As reported in the *Chapter 5.4*, the geometry of the Cathedral of Modena has many anomalies and due to the problem of the settlements, the apse has a not negligible vertical inclination. In addition, as can be seen in the *Appendix A*, the plan of the church is not regular but has some inclined walls. It is important to consider all these inclinations to have a correct structural behaviour, especially in modelling the walls where the domes will be connected. Precisely because the domes are the areas most affected by damage in the earthquake events and are those that determine some of the main mechanisms of collapse of macro-elements. On the other

hands, the only way to consider all these irregularities and to speed up the construction of the structural model is the use of data from a point cloud acquired with Laser Scanner. In this way, it was possible to follow the inclinations of the wall which would not have been possible with only plans and sections.

6.2.1 The point cloud model

The main problem if you don't have a point cloud is that you are not able to accurately model the vertical inclinations, instead in our case the construction of the model has been coupled with a point cloud, plans and sections. The point cloud used for modelling the geometry of the Modena Cathedral was acquired by Castagnetti with a terrestrial laser scanner survey, as reported in [53]. The acquisition was carried out with a time-of-flight instrument, model *ScanStation 2* by *Leica Geosystems*. The survey was realized both indoor and outdoor of the structure with a resolution equally to 8mm with respect to the operating distance between the surface and the instrument. In addition, a survey was also carried out with robotic total station, model *TCR1201+* by *Leica Geosystems*, necessary for the realization of an accurate alignment between the internal and external point cloud.

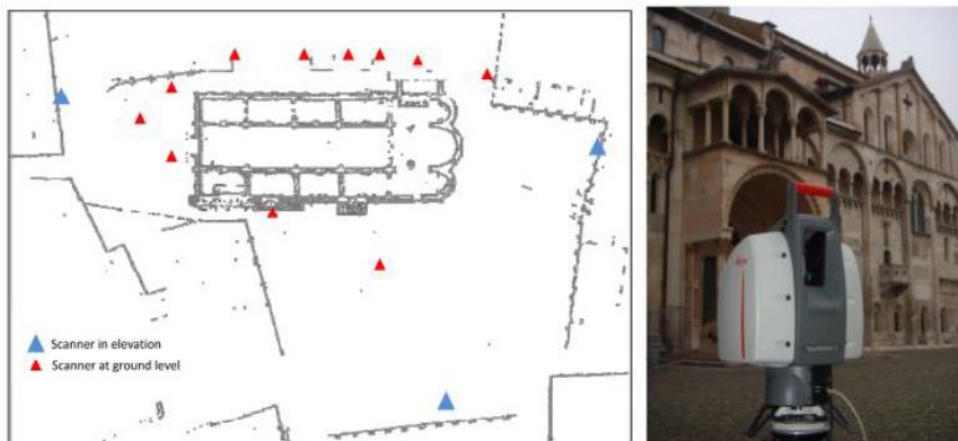


Figure 6.1 – a) Location map of the scanning positions b) Terrestrial laser scanner model *Scan Station 2* by *Leica Geosystems*, during survey operations [53].

As regards data processing, Castagnetti obtained an overall accuracy of the final alignment, which was also refined by means of the ICP (Iterative Closest Point) algorithm, of 10 cm. The final point cloud of the structure was obtained with two more refinement steps: noise filtering and data cleaning, aiming at removing every point which is not related to the structure. The software, that has been used to process and to manage the laser scanning dataset, is *Cyclone by Leica Geosystems*.

In another document made by Castagnetti et al. [54] and DICAM of the University of Bologna [51] are reported the data regarding the inclination anomalies of the main structural elements, as shown below.

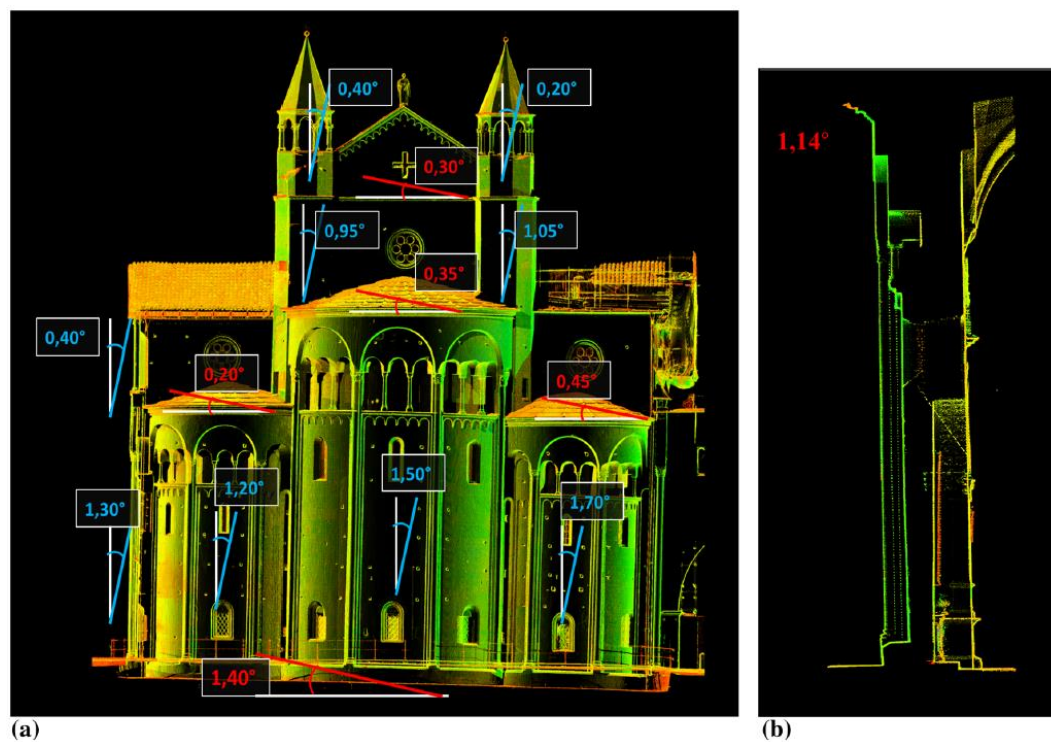


Figure 6.2 – a) Overhang analysis in south-north direction;
b) Anomaly with respect to verticality of a section [54].

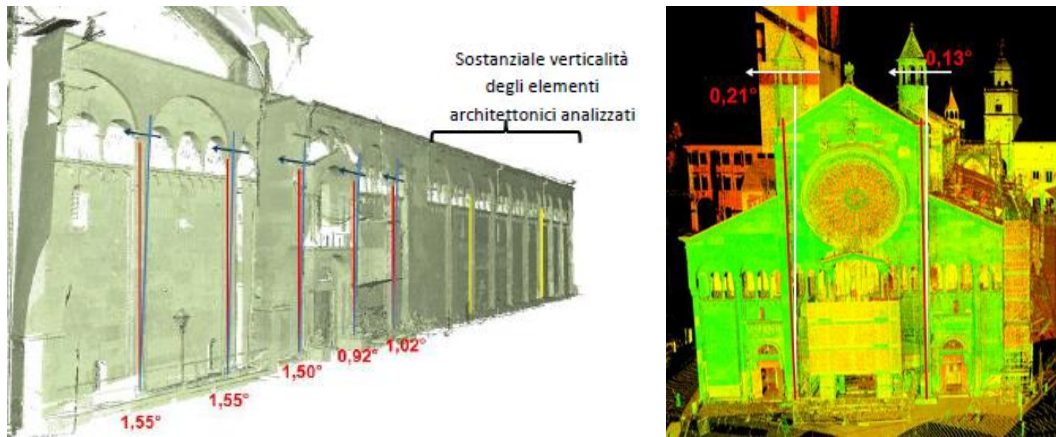


Figure 6.3 – a) Inclination analysis of the north side in the vertical plane;
b) Inclination analysis of the facade in the vertical plane [51].

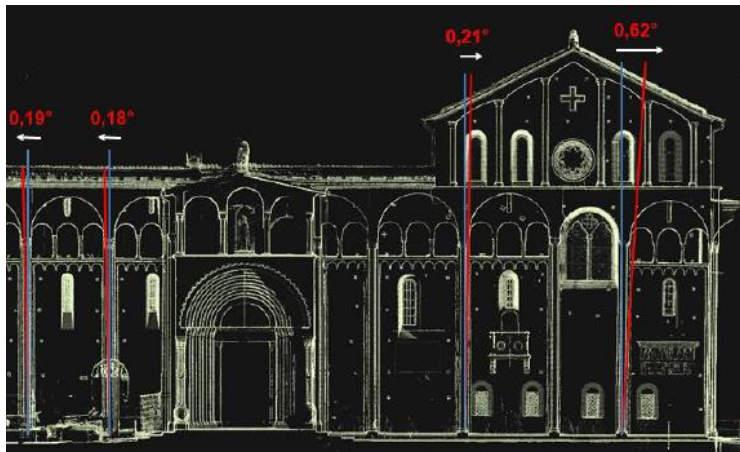


Figure 6.4 – Inclination analysis of the south side in the vertical plane [51].

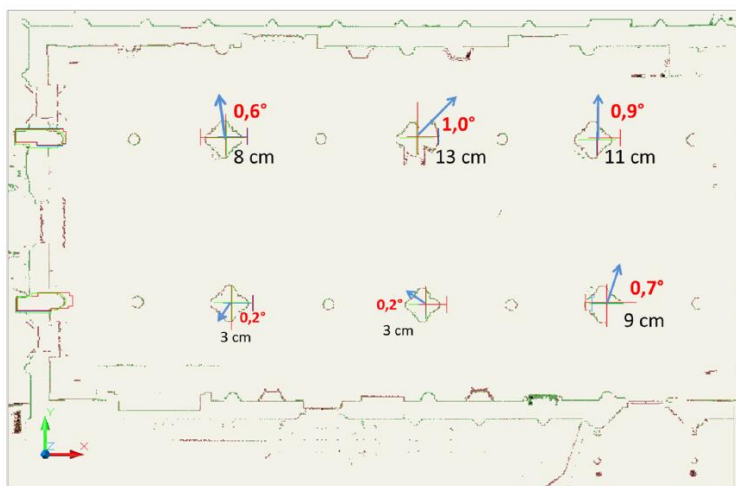


Figure 6.5 - Geometrical anomaly with respect to verticality of the pillars [54].

Below are reported different views of the point cloud model. This model consists of 261 836 235 points corresponding to a 22GB file which is difficult to manage in a modelling software. For this reason, it was possible with the *Infipoints ver.6.0* software to achieve an optimization of the file by decreasing the number of points in areas where detail was not necessary and delating the colour applied to every point. In this way, the file has been considerably lightened reaching 5 GB and becoming easy to manage.



Figure 6.6 – Point cloud model: overall view of the Cathedral [51].



Figure 6.7 – Point cloud model: internal view of the Cathedral [51].

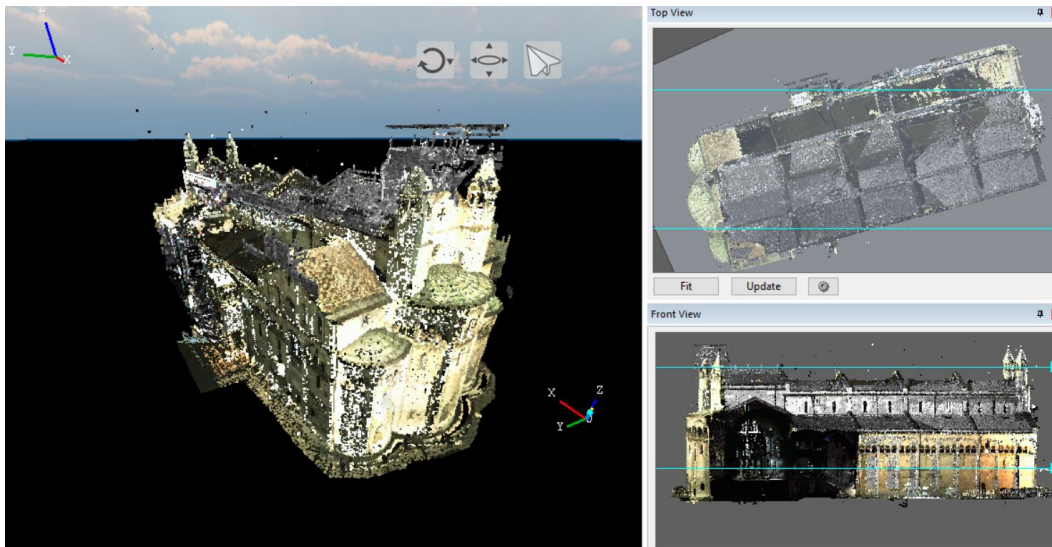


Figure 6.8 – Point cloud model in the Infipoints software: view of the apse.

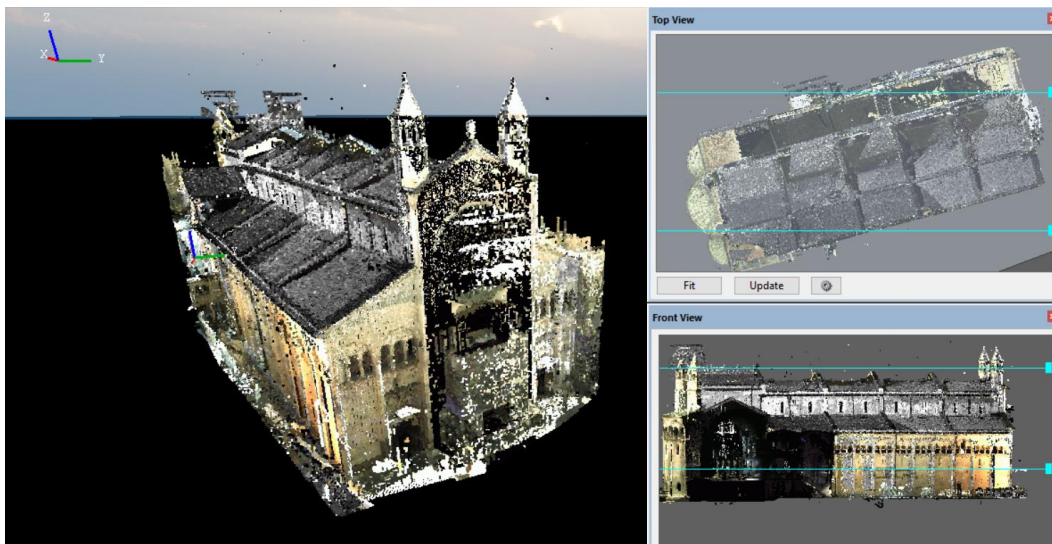


Figure 6.9 – Point cloud model in the Infipoints software: view of the façade.

After that, *CloudCompare* was used to manage this file, with this software was possible to divide some parts of the structure and decrease the number of the points. In this way, it was simpler to build the geometry by focusing only on some parts of the structure. In addition, a *Matlab* code was written, which allowed to section the point cloud in order to have plants and sections correctly positioned in space.

6.2.2 Construction of the geometry

The construction of the Cathedral geometry was created with the *Rhinoceros* 3D modelling software. It was decided to create the model with solid elements due to the complexity of the structure, the presence of different domes, which converge into a column and the high thickness of the walls. All these problems did not allow us to carry out a modelling with plates, which would lead to a too simplified modelling that does not describe well the real behaviour of the structure. To allow the structural software to read the elements as solids, the elements have been modelled on *Rhinoceros* as closed polysurfaces.

The modelling is achieved by importing both the plants and parts of the point cloud in order to follow the vertical inclinations and geometric irregularities. The same procedure was used both for the construction of the walls, arches and domes checking to have the best correspondence between the point cloud and the geometric model. Below are some views of the model created.

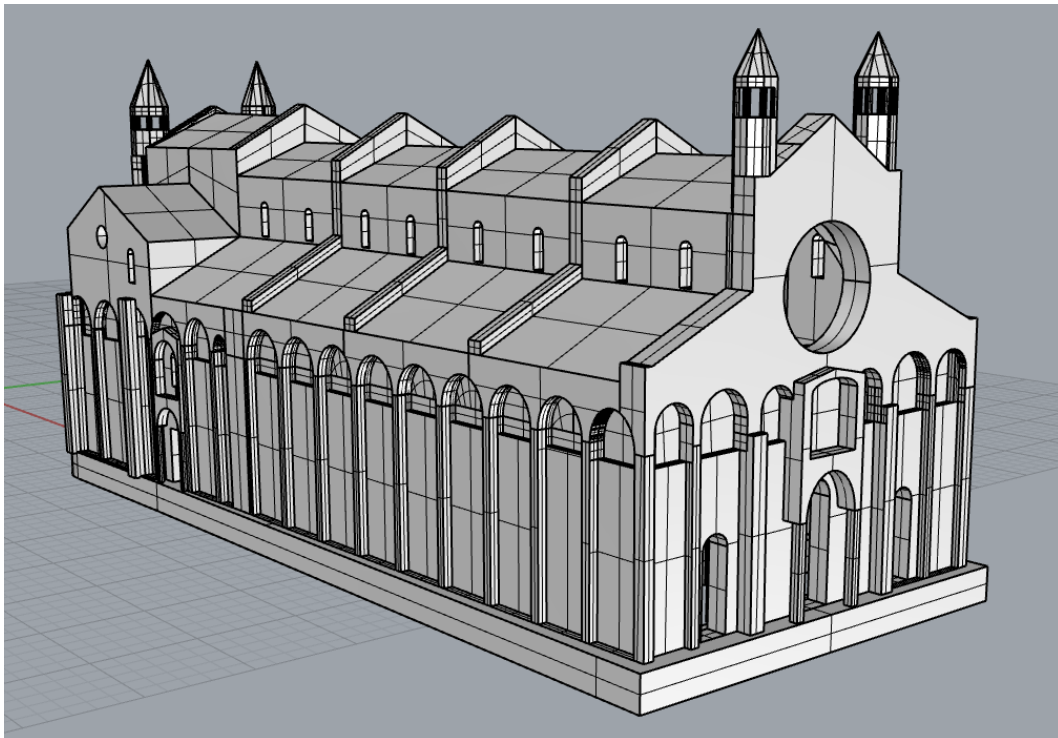


Figure 6.10 – 3D geometric model on *Rhinoceros* - Perspective view 1

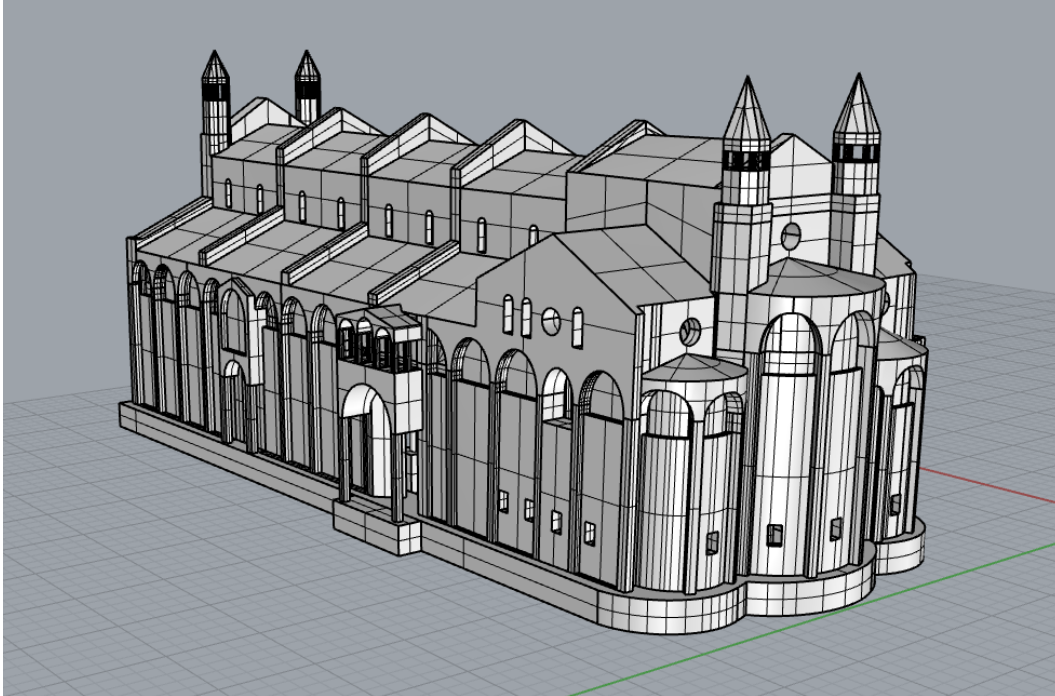


Figure 6.11 – 3D geometric model on Rhinoceros - Perspective view 2

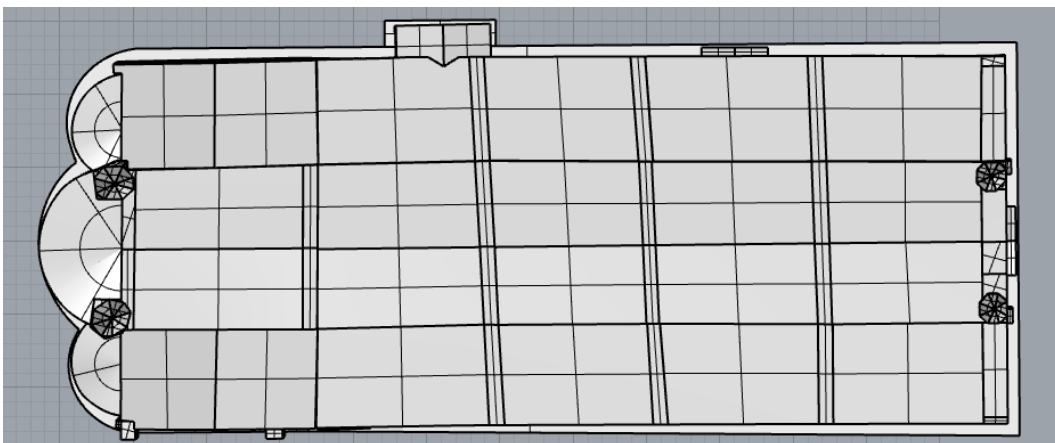


Figure 6.12 – 3D geometric model on Rhinoceros - Top view

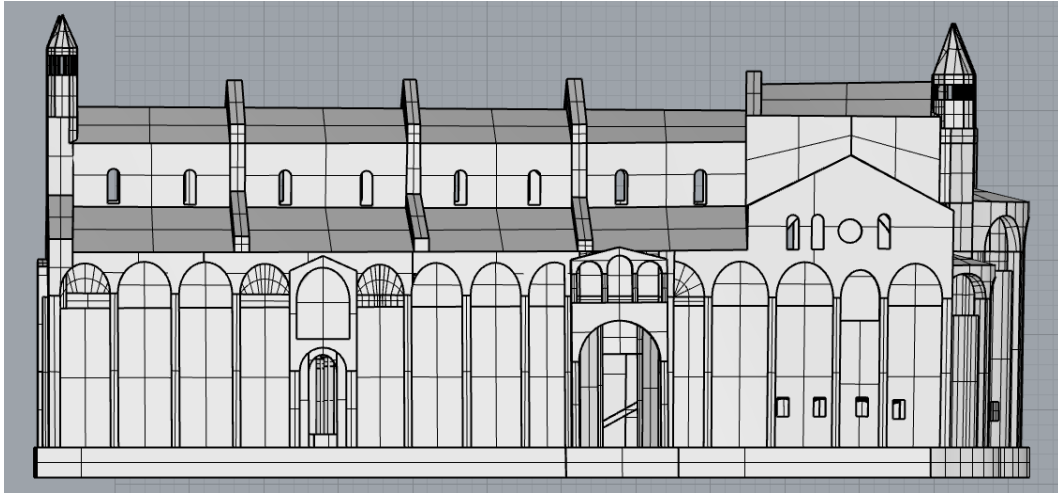


Figure 6.13 – 3D geometric model on Rhinoceros - South facade view

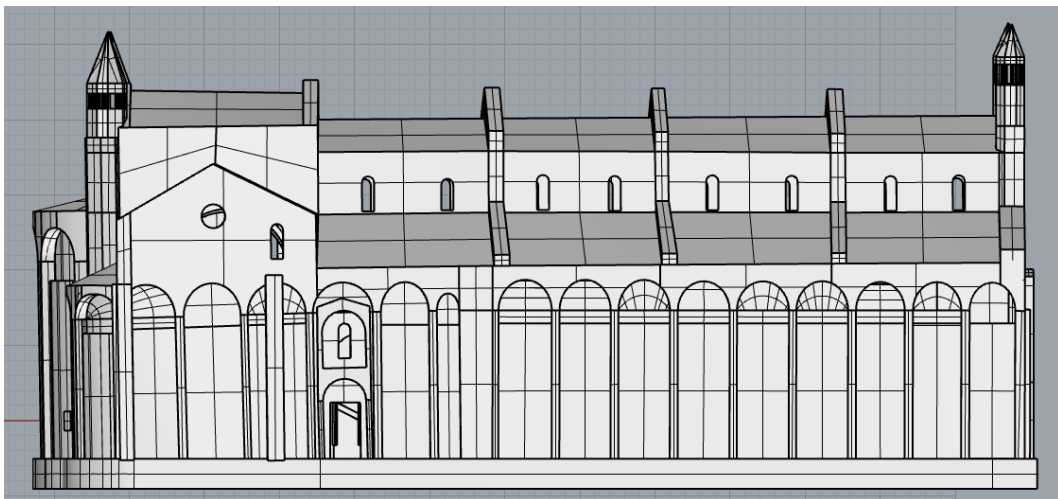


Figure 6.14 – 3D geometric model on Rhinoceros - North facade view

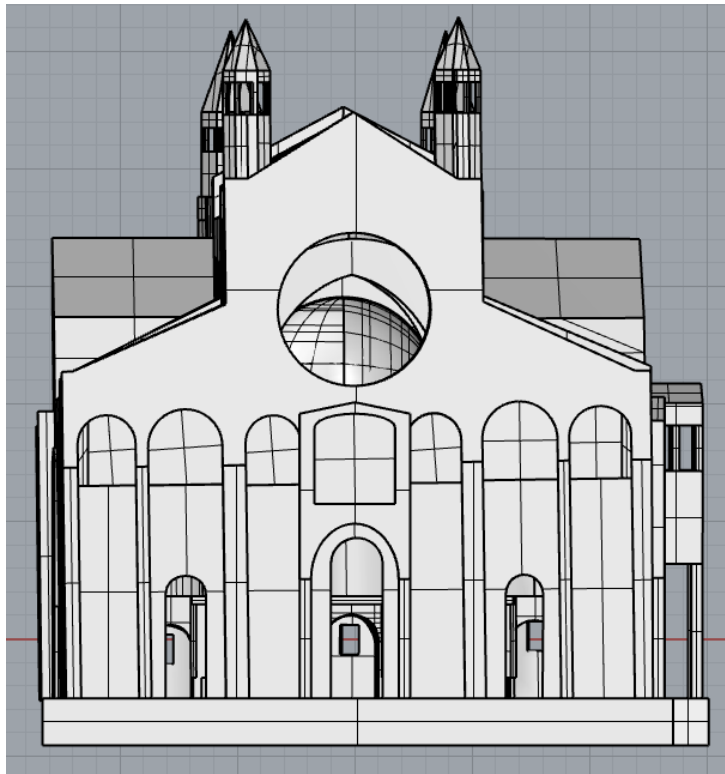


Figure 6.15 – 3D geometric model on Rhinoceros - West facade view

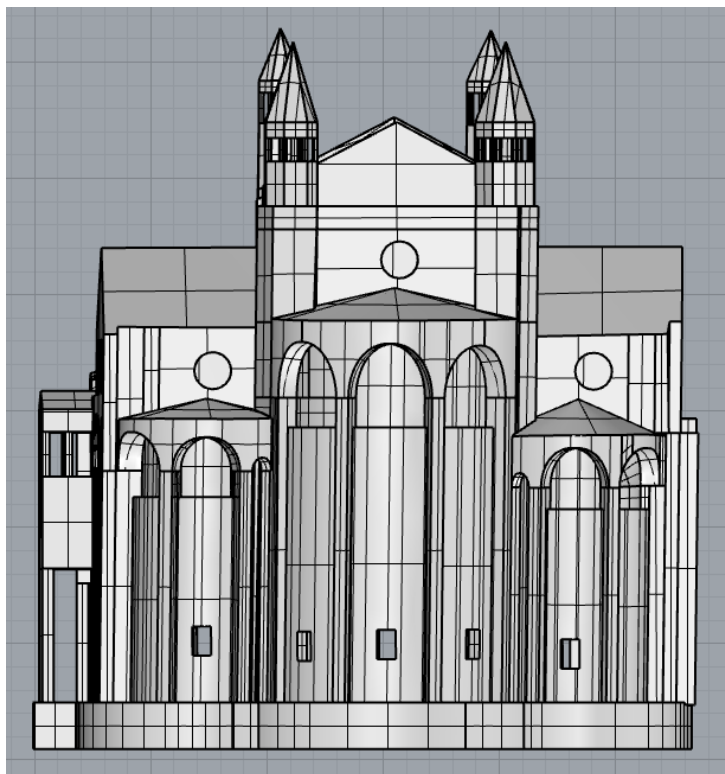


Figure 6.16 – 3D geometric model on Rhinoceros - East facade view

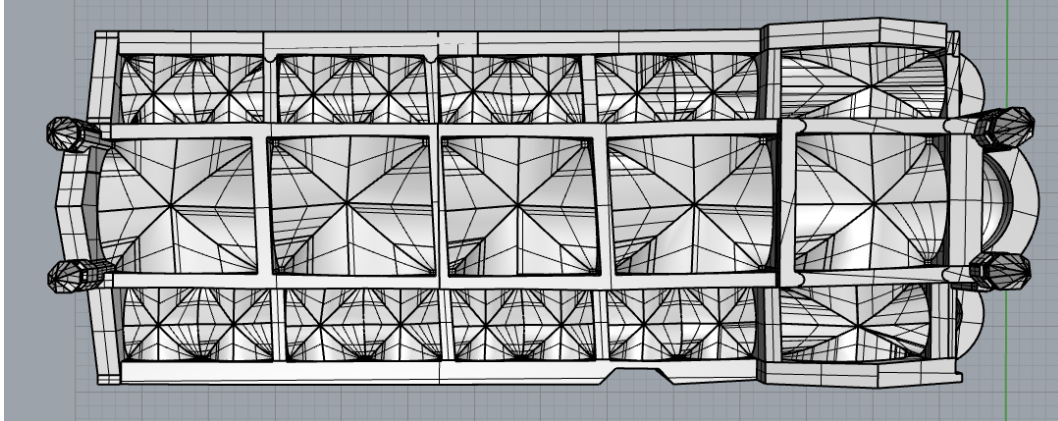


Figure 6.17 – 3D geometric model on Rhinoceros - Top view without roof

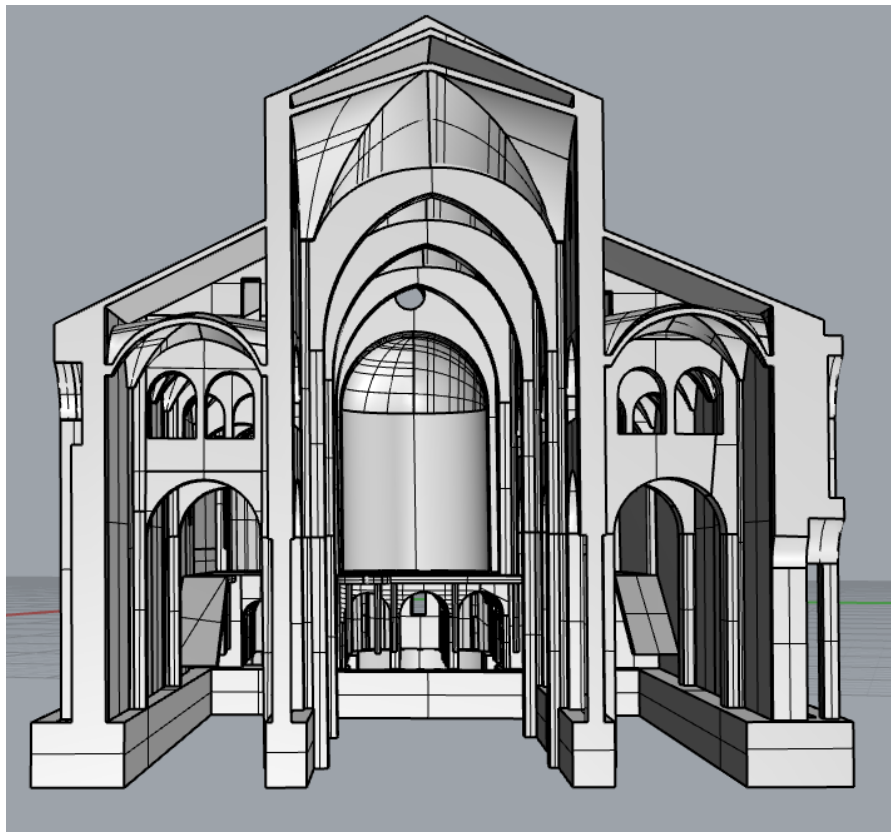


Figure 6.18 – 3D geometric model on Rhinoceros - Internal view of the sectioned model

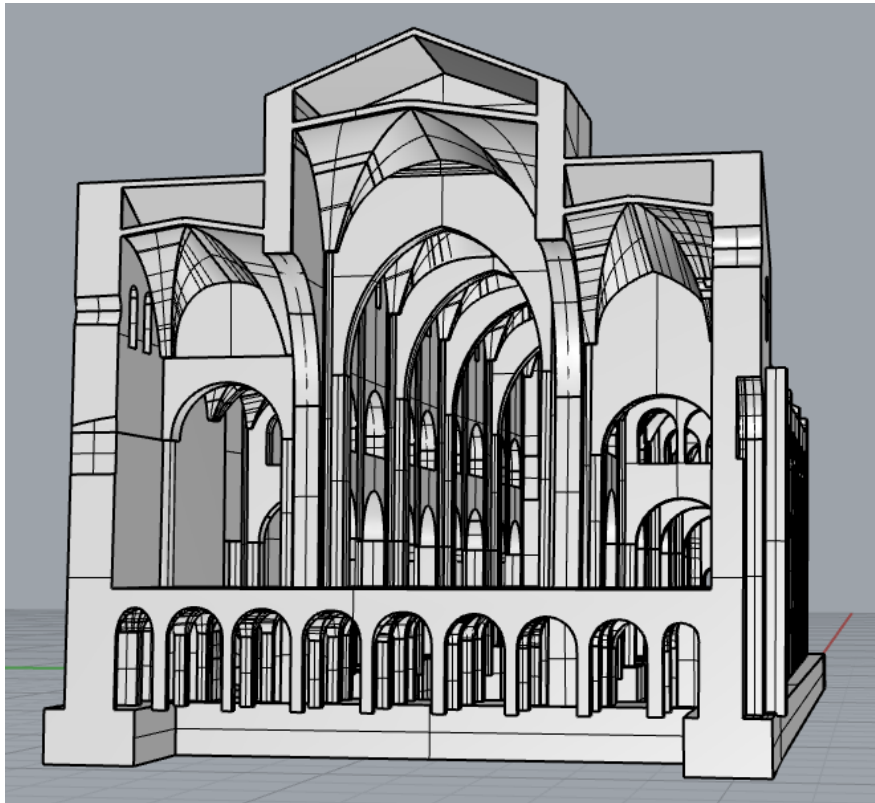


Figure 6.19 – 3D geometric model on Rhinoceros - Internal view of the sectioned model

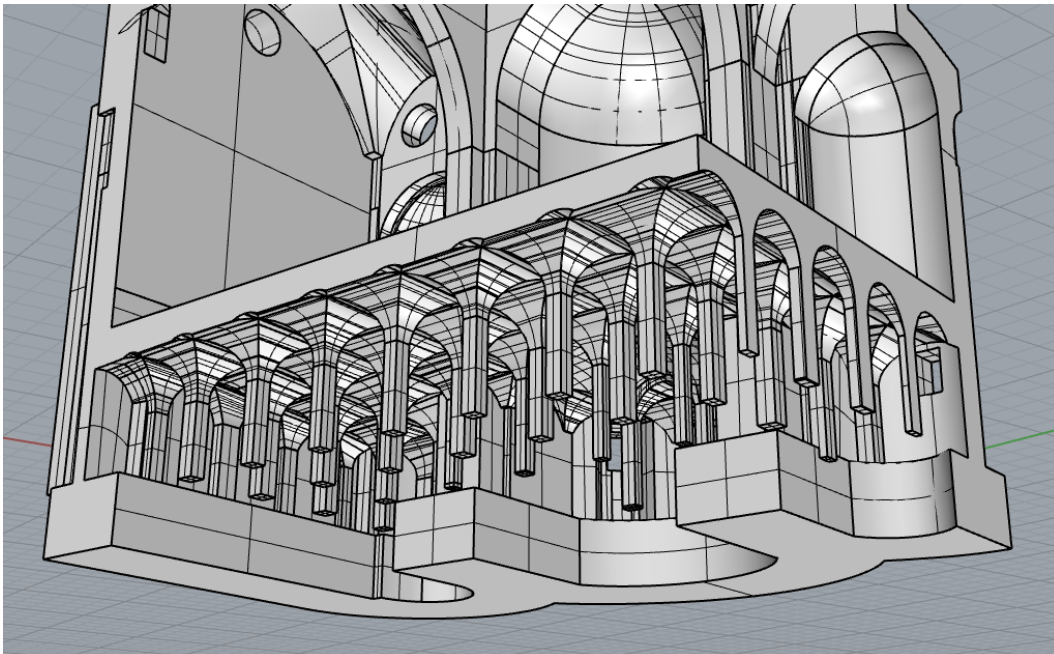


Figure 6.20 - 3D geometric model on Rhinoceros - Apse detail

6.3 Geometric simplifications adopted

When managing a structure with a high degree of detail such as the case in question, it is necessary to make some simplifications regarding geometry. This is needed mainly to reduce the number of elements and nodes of the structural model and therefore also to reduce the computational burden and analysis times. The high number of the elements is due to the presence of curved wall, domes, arches and elements detailed. Following are reported some of the main geometrical simplification adopted in the structural model.

- **Pillars supporting the arches on the facade**

In this case, to reduce the elements as much as possible and avoid a too dense mesh, it was decided to create a single pillar avoiding curvatures that represented the support of the arch of the facade.

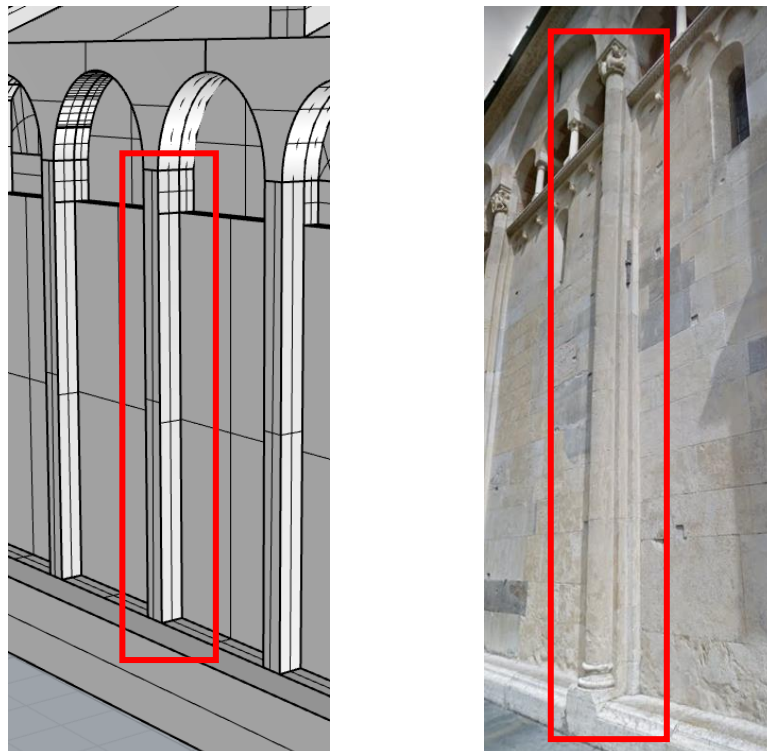


Figure 6.21 - Pillars supporting the arches on the facade: a) 3D geometric model on Rhinoceros; b) Real detail (Photography Manuel Rovesti survey 29-08-2019).

- **Arches on the facade**

In this case, considering that the modelling that is being carried out is for the purpose of the global analysis of the structure and therefore to describe an overall behaviour of it. It was decided to model this detail with a single arch.



Figure 6.22 - Arches on the facade: a) 3D geometric model on Rhinoceros; b) Real detail (Google Maps Street View).

- **Internal main columns**

In this case, being the main pillars composed of curved and very detailed elements, it was decided to model it as a union of four rectangular columns supporting the four arches.

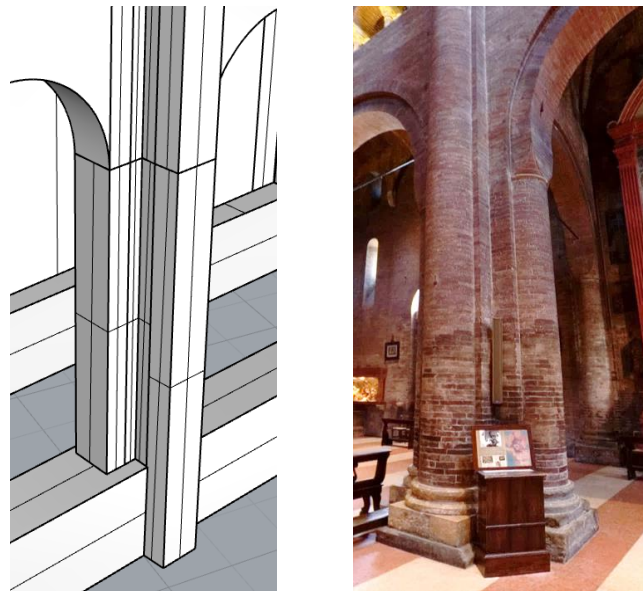


Figure 6.23 – Internal main columns: a) 3D geometric model on Rhinoceros; b) Real detail (UNESCO Modena Website).

- **Apse basement**

Regarding, the basement of the apse is made up of many domes. For this reason, two models were created, one having the domes in the apse area and one modelling the domes with an equivalent plate with a thickness equal to the average total height. This second case was possible due to the high rigidity of the apse area which makes it less prone to damage as the most vulnerable domes are those present in the central and lateral naves. The test was carried out to try to reduce the number of elements. Comparing the two models, the one with the equivalent plate did not lead to any advantage in terms of computational burden. This is because using tetragonal elements (*Chapter 6.4.1*), there was an increase in the elements at the supporting pillars. This does not happen for the other case because the dome generates a gradual change of the geometry and not as abrupt as it could be a 90° edge. For this reason, it was decided to proceed with the model with the domes modelled in the apse.

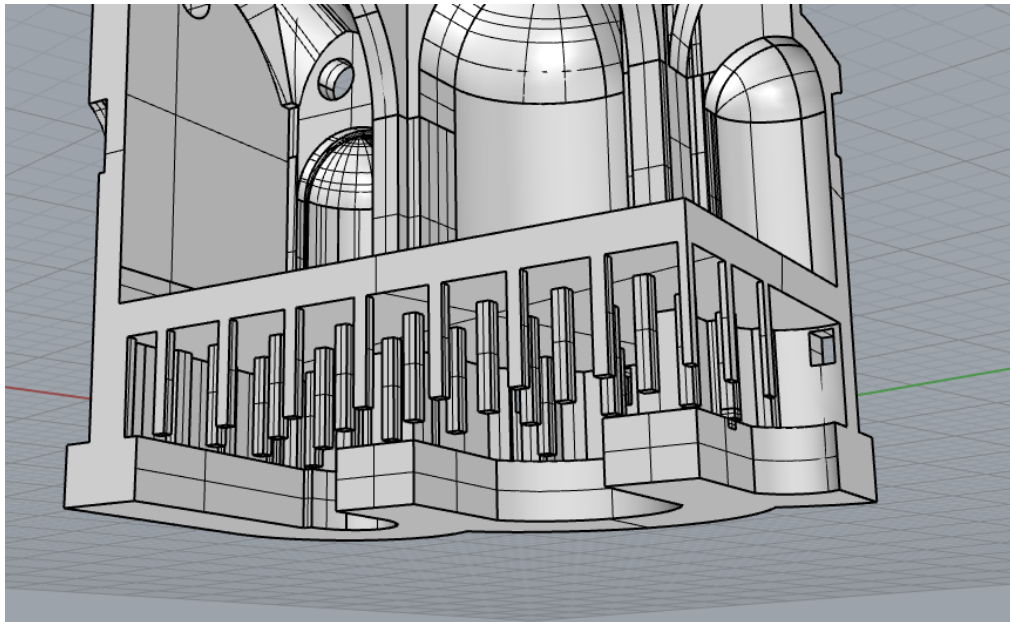


Figure 6.24 – Apse basement modelled with an equivalent plate: 3D geometric model on Rhinoceros.

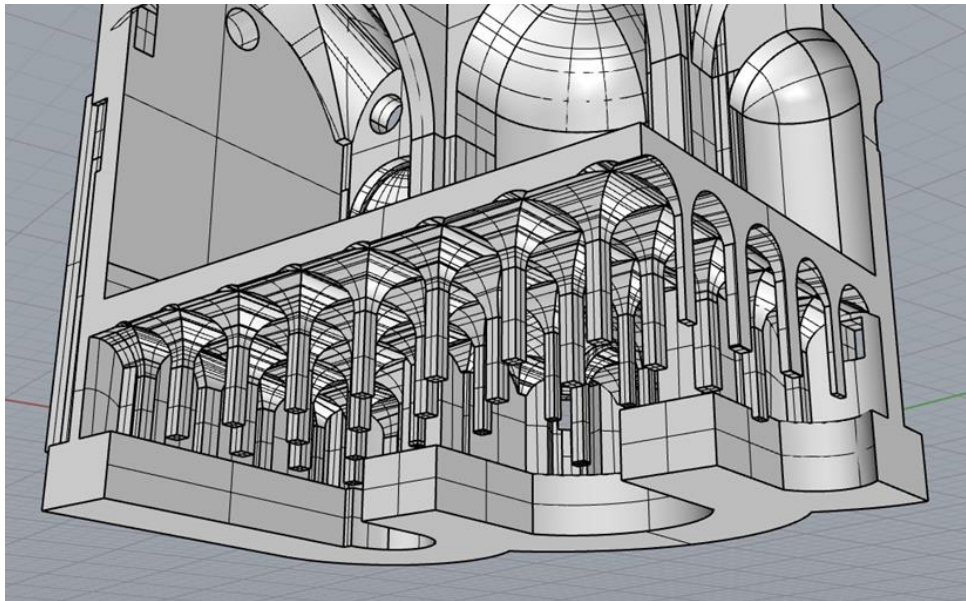


Figure 6.25 – Apse basement modelled with domes: 3D geometric model on Rhinoceros.

6.4 The structural model

ABAQUS/CAE software was used to implement seismic analysis on the model of the Cathedral of Modena. *ABAQUS/CAE* is a suite of powerful engineering simulation programs, based on the finite element method, that can solve problems ranging from relatively simple linear analyses to the most challenging nonlinear simulations.

6.4.1 Finite elements used

As reported in the *Chapter 6.2*, the structure is modelled with solid elements due to the high thickness of the walls and the complicated geometry like the arches, which converge in a column. These elements would have been difficult to model with plate elements without avoiding errors because they would have introduced an excessive level of simplification that would not have correctly described the behaviour of the structure. Furthermore, due to the presence of arches, domes and complicated geometries it was not possible to use hexahedral elements. For this reason, the C3D4 linear isoparametric tetrahedron elements were used. Finite elements with 4 nodes and not with 10 were used due to the high computational burden of the latter. Having performed the calibration of the materials, the response of the structure using one element or the other is practically similar. The 10-node second order elements, however, were used in nonlinear dynamic analysis of the dome, being an analysis in which the stress state is the main objective. Second order elements provide higher accuracy in *ABAQUS/Standard* than first order. They capture stress concentrations more effectively and are better for modelling geometric features: they can model a curved surface with fewer elements. Finally, second-order elements are very effective in bending-dominated problems [55]. T3D2 truss elements were used to model the Cathedral-Ghirlandina Tower interaction and the tie-rods system. Truss elements are one-dimensional bars or rods that are assumed to deform by axial stretching only. They are pin jointed at their nodes, and so only translational

displacements and the initial position vector at each node are used in the discretization [55].

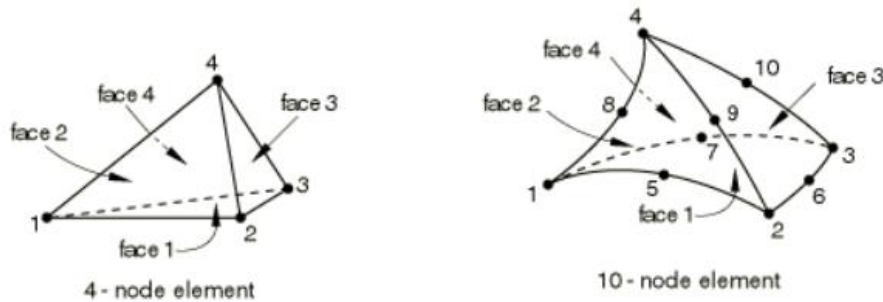


Figure 6.26 – a) ABAQUS/CAE C3D4 linear isoparametric tetrahedron element
 b) ABAQUS/CAE C3D10 quadratic isoparametric tetrahedron element [55].

The interpolation is defined in terms of the element coordinates g , h , and r . Since ABAQUS/CAE is a Lagrangian code for most applications, these are also material coordinates. They each span a range from 0 to 1 but satisfies the constraint $g + h + r \leq 1$. The node numbering convention used in ABAQUS/CAE for these elements is also shown in Figure 6.26, corner nodes are numbered first and then the midside nodes.

The interpolation functions of the C3D10 element is:

$$\begin{aligned}
 u = & (2(1-g-h-r)-1)(1-g-h-r)u_1 + (2g-1)gu_2 + (2h-1)hu_3 + \\
 & + (2r-1)ru_4 + 4(1-g-h-r)gu_5 + 4ghu_6 + 4(1-g-h-r)hu_7 + \\
 & + 4(1-g-h-r)ru_8 + 4gru_9 + 4hru_{10}
 \end{aligned} \quad (6.1)$$

The interpolation functions of the C3D4 element is:

$$u = (1-g-h-r)u_1 + gu_2 + hu_3 + ru_4 \quad (6.2)$$

The first order tetrahedron is constant stress elements and use a single integration point for the stiffness calculation when used in stress/displacement applications. A lumped mass matrix is used with the total mass divided equally over the nodes. For stress/displacement applications the second order tetrahedron uses 4 integration points for its stiffness matrix and 15 integration points for its consistent mass matrix [55].



The elements T3D2 are one-dimensional: a single material (isoparametric) coordinate, g , is defined along the element, with $-1 \leq g \leq 1$ in the element.

The interpolation functions of the T3D2 element is:

$$u = \frac{1}{2}(1-g)u_1 + \frac{1}{2}(1+g)u_2 \quad (6.3)$$

The linear truss is a constant strain element and so is integrated exactly [55].

6.4.2 Boundary condition

- **Soil-structure interaction**

The soil-structure interaction was modelled by defining for the foundation a material described from homogenization of the soil-masonry mechanical characteristics. In this way it was not needed to model the ground as Winkler springs and to fix the model at the base. It was possible to define the materials thanks to the Model Updating (*Chapter 7.4*), in such a way to allow that the experimental and theoretical mode shapes to be as coincident as possible. Regarding the layout of the foundations and the dimensions, refer to *Chapter 5.5.2*.

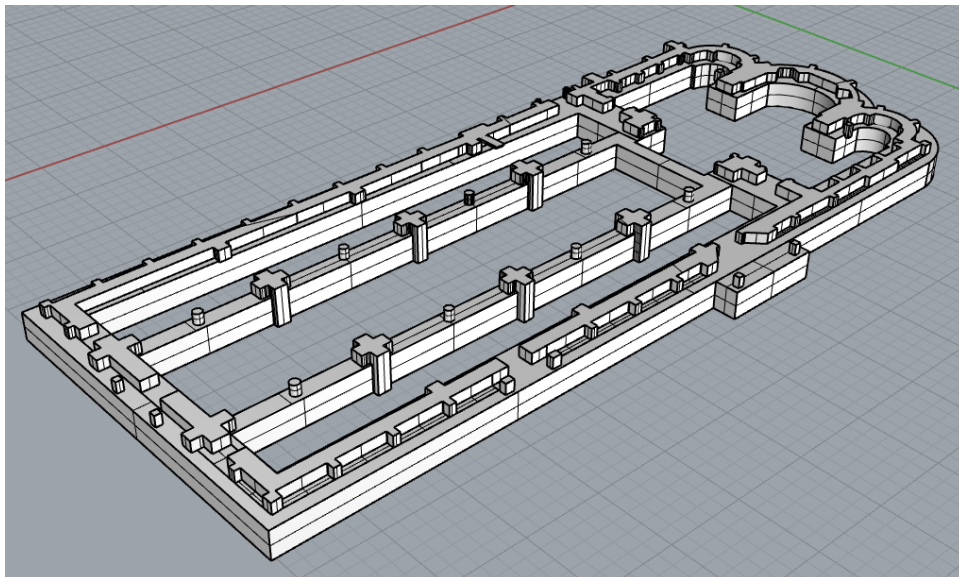


Figure 6.27 – Foundation layout adopted.

- **Interaction with the Ghirlandina tower**

Regarding the Cathedral-Ghirlandina Tower [56] interaction, it was modelled using 8 Truss elements having a certain rigidity. Also in this case, the stiffness of the truss elements were calibrated by comparing the experimental mode shape and the theoretical ones in the Model Updating analysis (*Chapter 7.4*).

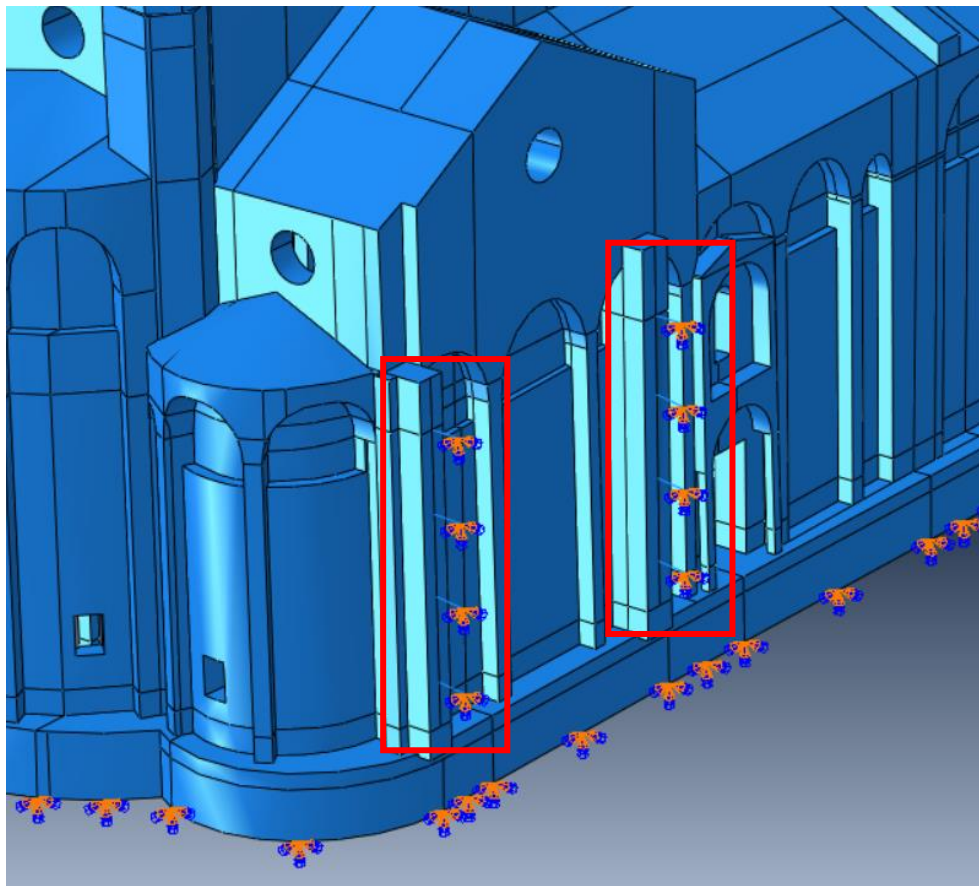


Figure 6.28 – Trusses disposition for modelling Cathedral-Ghirlandina Tower interaction.

- **Tie-rods system**

In the model used in the analysis, the tie-rods installed in the structure were positioned as reported in *Chapter 5.5.3*. T3D2 truss element was used to model these structural parts.

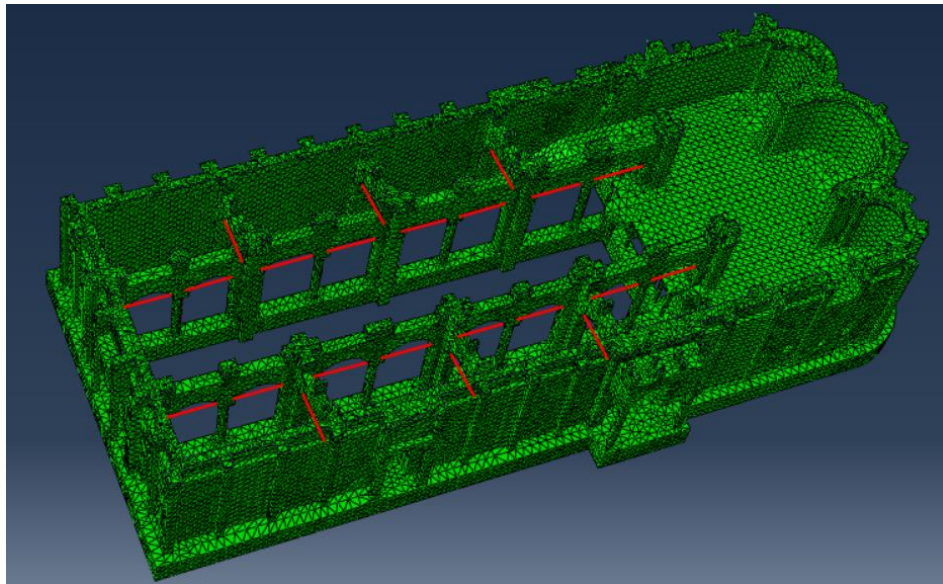


Figure 6.29 – Tie-rods reinforcement system at the base.

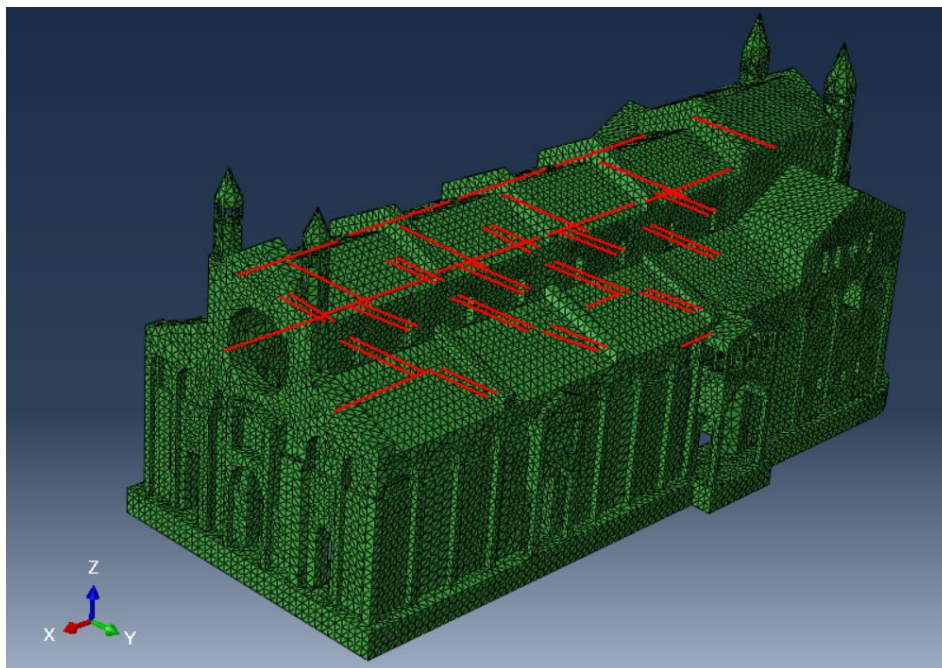


Figure 6.30 – Tie-rods reinforcement system at the top.

6.4.3 Mesh

The mesh was chosen in function of the dimension of the main structural element avoiding having elements that are too small but at the same time having as few distorted elements as possible. This is very important for the computational burden of the calculations, if there are too small elements the analyses become very heavy and instead if the elements are very distorted there may be convergence problems. Finding a balance between these two parameters, an element approximate global size of 0.7m was set. With this type of approximate global dimension, the model of the Modena Cathedral is composed by 304265 elements. In the *Figure 6.31* and *Figure 6.32* are reported two different views of the structural meshed model:

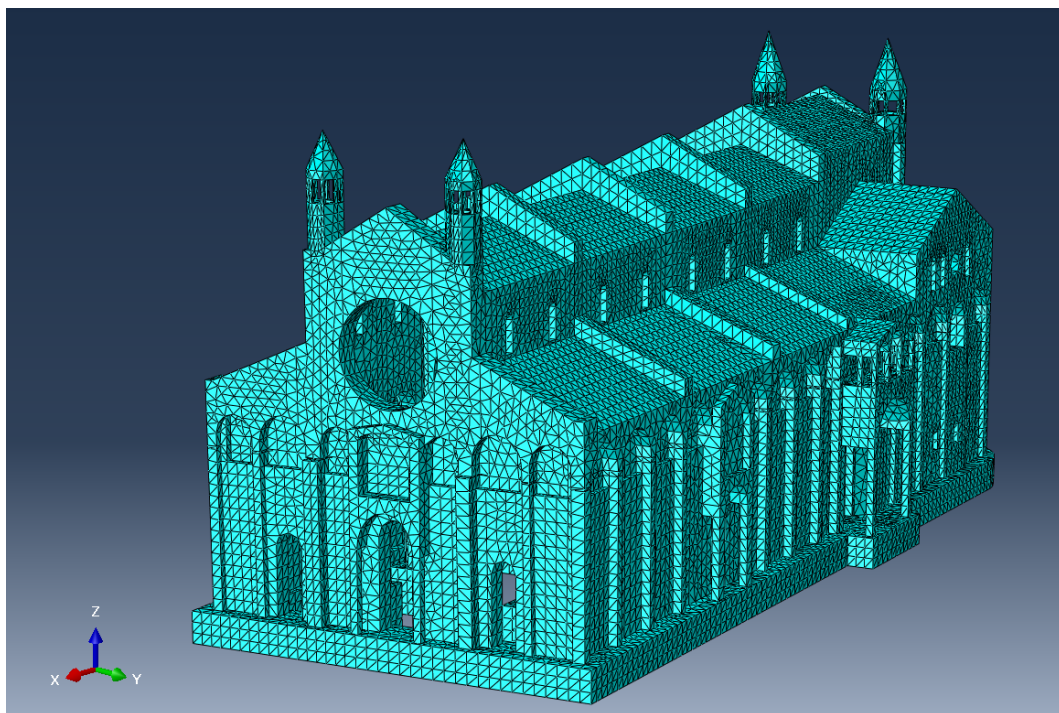


Figure 6.31 – Meshed model – View 1

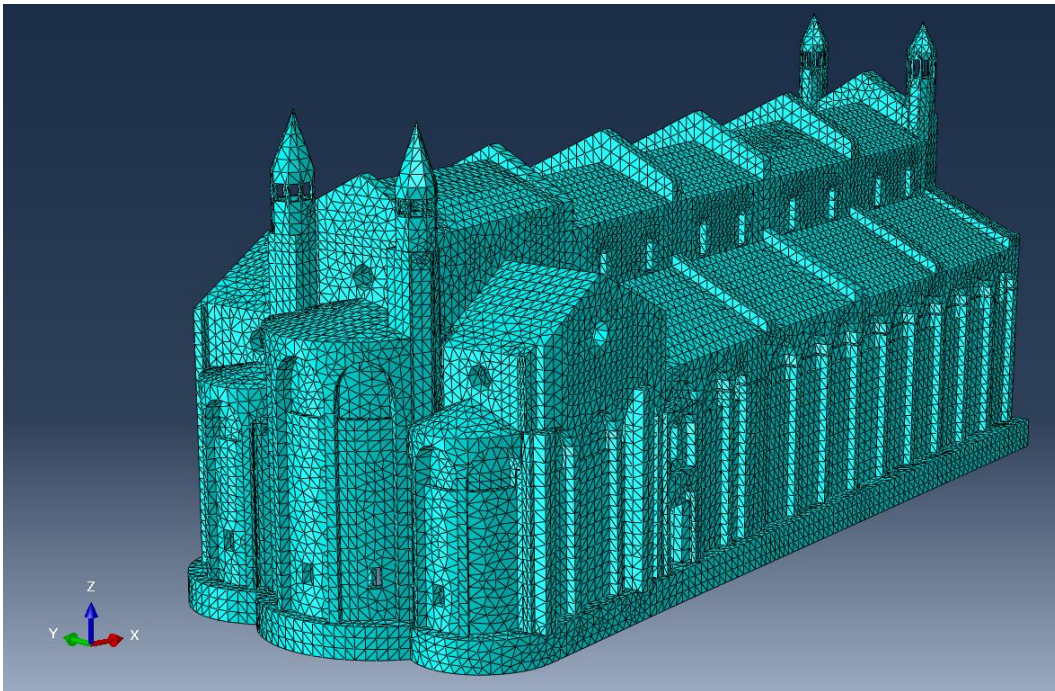


Figure 6.32 – Meshed model – View 2

Chapter 7

Calibration: Model Updating

7.1 Introduction

When studying a historical structure belonging to the *UNESCO Cultural Heritage* it is not easy to have information on the mechanical characteristics of the materials. In fact, as reported in the “*Guidelines for the evaluation and reduction of the seismic risk of cultural heritage with reference to technical standards for construction*” in Chapter 4.1.7: “*The direct measurement of the mechanical parameters of the masonry, in particular those of resistance, cannot be performed, therefore, except through weakly destructive or destructive tests, even if on limited portions. Non-destructive diagnostic techniques of an indirect type, such as sonic and ultrasonic tests, allow to evaluate the homogeneity of the mechanical parameters in the different parts of the building, but they do not provide reliable quantitative estimates of their values, since they are deduced from the measurement of other quantities (for example, the propagation speed of volume waves) ” [1].*

Regarding the Modena Cathedral, knowledge of the materials are very limited, non-destructive sonic tests were carried out only in limited areas of the structure (*Chapter 5.5.1*). For this reason, not having enough data for the definition of the materials, it was necessary to proceed with the model updating analysis. With this analysis it was possible to calibrate the materials in the different areas of the structure by means of the dynamic identification results obtained starting from the monitoring data. Starting from the incomplete information on the materials, was calibrated the theoretical model.

7.2 Model updating theory

Model updating aims to minimize the differences between the experimental measurements and the theoretical dynamic response of a model. In this chapter, the IEM (Inverse Eigensensitivity Method) [57] and MAC (Modal Assurance Criterion) [58] are presented through some theoretical notions.

7.2.1 Modal assurance criterion (MAC)

The modal assurance criterion is a technique to estimate the degree of correlation between modal shape vectors, mainly to pair analytical models with experimental results. This criterion does not require an estimate of the system matrices, but only to know the vectors of the modal deformed shape. The formulation is reported below:

$$MAC_{jk} = \frac{|\phi_{mj}^T \phi_{ak}|^2}{(\phi_{mk}^T \phi_{ak})(\phi_{mj}^T \phi_{aj})} \quad (7.1)$$

where:

ϕ_{mj} : measured mode;

ϕ_{aj} : analytical mode.

The value of the MAC is between 0 and 1, a value of 1 means that one vector is a multiple of the other. The two vectors must have the same size, if the accelerometers are positioned only in some nodes of the structure, as always happens, only the modal shape of those nodes must be inserted in the vector.

7.2.2 Modal updating technique

The model updating procedure is based on the computation of suitable correction coefficients a_i and b_i ; these coefficients are associated with the mass and stiffness of the i -th element, respectively, such that all the relations that refer to the corrected matrices of the model are satisfied as follows:

$$[M_u] = \sum_{i=1}^L a_i \cdot [M]_i \quad (7.2)$$

$$[K_u] = \sum_{i=1}^L b_i \cdot [K]_i \quad (7.3)$$

where:

$[M]_i$ and $[K]_i$: sub-matrices of the system and may correspond to the matrices of sub-elements, elements or macro elements (substructures);
 L : the number of elements or macro elements in the structure;

All models that employ sensitivity-based methods are generally based on the use of expansions in the Taylor series in which mode data, which are considered as a function of unknown parameters, are truncated. The expansion in the series is frequently truncated after the first two terms, which yields a linear approximation that is expressed as follows:

$$\{\Delta w\} = [S] \cdot \{\Delta p\} \quad (7.4)$$

where:

$\{\Delta w\} = \{\Delta \lambda_1, \{\Delta \phi_1\}, \Delta \lambda_2, \{\Delta \phi_2\}, \dots, \Delta \lambda_m, \{\Delta \phi_m\}\}^T$: error in the measured outputs;

$\Delta \lambda_i$: error in the i -th eigenvalue;

$\{\Delta \phi_i\}$: error in the corresponding mode shape;

$\{\Delta p\}$: perturbation in the parameters;

$[S]$: sensitivity matrix containing the first derivatives of the eigenvalues and eigenvectors with respect to the parameters estimated in the previous iteration.

The sensitivity matrix represents the relation between the variations in the physical parameters and the error in the dynamic structural response expressed in terms of the frequencies and mode shapes. By using a Taylor series expansion, the r -th eigenvalue and eigenvector contributions can be determined as follows:

$$\begin{Bmatrix} \Delta\lambda_r \\ \{\Delta\phi\}_r \end{Bmatrix} = \begin{bmatrix} \frac{\partial\lambda_{Ar}}{\partial a_1} / \lambda_{Ar} & \dots & \frac{\partial\lambda_{Ar}}{\partial a_L} / \lambda_{Ar} & \frac{\partial\lambda_{Ar}}{\partial b_1} / \lambda_{Ar} & \dots & \frac{\partial\lambda_{Ar}}{\partial b_L} / \lambda_{Ar} \\ \frac{\partial\{\phi_A\}_r}{\partial a_1} & \dots & \frac{\partial\{\phi_A\}_r}{\partial a_L} & \frac{\partial\{\phi_A\}_r}{\partial b_1} & \dots & \frac{\partial\{\phi_A\}_r}{\partial b_L} \end{bmatrix} \cdot \begin{Bmatrix} \Delta a_1 \\ \vdots \\ \Delta a_L \\ \Delta b_1 \\ \vdots \\ \Delta b_L \end{Bmatrix} \quad (7.5)$$

Eq. (7.5) can be simplified by using the vector $\{p\}$ that contains the correction coefficients $\{a_1, a_2, \dots, a_L, b_1, b_2, \dots, b_L\}^T$:

$$\{\Delta_r\}_{[(n+1) \times 1]} = [S_r]_{[(n+1) \times 2L]} \cdot \{\Delta p\}_{[2L \times 1]} \quad (7.6)$$

where:

n : number of coordinates measured.

Hence, from the Eq. (7.6), the vector $\{p\}$ can be determined as follows:

$$\{p\}_{new} = [p]_{old} + \{\Delta p\} \quad (7.7)$$

The solution of Eq. (7.7) is obtained by an iterative procedure involving the simultaneous updating of the mass and/or the stiffness matrices and a resolution of the dynamic model for each iteration. The process is iterated until the results converge.

The unknown parameters of the system are applied to each element as coefficients to define the changes in the structural characteristics. From a purely theoretical point of view, if a very large number of mode shapes are available, all the structural parameters can be modified with the same degree of reliability. However, in practice, the number of experimental mode shapes is measured at only a limited number of locations and over a limited frequency range. Consequently, some parameters will have very

little or even nil influence on the experimental response. In order to overcome the problem of the incompleteness of the measured data, a weight matrix $[W]$ is applied to assess the relative significance of the individual contributions. The updating parameter is expressed as follows:

$$\{\delta p\}_{new} = [W] \left([S]^T [S] [W] \right)^{-1} [S]^T \{\delta w\} \quad (7.8)$$

In general, it is difficult to define the weight matrix; further, many cases demand an empirical evaluation. In order to determine the $[W]$ matrix, it is necessary to analyse the ratio of the individual elements or macro elements to the mode shapes, as follows:

$$\xi_{i,j} = \frac{\{\phi_x\}_j^T [T]^T [K^e]_i [T] \{\phi_x\}_j}{\{\phi_x\}_j^T [T]^T [K] [T] \{\phi_x\}_j} \quad (7.9)$$

where:

$\{\phi_x\}_j^T$: eigenvector of the j -th experimental model;

$[K^e]_i$: stiffness matrix of the i -th macro element or element;

$[T]$: system's reduction transformation.

Under the assumption that m experimental vibration modes are available, the weight for each parameter can be given as follows:

$$W_{ii} = \frac{\sum_{j=1}^m \xi_{i,j}}{\max(W_{ii})} \quad (7.10)$$

Matrix $[W]$ considers both the structural sensitivity of the elements and their influence on the experimental mode shapes. Hence, it is very useful in the selection of the updating parameters.

7.3 Experimental dynamic identification

As reported in the *Chapter 5.5.1*, in July 2015 the Politecnico di Torino and the Nagoya City University installed a new dynamic monitoring system, composed by 12 points and 16 accelerometers.

Professor Donato Sabia and Takayoshi Aoki, by means of the data of this monitoring system, obtained the experimental dynamic identification of the Modena Cathedral. The experimental dynamic identification provides information on the main mode frequencies, on the mode shapes and on the damping of each mode as data.

Initially the identification was carried out considering all 12 measuring points, subsequently these data were used for the realization of the model updating but by calculating the MAC value the results were not satisfactory. Then, we proceeded with a new identification without the points of the dome (CH9, CH10, CH11) and tower (CH12), in order to avoid acquire local motions that compromise the calibration of the global model.

The results of the dynamic identification used for calibration are shown below. Mainly three vibration modes have been identified, the main characteristics of these vibration modes are shown in the following table:

Table 7-1 - Experimental vibration mode data

<i>Vibration Mode</i>	<i>Frequency (Hz)</i>	<i>Damping</i>
1	1.99	0.0525
2	3.20	0.0331
3	3.41	0.0123

7.3.1 Experimental vibration mode

- **Vibration mode 1**

The modal shape of the first mode obtained with the dynamic identification is shown below:

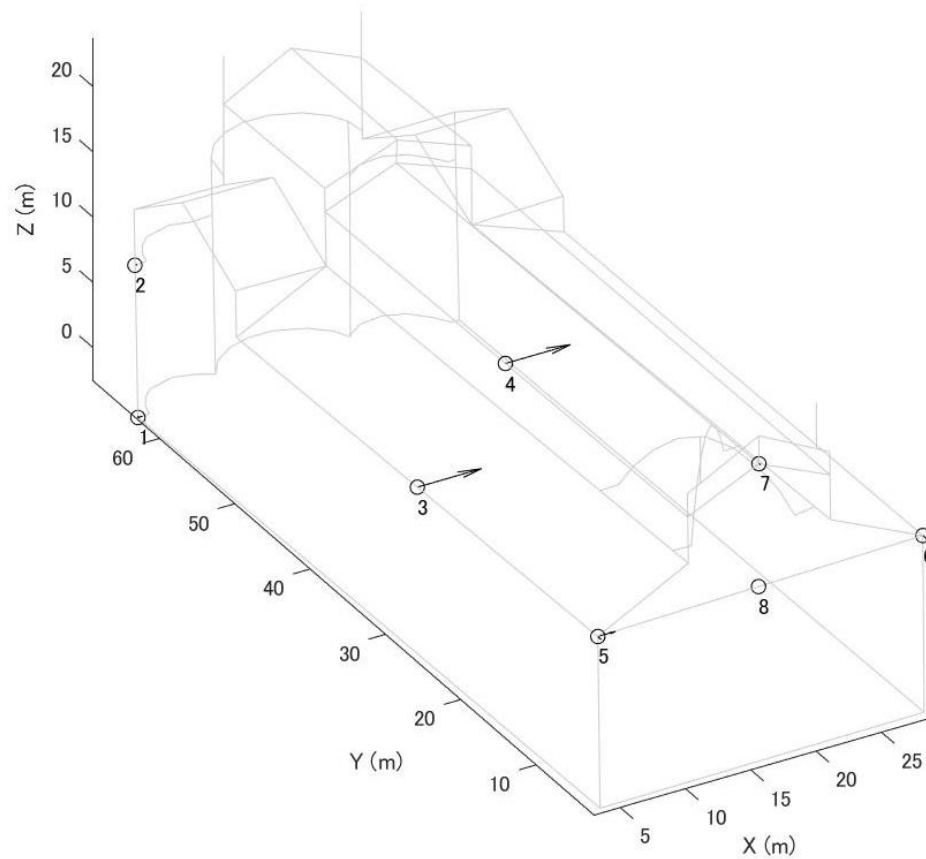


Figure 7.1 – 3D view of the first experimental mode
(Frequency 1.99Hz, Damping 5.25%).

- **Vibration mode 2**

The modal shape of the second mode obtained with the dynamic identification is shown below:

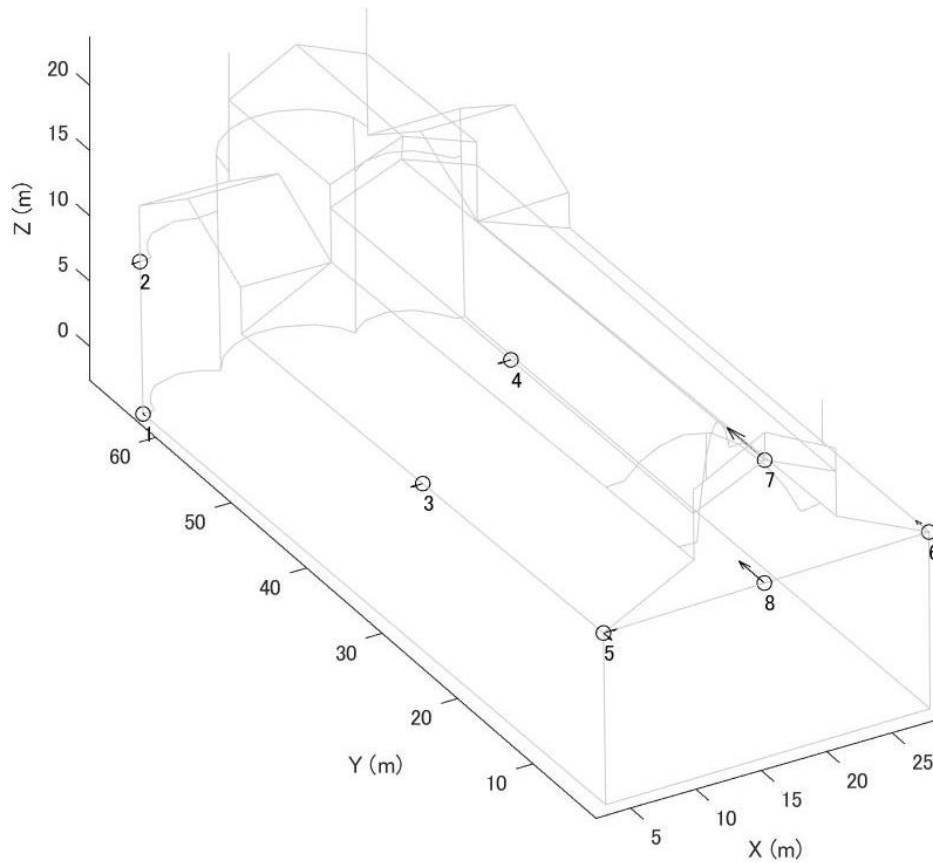


Figure 7.2 – 3D view of the second experimental mode
(Frequency 3.20Hz, Damping 3.31%).

- **Vibration mode 3**

The modal shape of the third mode obtained with the dynamic identification is shown below:

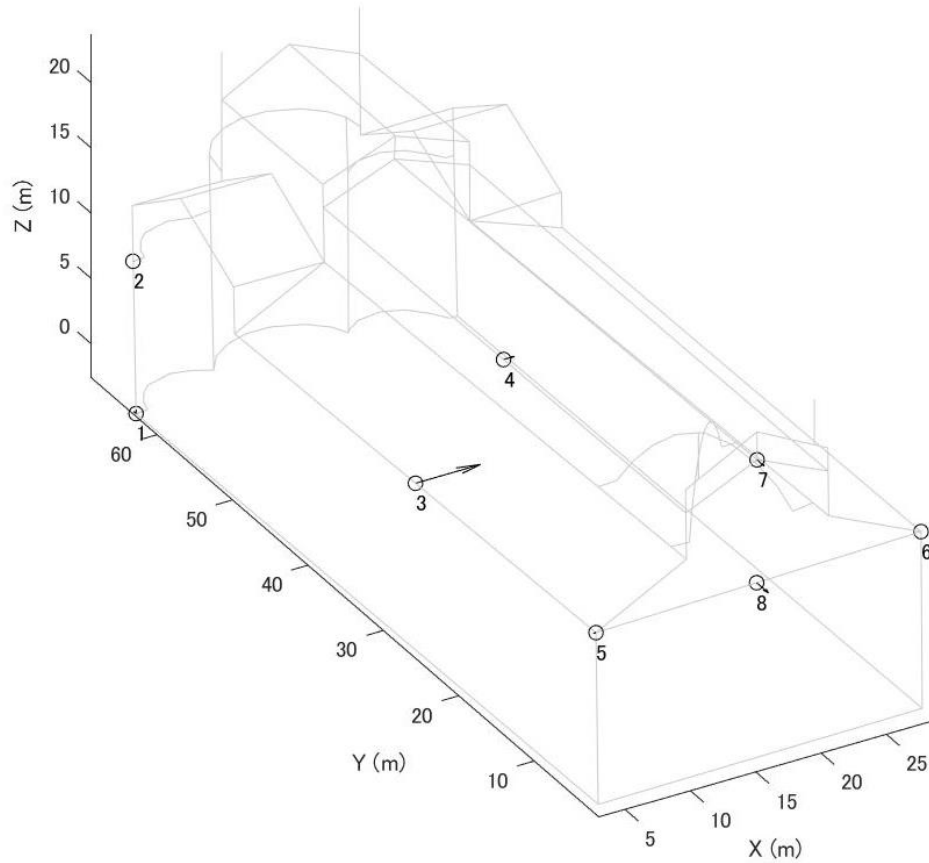


Figure 7.3 – 3D view of the third experimental mode
(Frequency 3.41Hz, Damping 1.23%).

7.4 Model updating results

The model updating was carried out with the *NASTRAN* software using the IEM (Modal Assurance Criterion). The model was divided into parts, which make macroelements, with different materials as will be reported in the next paragraph. In this chapter the results of the model updating will be reported by comparing the different models and the one that better describes the real structure response will be chosen.

7.4.1 Initial model

To allow the analysis to iterate and vary the materials, the structure was divided into 183 parts, each of which having a different material. Finally, a combination of materials that had a structural behaviour closer to the real one. The input materials inserted before the Model updating analysis (*Appendix B*) and the relative position in the model (*Figure 7.4- Figure 7.5*) are shown below.

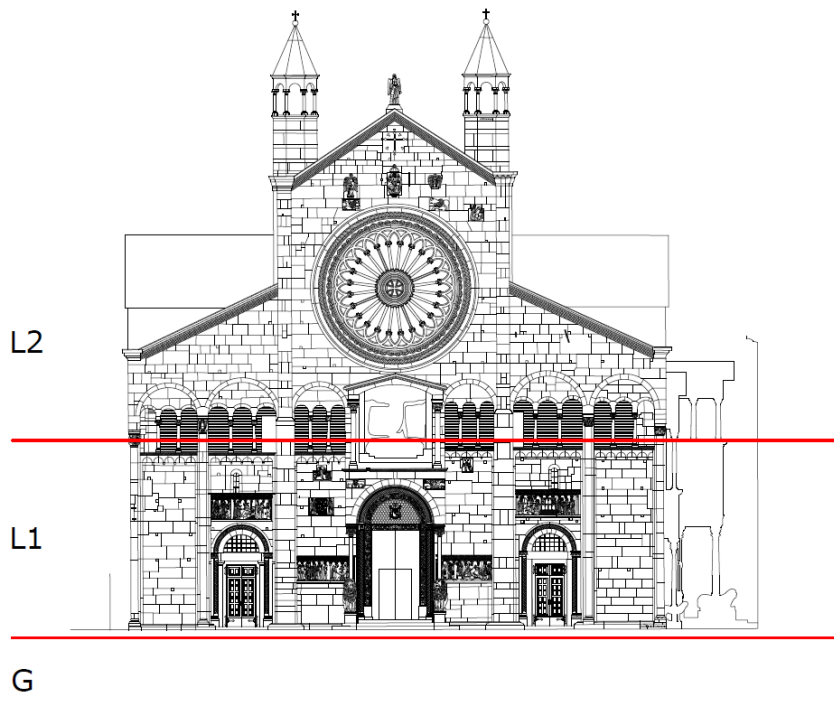


Figure 7.4 – Material ID explanation (Drawing of Giancarlo Palazzi).

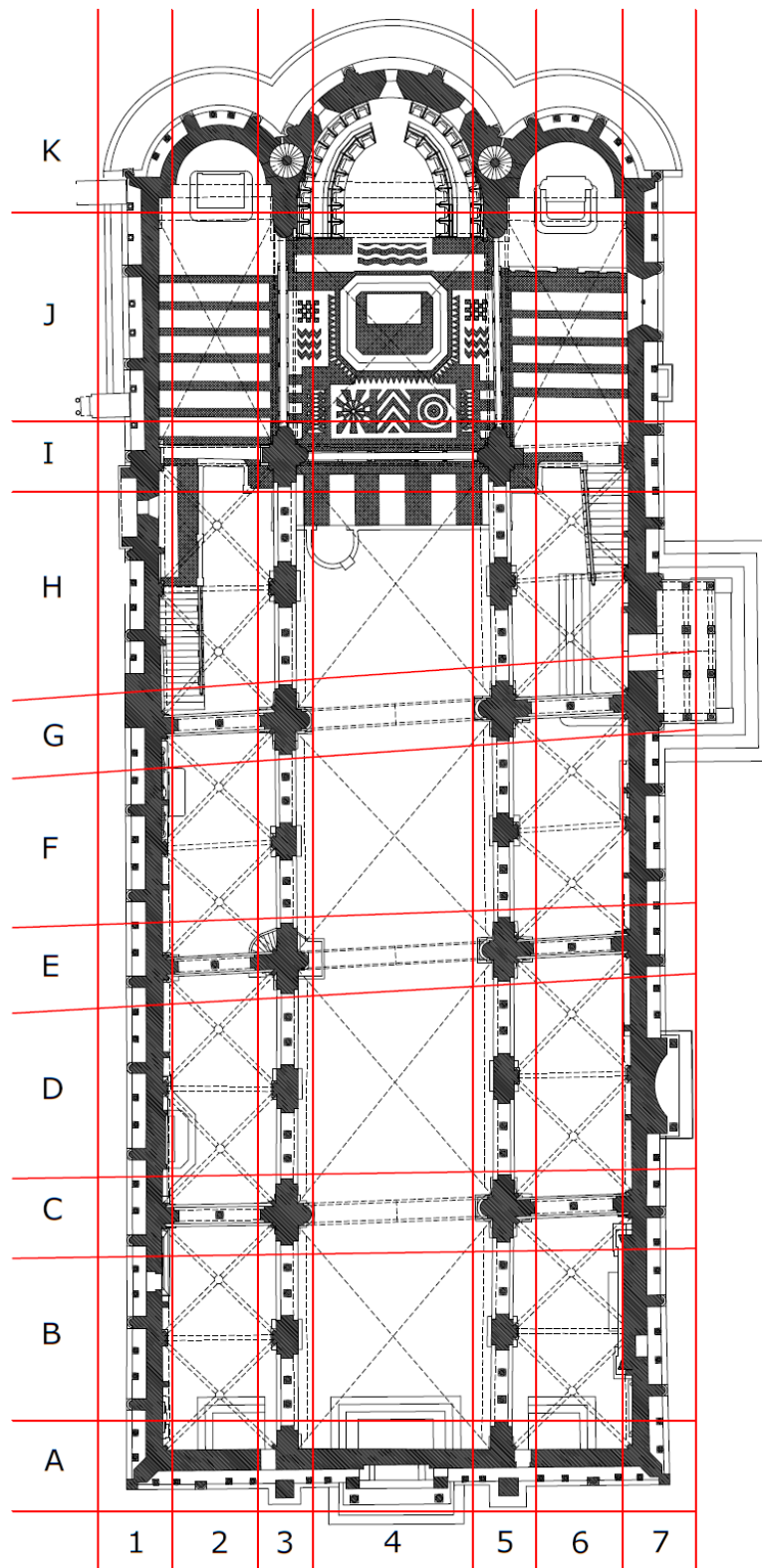


Figure 7.5 – Material ID explanation (Drawing of Giancarlo Palazzi).

As you can see in the *Figure 7.4*, the materials corresponding to the foundations begin with the letter *G*, those of the level 1 with *L1*, those of the level 2 with *L2* and finally the roof areas with the letter *T*. The materials having the name *Ghirlandina_n* correspond to the springs describing the Cathedral-Ghirlandina Tower interaction.

Below is the FEA model with the different materials assigned.

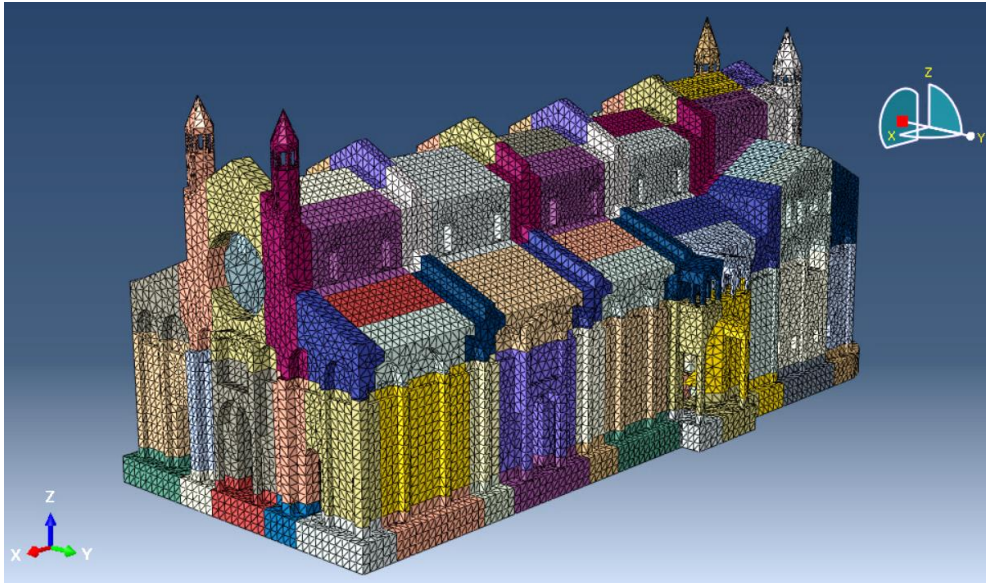


Figure 7.6 - FEA model with the different materials assigned – View1

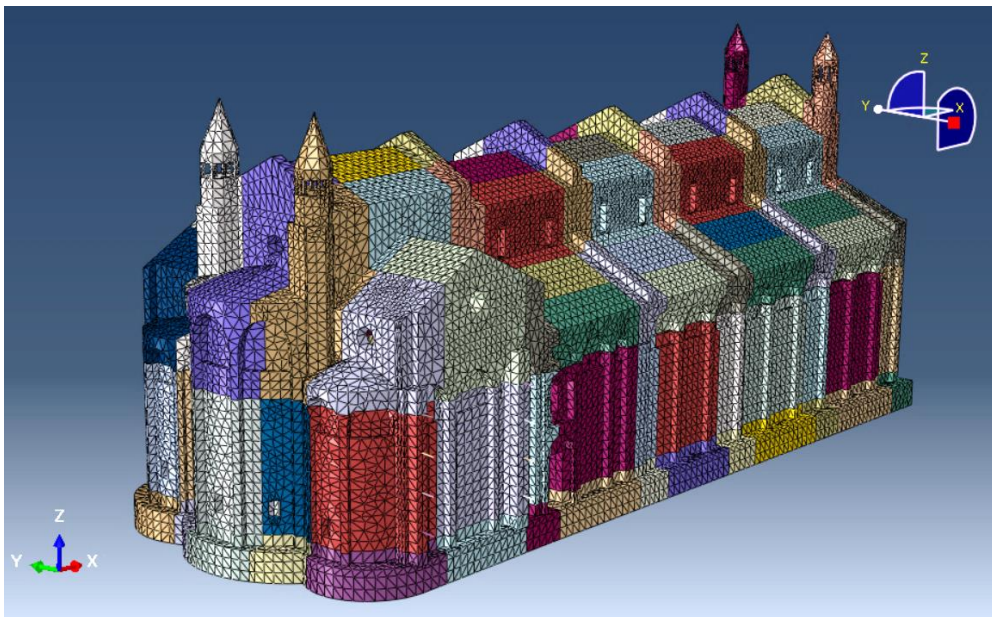


Figure 7.7 - FEA model with the different materials assigned – View 2

7.4.2 Modal analysis of the initial model

Before adopting the model updating technique, a modal analysis was carried out on the two models having the materials shown in the *Appendix B*. Comparing the experimental modal shapes with those of the model was obtained a correspondence between them. Observing the modal mass (*Table 7-3*) was possible to define the most significant modes are the first five:

- First mode: Translational in the Y direction;
- Second mode: Torsional around the Z axis;
- Third mode: Translational in the X direction;
- Fourth mode: Translational in the Z direction;
- Fifth mode: Translational in the Y direction.

Below are reported the main characteristics of the first ten modes of the FEM numerical models and the respective mode shapes.

Table 7-2 – Modal analysis results - Initial model: Frequency and Participation factor

Mode	Frequency (Hz)	Participation Factor		
		X - Component	Y - Component	Z - Component
1	2.22	-20.12	-3164.50	18.50
2	3.56	526.70	-482.41	50.68
3	4.01	-3511.60	25.76	-51.06
4	4.69	-272.93	-318.51	420.66
5	4.85	77.30	1368.40	58.31
6	5.70	307.73	341.34	175.48
7	5.89	-76.21	-44.13	-25.84
8	5.99	30.03	83.39	41.76
9	6.50	307.21	-59.65	-320.50
10	6.63	-232.52	-258.13	574.13



Table 7-3 – Modal analysis results - Initial model: Frequency and Modal mass

Mode	Frequency (Hz)	% Modal mass		
		X - Component	Y - Component	Z - Component
1	2.22	0.00%	51.61%	0.00%
2	3.56	0.23%	0.65%	0.01%
3	4.01	60.09%	0.00%	0.00%
4	4.69	0.05%	0.06%	2.10%
5	4.85	0.11%	7.15%	0.01%
6	5.70	0.08%	0.12%	0.07%
7	5.89	0.01%	0.07%	0.00%
8	5.99	0.40%	0.01%	0.21%
9	6.50	0.19%	0.00%	1.02%
10	6.63	0.01%	0.12%	0.05%
<i>Total</i>		61.17%	59.79%	3.47%

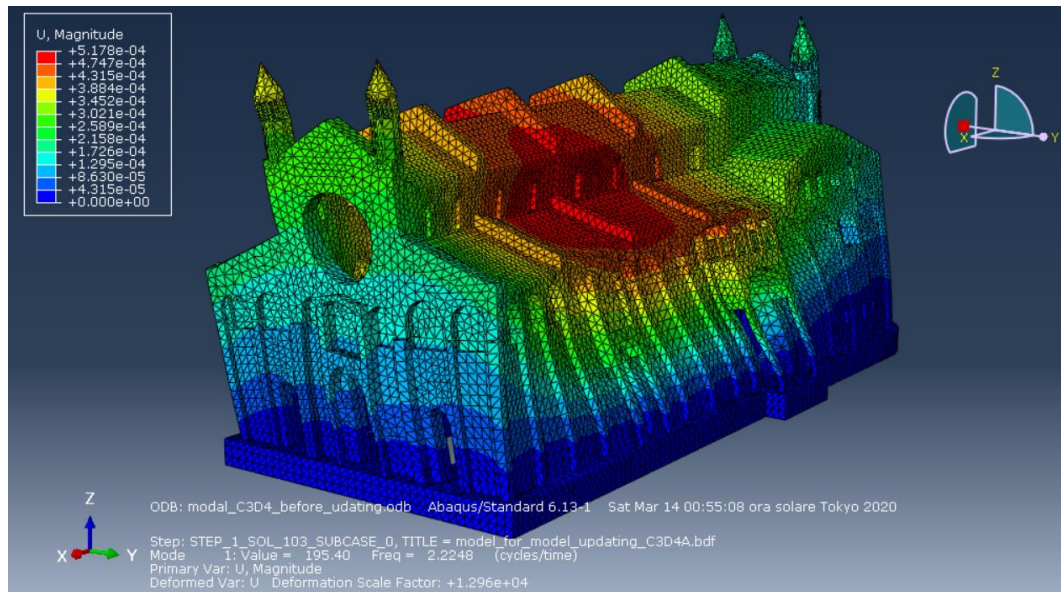


Figure 7.8 – First mode of the initial model – 4 nodes elements (2.22Hz).

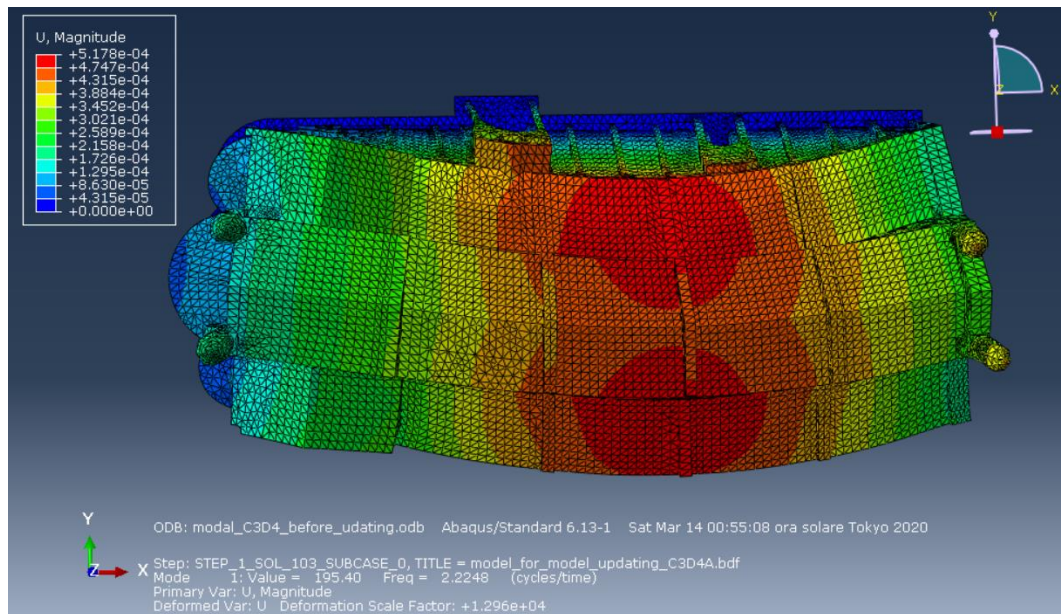


Figure 7.9 – First mode of the initial model – 4 nodes elements (2.22Hz).

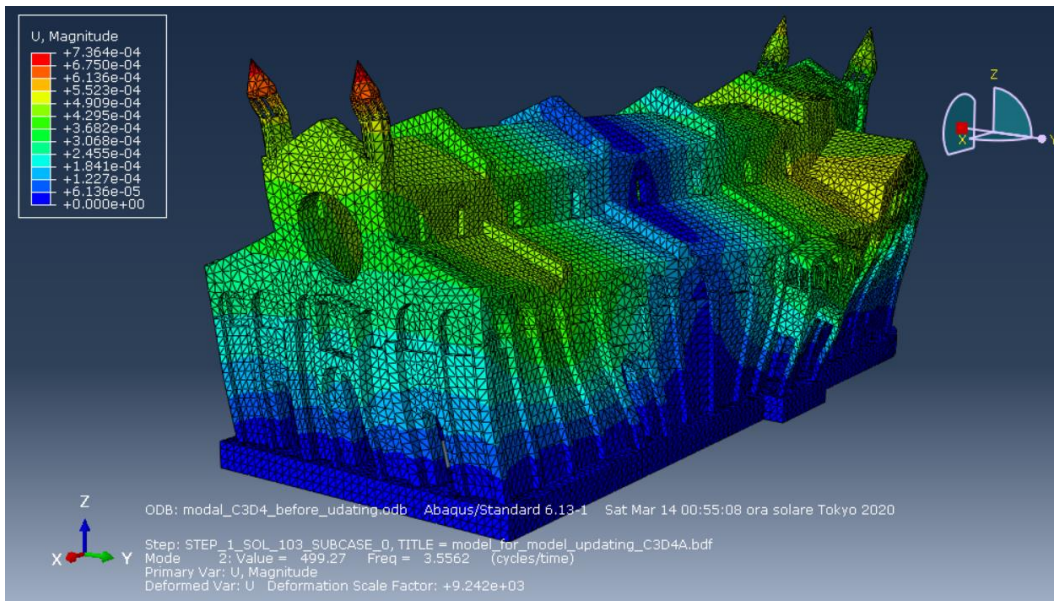


Figure 7.10 – Second mode of the initial model– 4 nodes elements (3.56Hz).

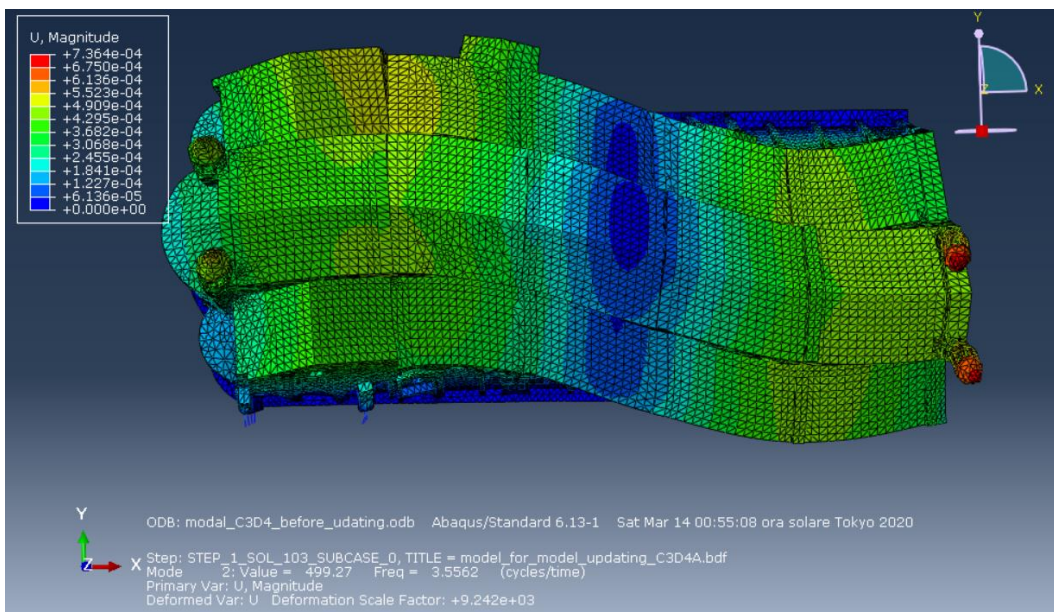


Figure 7.11 – Second mode of the initial model – 4 nodes elements (3.56Hz).

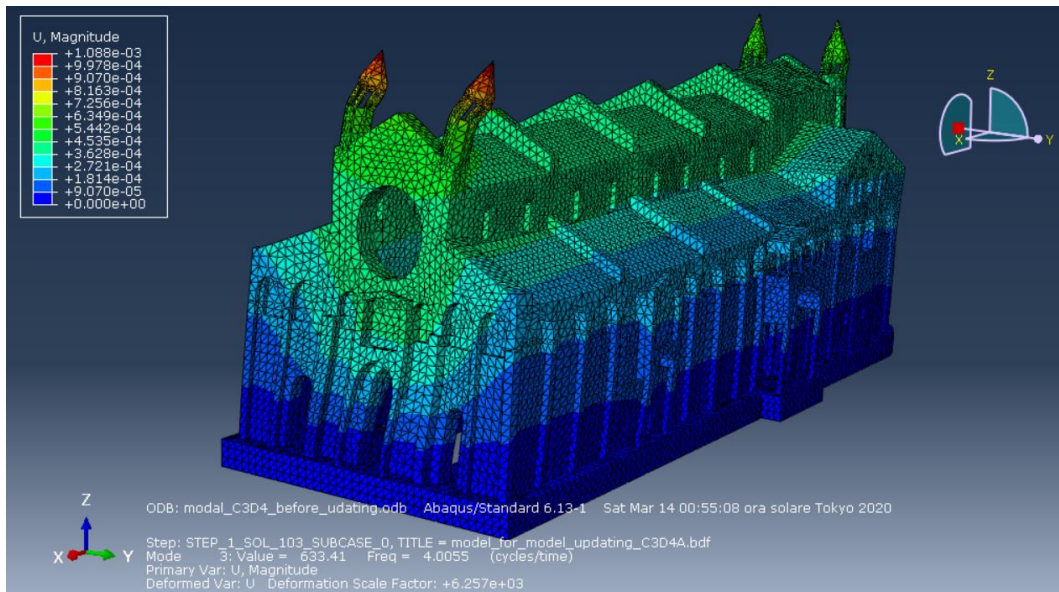


Figure 7.12 – Third mode of the initial model – 4 nodes elements (4.01Hz).

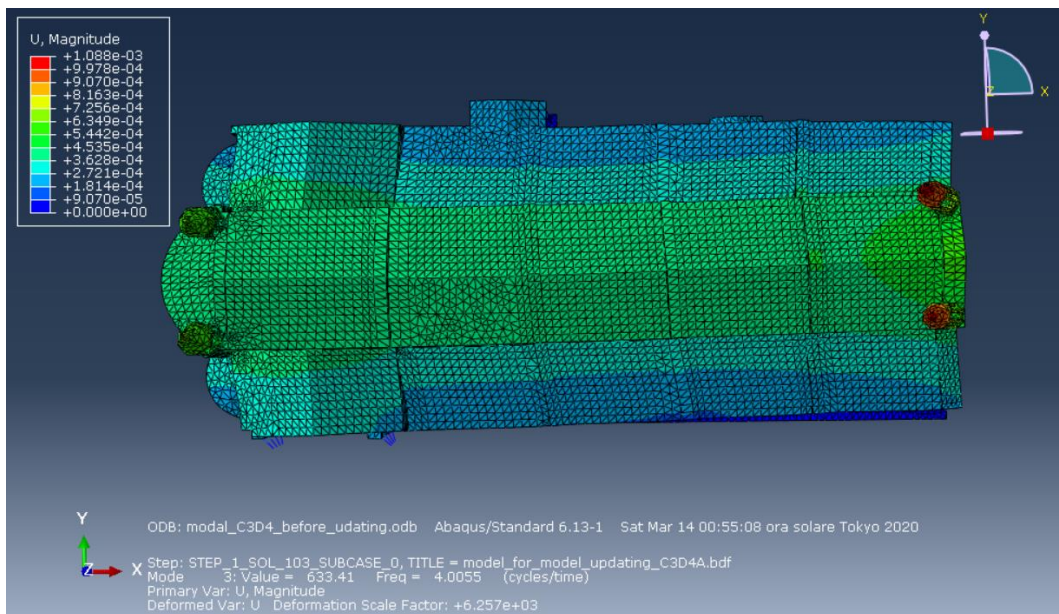


Figure 7.13 – Third mode of the initial model – 4 nodes elements (4.01Hz).

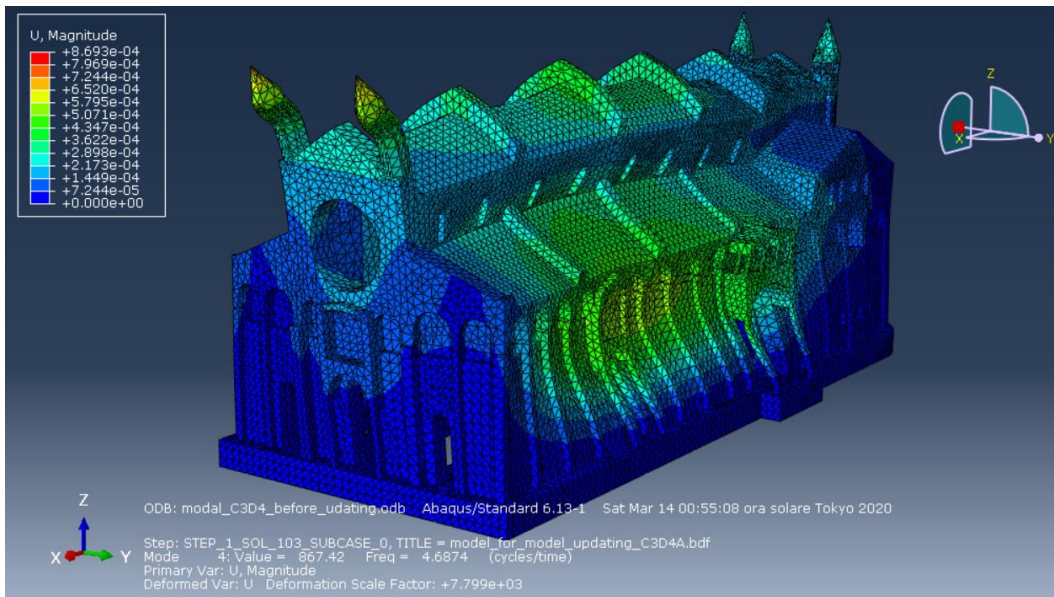


Figure 7.14 – Fourth mode of the initial model – 4 nodes elements (4.69Hz).

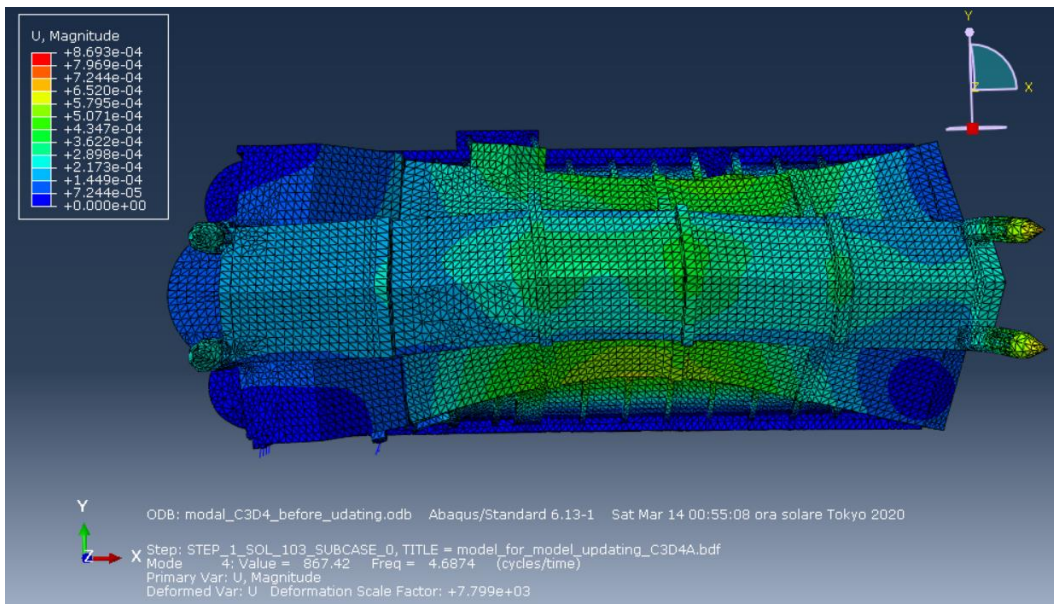


Figure 7.15 – Fourth mode of the initial model– 4 nodes elements (4.69Hz).

7.4.3 Comparison between the experimental and the initial model data

Now having both numerical and experimental data it was possible to compare them. Observing the mode shapes, the corresponding experimental modes were attributed to each numerical one. As can be seen from *Table 7-4*, the numerical model finds in the second mode of vibration a torsional mode around Z, not obtained by experimentation. This is probably due to the presence of a low number of accelerometers installed and not evenly distributed over the entire structure, this could compromise the acquisition of some fundamental modal shapes.

As reported in the following chapter, the model updating was carried out with the first, third and fourth mode, in *Table 7-4* it is possible to observe the starting difference between the frequencies:

Table 7-4 - Experimental and Numerical data – Initial model

<i>Vibration Mode</i>	<i>Experimental Frequency (Hz)</i>	<i>Initial model Frequency (Hz)</i>
1	1.99	2.22
2	-	3.56
3	3.20	4.01
4	3.41	4.69

7.4.4 Updated model

The model updating was performed on the model obtaining exactly all three experimental frequencies. By changing the elastic modulus of the 183 materials assigned to the structure, it was possible to obtain a model having an overall behaviour very close to that of the real structure.

The MAC, coefficient defines how close the eigenvector of the numerical modal shape is to the experimental one, is very close to 1 for the first and fourth mode, this means that the two modal shapes are almost coincident. As for the third mode, the MAC is lower but still acceptable.

Table 7-5 - Experimental and Numerical data – Initial model

Vibration Mode	Experimental	Numerical Initial model		
	Frequency (Hz)	Frequency (Hz)	Error (%)	MAC
1	1.99	2.22	11.56	0.96
2	-	3.56	-	-
3	3.20	4.01	25.31	0.73
4	3.41	4.69	37.54	0.94

Table 7-6 - Experimental and Numerical data – Updated model – 4 nodes elements

Vibration Mode	Experimental	Numerical Updated model		
	Frequency (Hz)	Frequency (Hz)	Error (%)	MAC
1	1.99	1.99	0.00	0.97
2	-	3.06	-	-
3	3.20	3.20	0.00	0.76
4	3.41	3.41	0.00	0.95



Below are the characteristics of the first ten modes of the FEM numerical updated model and the respective modal shapes. Refer to *Appendix B* for the updated materials.

Table 7-7 – Modal analysis results - Updated model: Frequency and Participation factor

Mode	Frequency (Hz)	Participation Factor		
		X - Component	Y - Component	Z - Component
1	1.99	7.55	-2923.30	4.86
2	3.06	-194.81	327.24	-40.48
3	3.20	-3154.50	10.64	13.55
4	3.41	-89.96	-98.57	589.19
5	3.98	137.12	1088.20	45.03
6	4.33	115.36	-140.35	-105.19
7	4.55	-42.95	107.50	-27.97
8	4.70	-255.97	-40.42	-186.98
9	5.27	-178.15	17.45	410.54
10	5.36	40.59	142.69	-92.69

Table 7-8 – Modal analysis results - Updated model: Frequency and Modal mass

Mode	Frequency (Hz)	% Modal mass		
		X - Component	Y - Component	Z - Component
1	1.99	0.00%	46.99%	0.00%
2	3.06	1.30%	1.09%	0.01%
3	3.20	57.87%	0.00%	0.01%
4	3.41	0.35%	0.48%	0.83%
5	3.98	0.03%	8.79%	0.02%
6	4.33	0.44%	0.55%	0.14%
7	4.55	0.03%	0.01%	0.00%
8	4.70	0.00%	0.03%	0.01%
9	5.27	0.44%	0.02%	0.48%
10	5.36	0.25%	0.31%	1.55%
<i>Total</i>		60.72%	58.27%	3.06%

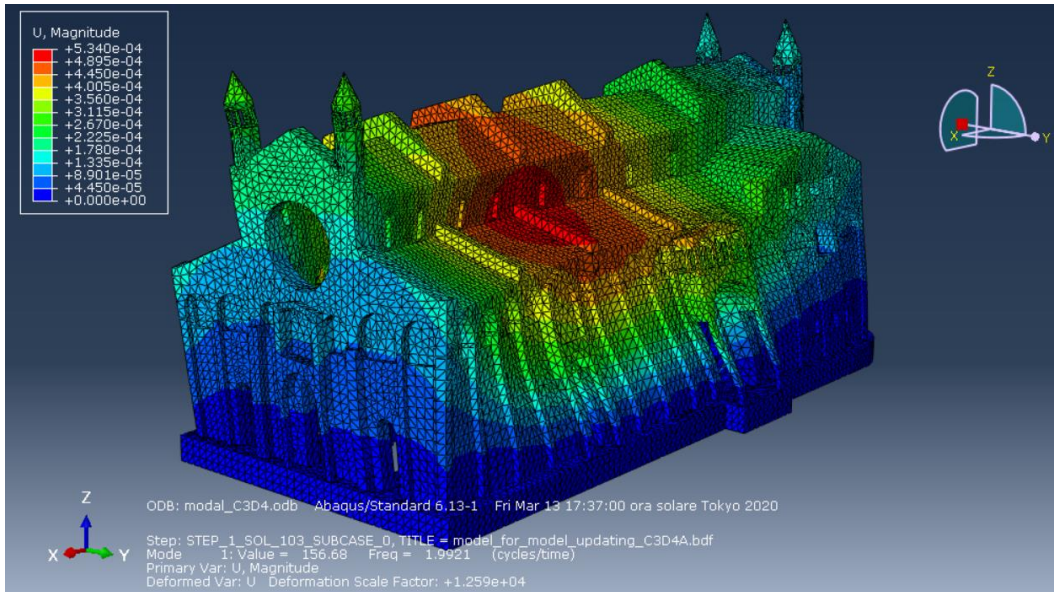


Figure 7.16 – First mode of the updated model – 4 nodes elements (1.99Hz).

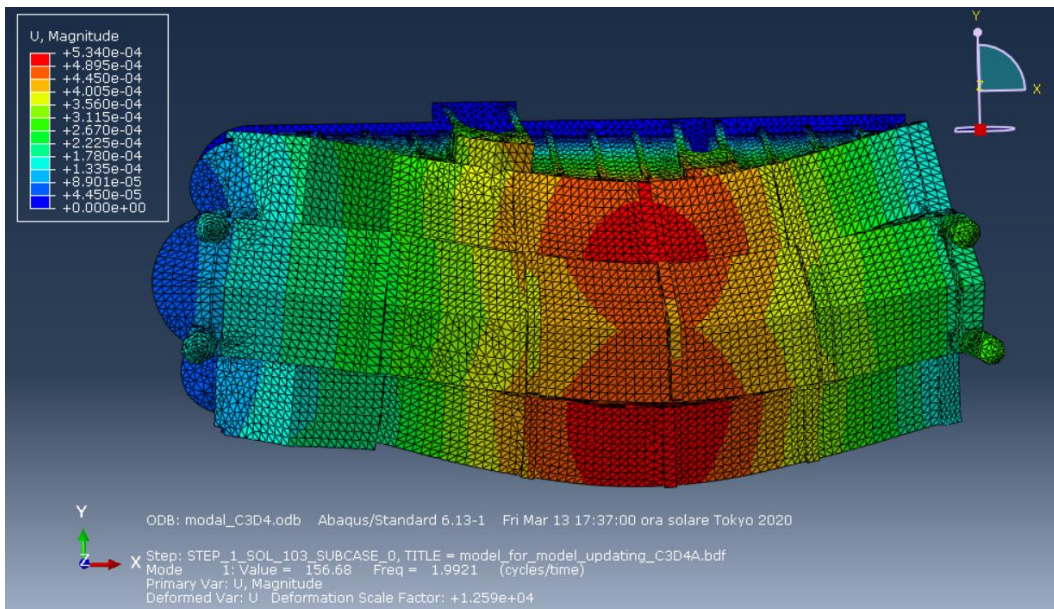


Figure 7.17 – First mode of the updated model – 4 nodes elements (1.99Hz).

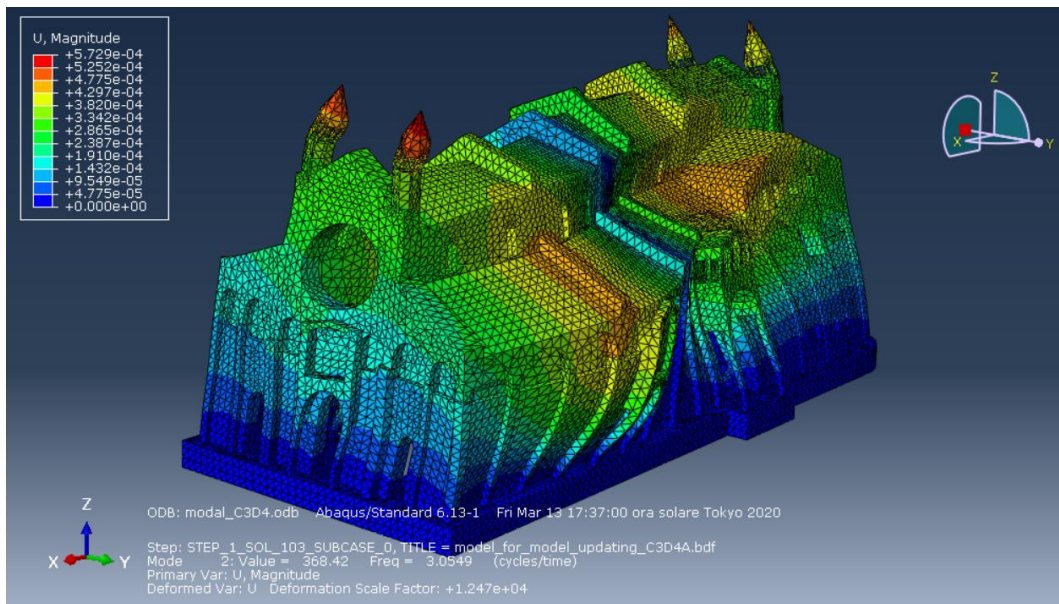


Figure 7.18 – Second mode of the updated model – 4 nodes elements (3.06Hz).

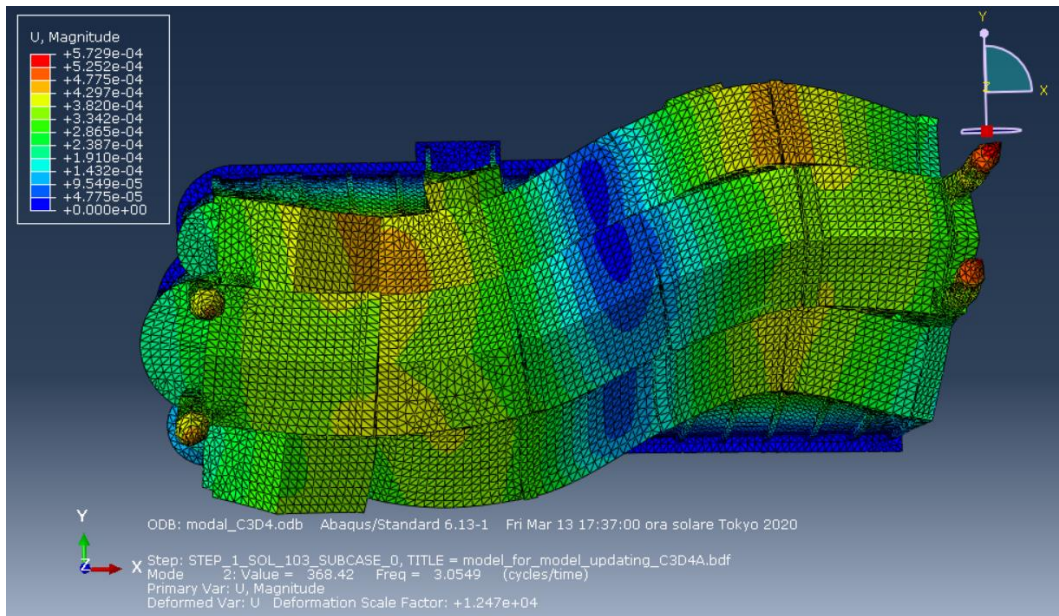


Figure 7.19 – Second mode of the updated model – 4 nodes elements (3.06Hz).

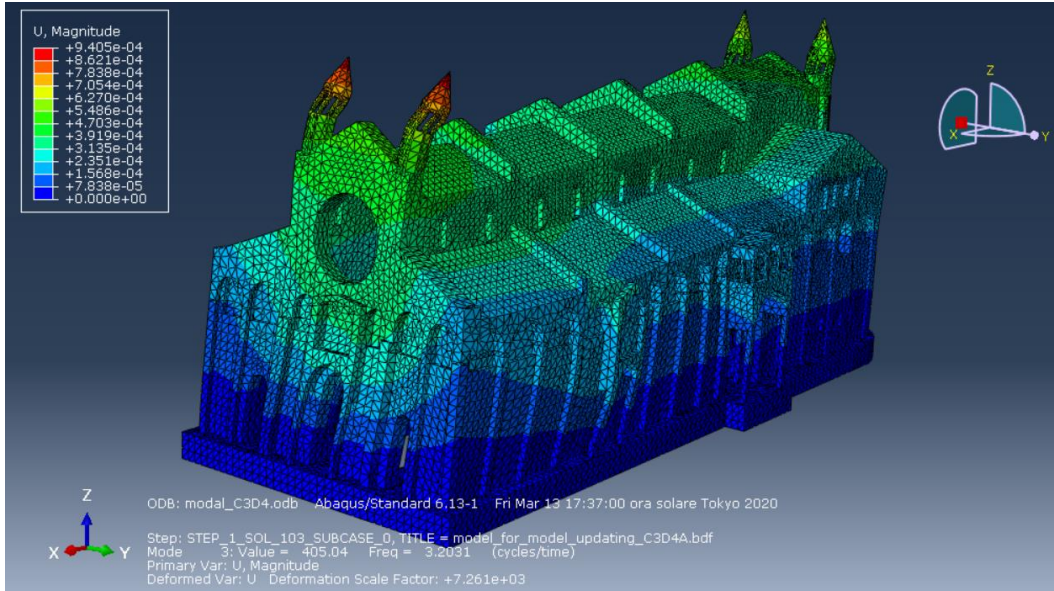


Figure 7.20 – Third mode of the updated model – 4 nodes elements (3.20Hz).

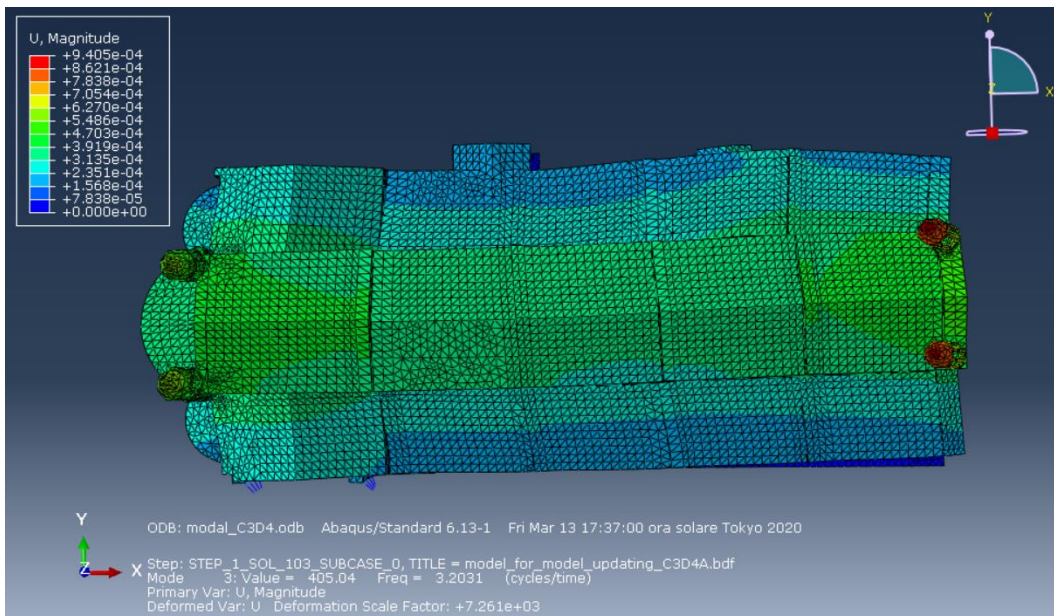


Figure 7.21 – Third mode of the updated model – 4 nodes elements (3.20Hz).

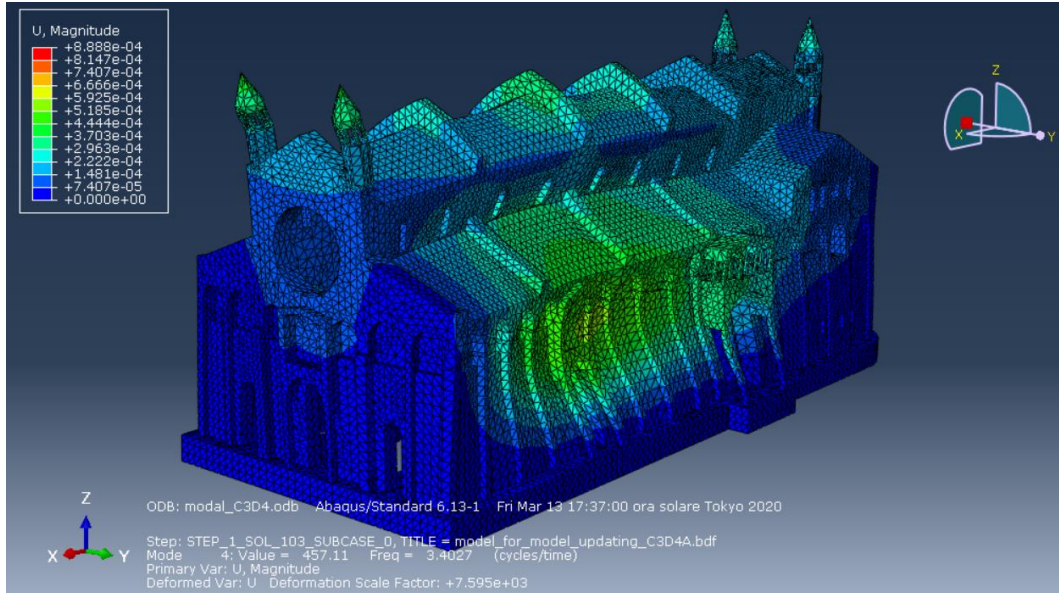


Figure 7.22 – Fourth mode of the updated model – 4 nodes elements (3.41Hz).

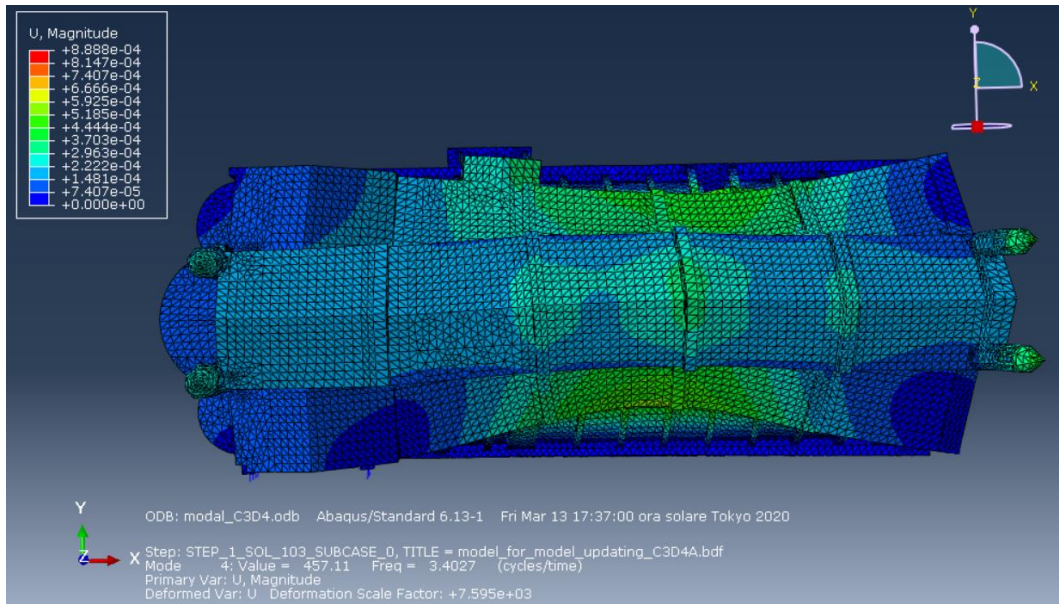


Figure 7.23 – Fourth mode of the updated model – 4 nodes elements (3.41Hz).



Chapter 8

Seismic analysis

8.1 Introduction

Once the model is calibrated, the behaviour of the structure is close to that of the real structure and therefore the structure can be analysed by carrying out some analysis. A linear dynamic analysis was carried out by applying the earthquakes to the base, in order to compare the time-history of the model with that of monitoring. Furthermore, to obtain the damaged areas and evaluate the safety of the dome, a nonlinear dynamic analysis was carried out in order to consider the non-linearity of the masonry. And then to obtain the possible damage scenario of dome 1, which was the most vulnerable in the last earthquakes that hit the structure.

8.2 Linear transient response analysis

Linear transient analysis gives the response of the model as a function of time based on a given time-dependent loading. The structural response is a superimposition of the mode shapes, which are extracted with a Modal analysis. It's important to choose the correct number of vibration mode that describe in the correct way the structural response. The modal amplitudes are integrated through time, and the response is synthesized from these modal responses [55]. This chapter will report the analysis carried out using an earthquake that occurred during the operation period of the monitoring system (2015-today), in order to compare the data. Subsequently an analysis with 2012 earthquake was reported in order to analyse the data as it was

one of the most significant earthquakes of recent years near Modena and it was also necessary for the assessment of the damage of the dome. The reference system is the same of the model, X is parallel to the long direction of the structure, Y is parallel to the short direction and finally the Z is the vertical direction.

8.2.1 Amatrice (Lazio) earthquake of 24-08-2016

- **Input data**

The main data of the earthquake examined are shown below:

Table 8-1 - Earthquake of 24-08-2016 - Main data.

Magnitude	Epicentral distance (Km)	PGA Amatrice (cm/s ²)	PGA Modena (cm/s ²)
6	282.8	850.8	2.318

The acceleration time histories in the three directions, recorded by accelerometer 1 at the base of the structure and the related pseudo acceleration spectrums are shown below:

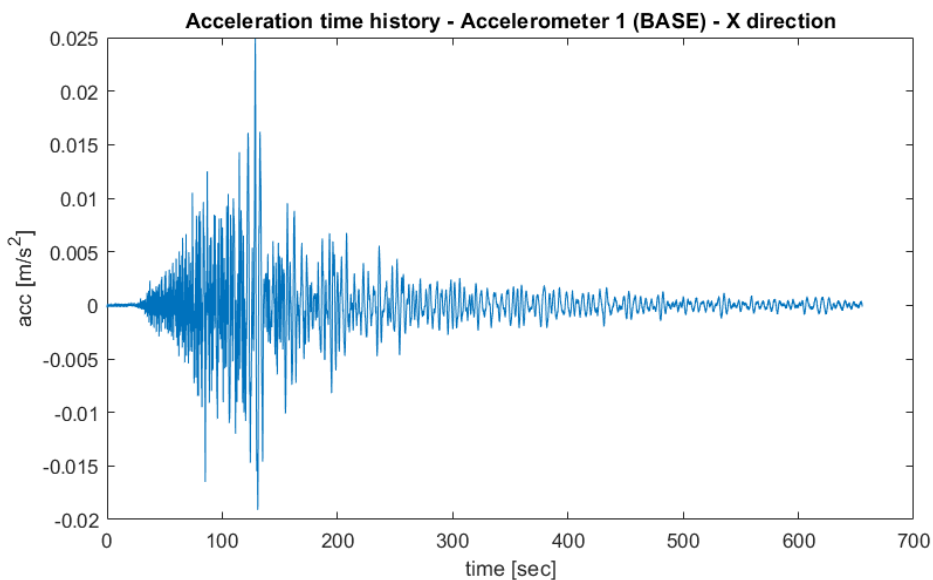


Figure 8.1 – Acceleration time history recorded during earthquake of 24-08-2016 X direction.

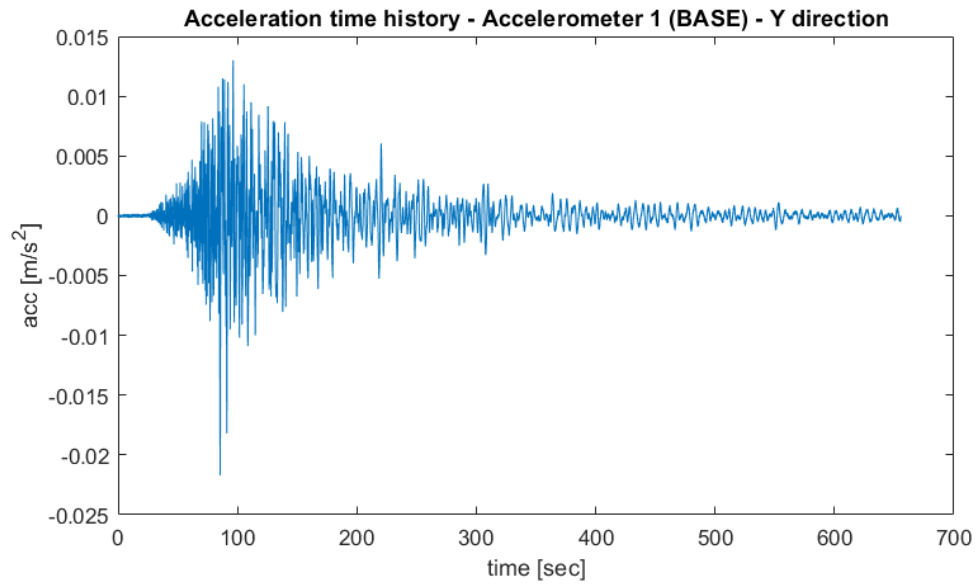


Figure 8.2 – Acceleration time history recorded during earthquake of 24-08-2016
Y direction.

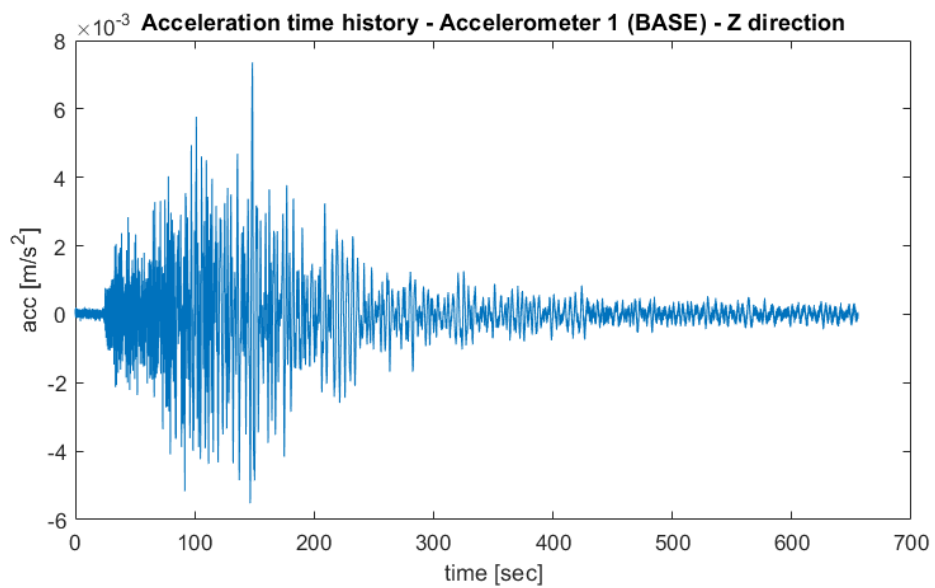


Figure 8.3 – Acceleration time history recorded during earthquake of 24-08-2016
Z direction.

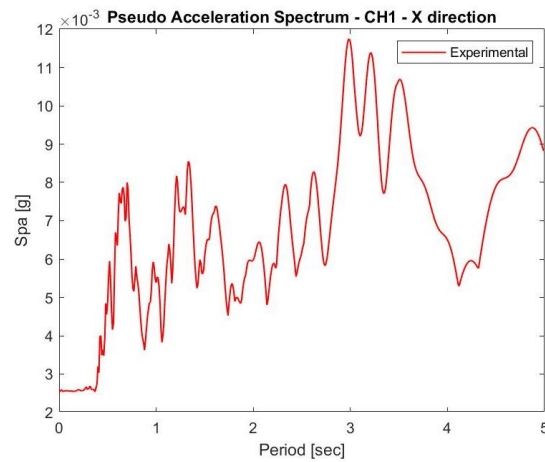


Figure 8.4 – Pseudo acceleration spectrum of the input signal – CH1-X (Base).

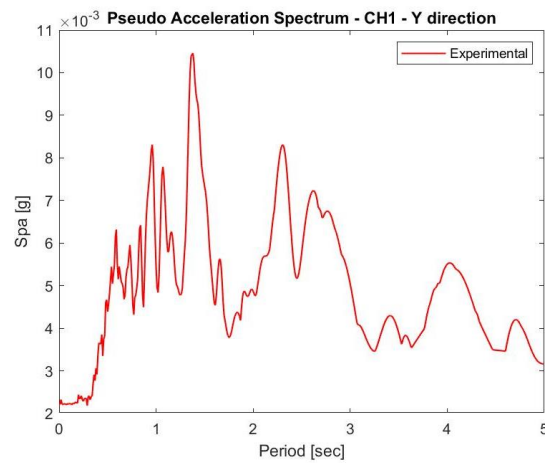


Figure 8.5 – Pseudo acceleration spectrum of the input signal – CH1-Y (Base).

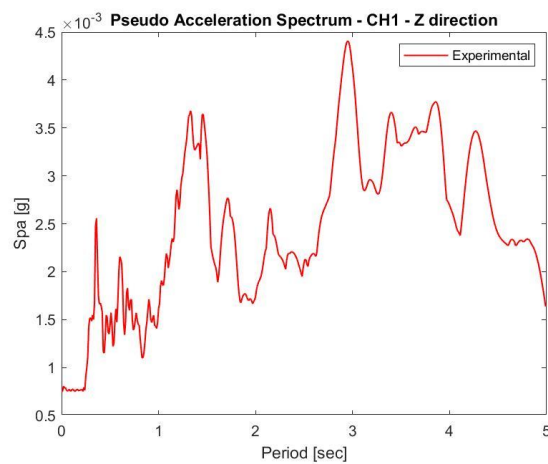


Figure 8.6 – Pseudo acceleration spectrum of the input signal – CH1-Z (Base).

- **Analysis results**

In this phase, the accelerograms measured from accelerometer 1 (Base) were applied to the base of the structure in order to compare the monitoring data with that of the numerical model. The pseudo acceleration spectrum corresponding to each accelerometer of the structure and the accelerations of the corresponding nodes of the model both initial and updated were graphed. The results of the 4-node element model are shown below comparing before, after updating models and the experimental data.

The results obtained are shown below:

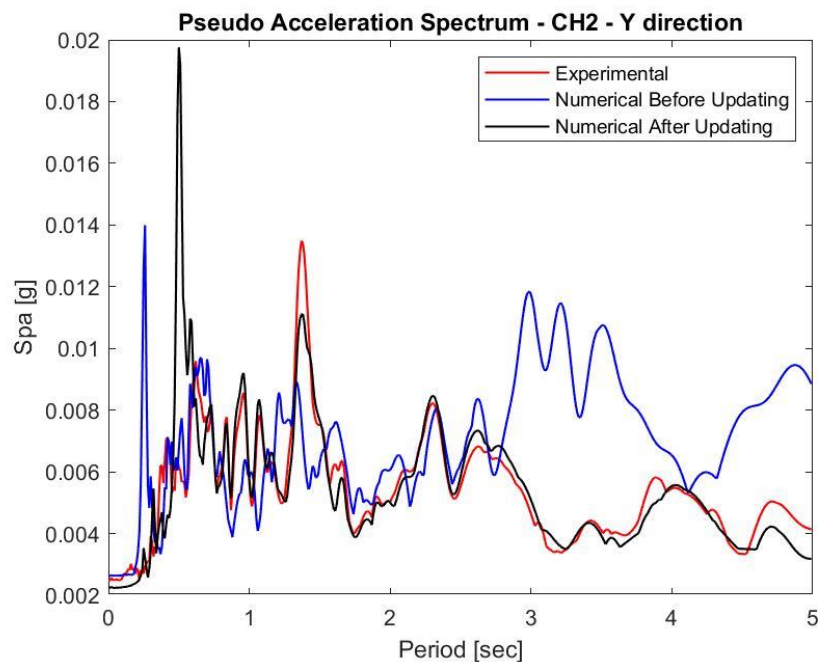


Figure 8.7 – Comparison pseudo acceleration spectrum: Experimental, Initial model and Updated model – CH2-Y.

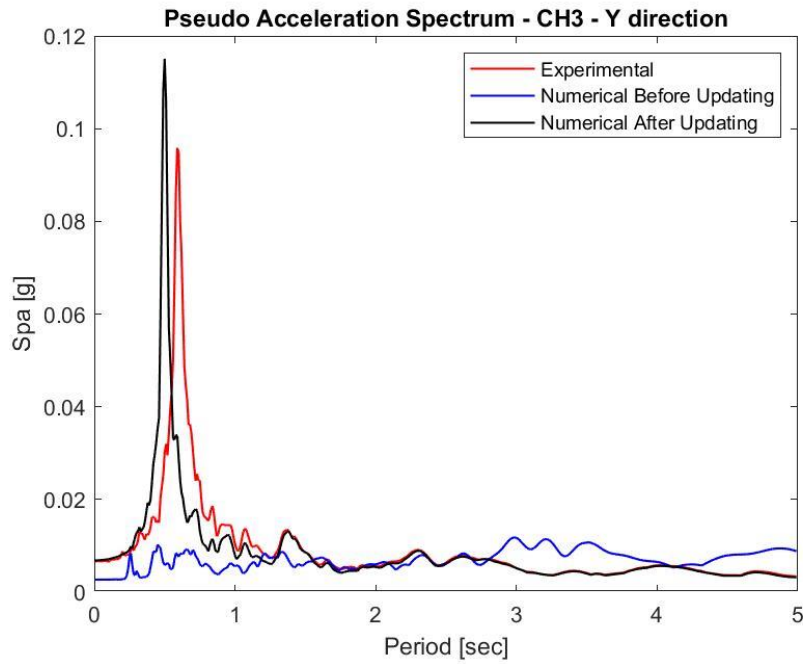


Figure 8.8 – Comparison pseudo acceleration spectrum: Experimental, Initial model and Updated model – CH3-Y.

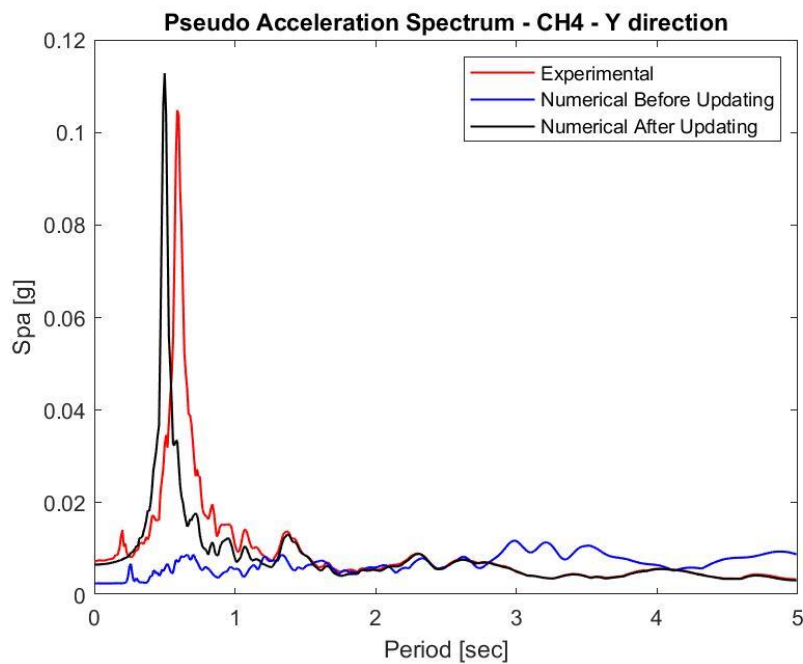


Figure 8.9 – Comparison pseudo acceleration spectrum: Experimental, Initial model and Updated model – CH4-Y.

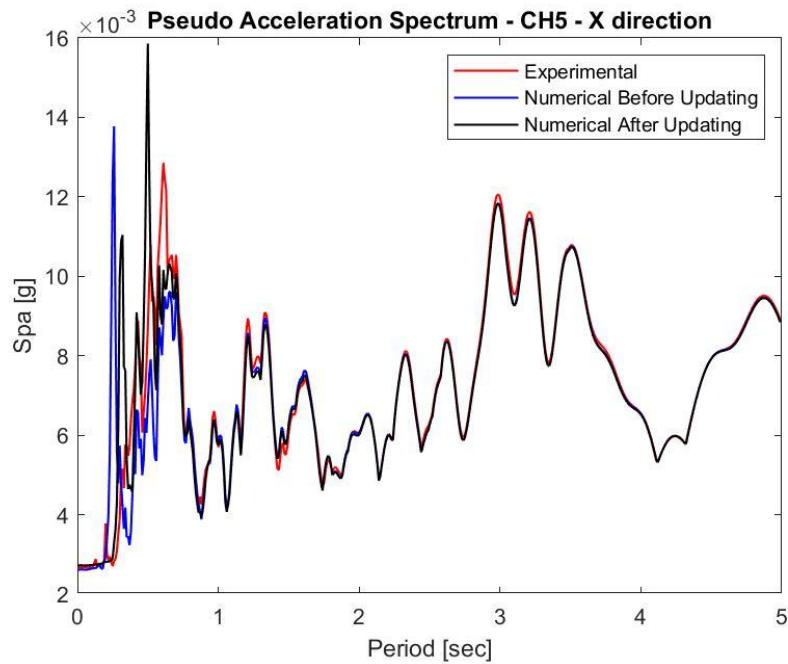


Figure 8.10 – Comparison pseudo acceleration spectrum: Experimental, Initial model and Updated model – CH5-X.

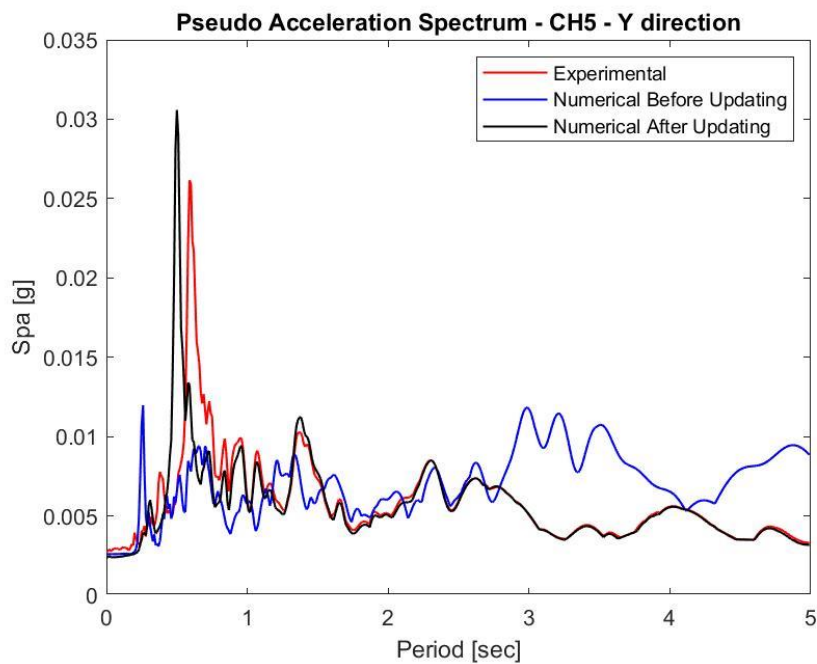


Figure 8.11 – Comparison pseudo acceleration spectrum: Experimental, Initial model and Updated model – CH5-Y.

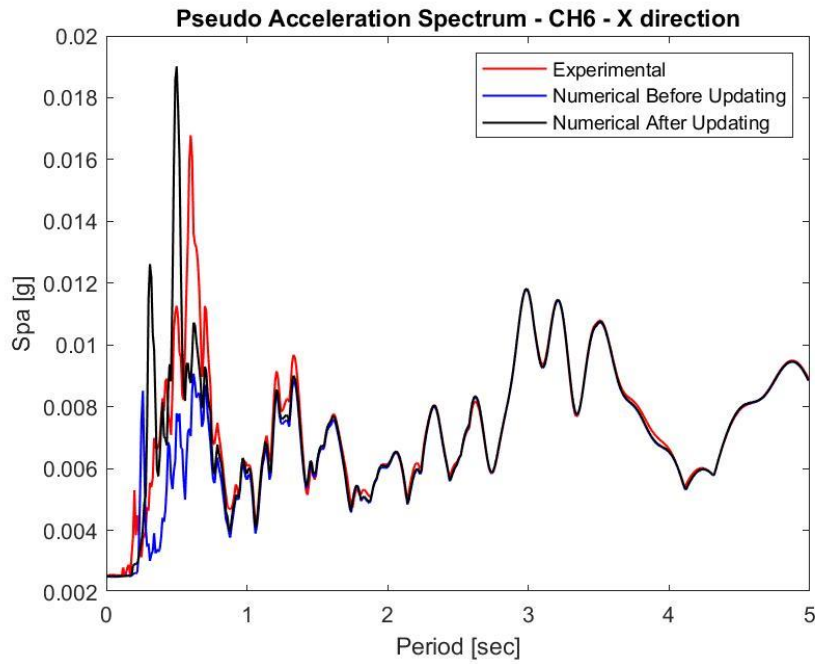


Figure 8.12 – Comparison pseudo acceleration spectrum: Experimental, Initial model and Updated model – CH6-X.

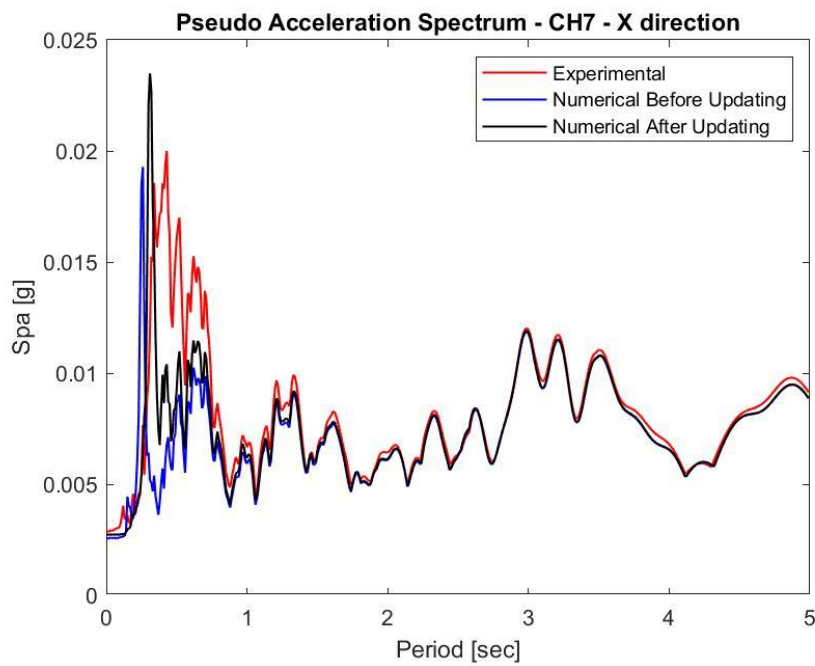


Figure 8.13 – Comparison pseudo acceleration spectrum: Experimental, Initial model and Updated model – CH7-X.

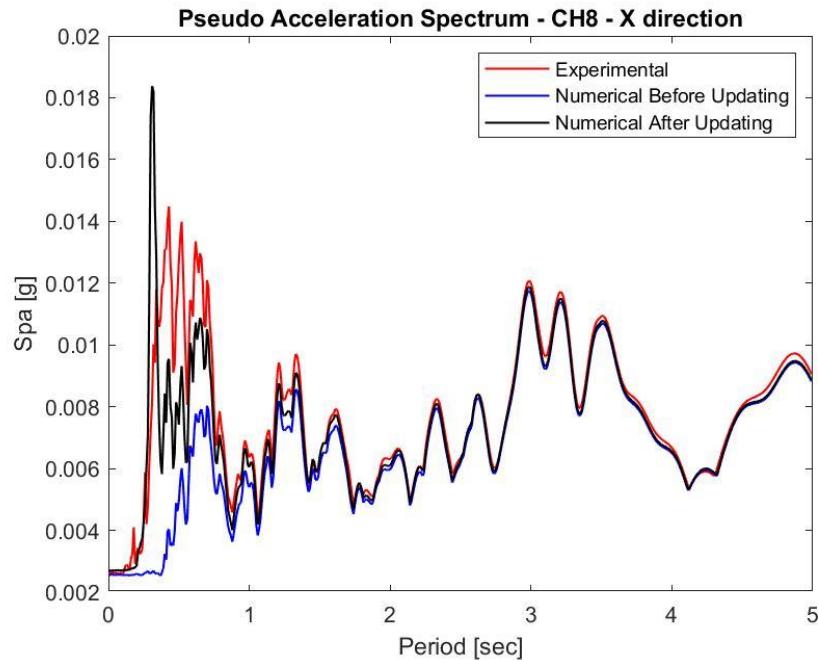


Figure 8.14 – Comparison pseudo acceleration spectrum: Experimental, Initial model and Updated model – CH8-X.

As can be seen, model updating has greatly improved the structural response by bringing it closer to the real one. The experimental and numerical response are similar and therefore the model is calibrated, and it has a response very close to the real one. This means that the model can be used for the following analysis by applying the desired earthquake to the base.

8.2.2 Finale Emilia (Emilia-Romagna) earthquake of 29-05-2012

- **Input data**

As last analysis it is carried out with an earthquake not recorded by the monitoring. The accelerograms of this event were downloaded from the *INGV Itaca* website. The main characteristics of the data acquisition station and the earthquake in question are shown below:

Table 8-2 - Main station data.

Network code	Station code	EC8 class	$V_{s,30}$ (m/s)
IV - Italian			
National Seismic Network (INSN)	MODE	C	204

Table 8-3 - Earthquake of 29-05-2012 - Main data.

Magnitude	Epicentral distance (Km)	PGA Finale Emilia (cm/s ²)	PGA Modena (cm/s ²)
5.8	25.3	441.3	42.256

The acceleration time histories in the three directions and the related pseudo acceleration spectrums are shown below:

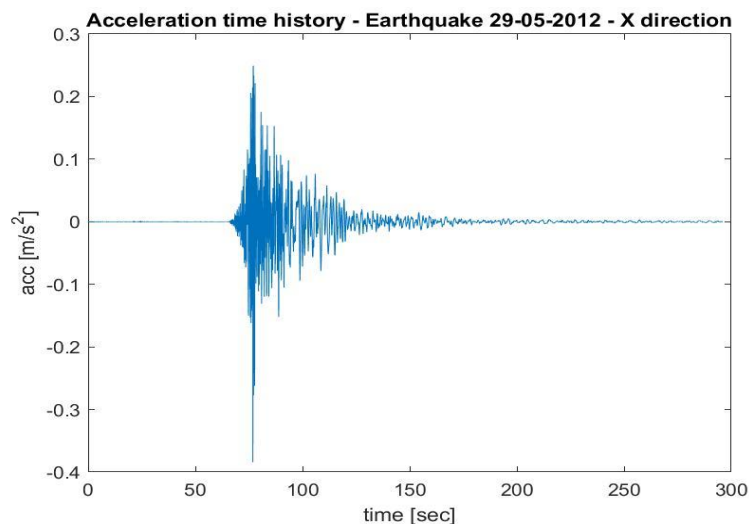


Figure 8.15 – Acceleration time history recorded during earthquake of 29-05-2012 X direction.

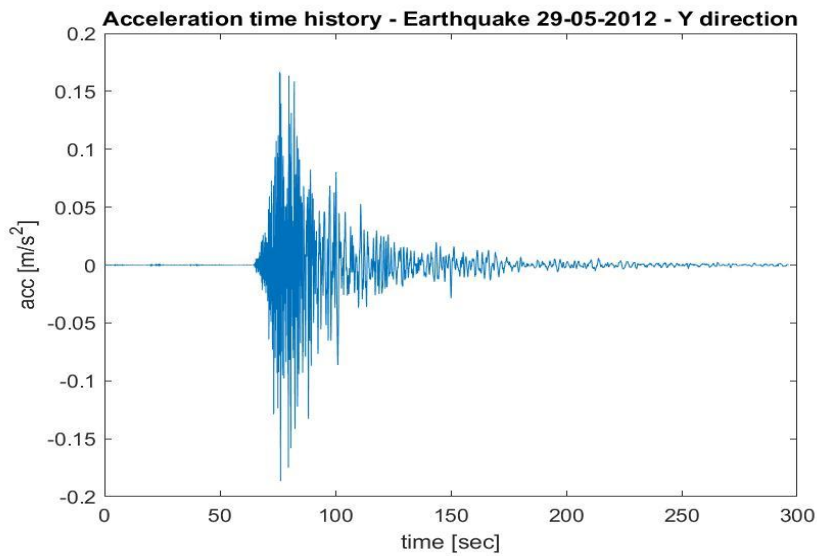


Figure 8.16 – Acceleration time history recorded during earthquake of 29-05-2012
Y direction.

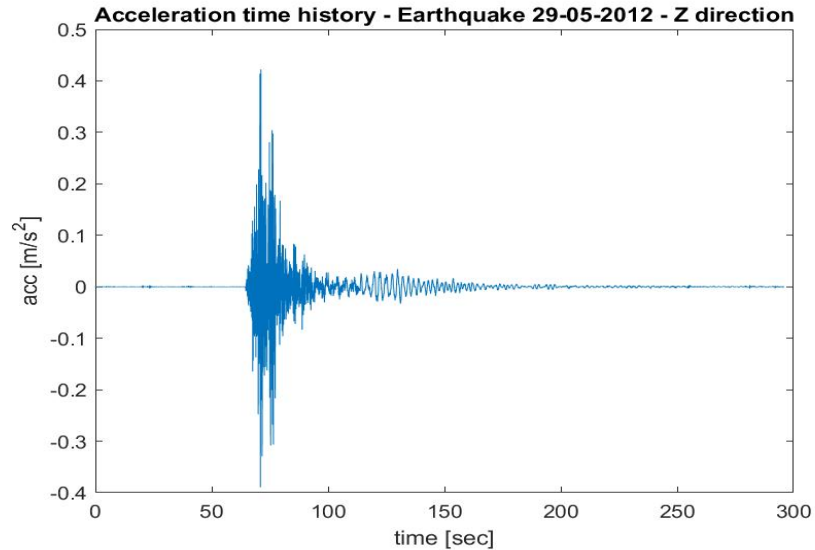


Figure 8.17 – Acceleration time history recorded during earthquake of 29-05-2012
Z direction.

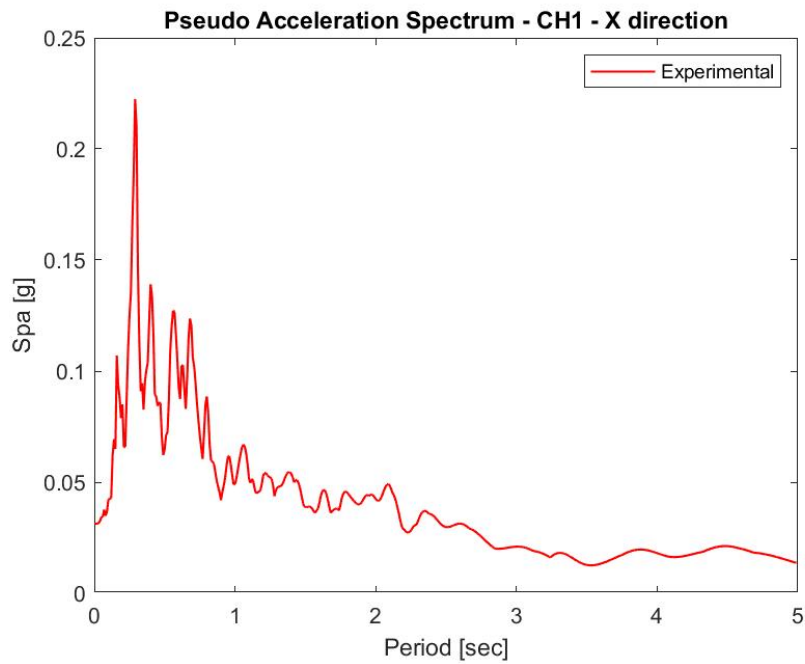


Figure 8.18 – Pseudo acceleration spectrum of the input signal – CH1-X (Base).

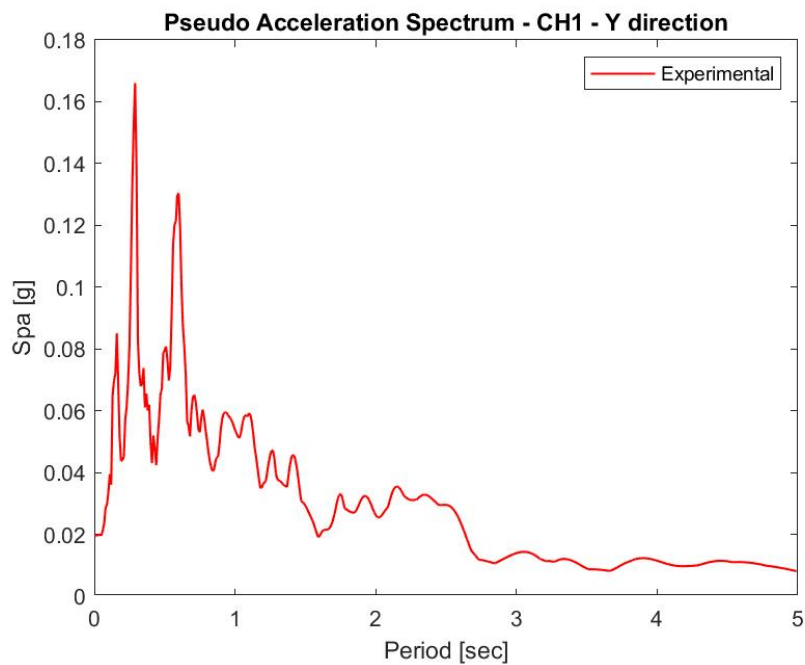


Figure 8.19 – Pseudo acceleration spectrum of the input signal – CH1-Y (Base).

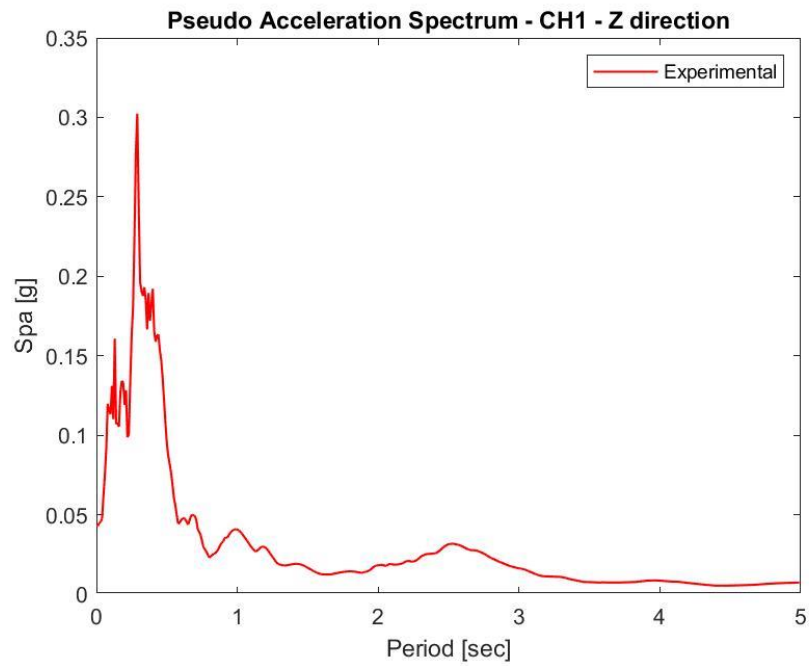


Figure 8.20 – Pseudo acceleration spectrum of the input signal – CH1-Z (Base).

- **Analysis results**

By carrying out a transient linear analysis on the global structure, the pseudo acceleration spectrums concerning to the accelerograms in correspondence of the accelerometers were plotted. Since the structure has a response very close to the real one, the amplifications of the input were obtained in some parts of the structure (*Table 8-4*). Furthermore, this analysis was necessary to derive the input data at the base of dome 1 necessary for the realization of the nonlinear dynamic analysis of *Chapter 8.3* to obtain the damage scenarios of the dome.

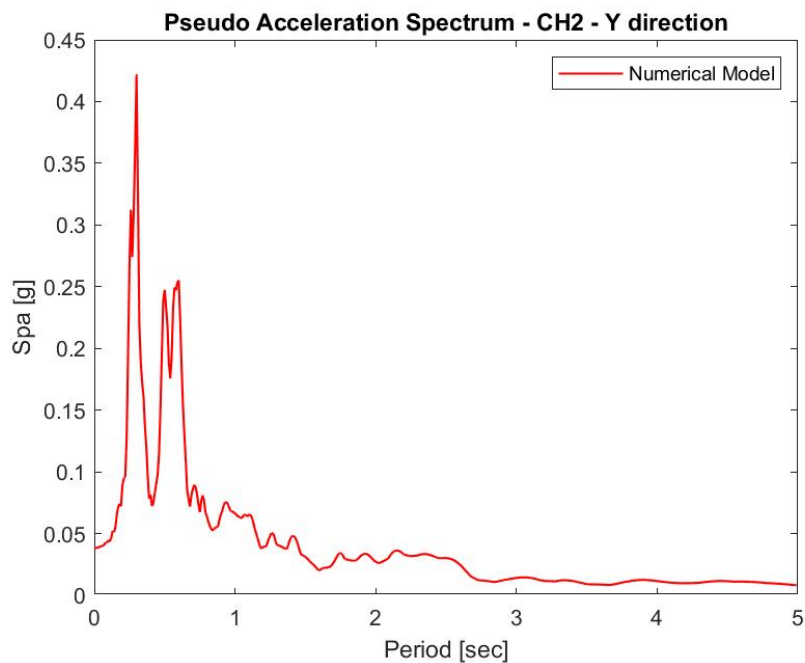


Figure 8.21 – Pseudo acceleration spectrum – Numerical model – CH2-Y.

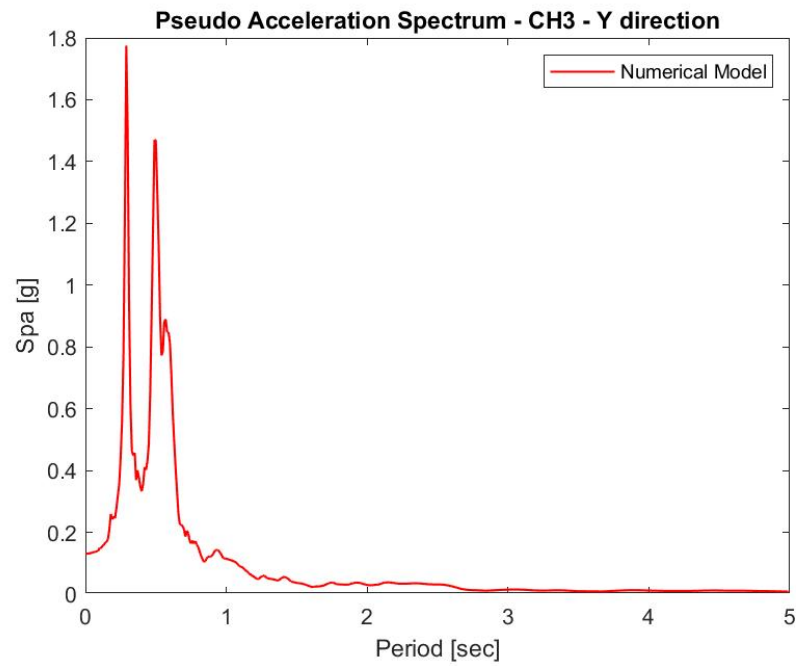


Figure 8.22 – Pseudo acceleration spectrum – Numerical model – CH3-Y.

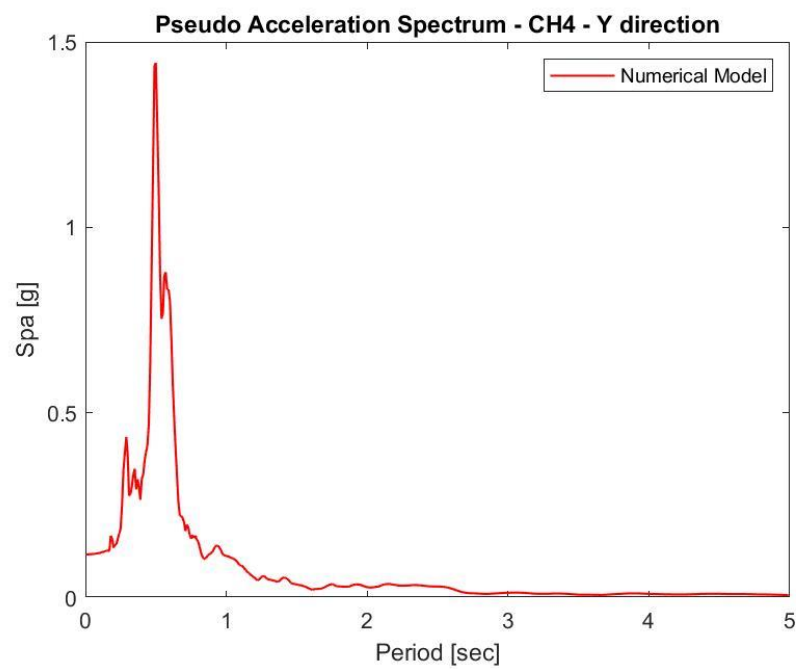


Figure 8.23 – Pseudo acceleration spectrum – Numerical model – CH4-Y.

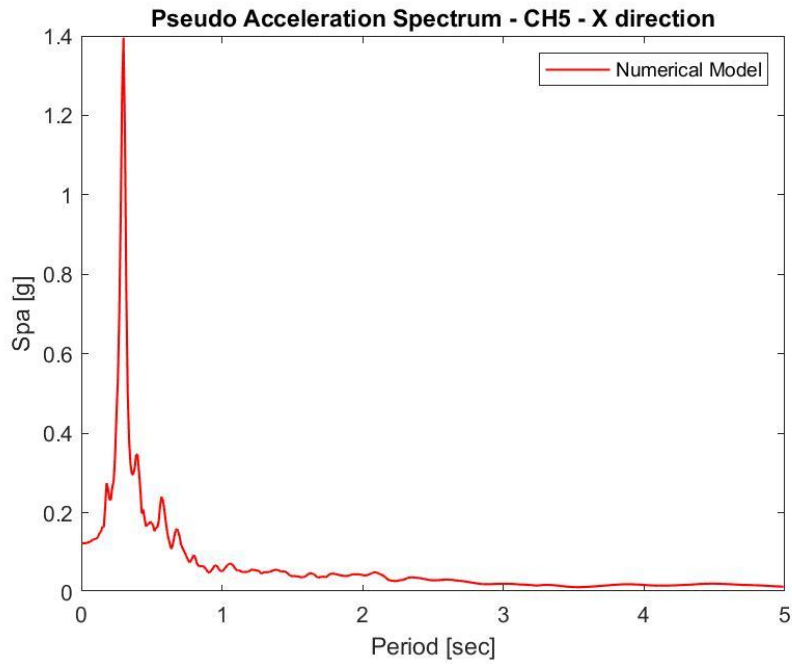


Figure 8.24 – Pseudo acceleration spectrum – Numerical model – CH5-X.

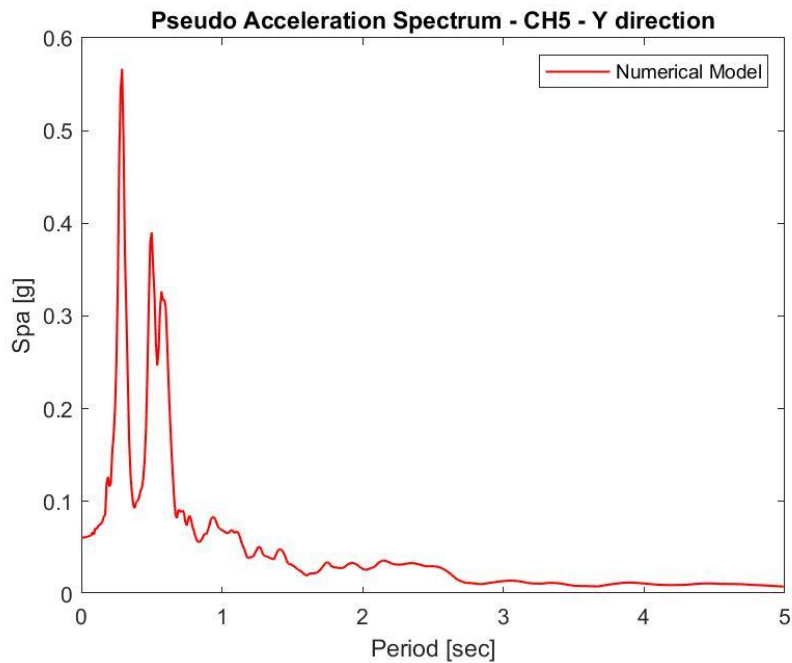


Figure 8.25 – Pseudo acceleration spectrum – Numerical model – CH5-Y.

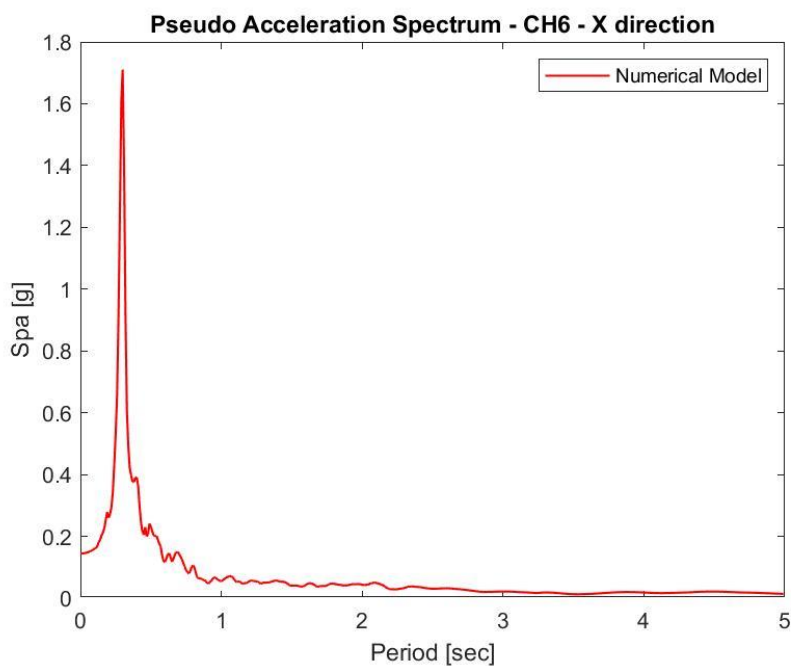


Figure 8.26 – Pseudo acceleration spectrum – Numerical model – CH6-X.

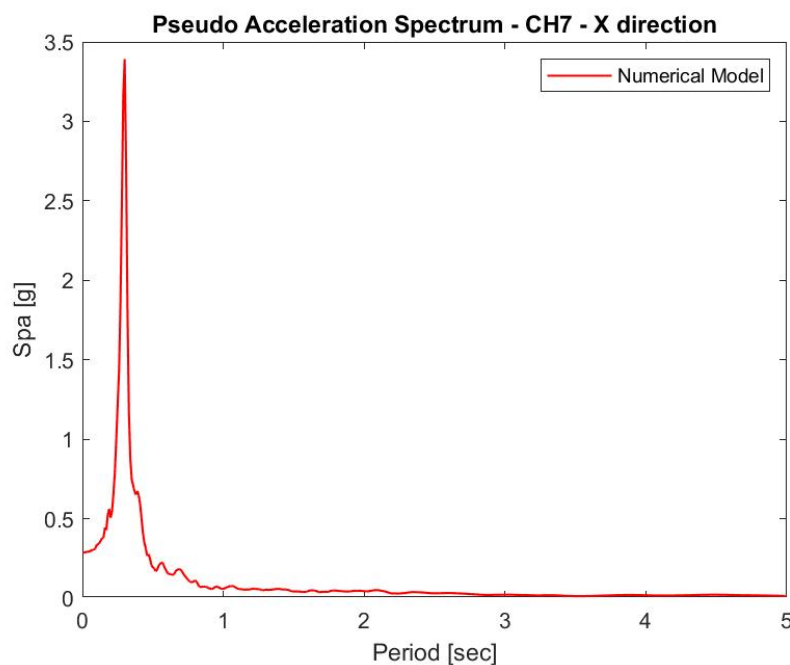


Figure 8.27 – Pseudo acceleration spectrum – Numerical model – CH7-X.

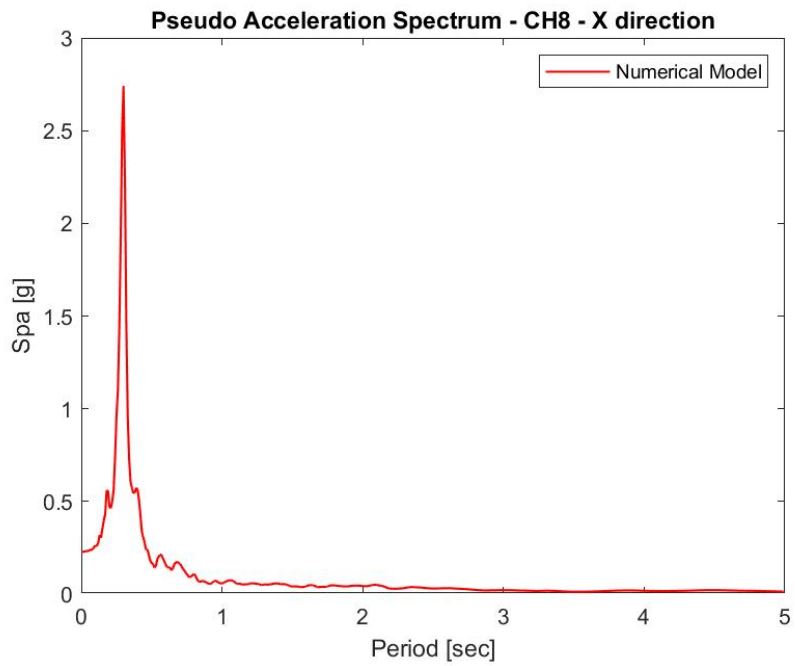


Figure 8.28 – Pseudo acceleration spectrum – Numerical model – CH8-X.

The pseudo acceleration spectrum of the acceleration time histories at the base of the dome are shown below in comparison with the input at the base of the structure, refer to the *Figure 8.29* to find the position of the output obtained.

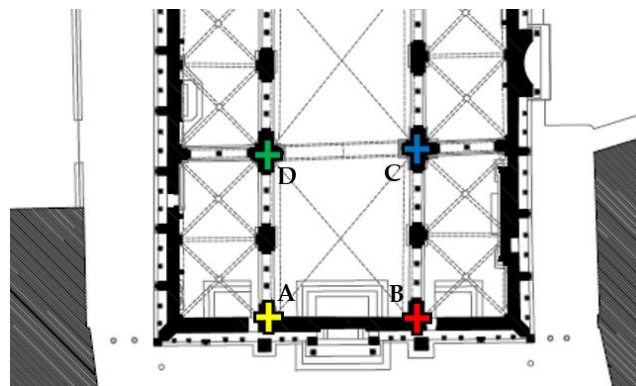


Figure 8.29 - Points of application of the time histories at the base of the dome.

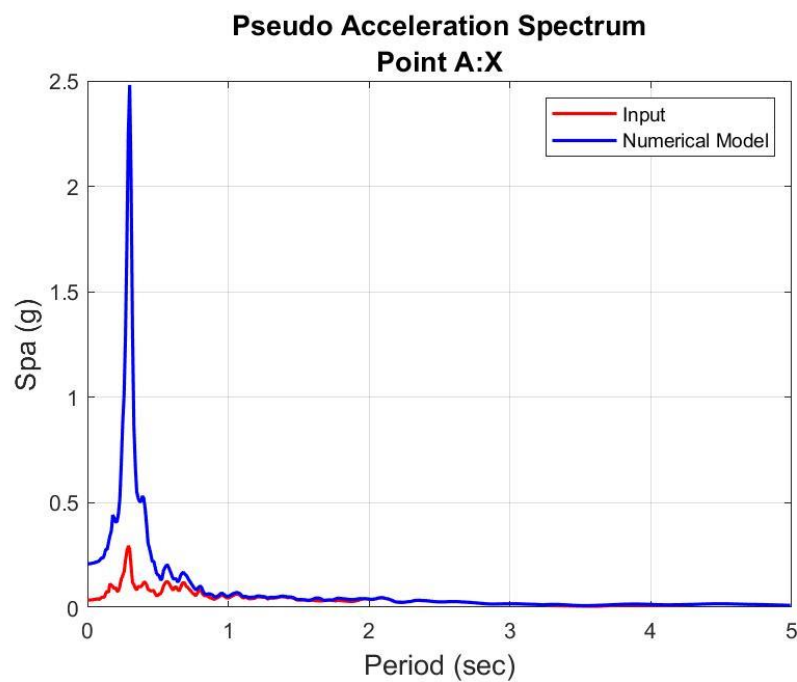


Figure 8.30 – Comparison pseudo acceleration spectrum: Input X and numerical PointA-X output.

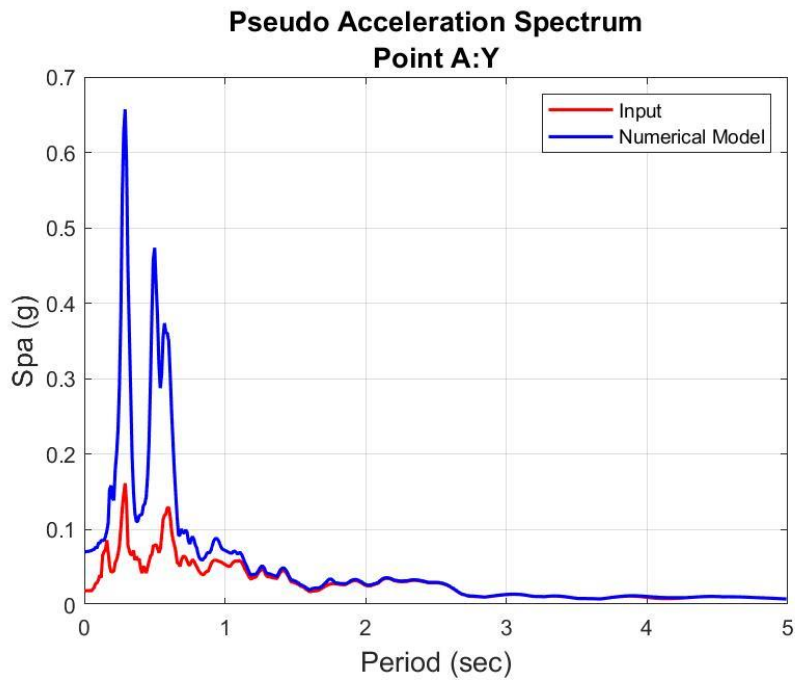


Figure 8.31 – Comparison pseudo acceleration spectrum: Input Y and numerical Point A-Y output.

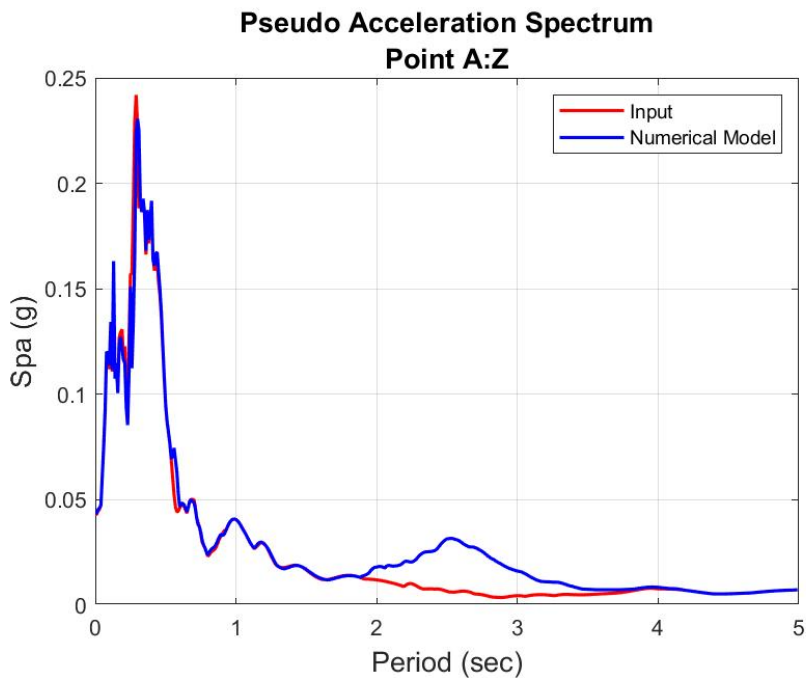


Figure 8.32 – Comparison pseudo acceleration spectrum: Input Z and numerical Point A-Z output.

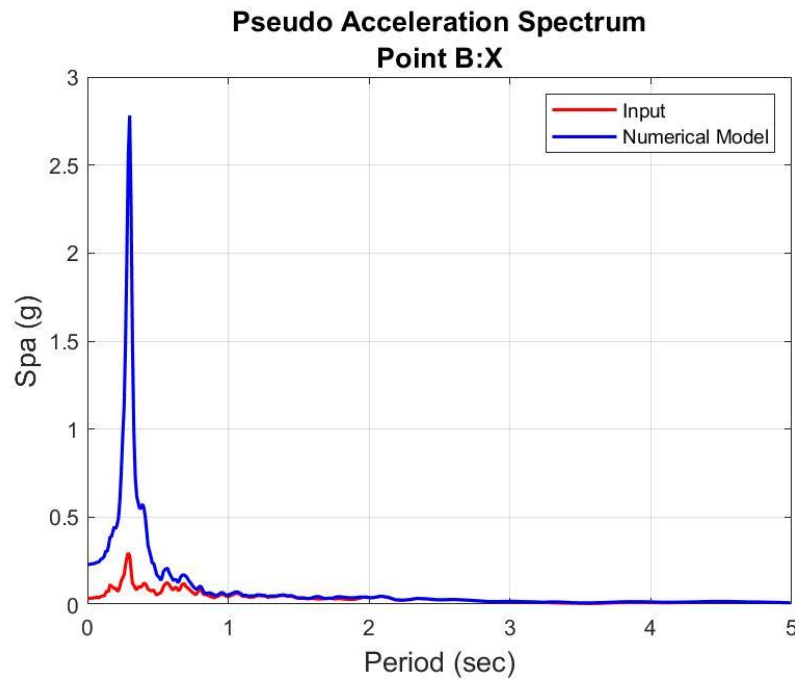


Figure 8.33 – Comparison pseudo acceleration spectrum: Input X and numerical Point B-X output.

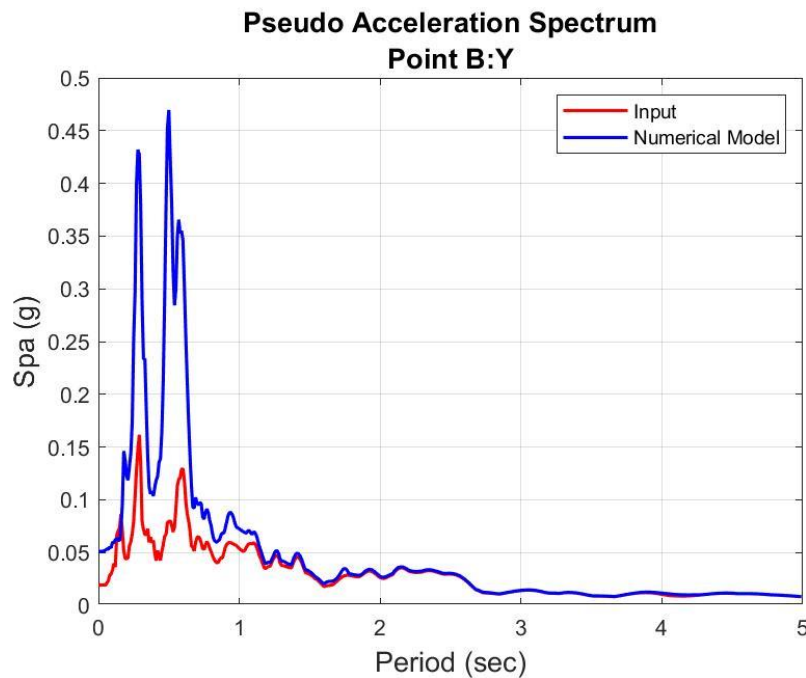


Figure 8.34 – Comparison pseudo acceleration spectrum: Input Y and numerical Point B-Y output.

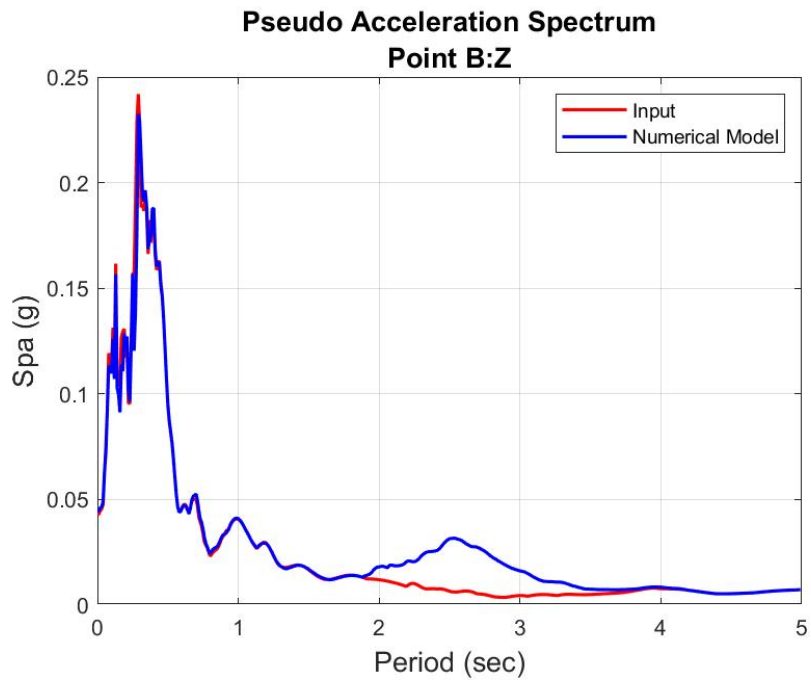


Figure 8.35 – Comparison pseudo acceleration spectrum: Input Z and numerical Point B-Z output.

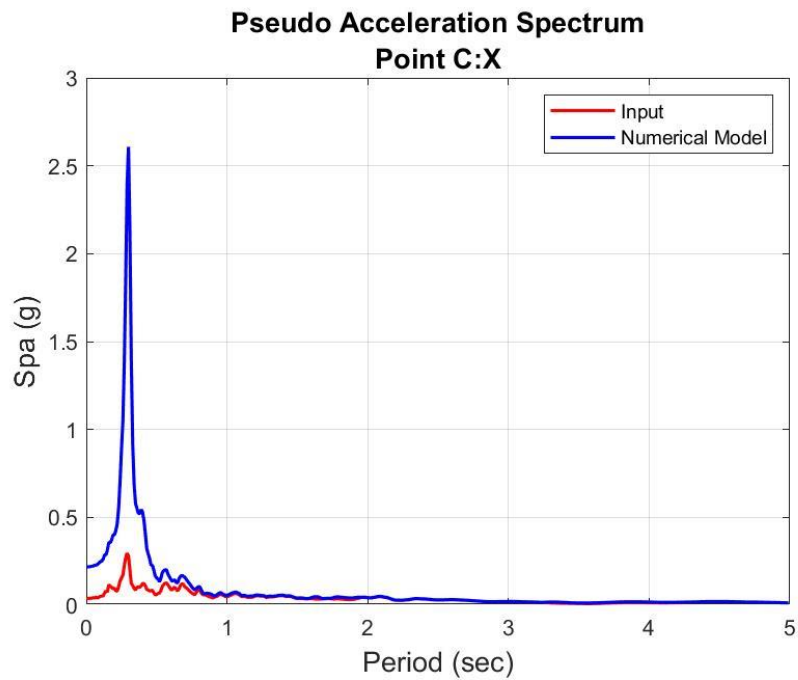


Figure 8.36 – Comparison pseudo acceleration spectrum: Input X and numerical Point C-X output.

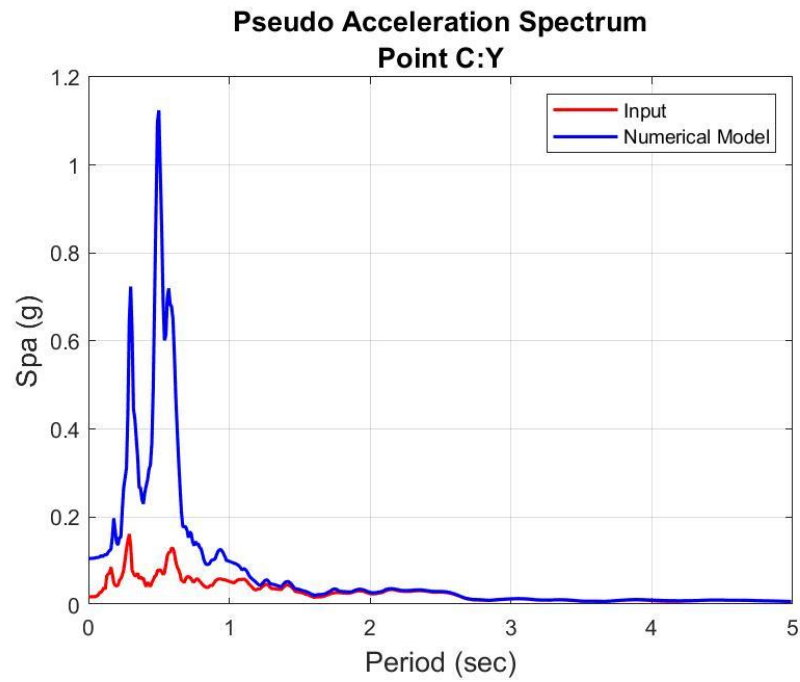


Figure 8.37 – Comparison pseudo acceleration spectrum: Input Y and numerical Point C-Y output.

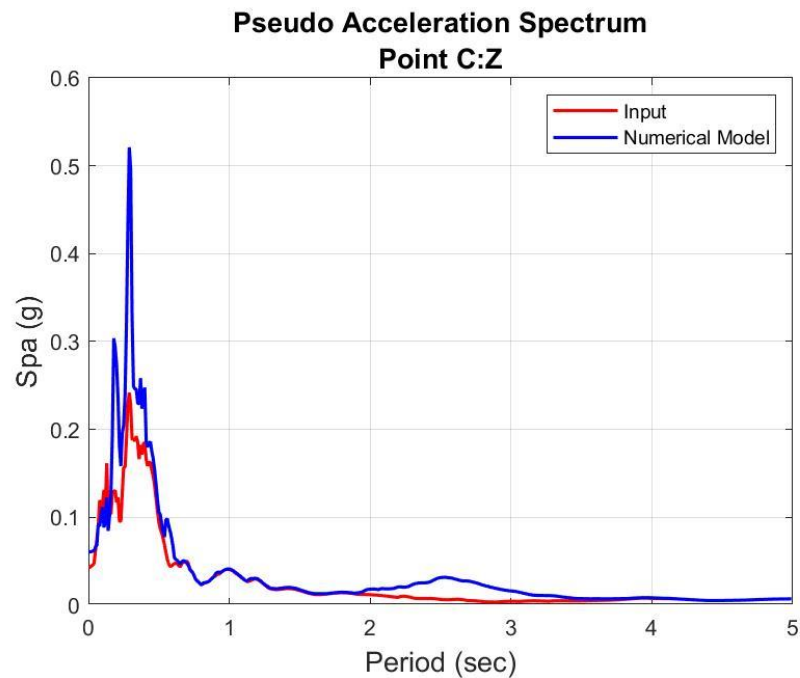


Figure 8.38 – Comparison pseudo acceleration spectrum: Input Z and numerical Point C-Z output.

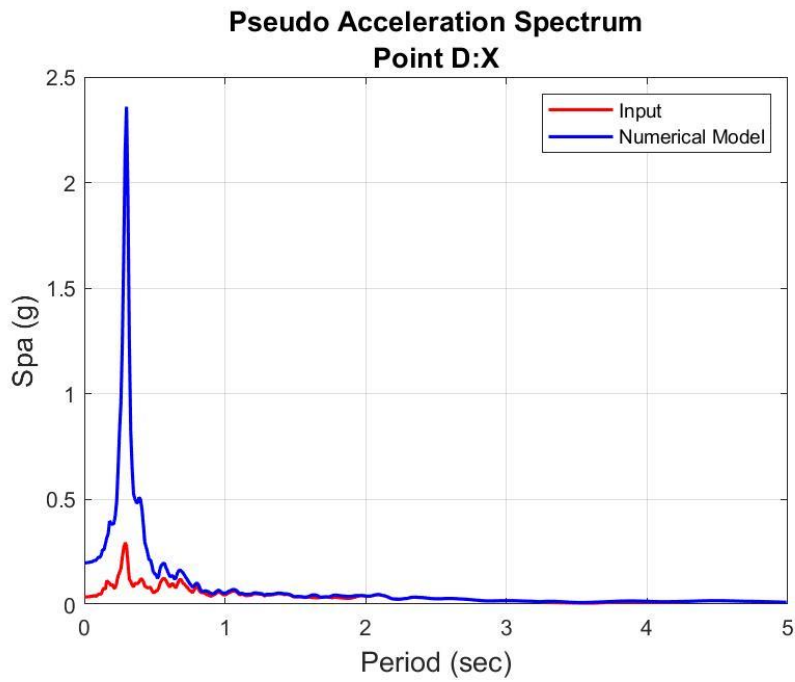


Figure 8.39 – Comparison pseudo acceleration spectrum: Input X and numerical Point D-X output.

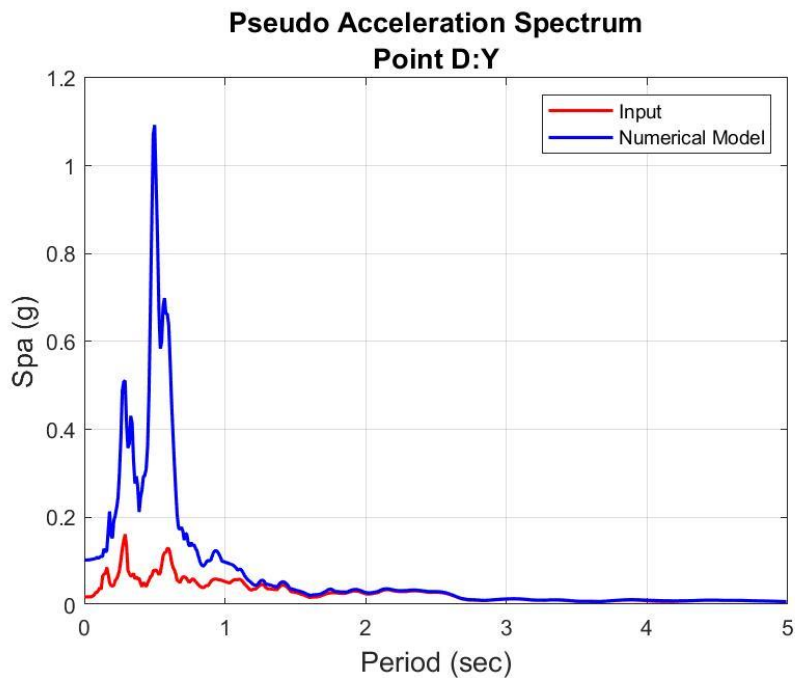


Figure 8.40 – Comparison pseudo acceleration spectrum: Input Y and numerical Point D-Y output.

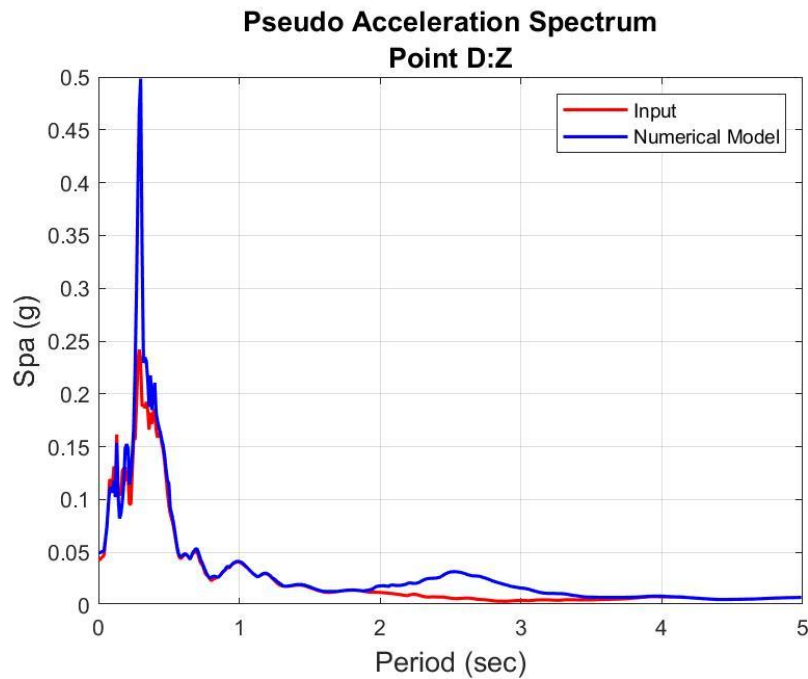


Figure 8.41 – Comparison pseudo acceleration spectrum: Input Z and numerical Point D-Z output.

By analysing the time histories of accelerations obtained from the analysis, the amplifications of the response were extrapolated. These amplifications are due to the structure that acts as a filter for the seismic input signal. The signal amplifications are listed in the *Table 8-4* and shown in the follow figures:

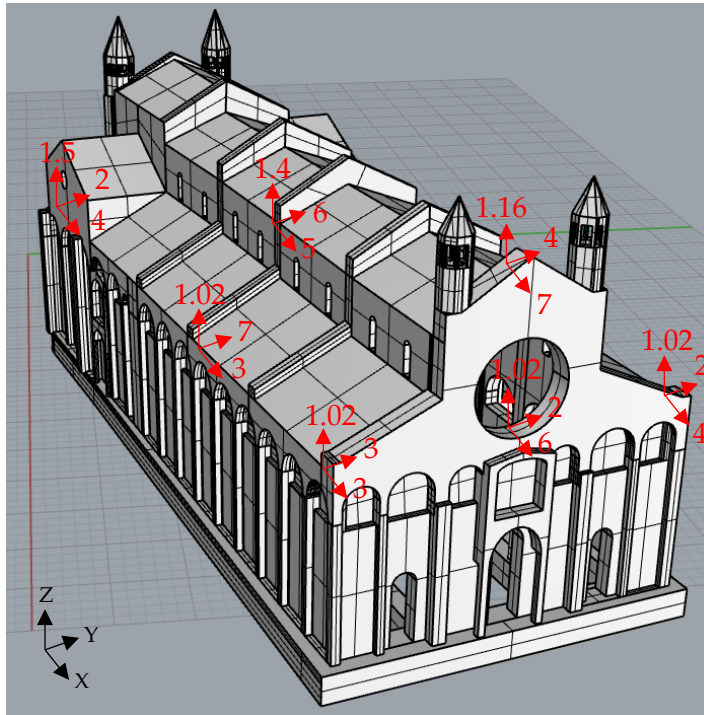


Figure 8.42 – Amplifications on the structure at the accelerometers.

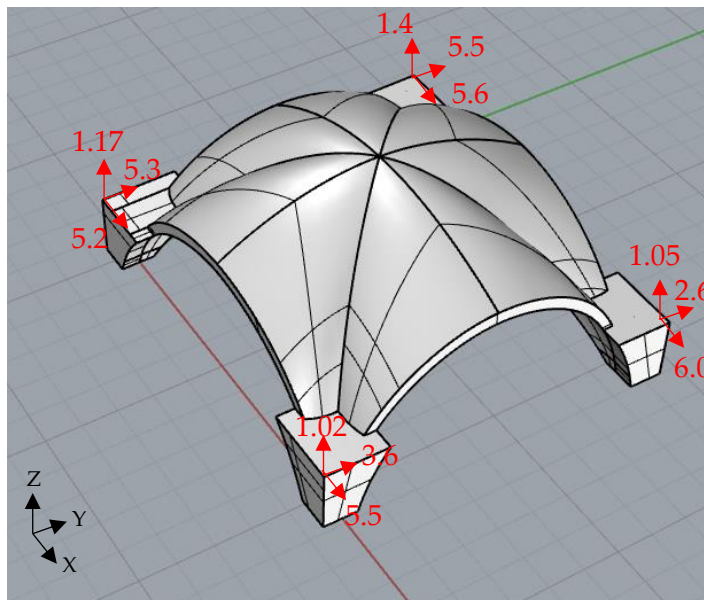


Figure 8.43 – Amplifications at the base of the dome..



Table 8-4 – Amplification of the input acceleration.

	<i>Position</i>	<i>PGA input</i> (m/s ²)	<i>Acc. output</i> (m/s ²)	<i>Amplification</i>
<i>Overall Structure</i>	2X	0.38	1.42	3.74
	2Y	0.19	0.38	2.00
	2Z	0.42	0.62	1.48
	3X	0.38	1.13	2.97
	3Y	0.19	1.28	6.74
	3Z	0.42	0.43	1.02
	4X	0.38	1.99	5.24
	4Y	0.19	1.16	6.11
	4Z	0.42	0.58	1.38
	5X	0.38	1.2	3.16
	5Y	0.19	0.6	3.16
	5Z	0.42	0.43	1.02
	6X	0.38	1.42	3.74
	6Y	0.19	0.41	2.16
	6Z	0.42	0.43	1.02
	7X	0.38	2.82	7.42
	7Y	0.19	0.77	4.05
	7Z	0.42	0.45	1.16
<i>Dome</i>	8X	0.38	2.24	5.89
	8Y	0.19	0.44	2.32
	8Z	0.42	0.43	1.02
	AX	0.38	2.07	5.45
	AY	0.19	0.69	3.63
	AZ	0.42	0.43	1.02
	BX	0.38	2.27	5.97
	BY	0.19	0.5	2.63
	BZ	0.42	0.44	1.05
	CX	0.38	2.14	5.63
	CY	0.19	1.04	5.47
	CZ	0.42	0.6	1.43
DX	0.38	1.96	5.16	
DY	0.19	1.01	5.32	
DZ	0.42	0.49	1.17	

8.3 Non-linear dynamic analysis - Dome

This section reports the nonlinear dynamic analysis carried out on dome 1, the most vulnerable, to obtain the damage scenarios under the action of the earthquake. In this case the time histories at the base of the connection of the dome with the structure were obtained by means of linear dynamic analysis on the global structure. In this way the seismic input is filtered by the structure and it was possible to apply these time histories directly to the base of the dome without analysing the overall structure. Thus, avoiding analysis with very high computational burden but still obtaining reliable results. The time histories at the base were then increased by multiplying in such a way as to bring the dome to collapse, obtaining the damage scenarios. And then, it was possible to compare the damage that occurred with the earthquake of Finale Emilia in May 2012 with the results of the model created.

8.3.1 Input data

For the simulation of the damage to the dome, a linear transient analysis was performed on the overall structure. By applying the accelerograms of the 2012 earthquake to the base of the structure, the acceleration time histories were obtained at the bases connecting the dome with the wall (*Figure 8.44*). The input acceleration time histories applied simultaneous to the base of the dome are shown below:

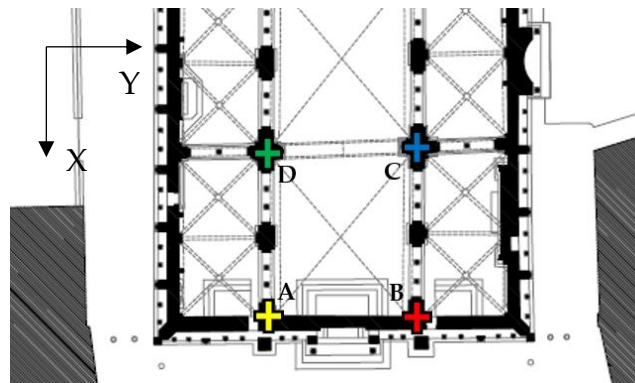


Figure 8.44 - Points of application of the time histories at the base of the dome.

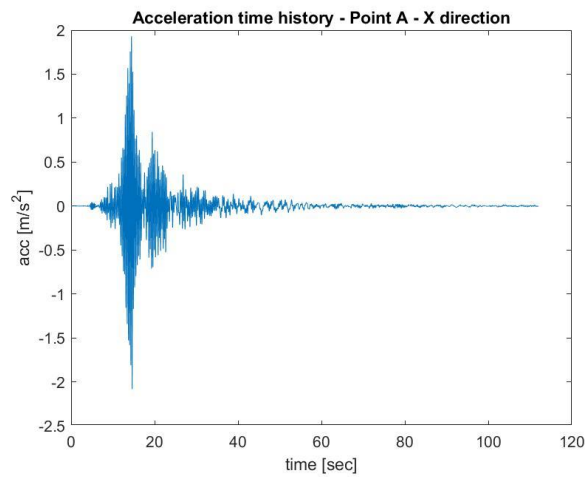


Figure 8.45 – Acceleration time history: 2012 earthquake - point A - X direction.

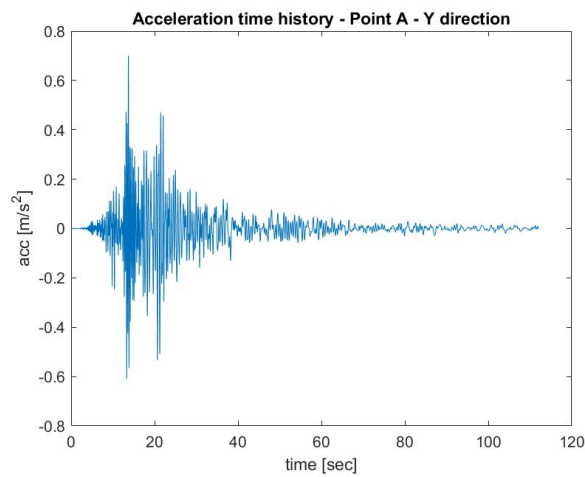


Figure 8.46 – Acceleration time history: 2012 earthquake - point A - Y direction.

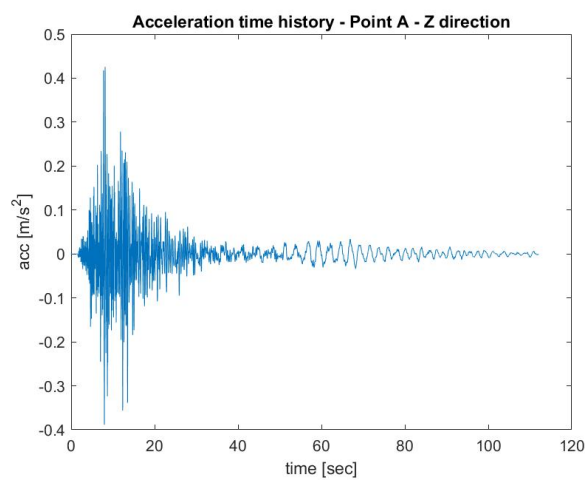


Figure 8.47 – Acceleration time history: 2012 earthquake - point A - Z direction.

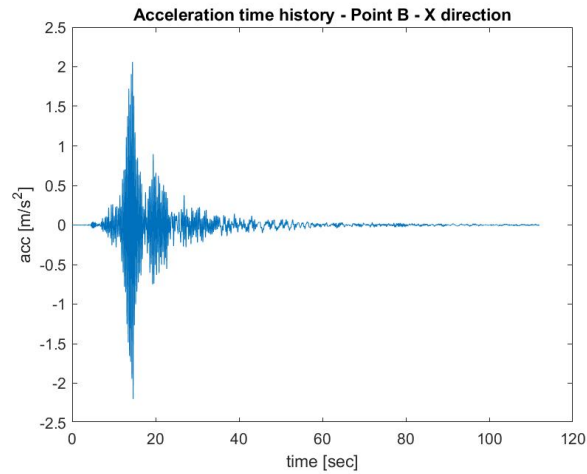


Figure 8.48 – Acceleration time history: 2012 earthquake - point B - X direction.

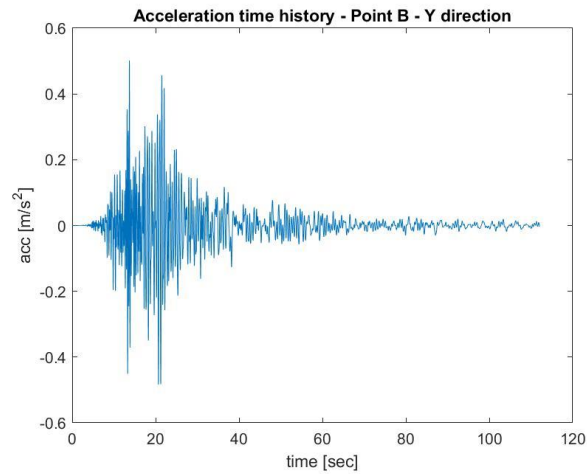


Figure 8.49 – Acceleration time history: 2012 earthquake - point B - Y direction.

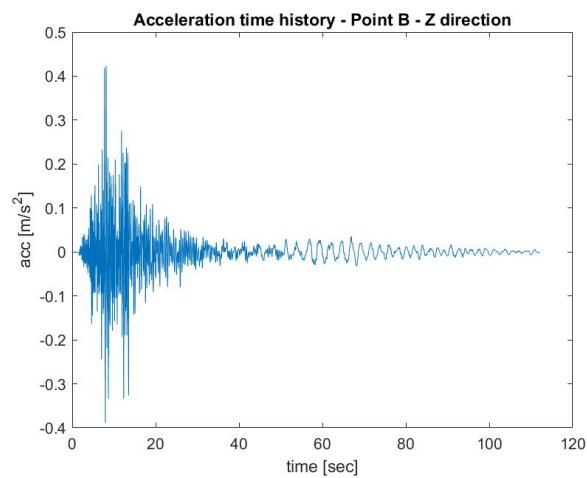


Figure 8.50 – Acceleration time history: 2012 earthquake - point B - Z direction.

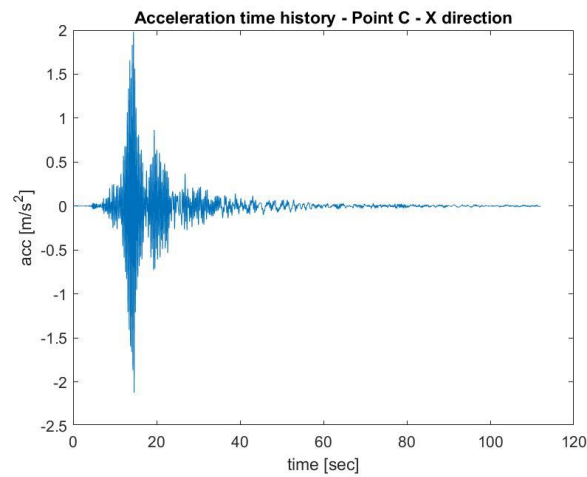


Figure 8.51 – Acceleration time history: 2012 earthquake - point C - X direction.

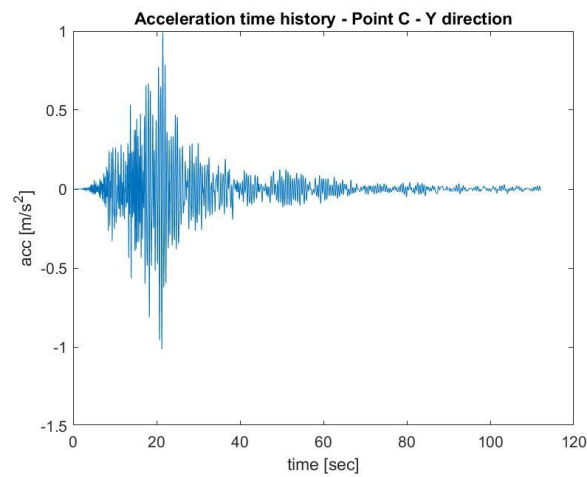


Figure 8.52 – Acceleration time history: 2012 earthquake - point C - Y direction.

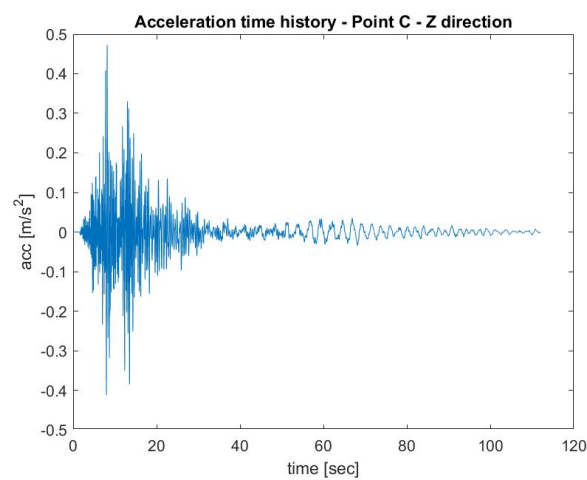


Figure 8.53 – Acceleration time history: 2012 earthquake - point C - Z direction.

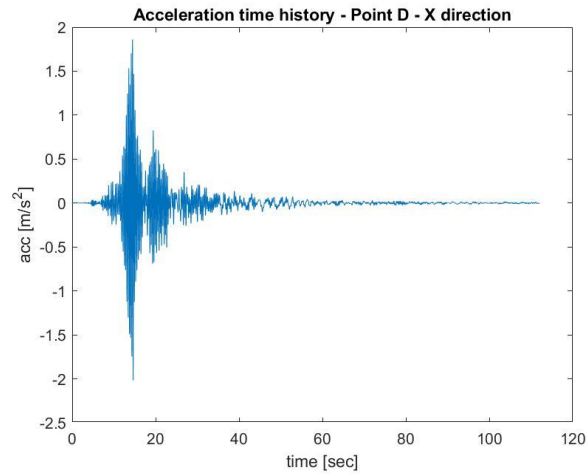


Figure 8.54 – Acceleration time history: 2012 earthquake - point D - X direction.

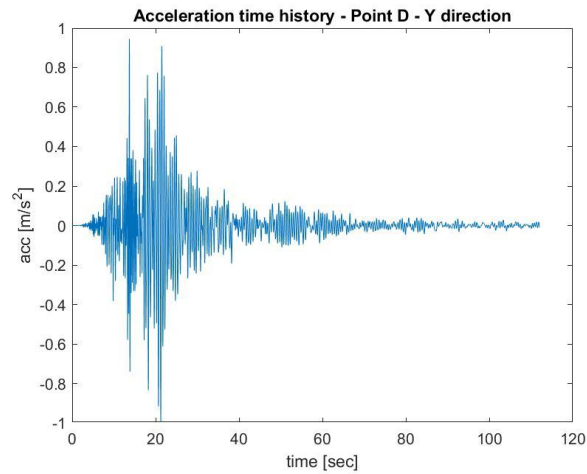


Figure 8.55 – Acceleration time history: 2012 earthquake - point D - Y direction.

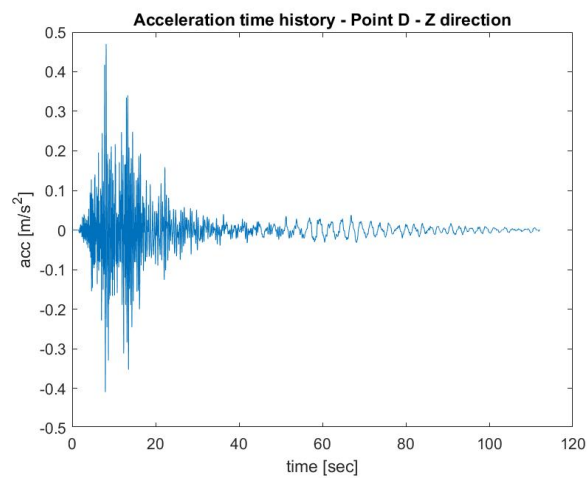


Figure 8.56 – Acceleration time history: 2012 earthquake - point D - Z direction.

8.3.2 Assumptions adopted in modelling

As for the modelling of the dome, the 10 node C3D10 elements were used because the aim of the analysis is based on the stress state and this type of elements allows a better and more precise description of it. As can be seen in *Figure 8.57*, a mesh having an average size of 0.5m was used. The main hypothesis adopted in this modelling is to consider the connection between domes and wall not effective and therefore that the connection takes place only through the support bases and the surrounding areas. The section enlargements were made in the connections at the base of the dome, these are present and have the function of simulating the connection with the walls.

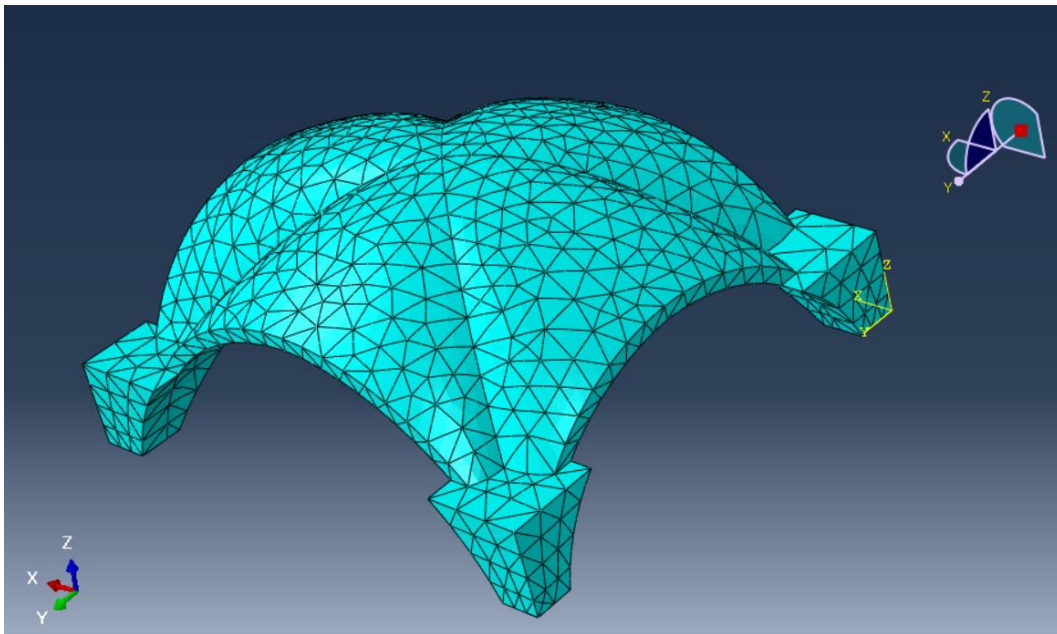


Figure 8.57 - Mesh and subdivision of the dome material.

8.3.3 Material properties

The elastic mechanical properties used in this analysis are those obtained in the model updating of the global model. The material used refer to [59] assuming that the materials is similar to that of Ghirlandina Tower, being that the two buildings were built in the same period. As regards the description of the damage, the *Concrete Damage Plasticity criterion* was used. The *Concrete Damage Plasticity criterion* is a constitutive model which simulate the cracking and crushing behaviours of concrete through softening and hardening behaviours as well as the changes in the elastic stiffness using two scalar damage parameters, namely D_t and D_c . The characteristics of the materials are shown below:

Table 8-5 – Material elastic parameter

E (MPa)	ν
2500	0.2

Table 8-6 – Material plasticity parameters

Dilatation angle	Eccentricity	f_{bol}/f_{c0}	K	Viscosity parameters
30°	0.1	1.16	0.667	0.0005

Table 8-7 – Material compressive inelastic behaviour

Yield stress (MPa)	Inelastic strain (-)
3	0
3	0.002
0.03	0.005

Table 8-8 – Material tensile cracking behaviour

Yield stress (MPa)	Cracking strain (-)
0.08	0
0.007	0.00025
0.003	0.001

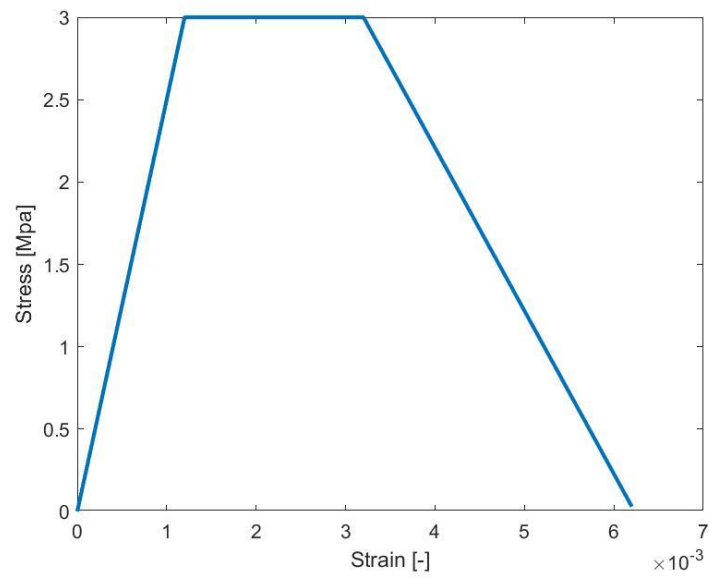


Figure 8.58 – Stress-strain compressive masonry behaviour.

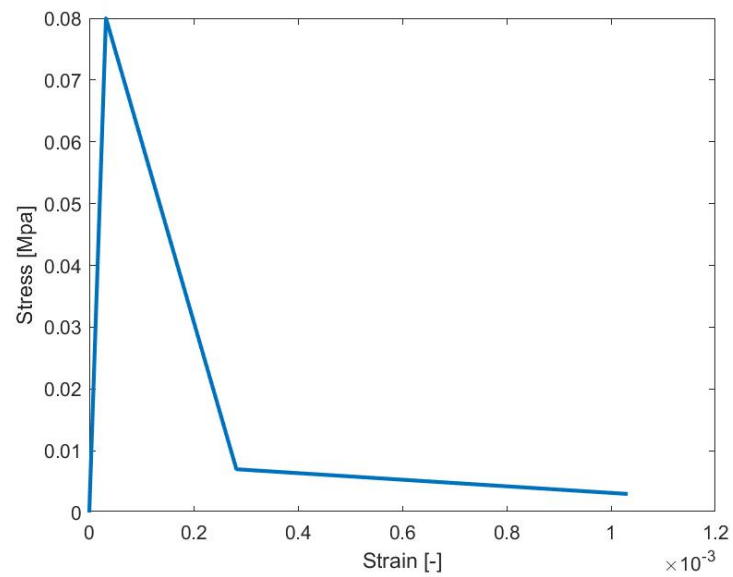


Figure 8.59 – Stress-strain tensile masonry behaviour.

8.3.4 Results

To obtain the damage scenarios of the dome, 3 different analyses were carried out by increasing the acceleration at the base of the structure and observing the variation in damage. The structure was analysed with an earthquake equal to 80%, 100%, 120% and 160% of that of 2012 (*Table 8-9*). Having used the *Concrete Damage Criterion*, it is possible to plot on the dome the degree of damage to the masonry on a scale from 0 to 1. The value 1 means that the material is broken and has no more resistance remain, instead 0 means material that is not damaged. It is therefore possible to obtain the crack pattern of the dome by following the areas with damage equal or close to 1. The following are some characteristic steps of the damage scenarios obtained:

Table 8-9 – PGA input at the base of the structure

<i>Percentage compared to 2012</i>	<i>PGA-X (m/s²)</i>	<i>PGA-Y (m/s²)</i>	<i>PGA-Z (m/s²)</i>
80%	0.30	0.15	0.34
100%	0.38	0.19	0.42
120%	0.46	0.23	0.50
160%	0.61	0.30	0.67

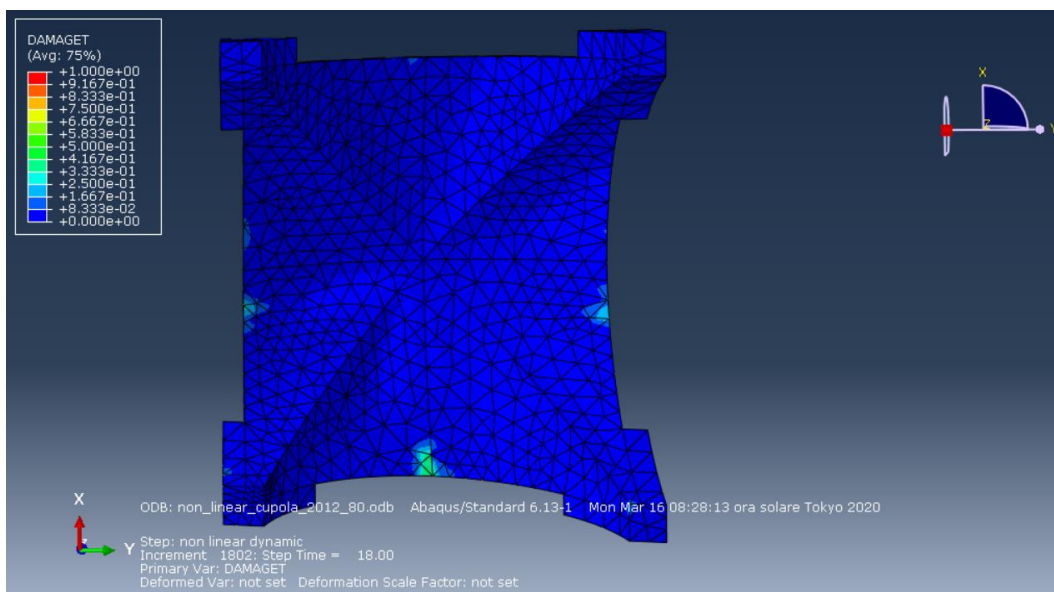


Figure 8.60 - Damage scenario corresponding to 80% of the 2012 earthquake - Step: 18 seconds - Bottom view.

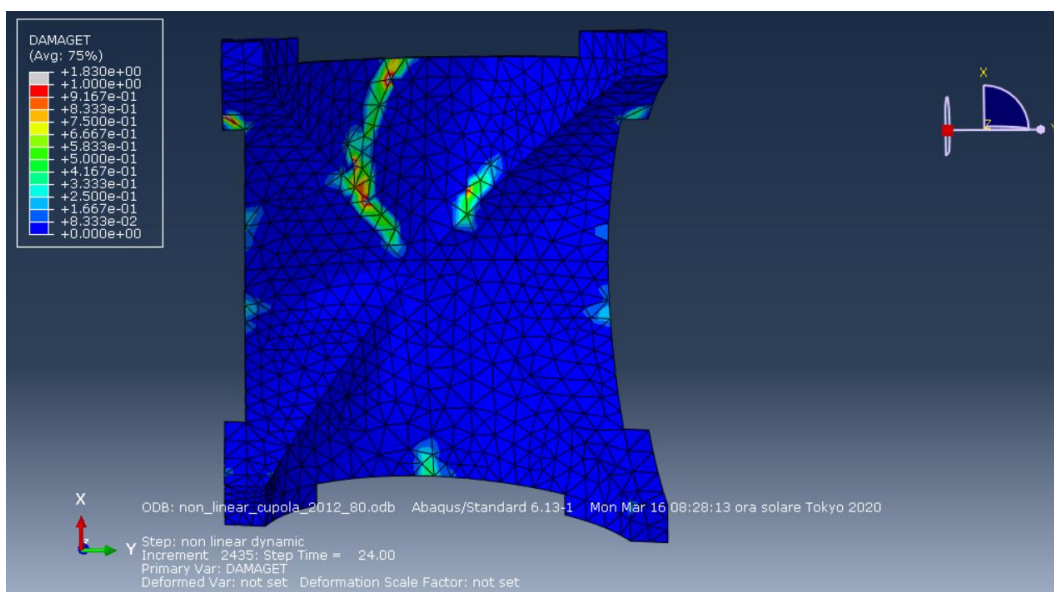


Figure 8.61 - Damage scenario corresponding to 80% of the 2012 earthquake - Step: 24 seconds - Bottom view.

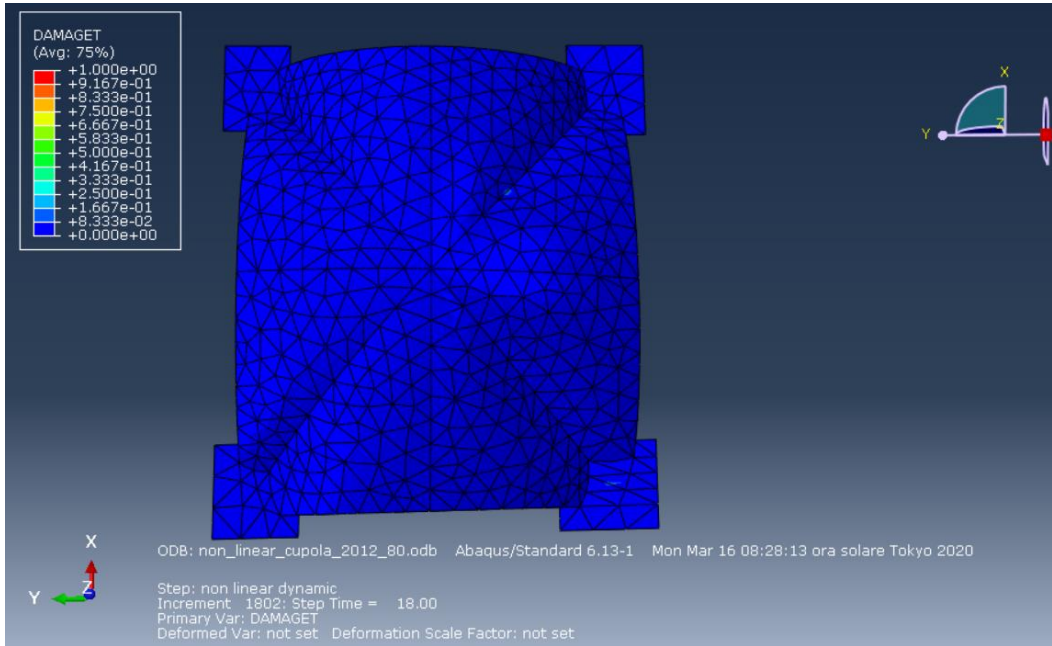


Figure 8.62 - Damage scenario corresponding to 80% of the 2012 earthquake - Step: 18 seconds - Top view.

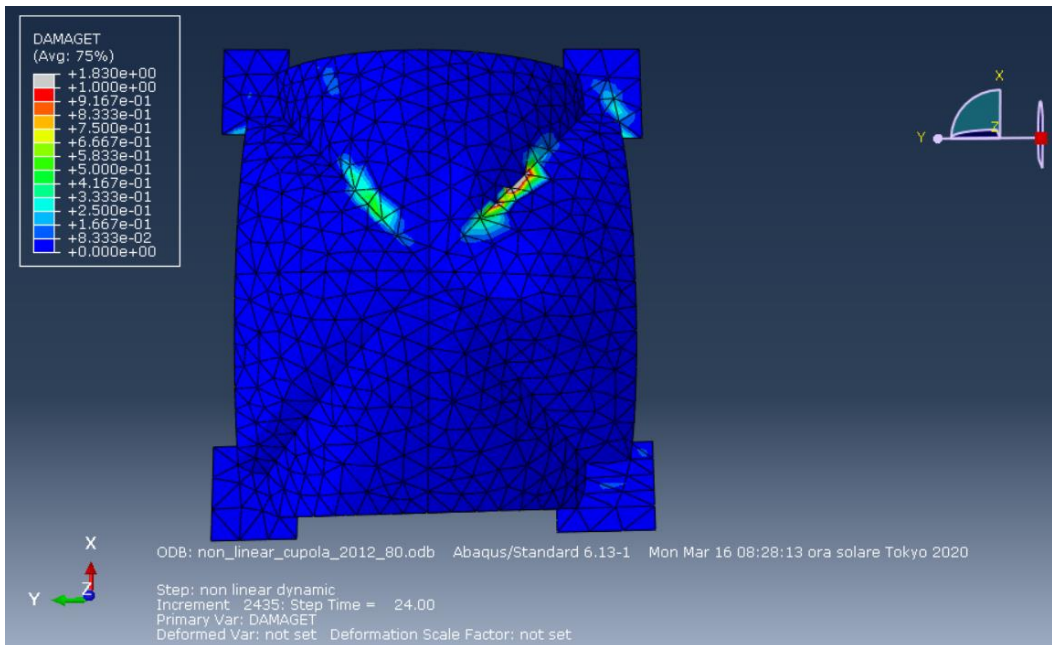


Figure 8.63 - Damage scenario corresponding to 80% of the 2012 earthquake - Step: 24 seconds - Top view.

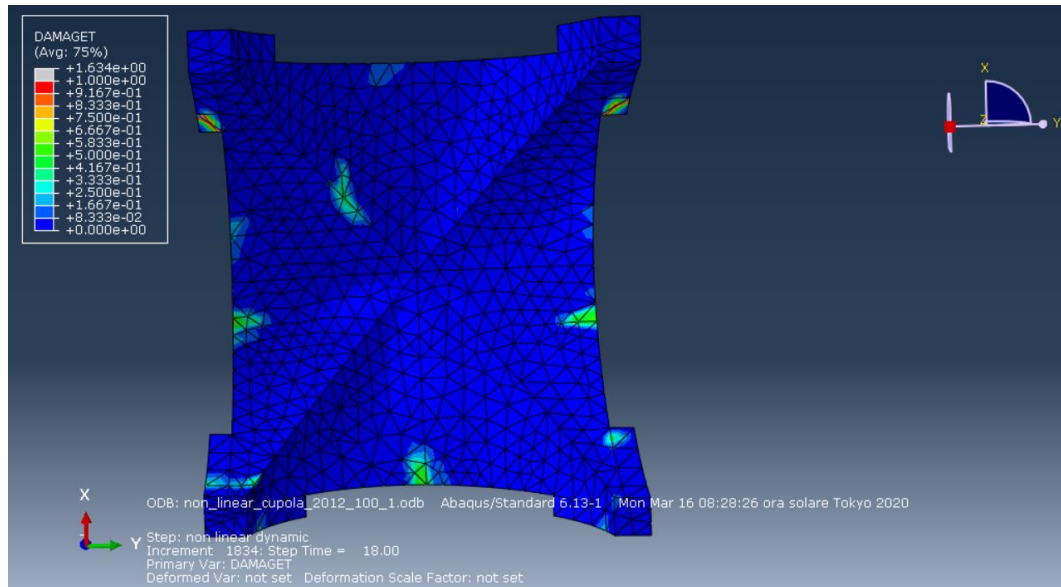


Figure 8.64 - Damage scenario corresponding to 100% of the 2012 earthquake - Step: 18 seconds - Bottom view.

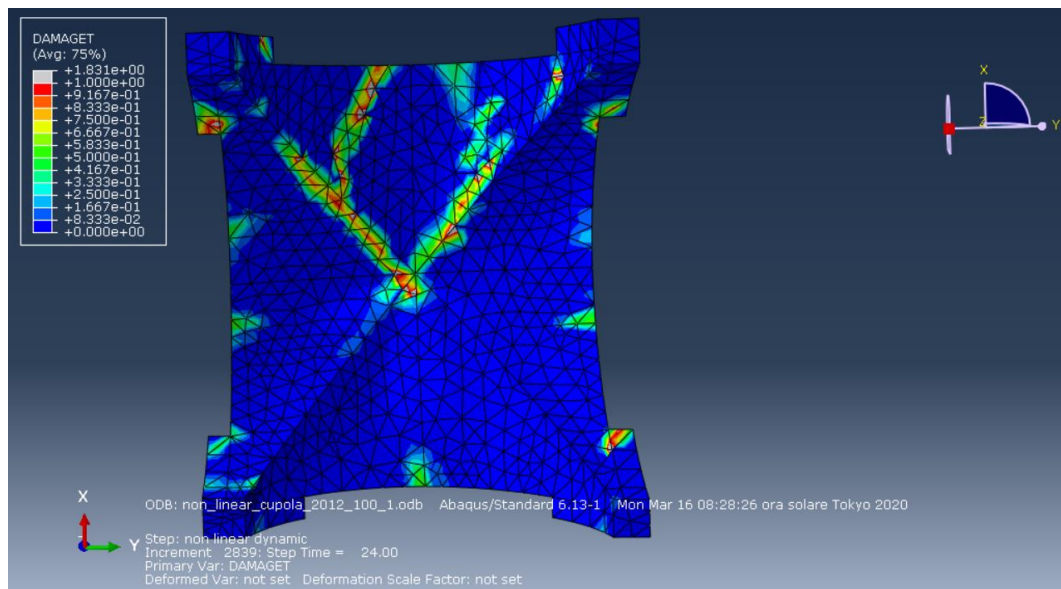


Figure 8.65 - Damage scenario corresponding to 100% of the 2012 earthquake - Step: 24 seconds - Bottom view.

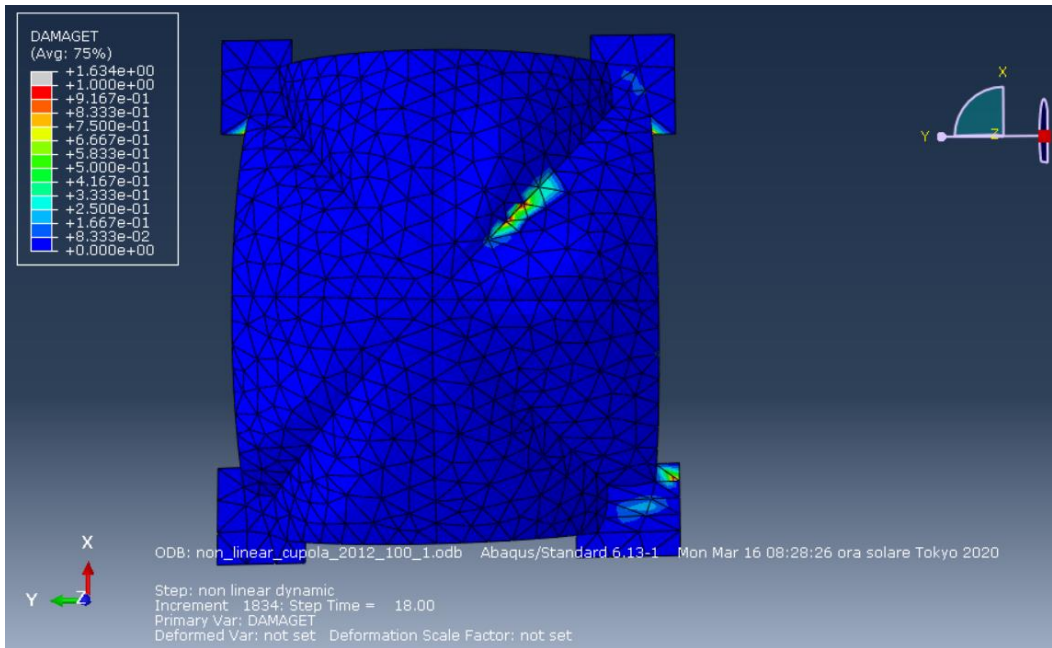


Figure 8.66 - Damage scenario corresponding to 100% of the 2012 earthquake - Step: 18 seconds - Top view.

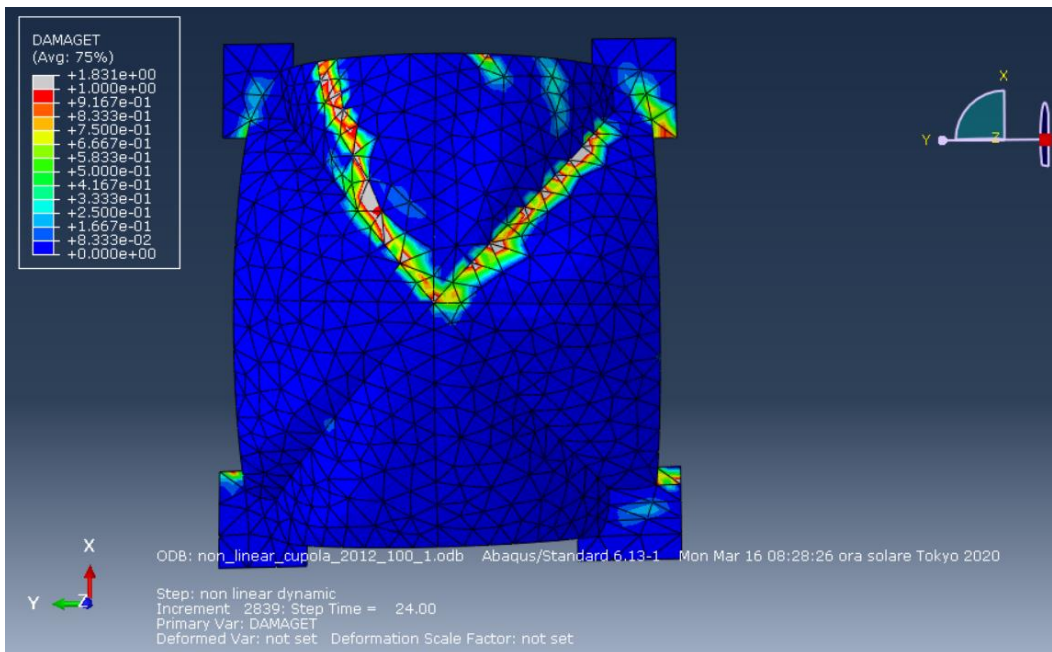


Figure 8.67 - Damage scenario corresponding to 100% of the 2012 earthquake - Step: 24 seconds - Top view.

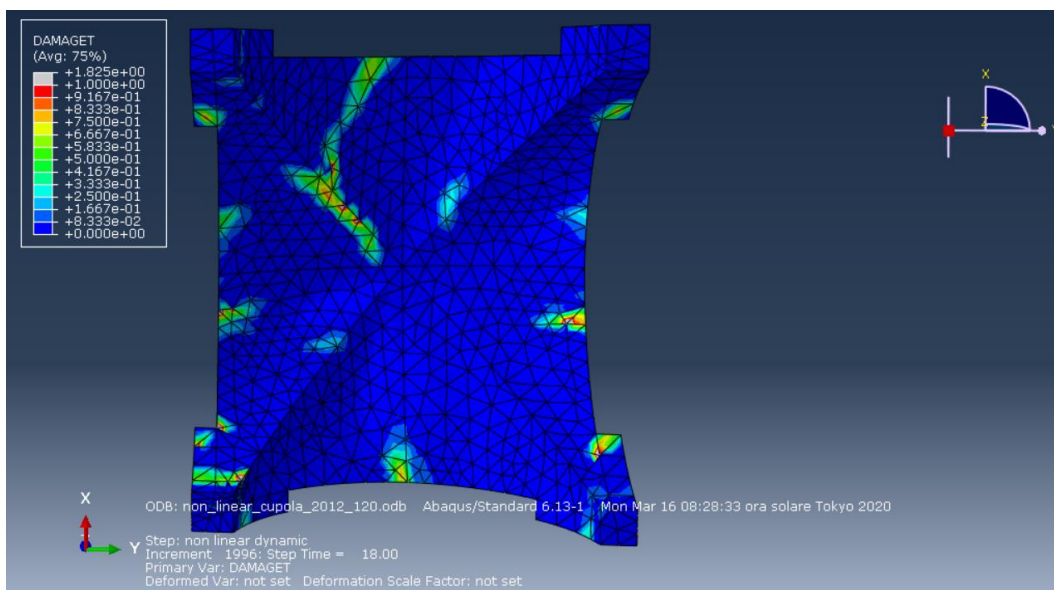


Figure 8.68 - Damage scenario corresponding to 120% of the 2012 earthquake - Step: 18 seconds - Bottom view.

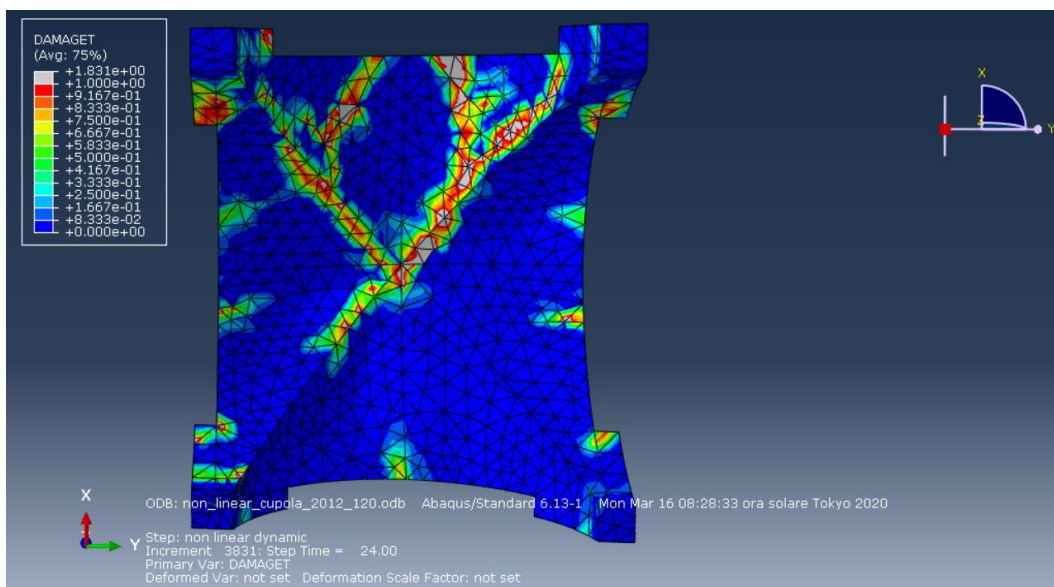


Figure 8.69 - Damage scenario corresponding to 120% of the 2012 earthquake - Step: 24 seconds - Bottom view.

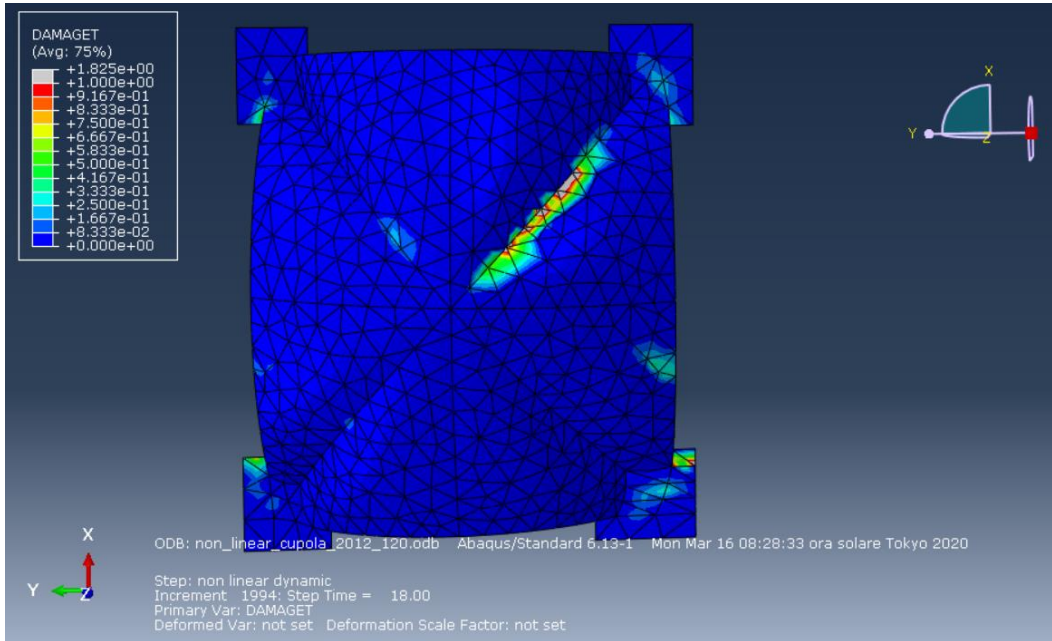


Figure 8.70 - Damage scenario corresponding to 120% of the 2012 earthquake - Step: 18 seconds - Top view.

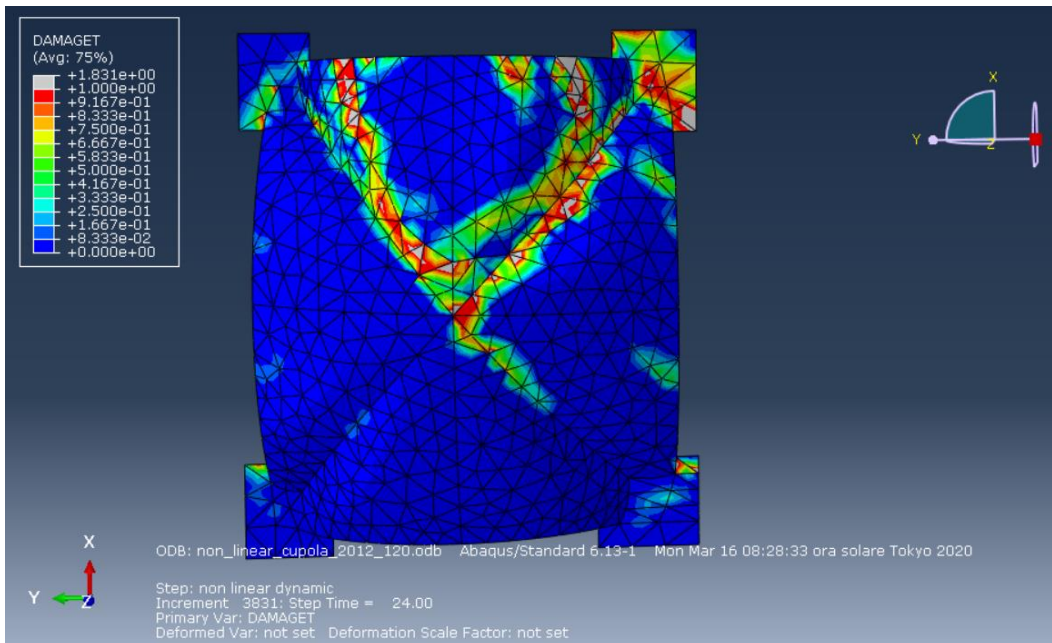


Figure 8.71 - Damage scenario corresponding to 120% of the 2012 earthquake - Step: 24 seconds - Top view.

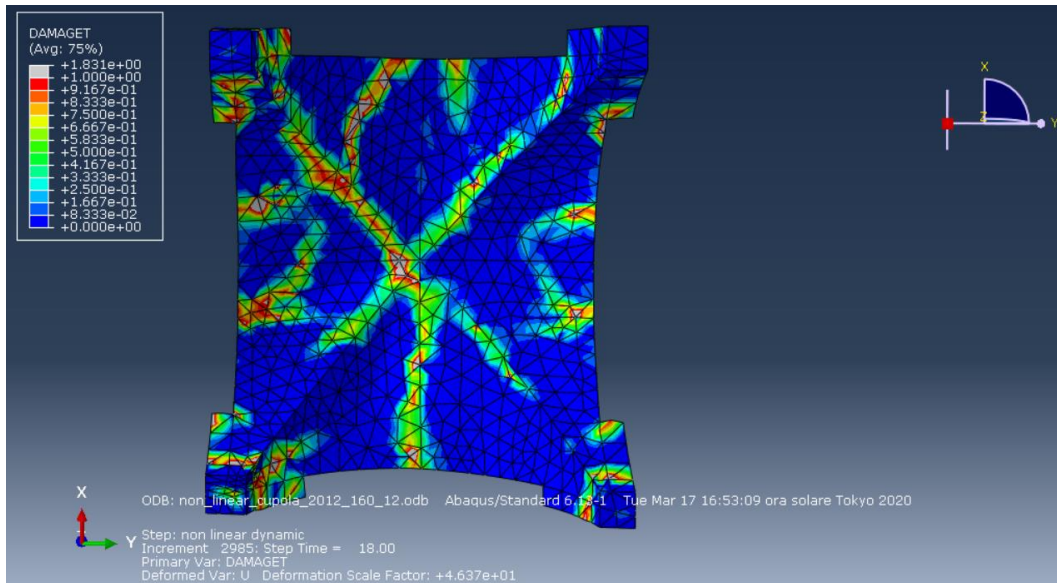


Figure 8.72 - Damage scenario corresponding to 160% of the 2012 earthquake - Step: 18 seconds - Bottom view.

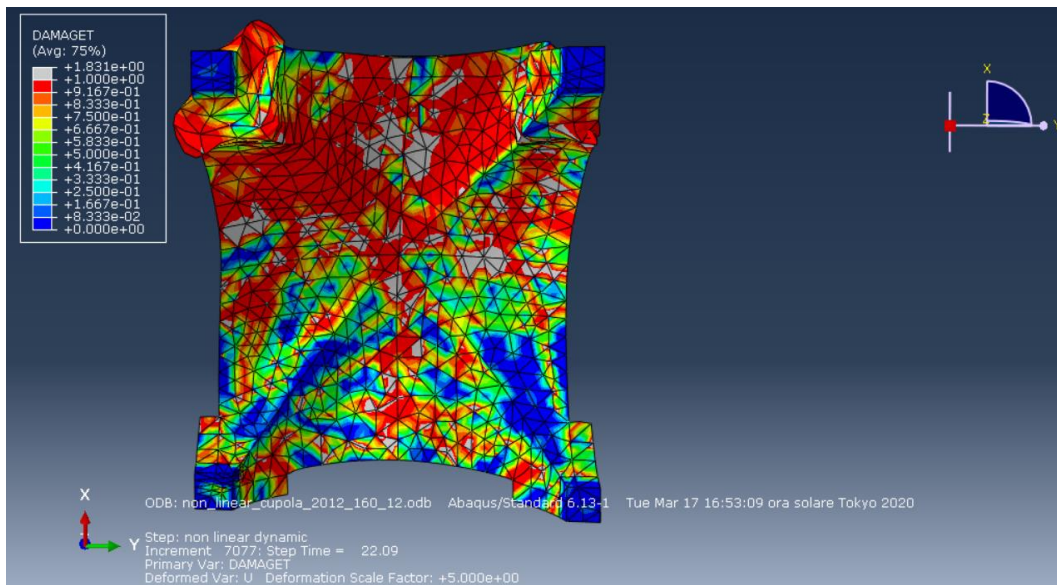


Figure 8.73 - Damage scenario corresponding to 160% of the 2012 earthquake - Step: 22 seconds (Collapse) - Bottom view.

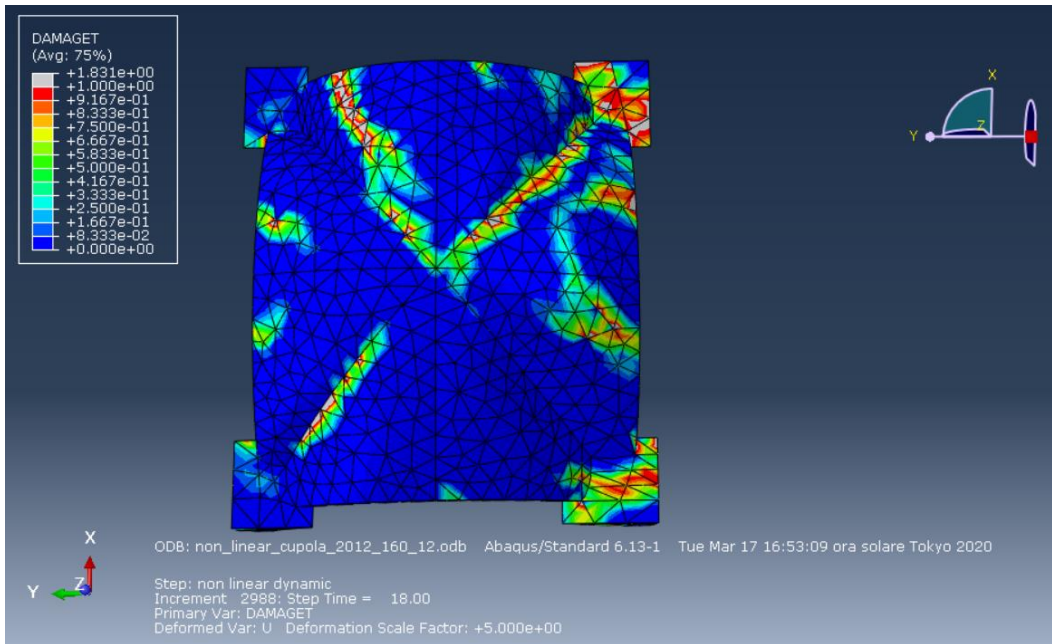


Figure 8.74 - Damage scenario corresponding to 160% of the 2012 earthquake - Step: 18 seconds - Top view.

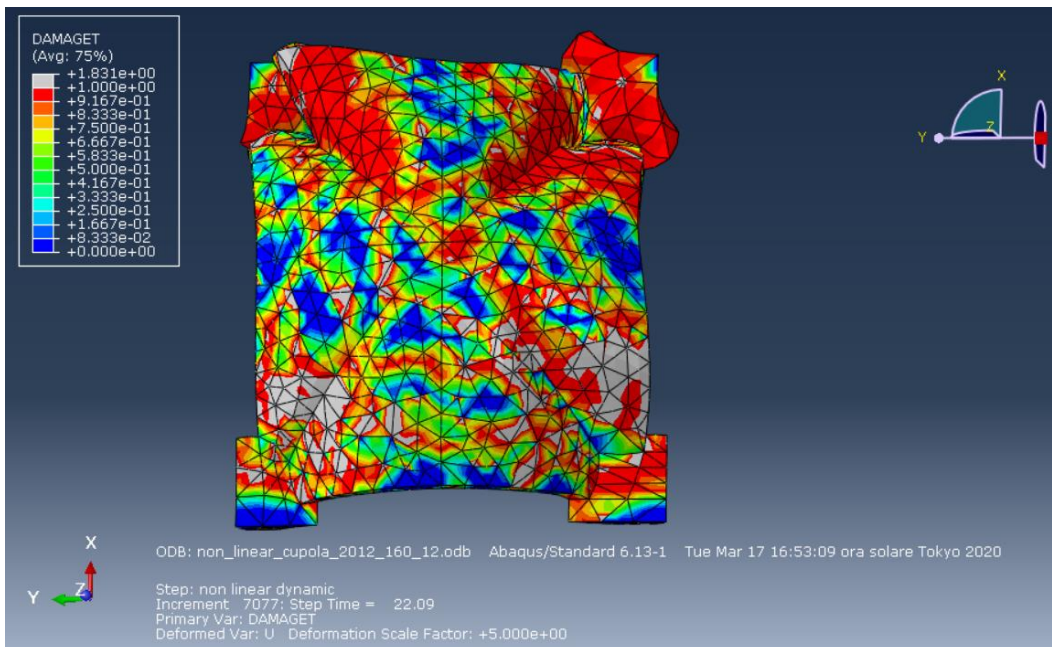


Figure 8.75 - Damage scenario corresponding to 160% of the 2012 earthquake - Step: 22 seconds (Collapse) - Top view.

Plotting the acceleration at the same time at points A and B (part of the facade), i.e. those where damage mainly occurs, it can be observed that for the signal in the X direction in the first peak phase the signals are in phase, instead in the second the signals are no longer in phase. The same phenomenon happens in the Y direction. It can be observed that at the 18th second, the damage is minimal and instead the cracking propagates in the second peak phase of the accelerogram, this happens due to the accelerations in phase opposition which are more severe than those in phase.

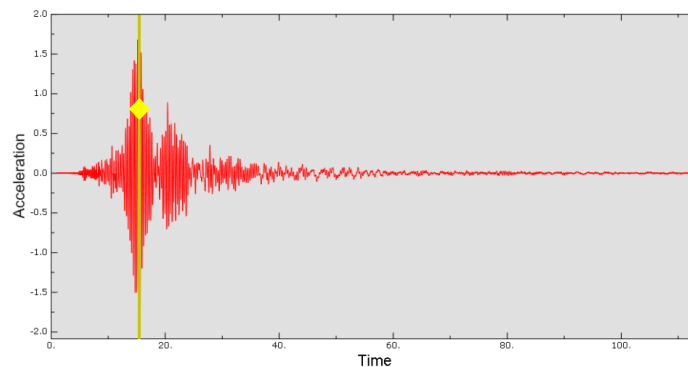


Figure 8.76 – Acceleration time history point A – X direction - 16 seconds.

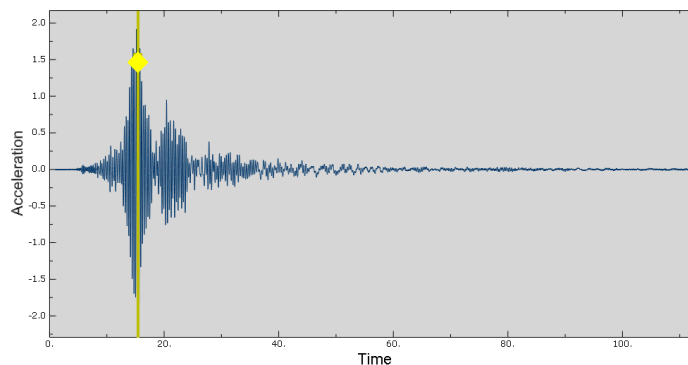


Figure 8.77 – Acceleration time history point B – X direction - 16 seconds.

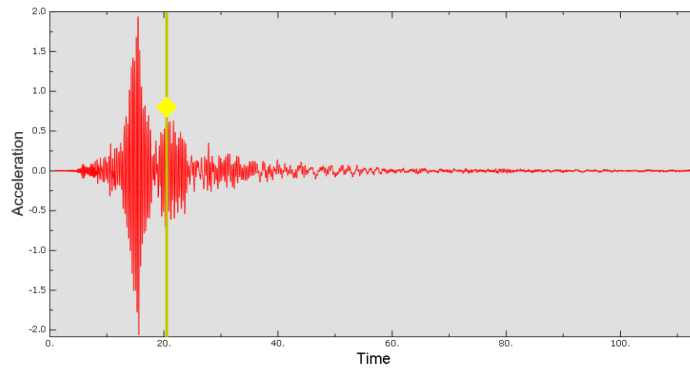


Figure 8.78 – Acceleration time history point A – X direction - 21 seconds.

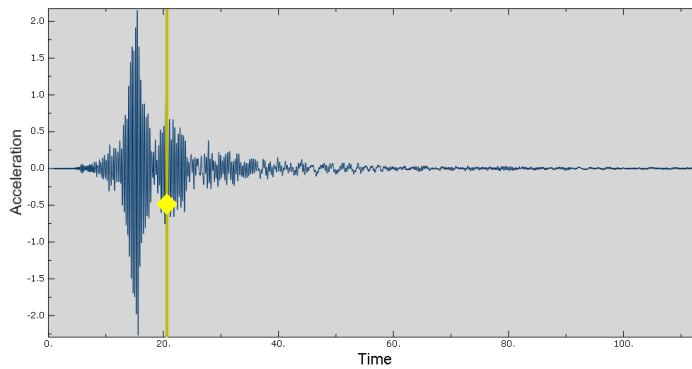


Figure 8.79 – Acceleration time history point B – X direction - 21 seconds.

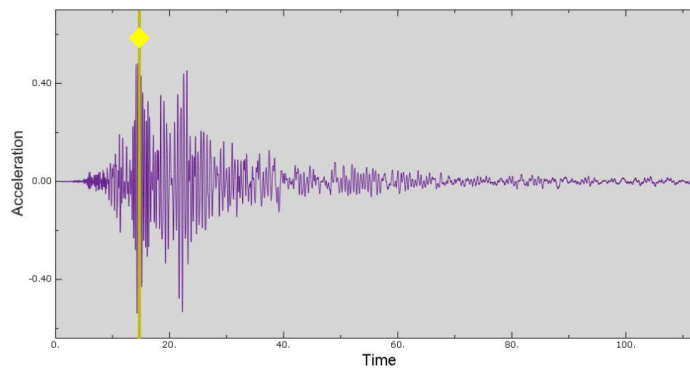


Figure 8.80 – Acceleration time history point A – Y direction - 15 seconds.

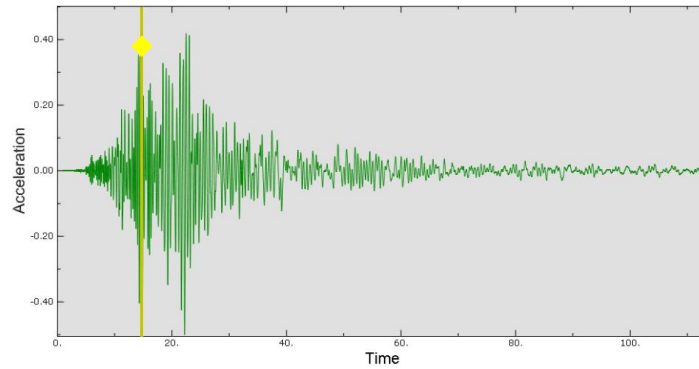


Figure 8.81 – Acceleration time history point B – Y direction - 15 seconds.

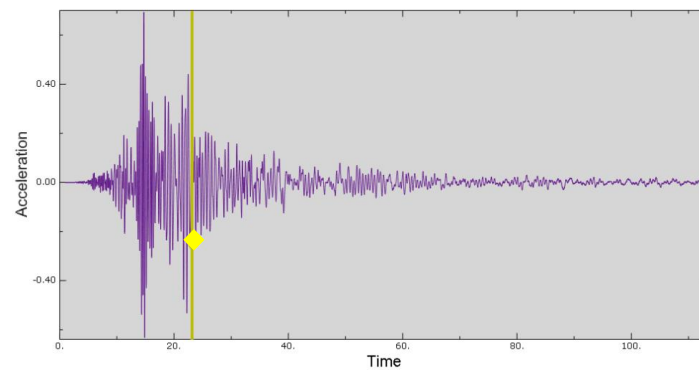


Figure 8.82 – Acceleration time history point A – Y direction - 23 seconds.

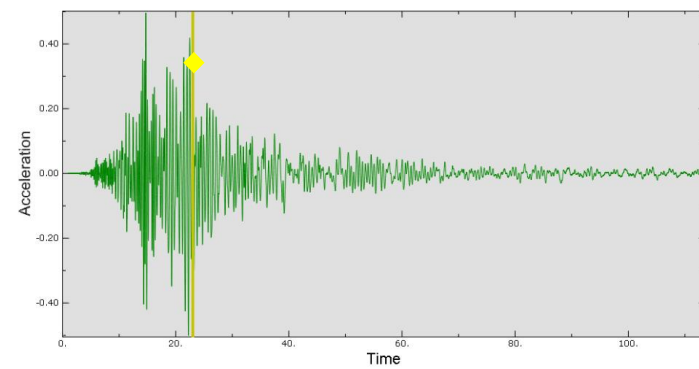


Figure 8.83 – Acceleration time history point B – Y direction - 23 seconds.

The results obtained corresponding to the 100% of the 2012 earthquake were then compared with some photos and damage maps made from inspections carried out in the aftermath of the earthquake. The data on the damage are shown below:

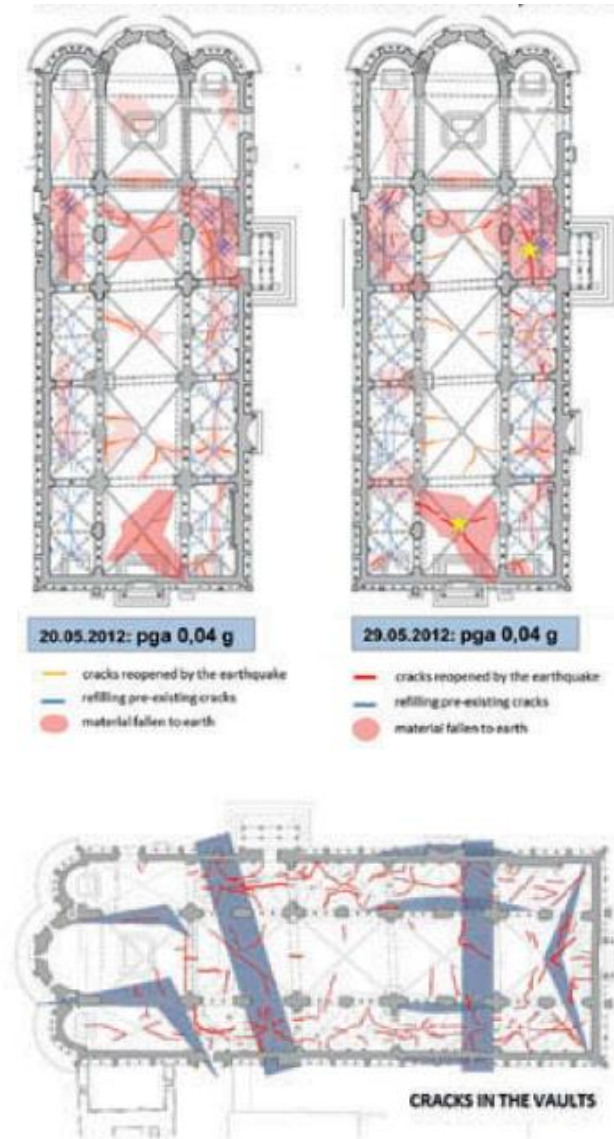


Figure 8.84 - Damage obtained by recent earthquakes



Figure 8.85 - Damage obtained by recent earthquakes.

By comparing the results of the analysis with the photos regarding the damage, some correspondences are highlighted on the cracking pattern of recent earthquakes. It can be seen how the model interprets the main damages on the vault well, such as the opening of cracks at the change of curvature and the crack that starts from the openings such as the rose window and develops up to the change of curvature of the dome. This allows us to say that the model correctly underline the main criticalities of the vault by going to report which are the most vulnerable and critical areas under seismic action.

Finally, the collapse of the dome was obtained by increasing the 2012 earthquake up to a percentage value of 150%, that is corresponding to a PGA at the base of the structure equal to 0.67 m/s^2 .

Chapter 9

Conclusions

The thesis work centred on the study of historical and monumental buildings was divided into two main phases:

- The first phase focused on the behaviour of the masonry and its modelling;
- The second phase focused on the modelling and analysis of the Cathedral of Modena based on the notions developed in the first phase.

Once the basics of masonry behaviour and its modelling using the FEM methodology were treated, the work focused on creating the geometry of the structure. In this very complex phase, due to the various complications such as irregularities, complicated geometries and inclinations present in the structure, a point cloud acquired with Laser Scanner was used. Subsequently, the 3D model was divided into several parts (macro elements) in order to carry out the Model Updating analysis, which consists in the variation of the elastic modulus and specific weight of the materials. This means varying the elements of the stiffness and mass matrix of the model, in order to reduce the errors between the numerical and experimental response. The monitoring system installed since 2015 has been fundamental for the calibration and for the comparison of the data of the numerical model and experimentation. Once the model was created and calibrated, some linear and non-linear analyses were carried out, both on the structure and on the dome.

The main objective was to obtain the damage scenarios of the dome under the action of the 2012 earthquake. It was chosen to carry out this analysis since in this type of structures the domes are the most prone to damage and then in the last earthquakes that hit the Modena cathedral there were no damages to the walls. Moreover, being a complex structure and having a high number of elements, the nonlinear analyses on the whole structure would have had a very high computational burden and therefore difficult to carry out.

To obtain the scenarios, the accelerograms relating to the 2012 earthquake were applied to the base of the structure, the acceleration time histories were obtained at the base of the dome by means of a transient linear dynamic analysis. Finally, applying the time acceleration histories at the base of the single dome model, a nonlinear dynamic analysis was performed. The input at the base of the structure was increased until the collapse of the dome was reached. From the results obtained, the damage to the 2012 earthquake is well interpreted by the numerical model, as can be seen in *Figure 9.1*. This allows us to say that the model correctly underline the main criticalities of the vault by going to report which are the most vulnerable and critical areas under seismic action.

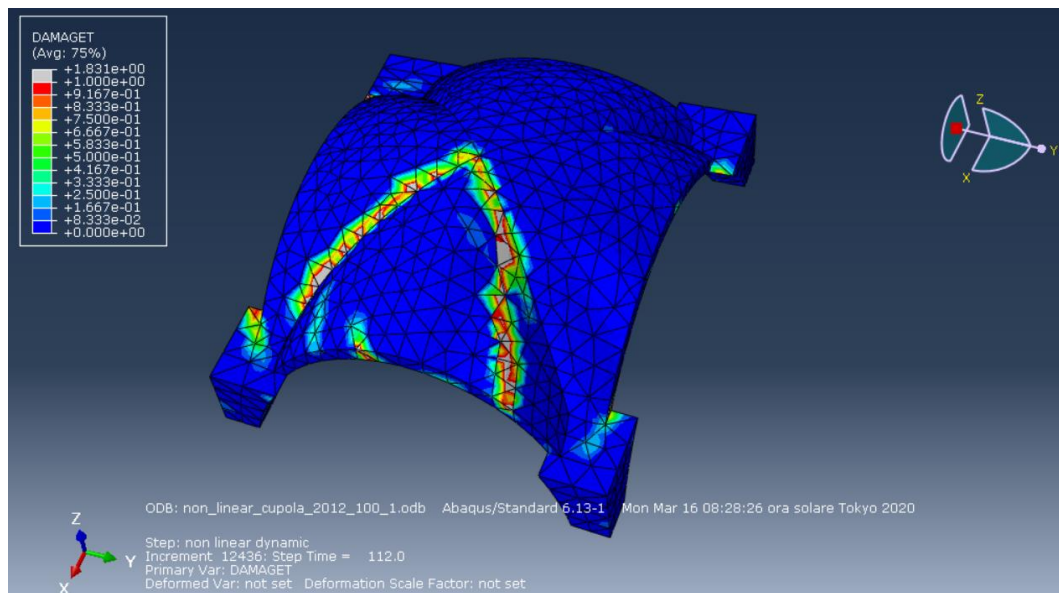


Figure 9.1 - Damage scenario corresponding to 100% of the 2012 earthquake - Step: 24 seconds.

Furthermore, by increasing the input at the base of the structure, the collapse occurs with an input having PGA equal to 0.67 m/s^2 , equal to 1.6 times that of the 2012 earthquake (Figure 9.2).

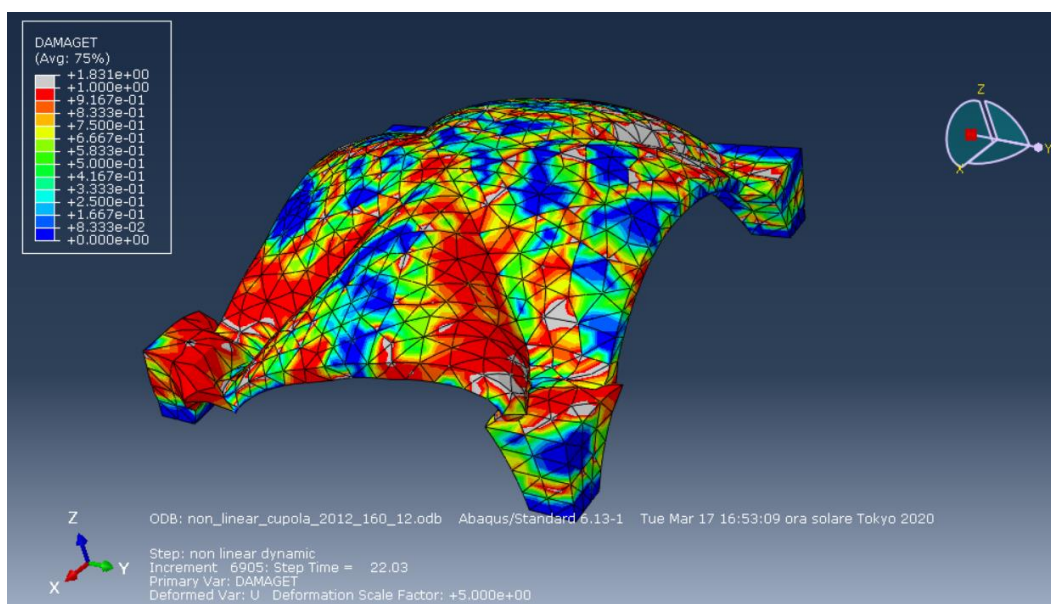


Figure 9.2 - Damage scenario corresponding to 160% of the 2012 earthquake - Step: 22 seconds (Collapse).

These results were obtained considering the various interventions carried out over the years to safeguard the safety of the structure such as the installation of tie-rods. The latter prevent the formation of macro-elements and allow the structure to behave as much as possible as a box-like structure. Surely this intervention has helped to improve the vulnerability of the domes, by reducing the displacements at their base and minimizing the opening of the side walls of the central nave and the overturning of the facade.

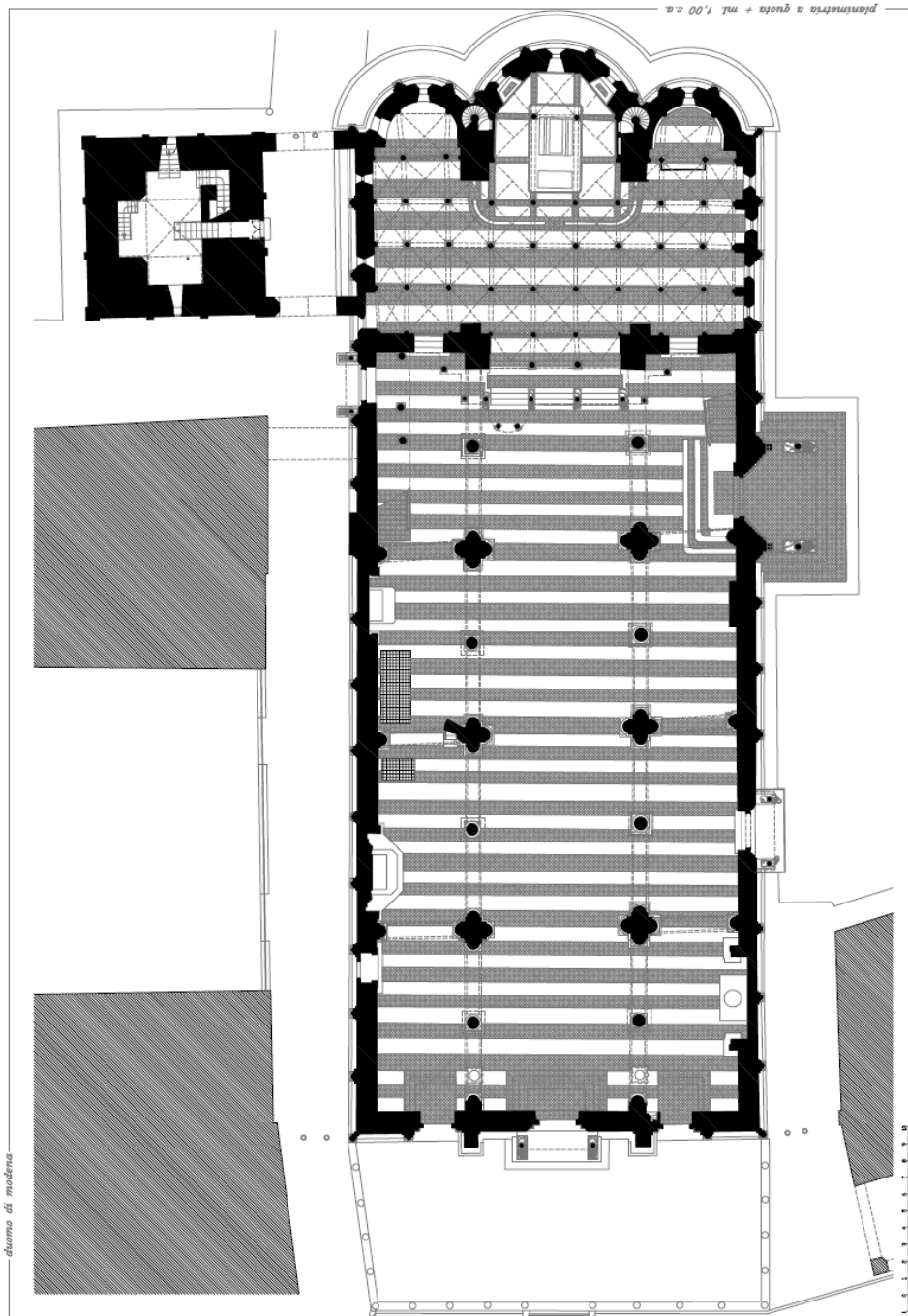
To safeguard our historical and cultural heritage, it would be necessary to intervene on the structures by inserting a monitoring system that allows the control and identification of critical areas of the structure. Moreover, as reported in this thesis it is also necessary for the construction of structural models, which correctly describe the behaviour under seismic action. Not knowing the materials and not being able to carry out destructive tests, the only way to reduce the errors concerning the dynamic



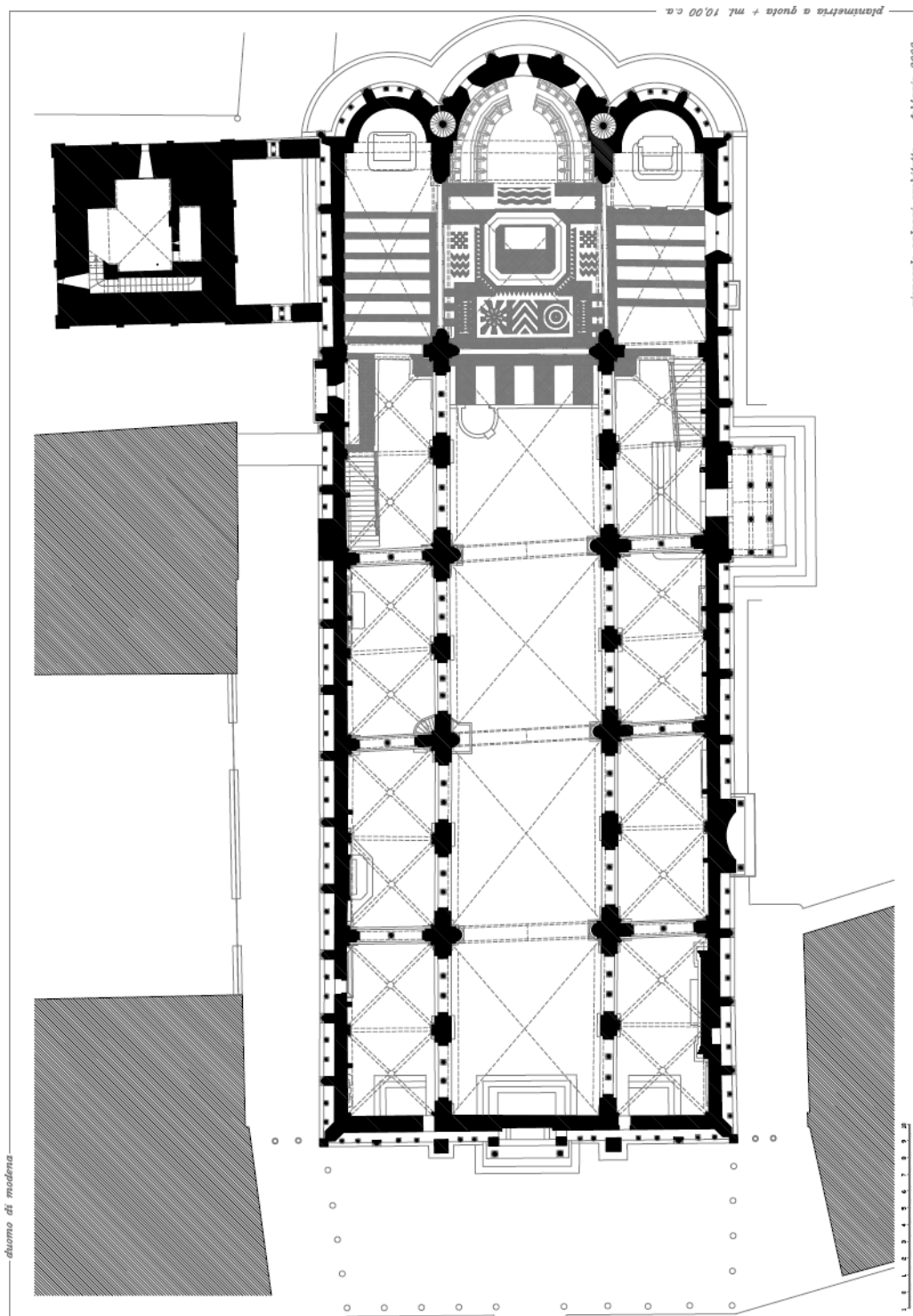
behaviour of the structural model is to proceed with the Model Updating methodology. It is important to have a model that correctly simulates the response of the structure for the design of consolidation interventions, which must be carried out in order to have a conservation and limit the damage even in the aftermath of major earthquakes.



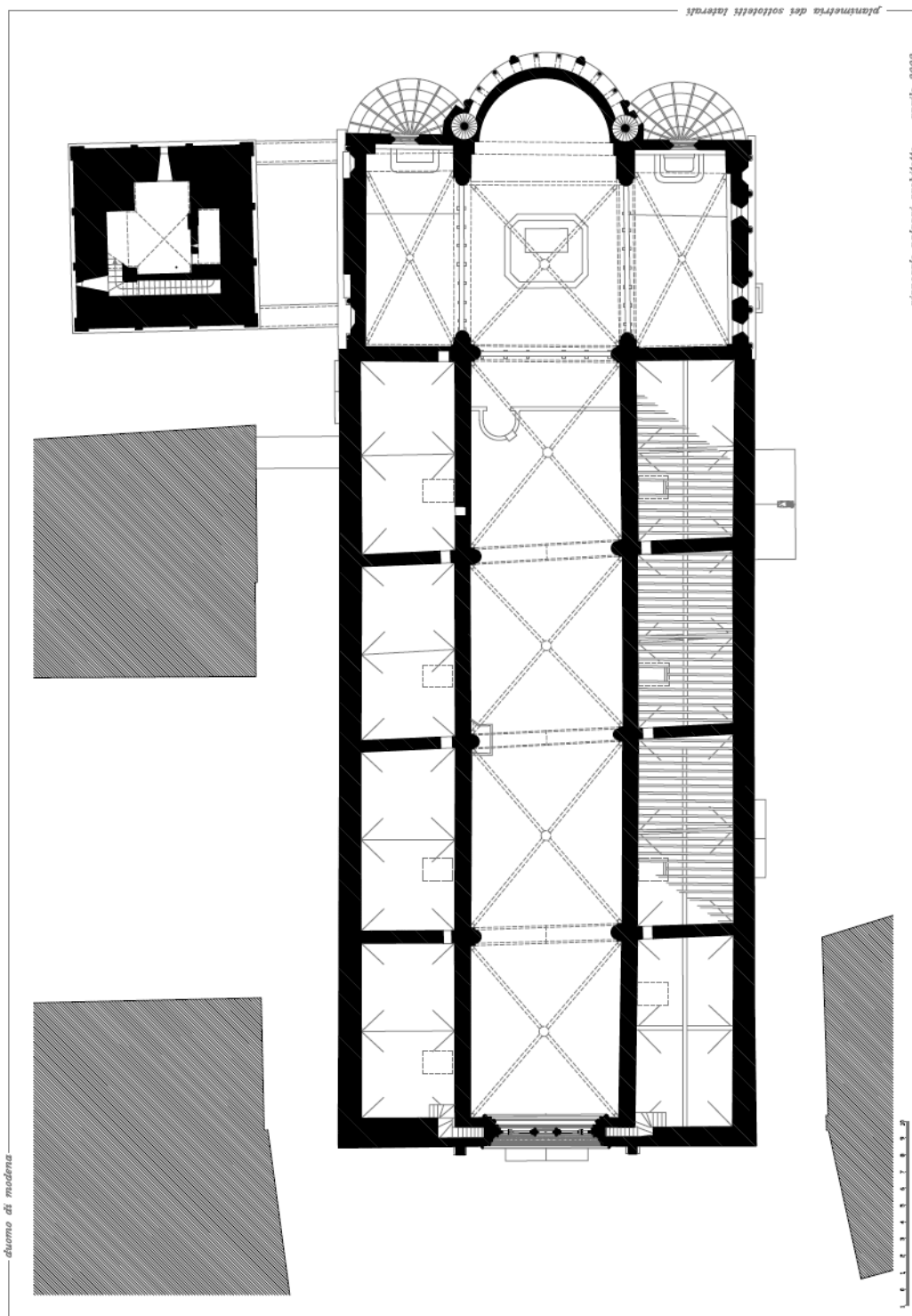
Appendix A – Drawings



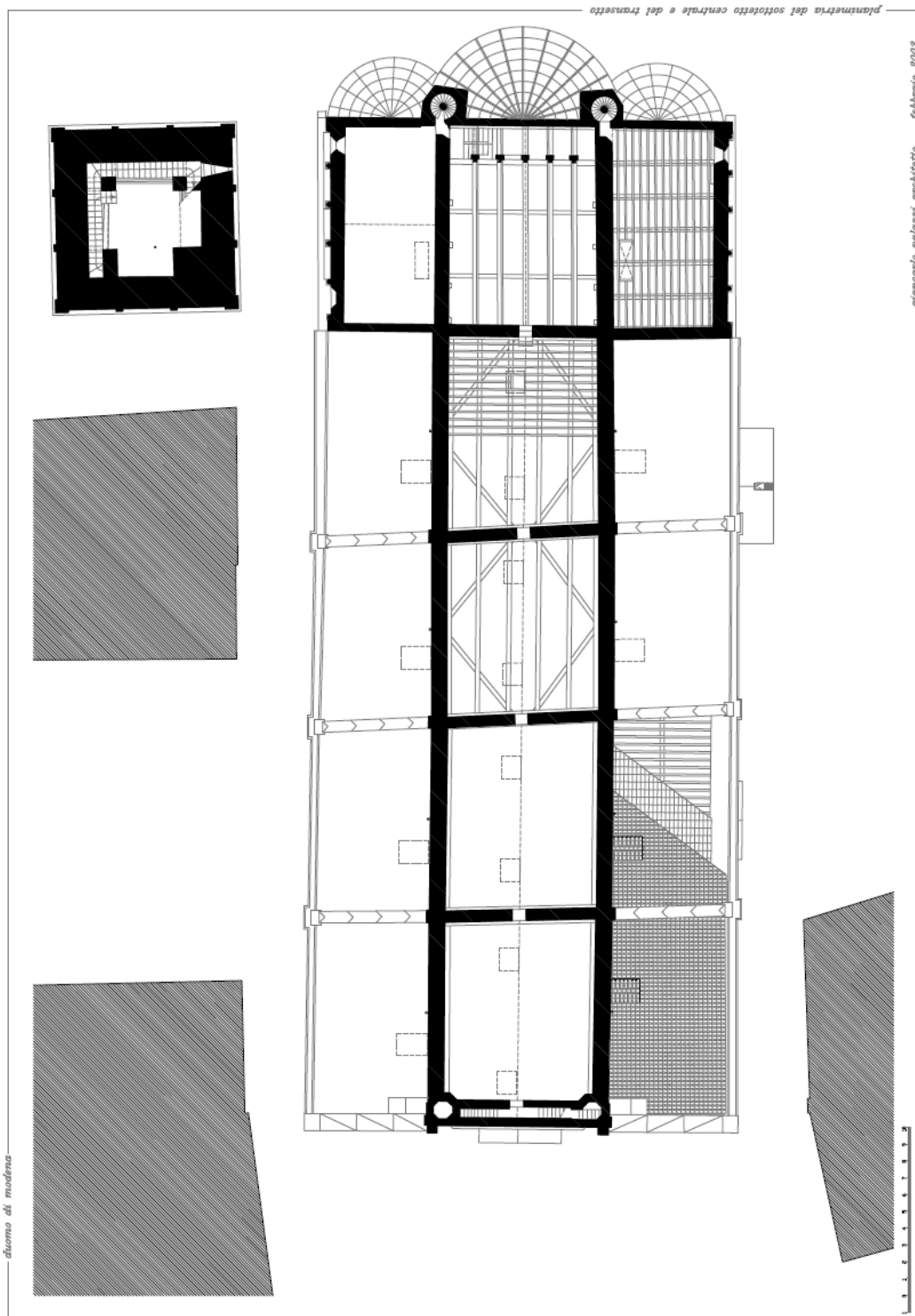
Plan at 1m altitude (Giancarlo Palazzi).



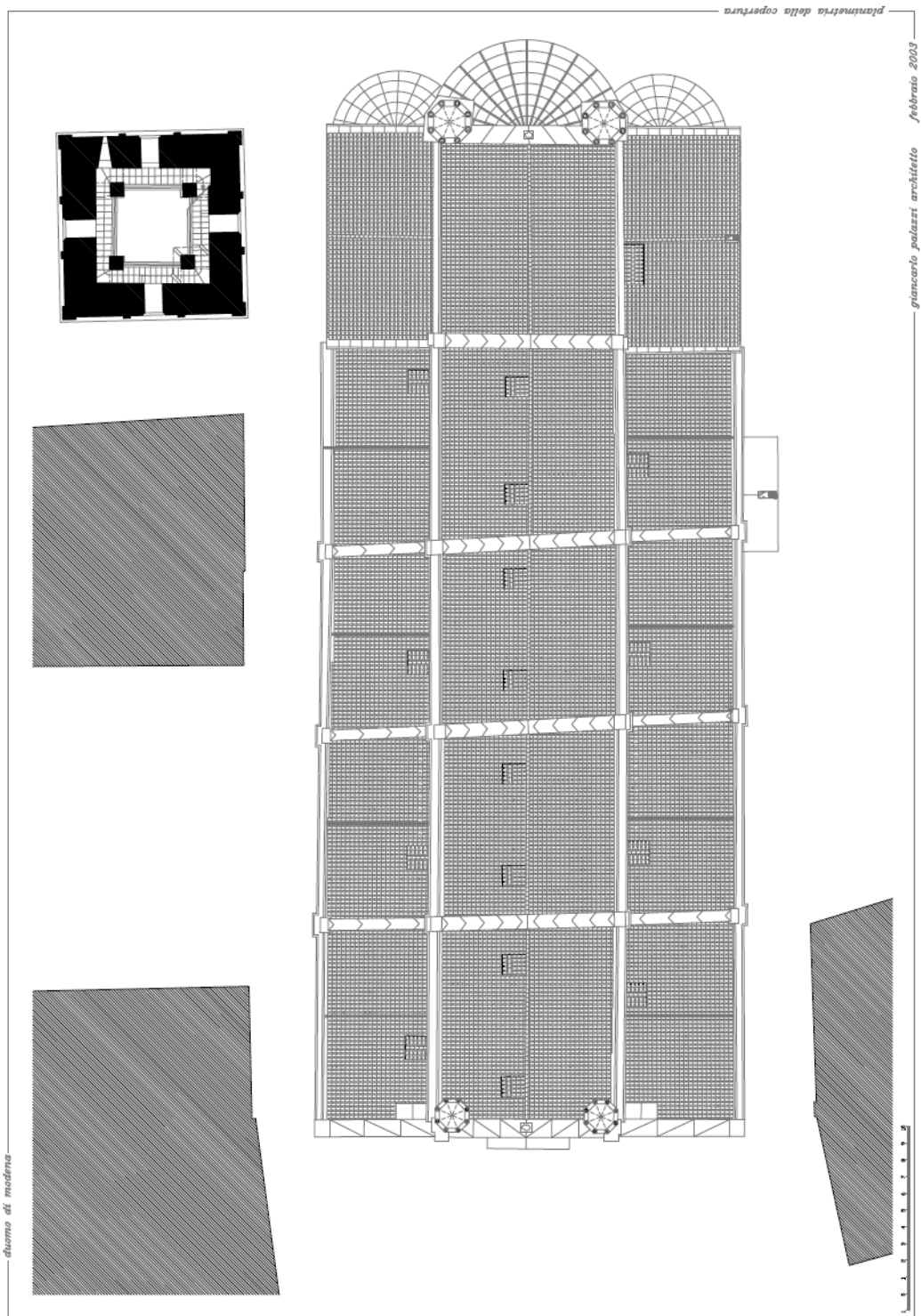
Plan at 10m altitude (Giancarlo Palazzi).



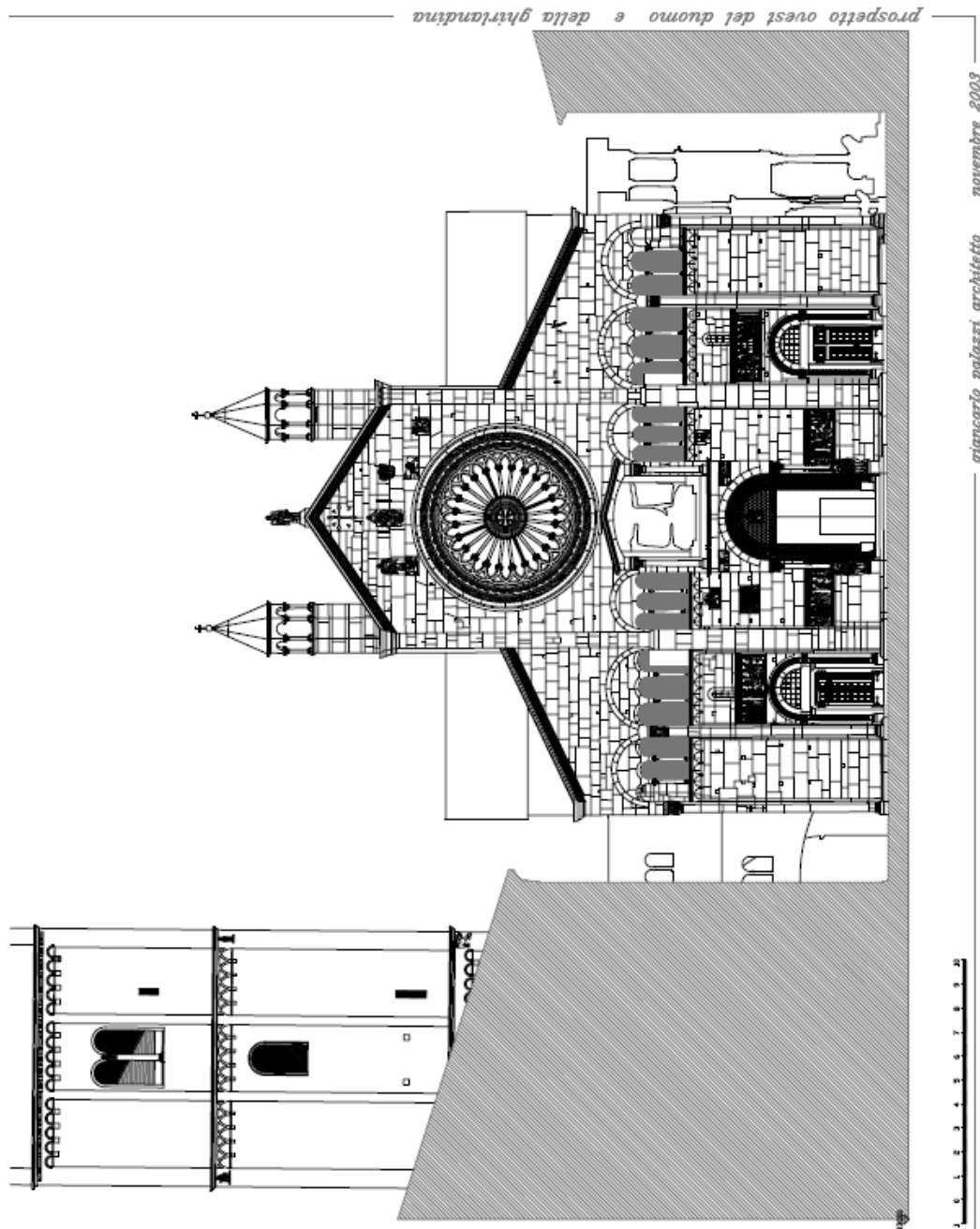
Side attics plan (Giancarlo Palazzi).



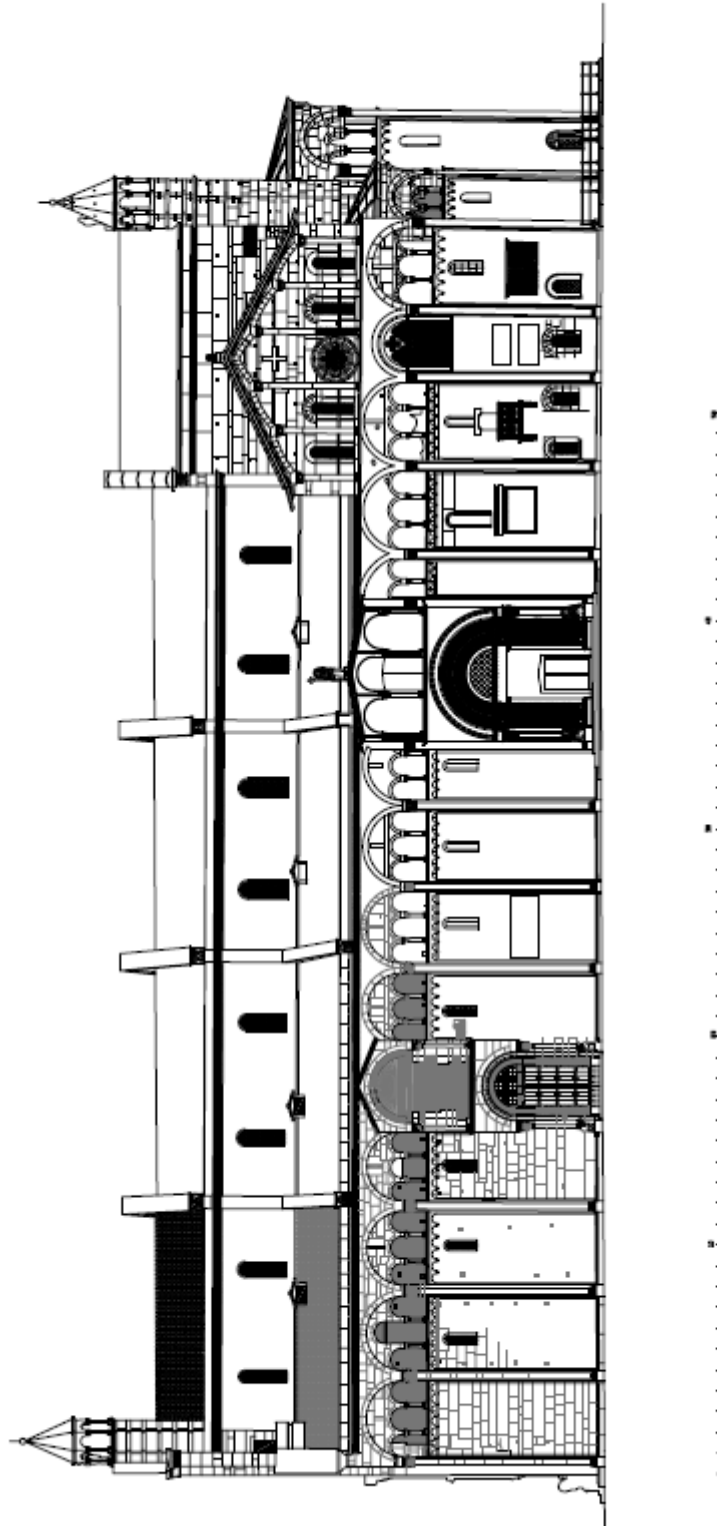
Central and transept attics plan (Giancarlo Palazzi).



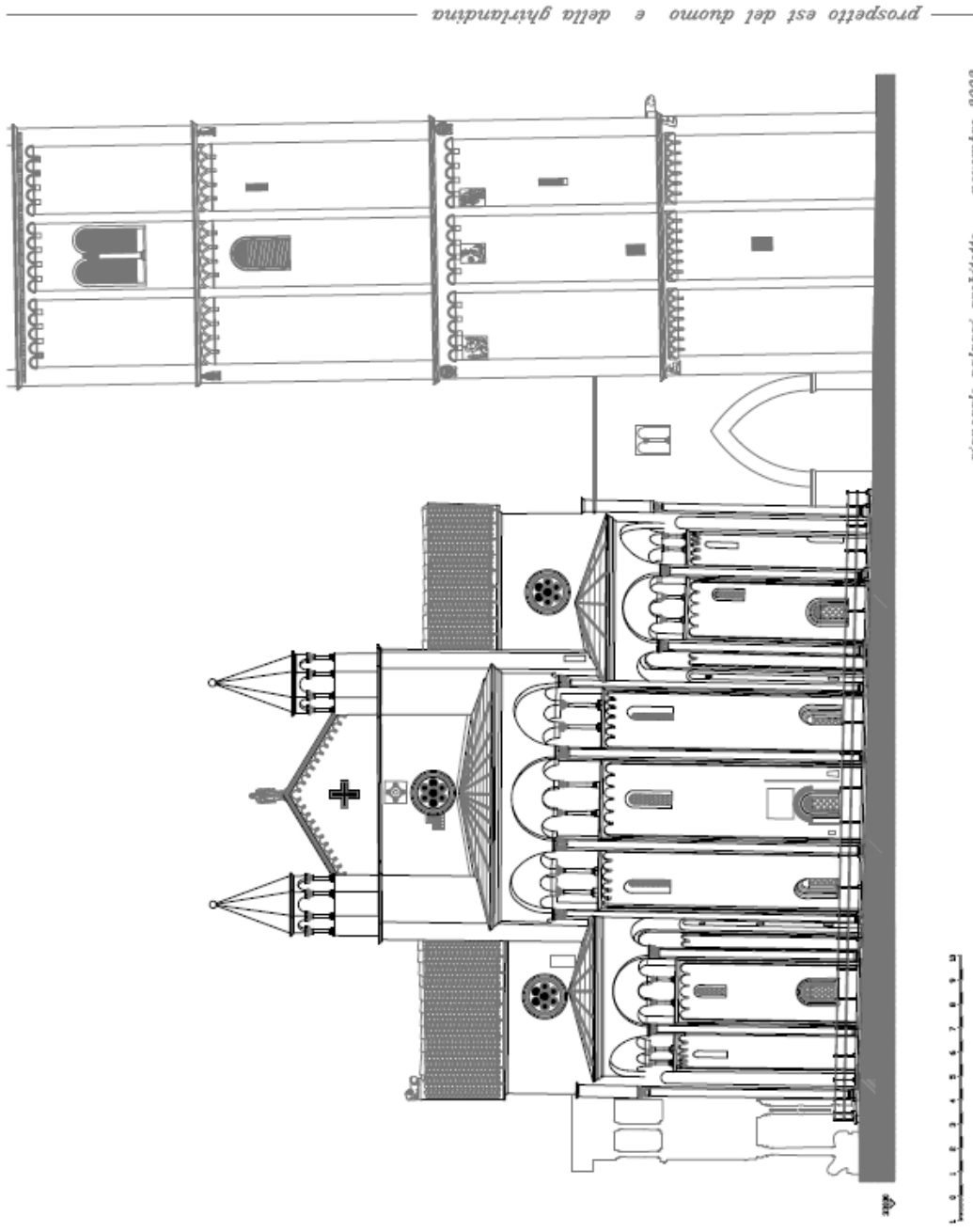
Roof plan (Giancarlo Palazzi).



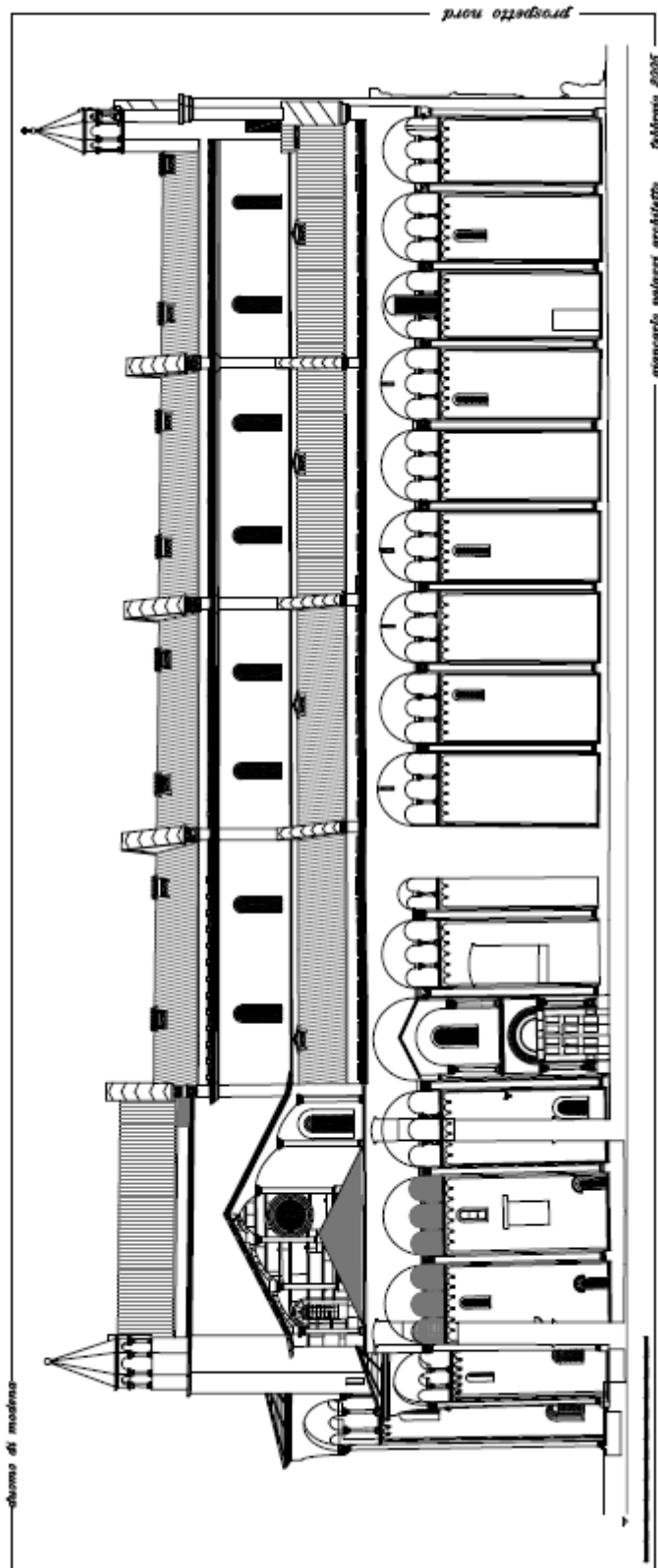
West facade of the Cathedral and Ghirlandina (Giancarlo Palazzi).



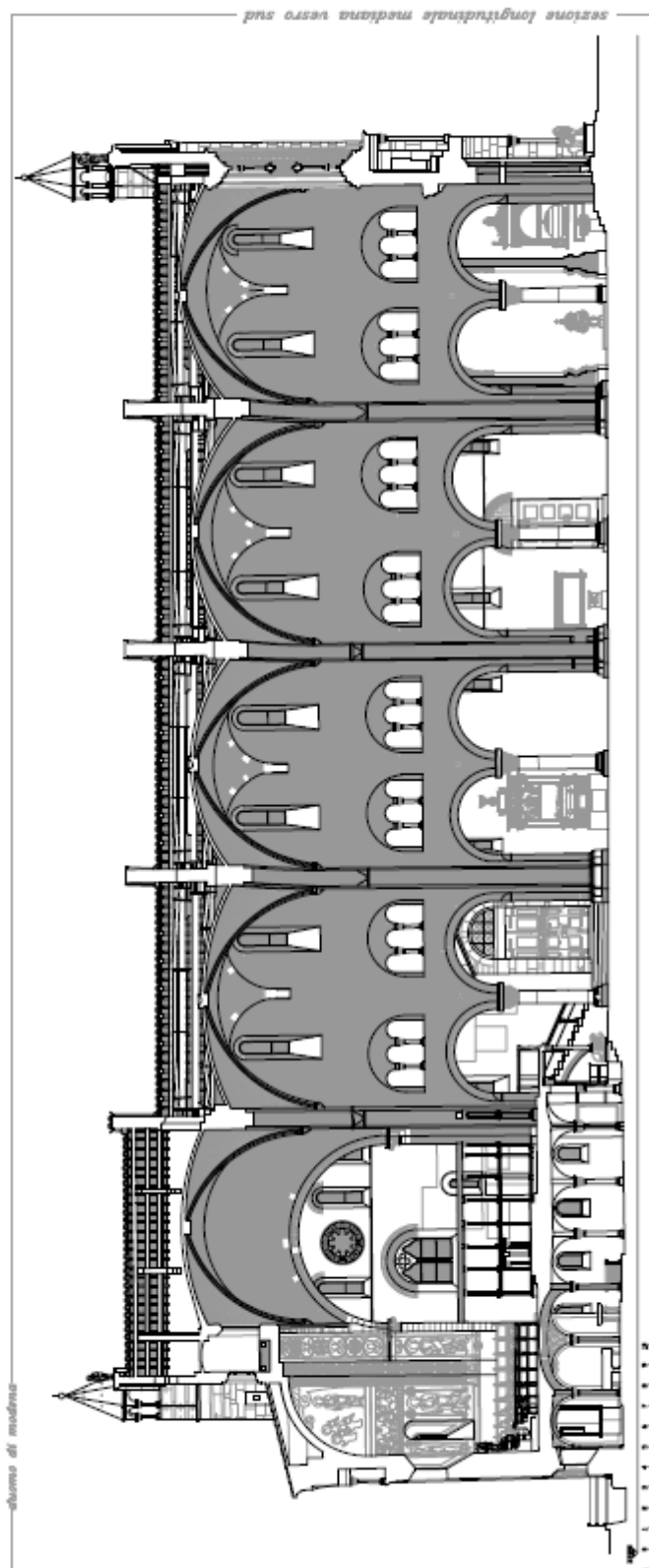
South facade of the Cathedral (Giancarlo Palazzi).



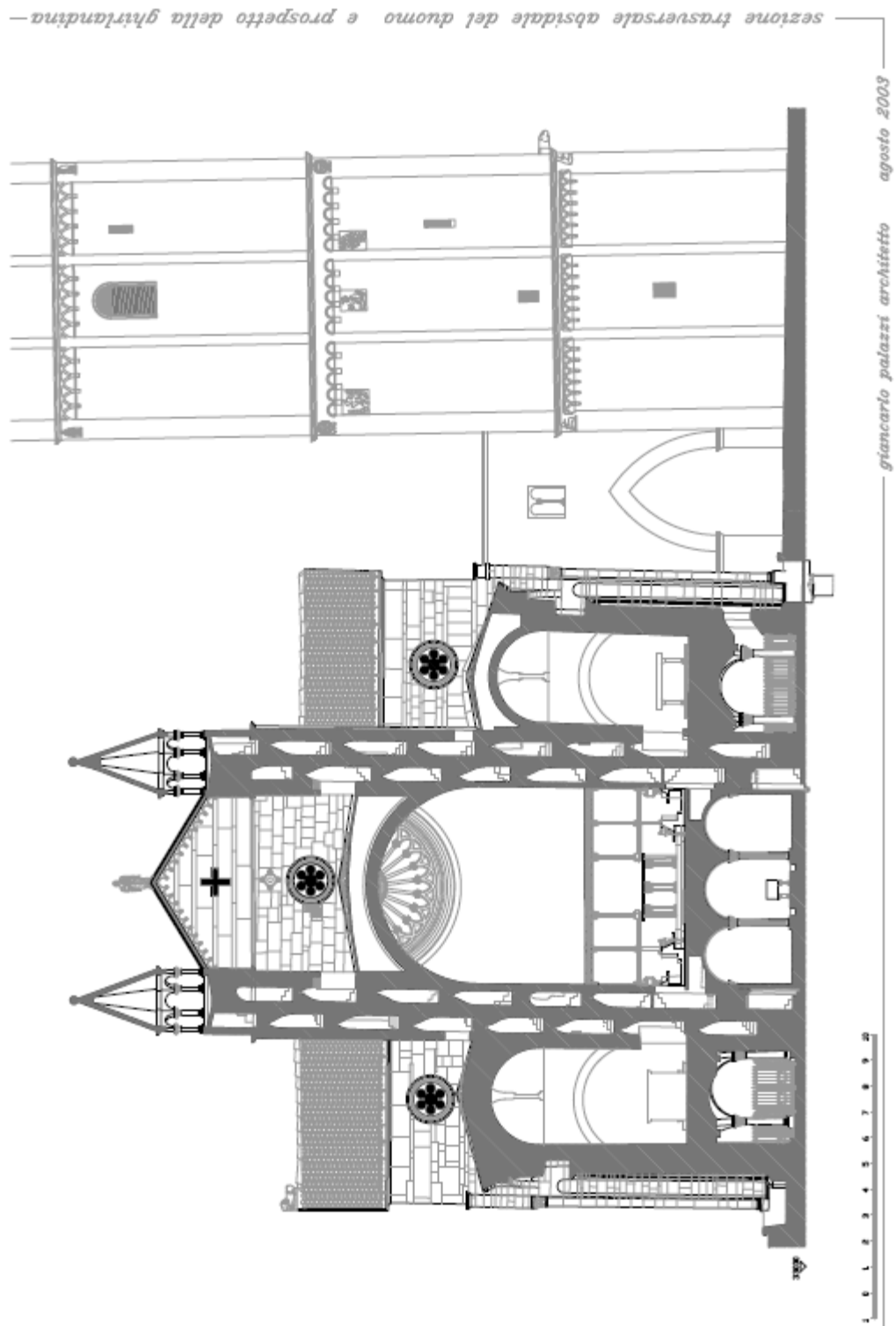
East facade of the Cathedral and Ghirlandina (Giancarlo Palazzi).



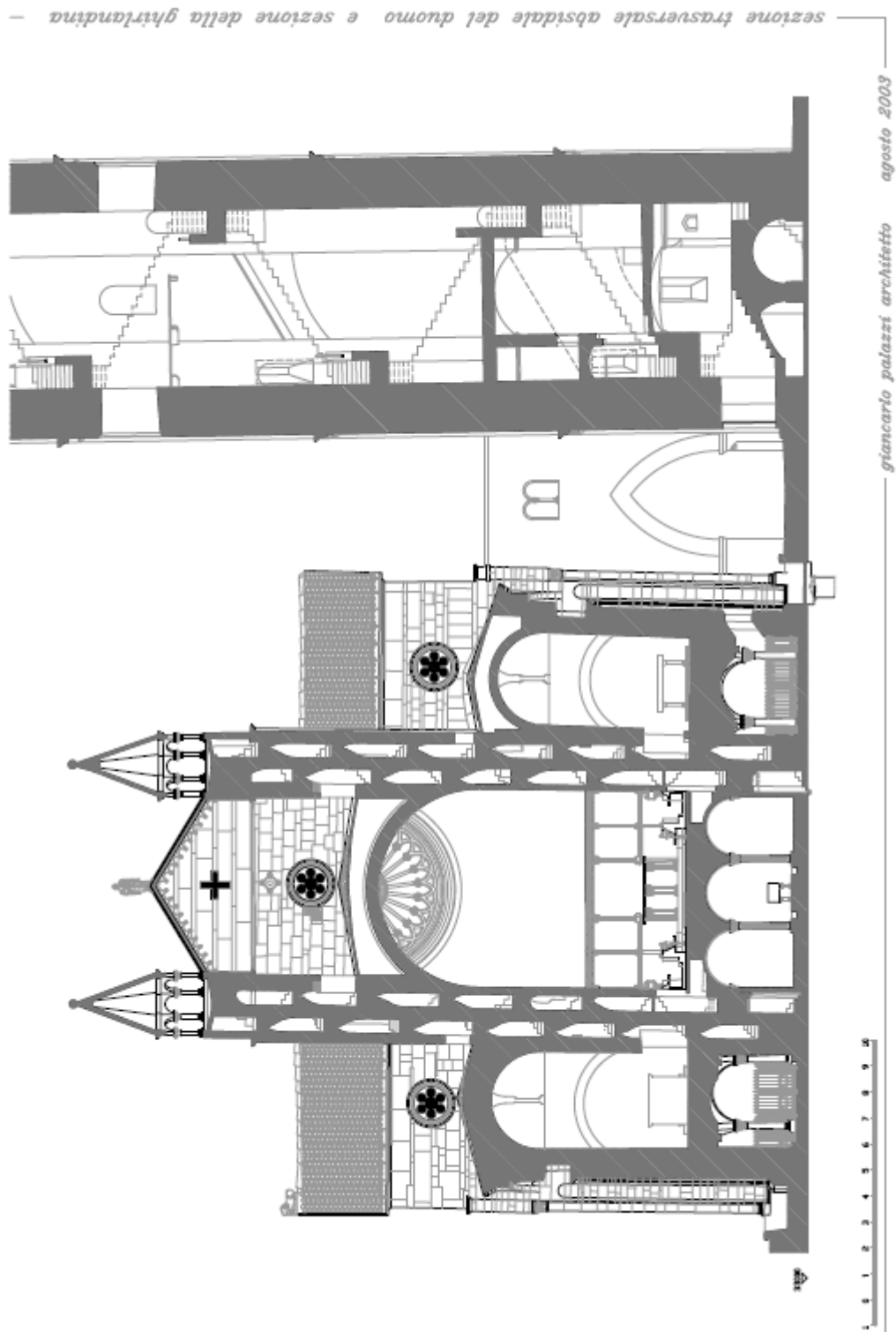
North facade of the Cathedral (Giancarlo Palazzi).



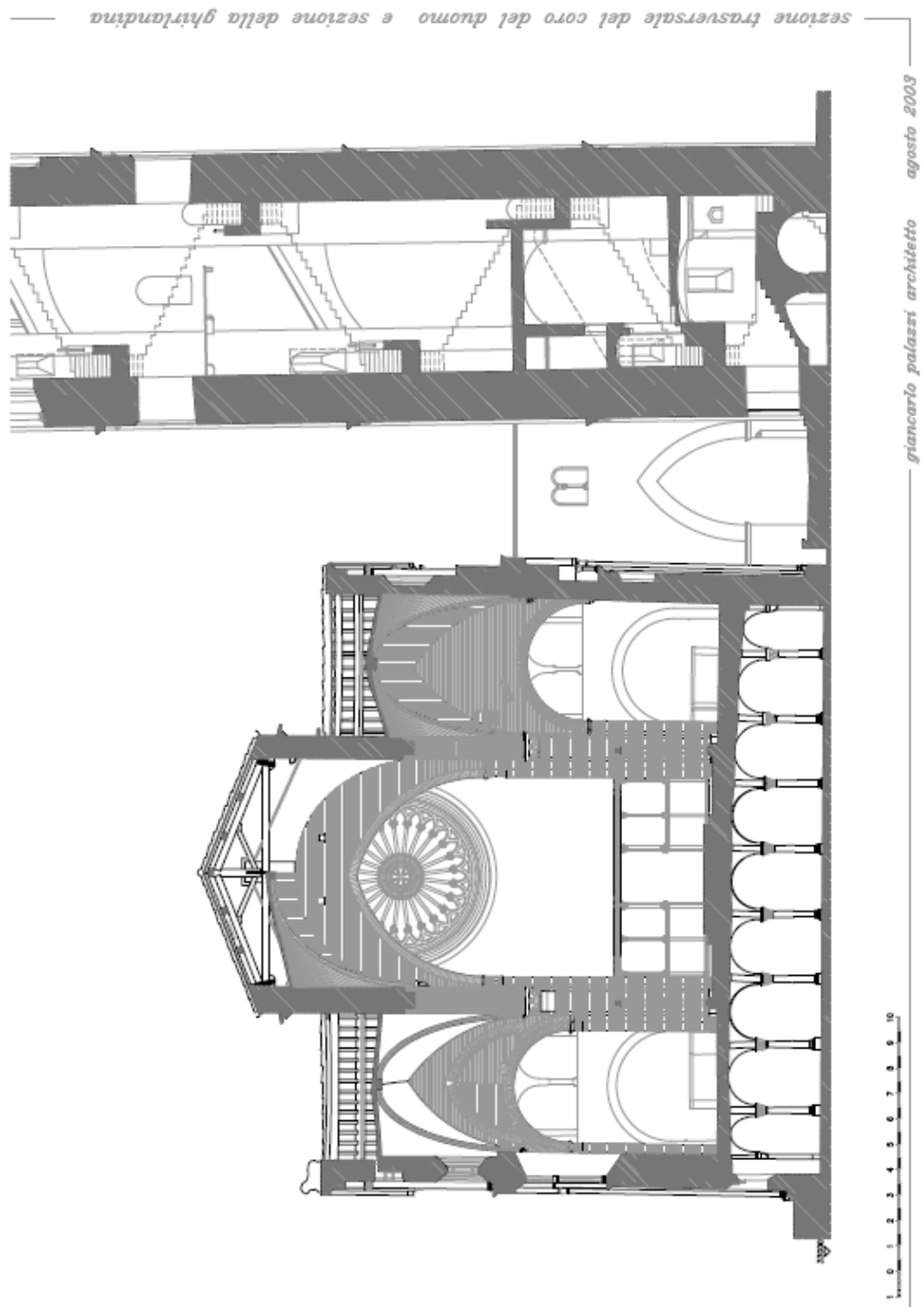
Median longitudinal section facing south (Giancarlo Palazzi).



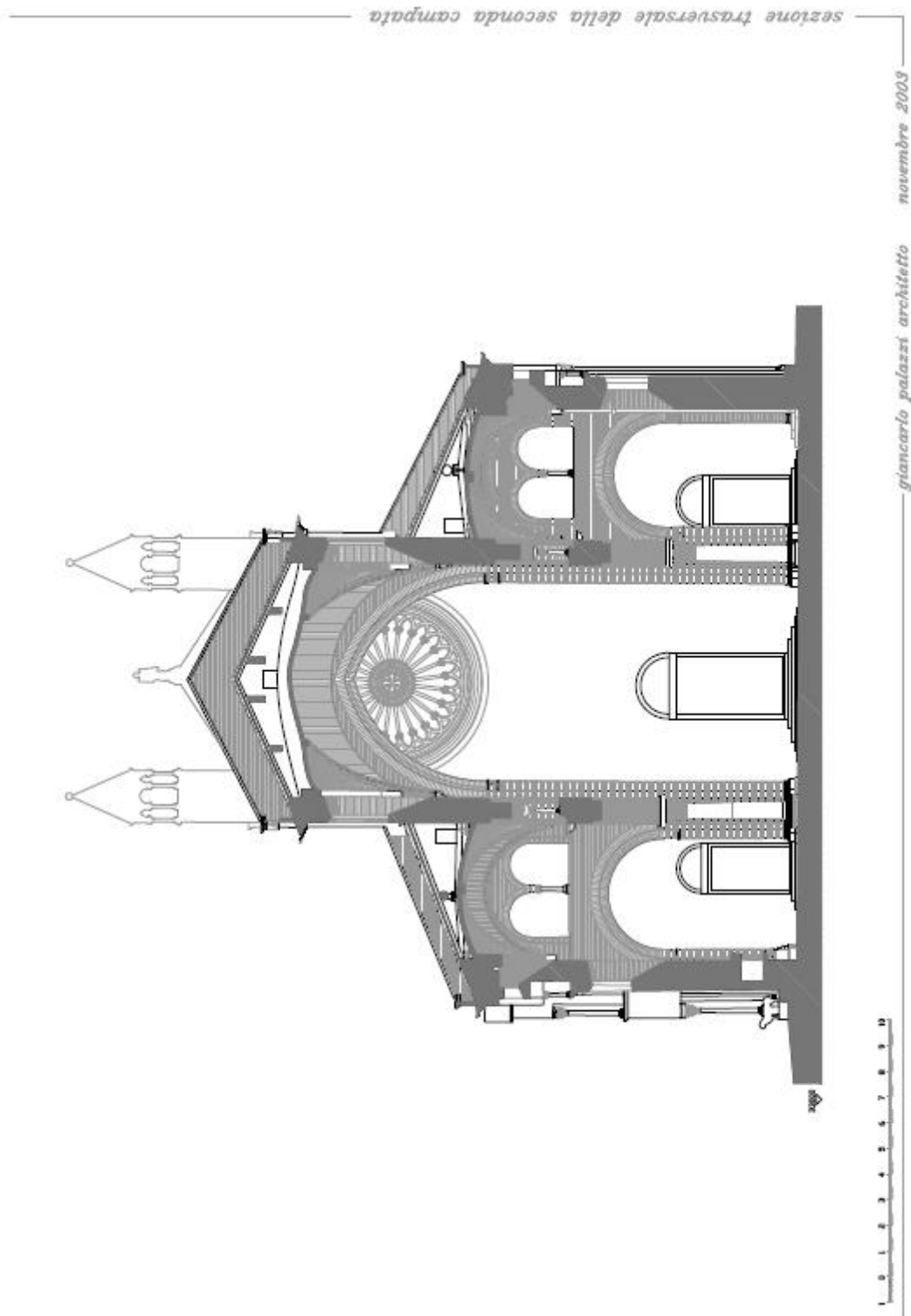
Apsidal cross section of the Cathedral and façade of the Ghirlandina (Giancarlo Palazzi).



Apsidal cross section of the Cathedral and section of the Ghirlandina (Giancarlo Palazzi).



Cross section of the Cathedral choir and section of the Ghirlandina (Giancarlo Palazzi).



Cross section of the second span (Giancarlo Palazzi).

Appendix B – Model Material

Table-1 – Initial and Updated material - Masonry

Material ID	ν	Initial model		Updated model	
		E (Pa)	ρ (Kg/m ³)	E (Pa)	ρ (Kg/m ³)
G-A1,2	0.2	2.00E+09	2000	3.00E+09	2398
G-A3	0.2	2.00E+09	2000	2.92E+09	2403
G-A4	0.2	2.00E+09	2000	2.93E+09	2404
G-A5	0.2	2.00E+09	2000	1.95E+09	2405
G-A6,7	0.2	2.00E+09	2000	3.01E+09	2402
G-B1	0.2	2.00E+09	2000	2.95E+09	2421
G-B3	0.2	2.00E+09	2000	1.28E+09	2408
G-B5	0.2	2.00E+09	2000	1.28E+09	2414
G-B7	0.2	2.00E+09	2000	1.94E+09	2457
G-C1	0.2	2.00E+09	2000	1.95E+09	2464
G-C3	0.2	2.00E+09	2000	1.33E+09	2635
G-C5	0.2	2.00E+09	2000	1.31E+09	2745
G-C7	0.2	2.00E+09	2000	1.30E+09	2487
G-D1	0.2	2.00E+09	2000	1.30E+09	2687
G-D3	0.2	2.00E+09	2000	1.27E+09	2455
G-D5	0.2	2.00E+09	2000	1.28E+09	2447
G-D7	0.2	2.00E+09	2000	1.28E+09	2581
G-E1	0.2	2.00E+09	2000	1.28E+09	2673
G-E3	0.2	2.00E+09	2000	1.30E+09	2881
G-E5	0.2	2.00E+09	2000	1.35E+09	2857
G-E7	0.2	2.00E+09	2000	1.35E+09	2540
G-F1	0.2	2.00E+09	2000	1.26E+09	2780
G-F3	0.2	2.00E+09	2000	1.27E+09	2466
G-F5	0.2	2.00E+09	2000	1.28E+09	2438
G-F7	0.2	2.00E+09	2000	1.35E+09	2567
G-G1	0.2	2.00E+09	2000	1.30E+09	2634
G-G3	0.2	2.00E+09	2000	1.32E+09	2881
G-G5	0.2	2.00E+09	2000	2.00E+09	2000
G-G7	0.2	2.00E+09	2000	2.05E+09	2713
G-H1	0.2	2.00E+09	2000	1.29E+09	2536



Material ID	ν	Initial model		Updated model	
		ρ (Kg/m ³)	ρ (Kg/m ³)	E (Pa)	ρ (Kg/m ³)
G-H3	0.2	2.00E+09	2000	1.28E+09	2420
G-H4	0.2	2.00E+09	2000	2.42E+09	2012
G-H5	0.2	2.00E+09	2000	1.28E+09	2410
G-H7	0.2	2.00E+09	2000	1.92E+09	2438
G-I1,2	0.2	2.00E+09	2000	1.26E+09	2412
G-I3	0.2	2.00E+09	2000	1.66E+09	2406
G-I5	0.2	2.00E+09	2000	1.28E+09	2406
G-I6,7	0.2	2.00E+09	2000	1.93E+09	2418
G-J1	0.2	2.00E+09	2000	1.27E+09	2429
G-J7	0.2	2.00E+09	2000	1.92E+09	2416
G-K1,2	0.2	2.00E+09	2000	1.27E+09	2433
G-K3	0.2	2.00E+09	2000	1.24E+09	2433
G-K4	0.2	2.00E+09	2000	1.23E+09	2428
G-K5	0.2	2.00E+09	2000	1.24E+09	2434
G-K6,7	0.2	2.00E+09	2000	1.93E+09	2421
L1-A1,2	0.2	2.00E+09	2000	3.32E+09	2879
L1-A3	0.2	2.00E+09	2000	3.04E+09	2901
L1-A4	0.2	2.00E+09	2000	3.14E+09	2933
L1-A5	0.2	2.00E+09	2000	2.03E+09	2910
L1-A6,7	0.2	2.00E+09	2000	3.35E+09	2887
L1-B1	0.2	2.00E+09	2000	1.98E+09	2838
L1-B3	0.2	2.00E+09	2000	1.27E+09	2885
L1-B5	0.2	2.00E+09	2000	1.26E+09	2929
L1-B7	0.2	2.00E+09	2000	1.20E+09	2901
L1-C1,2	0.2	2.00E+09	2000	2.05E+09	2861
L1-C3	0.2	2.00E+09	2000	1.30E+09	2896
L1-C5	0.2	2.00E+09	2000	1.27E+09	2971
L1-C6,7	0.2	2.00E+09	2000	1.99E+09	2943
L1-D1	0.2	2.00E+09	2000	1.13E+09	2986
L1-D3	0.2	2.00E+09	2000	1.22E+09	2990
L1-D5	0.2	2.00E+09	2000	1.23E+09	2991
L1-D7	0.2	2.00E+09	2000	1.11E+09	2984
L1-E1,2	0.2	2.00E+09	2000	1.37E+09	2985
L1-E3	0.2	2.00E+09	2000	1.24E+09	2987
L1-E5	0.2	2.00E+09	2000	1.30E+09	2955
L1-E6,7	0.2	2.00E+09	2000	2.06E+09	2936
L1-F1	0.2	2.00E+09	2000	1.06E+09	2983
L1-F3	0.2	2.00E+09	2000	1.23E+09	2989



Material ID	ν	Initial model		Updated model	
		E (Pa)	ρ (Kg/m ³)	E (Pa)	ρ (Kg/m ³)
L1-F5	0.2	2.00E+09	2000	1.25E+09	2930
L1-F7	0.2	2.00E+09	2000	1.19E+09	2908
L1-G1,2	0.2	2.00E+09	2000	1.42E+09	2964
L1-G3	0.2	2.00E+09	2000	1.28E+09	2992
L1-G5	0.2	2.00E+09	2000	1.33E+09	2886
L1-G6,7	0.2	2.00E+09	2000	2.16E+09	2824
L1-H1	0.2	2.00E+09	2000	1.18E+09	2897
L1-H3	0.2	2.00E+09	2000	1.25E+09	2922
L1-H5	0.2	2.00E+09	2000	1.26E+09	2885
L1-H7	0.2	2.00E+09	2000	1.25E+09	2820
L1-I1,2	0.2	2.00E+09	2000	1.98E+09	2882
L1-I3	0.2	2.00E+09	2000	1.98E+09	2887
L1-I4	0.2	2.00E+09	2000	1.93E+09	2882
L1-I5	0.2	2.00E+09	2000	2.03E+09	2884
L1-I6,7	0.2	2.00E+09	2000	2.00E+09	2015
L1-J1	0.2	2.00E+09	2000	3.28E+09	2895
L1-J2	0.2	2.00E+09	2000	1.93E+09	2883
L1-J3	0.2	2.00E+09	2000	1.28E+09	2884
L1-J4	0.2	2.00E+09	2000	1.92E+09	2885
L1-J5	0.2	2.00E+09	2000	1.27E+09	2883
L1-J6	0.2	2.00E+09	2000	1.28E+09	2883
L1-J7	0.2	2.00E+09	2000	1.96E+09	2880
L1-K1,2	0.2	2.00E+09	2000	2.00E+09	2905
L1-K3	0.2	2.00E+09	2000	1.23E+09	2925
L1-K4	0.2	2.00E+09	2000	1.21E+09	2922
L1-K5	0.2	2.00E+09	2000	1.24E+09	2927
L1-K6,7	0.2	2.00E+09	2000	1.97E+09	2901
L2-A1,2	0.2	2.00E+09	2000	2.98E+09	2880
L2-A3	0.2	2.00E+09	2000	2.04E+09	2990
L2-A4	0.2	2.00E+09	2000	3.05E+09	2987
L2-A5	0.2	2.00E+09	2000	2.05E+09	2989
L2-A6,7	0.2	2.00E+09	2000	2.99E+09	2896
L2-B1	0.2	2.00E+09	2000	1.96E+09	1229
L2-B2	0.2	2.00E+09	2000	1.96E+09	1914
L2-B3	0.2	2.00E+09	2000	2.00E+09	1852
L2-B4	0.2	2.00E+09	2000	3.00E+09	2869
L2-B5	0.2	2.00E+09	2000	2.00E+09	2817
L2-B6	0.2	2.00E+09	2000	1.96E+09	2875



Material ID	ν	Initial model		Updated model	
		E (Pa)	ρ (Kg/m ³)	E (Pa)	ρ (Kg/m ³)
L2-B7	0.2	2.00E+09	2000	1.96E+09	2827
L2-C1,2	0.2	2.00E+09	2000	1.32E+09	1828
L2-C3	0.2	2.00E+09	2000	1.22E+09	1781
L2-C4	0.2	2.00E+09	2000	1.12E+09	1839
L2-C5	0.2	2.00E+09	2000	1.21E+09	1888
L2-C6,7	0.2	2.00E+09	2000	1.31E+09	2752
L2-D1	0.2	2.00E+09	2000	1.32E+09	2721
L2-D2	0.2	2.00E+09	2000	1.25E+09	2846
L2-D3	0.2	2.00E+09	2000	1.18E+09	1656
L2-D4	0.2	2.00E+09	2000	1.30E+09	1871
L2-D5	0.2	2.00E+09	2000	1.14E+09	1662
L2-D6	0.2	2.00E+09	2000	1.25E+09	2675
L2-D7	0.2	2.00E+09	2000	2.00E+09	2000
L2-E1,2	0.2	2.00E+09	2000	1.18E+09	2697
L2-E3	0.2	2.00E+09	2000	1.07E+09	2066
L2-E4	0.2	2.00E+09	2000	1.05E+09	1762
L2-E5	0.2	2.00E+09	2000	1.06E+09	1669
L2-E6,7	0.2	2.00E+09	2000	1.19E+09	1765
L2-F1	0.2	2.00E+09	2000	1.27E+09	2787
L2-F2	0.2	2.00E+09	2000	1.25E+09	2853
L2-F3	0.2	2.00E+09	2000	1.16E+09	1760
L2-F4	0.2	2.00E+09	2000	1.27E+09	1867
L2-F5	0.2	2.00E+09	2000	1.18E+09	1610
L2-F6	0.2	2.00E+09	2000	1.24E+09	1898
L2-F7	0.2	2.00E+09	2000	1.29E+09	1829
L2-G1,2	0.2	2.00E+09	2000	1.23E+09	2687
L2-G3	0.2	2.00E+09	2000	1.16E+09	2483
L2-G4	0.2	2.00E+09	2000	1.04E+09	1787
L2-G5	0.2	2.00E+09	2000	1.16E+09	1717
L2-G5,6	0.2	2.00E+09	2000	1.29E+09	1772
L2-H1	0.2	2.00E+09	2000	1.29E+09	2729
L2-H2	0.2	2.00E+09	2000	1.32E+09	2855
L2-H3	0.2	2.00E+09	2000	1.43E+09	1759
L2-H4	0.2	2.00E+09	2000	2.01E+09	1895
L2-H5	0.2	2.00E+09	2000	1.35E+09	1764
L2-H6	0.2	2.00E+09	2000	1.93E+09	1908
L2-H7	0.2	2.00E+09	2000	1.96E+09	1819
L2-I1,2	0.2	2.00E+09	2000	3.33E+09	1889



Material ID	ν	Initial model		Updated model	
		E (Pa)	ρ (Kg/m ³)	E (Pa)	ρ (Kg/m ³)
L2-I3	0.2	2.00E+09	2000	2.01E+09	2848
L2-I4	0.2	2.00E+09	2000	1.98E+09	2869
L2-I5	0.2	2.00E+09	2000	1.99E+09	1890
L2-I6,7	0.2	2.00E+09	2000	3.05E+09	1865
L2-J1	0.2	2.00E+09	2000	3.30E+09	1915
L2-J2	0.2	2.00E+09	2000	1.92E+09	2882
L2-J3	0.2	2.00E+09	2000	1.27E+09	2963
L2-J4	0.2	2.00E+09	2000	2.91E+09	2903
L2-J5	0.2	2.00E+09	2000	1.27E+09	2951
L2-J6	0.2	2.00E+09	2000	1.93E+09	1978
L2-J7	0.2	2.00E+09	2000	1.94E+09	1885
L2-K1,2	0.2	2.00E+09	2000	3.02E+09	2936
L2-K3	0.2	2.00E+09	2000	1.93E+09	2980
L2-K4	0.2	2.00E+09	2000	2.94E+09	2980
L2-K5	0.2	2.00E+09	2000	1.92E+09	2980
L2-K6,7	0.2	2.00E+09	2000	1.93E+09	2943
T-B2	0.2	2.00E+09	2000	1.96E+09	1271
T-B4	0.2	2.00E+09	2000	1.29E+09	2870
T-B6	0.2	2.00E+09	2000	1.98E+09	2394
T-D2	0.2	2.00E+09	2000	1.27E+09	1892
T-D4	0.2	2.00E+09	2000	1.25E+09	1879
T-D6	0.2	2.00E+09	2000	1.23E+09	1890
T-F2	0.2	2.00E+09	2000	1.24E+09	2824
T-F4	0.2	2.00E+09	2000	1.25E+09	1876
T-F6	0.2	2.00E+09	2000	1.24E+09	1886
T-H2	0.2	2.00E+09	2000	1.96E+09	1904
T-H4	0.2	2.00E+09	2000	1.95E+09	1899
T-H6	0.2	2.00E+09	2000	1.95E+09	1903
T-J2	0.2	2.00E+09	2000	1.92E+09	2637
T-J4	0.2	2.00E+09	2000	1.92E+09	2901
T-J6	0.2	2.00E+09	2000	1.92E+09	2091

Table 2 – Initial and Updated material – Truss Ghirlandina Tower

Material ID	ν	Initial model		Updated model	
		E (Pa)	Area (m ²)	E (Pa)	Area (m ²)
Ghirlandina_1	0.2	2.00E+09	2.8	1.84E+09	3.76
Ghirlandina_2	0.2	2.00E+09	2.8	2.89E+09	4.04
Ghirlandina_3	0.2	2.00E+09	2.8	2.77E+09	4.03
Ghirlandina_4	0.2	2.00E+09	2.8	1.73E+09	2.44
Ghirlandina_5	0.2	2.00E+09	2.8	2.88E+09	4.04
Ghirlandina_6	0.2	2.00E+09	2.8	2.49E+09	3.52
Ghirlandina_7	0.2	2.00E+09	2.8	2.58E+09	3.69
Ghirlandina_8	0.2	2.00E+09	2.8	2.92E+09	4.10

Table 3 – Tie-rods properties (for the position refer to chapter 5.5.3)

Material ID	ν	E (Pa)	Diameter (mm)
Model type A	0.3	2.10E+011	32
Model type B	0.3	2.10E+011	38
Model type C	0.3	2.10E+011	28
Model type D	0.3	2.10E+011	26
Model type E	0.3	2.10E+011	32
Model type F	0.3	2.10E+011	30

Bibliography

- [1] d. M. d. I. e. d. T. Consiglio Superiore dei Lavori Pubblici, *Linee Guida per la valutazione e riduzione del rischio sismico del patrimonio culturale con riferimento alle norme tecniche per le costruzioni*, Roma, 2006.
- [2] G. Di Pasquale and S. Papa, *Manuale per la compilazione della scheda per il rilievo del danno ai beni culturali, Chiese MODELLO A – DC*, Presidenza del consiglio dei ministri - Dipartimento della protezione civile.
- [3] R. Antonucci, *Restauro e recupero degli edifici a struttura muraria, Analisi e interventi sul "costruito storico"*, Rimini: Maggioli Editore, 2009.
- [4] R. Parenti, *Una proposta di classificazione tipologica delle murature postclassiche - Atti del Convegno "Conoscenze e sviluppi teorici per la conservazione di sistemi tradizionali in muratura"*, Bressanone, 1987.
- [5] A. Giuffrè, *Lecture sulla meccanica delle murature storiche*, Roma: Kappa, 1991.
- [6] S. Bufarini, V. D'Aria and D. Squillacioti, *Meccanica delle murature, Dalla definizione della qualità muraria alle indagini sperimentali mediante la tecnica dei martinetti piatti*, Roma: EPC editore, 2012.
- [7] G. Margani, *Costruzione e recupero dell'opera muraria, "regole dell'arte" e interventi di consolidamento*, Enna: IL LUNARIO, 2009.

-
- [8] G. Cangi, *Manuale del recupero strutturale e antisismico*, Roma: DEI, tipografia del genio civile, 2012.
- [9] D. Abrams and S. McNary, *Mechanics of masonry in compression*, vol. *Journal of structural engineering*, ASCE, 1985.
- [10] B. P. Amedei, R. H. Atkinson, S. Sture and S. Saeb, *Response of masonry bed joints in direct shear*, vol. *Journal of Structural Engineering*, ASCE, 1989.
- [11] R. Van Der Pluijm, *Material properties and its components under tension and shear*, Vols. Proc., 6th Can. Masonry Symp., Canada: Saskatoon, 1992.
- [12] R. Van Der Pluijm, *Shear behaviour of bed joints*, Vols. Proc., 6th North Am. Masonry Conf., Philadelphia, 1993.
- [13] C. Khoo, *A failure criterion for brickwork in axial compression*, vol. Ph.D. thesis University of Edinburgh, Edinburgh, Scotland, 1972.
- [14] H. Hilsdorf, *Investigation into the failure of brick masonry loaded in axial compression*, Vols. *Designing, Engineering, and constructing with masonry*, Gulf Publishing Co., 1969.
- [15] L. Binda, G. M. Roberti and C. Tiraboschi, *Problemi di misura dei parametri meccanici della muratura e dei suoi componenti*, Vols. *Atti del Convegno Nazionale, La Meccanica delle Murature tra Teoria e Progetto*, Messina, 1996.
- [16] A. Page, *A finite element model for masonry*, vol. *Journal of the Structural Division*, ASCE, 1978.
- [17] J. Colville and W. Samarasinghe, *Finite element model for brick masonry*, USA: University of Maryland, 1991.
- [18] A. J. Francis, C. B. Horman and L. E. Jerrems, *The effect of joint thickness and other factors on the compressive strength of brickwork*, vol. Proc. 2nd International Brick Masonry Conference, Melbourne: British Ceramic Research Assoc., 1970.
-



- [19] H. P. Backes, *Tensile strength of the masonry*, Germany: Technical University of Aachen, 1985.
- [20] A. W. Page, *An experimental investigation of the biaxial strength of brick masonry*, Newcastle, Australia, 1980.
- [21] M. Dhanasekar, P. W. Kleeman and A. W. Page, *Biaxial stress-strain relations for brick masonry*, vol. *Journal of structural engineering*, ASCE, 1985.
- [22] P. Lourenco, *Computational Strategy for Masonry Structures*, Netherlands: Delft University Press, 1996.
- [23] H. R. Lofti and P. B. Shing, *Interface model applied to fracture of masonry structure*, ASCE, 1994.
- [24] C. Baggio and P. Trovalusci, *Discrete models for jointed block masonry walls*, Philadelphia, Pennsylvania, 1993.
- [25] P. Lourenço and J. Rots, *Multisurface interface model for analysis of masonry structures*, ASCE, 1997.
- [26] G. Giambanco, S. Rizzo and R. Spallino, *Numerical analysis of masonry structures via interface models*, Palermo: Elsevier Science, 2001.
- [27] S. Pietruszczak and X. Niu, *A mathematical description of macroscopic behaviour of the brick masonry*, Canada: McMaster University, 1991.
- [28] G. Alpa and I. Monetto, *Microstructural model for dry block masonry walls with in-plane loading*, Genova: Elsevier Science, 1994.
- [29] U. Andreaus, *Failure criteria for masonry panels under in-plane loading*, *Journal of structural engineering*, 1996.
- [30] R. Luciano and E. Sacco, *Homogenization technique and damage model for old masonry material*, Cassino: Elsevier Science, 1996.

- [31] P. Lourenco, R. De Borst and J. Rots, A plane stress softening plasticity model for orthotropic materials, Netherlands: International journal for numerical methods in engineering, 1997.
- [32] L. Gambarotta and S. Lagomarsino , Damage models for the seismic response of brick masonry shear walls. Part II: The continuum model and its applications, Genova: Earthquake engineering and structural dynamics, 1997.
- [33] G. Valenzano e G. Lorenzoni, Il duomo di Modena e la basilica di San Zeno, Verona - Modena: Banca Popolare di Verona - Banco S. Geminiano e S. Prospero., 2000.
- [34] E. Silvestri, Una rilettura delle fasi costruttive del Duomo di Modena, Vols. Atti e Memorie, Serie XI, Vol.XXXV, Deputazione di Storia Patria per le antiche province modenesi, Modena: Aedes Muratoriana, 2013.
- [35] R. Lancellotta and D. Sabia, Monitoraggio sismico del Duomo di Modena, Rapporto sulla installazione del sistema di monitoraggio, Torino: Politecnico di Torino, 2015.
- [36] F. Gandolfo, Il cantiere dell'architetto Lanfranco e la cattedrale del vescovo Eriberto, Viella, 1989.
- [37] G. Bertoni, La cattedrale modenese preesistente all'attuale, Modena: U. Orlandini, 1914.
- [38] A. Peroni, L'architetto Lanfranco e la struttura del duomo, in Lanfranco e Wiligelmo. Il duomo di Modena, Modena: Panini, 1985.
- [39] A. K. Porter, Lombard Architecture, New Haven: Yale University Press, 1917.
- [40] P. Frankl, Der Dom in Modena, 1927.

- [41] W. Montorsi, Riedificazione del Duomo di Modena e traslazione dell'arca di San Geminiano: cronaca e miniature della prima età romanica, Modena: Aedes Muratoriana, 1984.
- [42] F. Gandolfo, Problemi della cattedrale di Modena, in "Commentari", 1971.
- [43] A. Peroni, Architettura e scultura: aggiornamenti, in Wiligelmo e Lanfranco nell'Europa romanica, Vols. Atti del convegno (Modena, 24-27 ottobre 1985), Modena: Franco Cosimo Panini, 1989.
- [44] M. Armandi, Copie e originali. Il repertorio di mensole figurate del Duomo di Modena, vol. Il Duomo di Modena, 1999.
- [45] S. Lomartire, Analisi dei paramenti murari del Duomo di Modena, Modena: Panini, 1985.
- [46] A. Peroni, Il Duomo di Modena. Atlante grafico, Rilievi architettonici e topografici di Giancarlo Palazzi, Rilievo fotogrammetrico di Lamberto Ippolito, Modena: Panini, 1988.
- [47] R. Lancellotta, Aspetti geotecnici nella conservazione della torre, in La torre Ghirlandina: un progetto per la conservazione, R. Cadignani, Ed., Roma: Sossella, 2009.
- [48] S. T. Silvestri, Studio dei dissesti, Relazione sui danni dei sismi di maggio 2012, Messa in sicurezza post sismi maggio 2012, Modena, 2012.
- [49] M. Armandi, Il Duomo di Modena, Atlante fotografico, Fotografie di Cesare Leonardi, Modena: Panini, 1985.
- [50] C. Colla, Prove soniche non distruttive presso il Duomo di Modena, Bologna: DICAM Università di Bologna, 2010.
- [51] S. Silvestri, S. Baraccani, M. Palermo, A. Montanari and T. Trombetti, Valutazione della sicurezza strutturale del Duomo di Modena - ACQUISIZIONE DELLE CONOSCENZE -

- DOCUMENTO 1, Bologna: Dipartimento di ingegneria civile, ambientale e dei materiali - Università di Bologna, 2015.
- [52] S. Baraccani, S. Silvestri, G. Gasparini, M. Palermo, T. Trombetti, E. Silvestri, R. Lancellotta and A. Capra, *A Structural Analysis of the Modena Cathedral*, Taylor&Francis, 2016.
- [53] C. Castagnetti, A. Capra and E. Silvestri, *Diagnostic Use of Laser Scanning Data to Identify Current and Historical Deformations and Geometries: the case of the Modena Cathedral*, Reggio Emilia, 2016.
- [54] A. Capra, E. Bertacchini, C. Castagnetti, R. Rivola and M. Dubbini, *Recent approaches in geodesy and geomatics for structures monitoring*, Springer, 2015.
- [55] A. Simulia, *ABAQUS Theory Manual - Online Documentation*, ABAQUS, Inc., 2006.
- [56] D. Sabia, T. Aoki, R. Cosentini and R. Lancellotta, *Model Updating to Forecast the Dynamic Behavior of the Ghirlandina Tower in Modena, Italy: Journal of Earthquake Engineering*, Vol.19, Issue 1, pp.1-24, 2015.1.
- [57] D. Sabia, T. Aoki and D. Rivella, *Influence of experimental data and FE model on updating results of a brick chimney*, Elsevier, 2007.
- [58] M. Friswell and J. Mottershead, *Finite element model updating in structural dynamics*, Dordrecht : Kluwer Academic, 1995.
- [59] G. Pascale and C. Colla, *Caratterizzazione meccanica della muratura della torre Ghirlandina di Modena*, Bologna: Università di Bologna e Comune di Modena.
- [60] S. Baraccani, M. Palermo, S. Silvestri, G. Gasparini, T. Trombetti and E. Silvestri, *The structural strengthening of the Cathedral of Modena*, Bologna, 2015.
-